TESI DI DOTTORATO DI RICERCA IN COTUTELA
THÈSE DE DOCTORAT EN COTUTELLE

Università degli studi di Milano
Corso di Dottorato in Fisica, Astrofisica e Fisica Applicata
Ciclo XXXVIII
Dipartimento di Fisica

Université de Caen Normandie
Ecole Doctorale PSIME 591
LPC Caen

Bayesian inference on nuclear data and neutron star observations for the nuclear equation of state

Dottorando/Docorant: Pietro Klausner
Matr. [R14001]

Direttore di Tesi (Milano):
Prof. Gianluca Colò

Directrice de Thèse (Caen):
Prof. Francesca Gulminelli

Coordinatori del Dottorato / Coordinateur du Doctorat: Prof. Aniello Mennella (UniMi), Prof. Alexandre Vivet (ED PSIME 591)

A.A. 2024/2025

Referees of the thesis:

Prof. William G. Newton
Department of Physics and Astronomy, Texas A&M University-Commerce, Commerce, 75429, Texas, United States of America

Dr. Esra Yüksel,
School of Mathematics and Physics, University of Surrey, Guildford, Surrey GU2 7XH, United Kingdom

Commission of the final examination:

Prof. Gianluca Colò
Dipartimento di Fisica, Università degli Studi di Milano, Milano, Italy

Prof. Francesca Gulminelli
Université de Caen Normandie, ENSICAEN, CNRS/IN2P3, LPC Caen UMR6534, 14000 Caen, France

Prof. Niels Paar
Department of Physics, Faculty of Science, University of Zagreb, Bijenička cesta 32, HR-10000 Zagreb, Croatia

Dr. Esra Yüksel,
School of Mathematics and Physics, University of Surrey, Guildford, Surrey GU2 7XH, United Kingdom

Dr. Wouter Ryssens
Institut d'Astronomie et d'Astrophysique, Université Libre de Bruxelles, Brussels, Belgium

Dr. Anthea Francesca Fantina
Grand Accélérateur National d'Ions Lourds (GANIL), CEA/DRF – CNRS/IN2P3, Boulevard Henri Becquerel, 14076 Caen, France

Final examination:

Date: 9$^{\text{th}}$ December 2025

Dipartimento di Fisica, Università degli Studi di Milano, 20133 Milano, Italy

MIUR subject:

PHYS/02 - Nuclear and subnuclear physics

PACS:

21.60.Jz, 21.65.Mn, 21.60.Ka

Contents

List of Acronyms

BCS: Bardeen Cooper Schrieffer
BNM: Binary Neutron star Merger
CLDM: Compressible Liquid Drop Model
DFT: Density Functional Theory
EDF: Energy Density Functional
EOS: Equation Of State
ETF: Extended Thomas Fermi
GP: Gaussian Process
HF: Hartree–Fock
HFB: Hartree Fock Bogoliubov
KS: Kohn–Sham
MH: Metropolis Hastings
MM: Meta Model
nEOS: nuclear Equation Of State
NMP: Nuclear Matter Parameter
NS: Neutron
PNM: Pure Neutron Matter
RMF: Relativistic Mean Field
RPA: Random Phase Approximation
SNM: Symmetric Nuclear Matter
TOV: Tolman–Oppenheimer–Volkoff

List of Figures

List of Tables

Introduction

Almost a century after its birth, nuclear physics still has several unanswered questions. First and foremost, the Hamiltonian representing two- and three-body nuclear interactions is not accurately known; and, even if it were perfectly known, the nucleus is a composite system and one is left with the daunting task of solving the many-body problem. In this regard, the mean field approach has known great success since its first implementation.

Born as an implementation of the Hartree–Fock (HF) theory [1], this approach was later reframed within the density functional theory (DFT) [2, 3], which was originally developed for atomic systems [4, 5]. The DFT theorem proves that, for a fermionic system, the total energy is a universal functional of its density, the so-called energy density functional (EDF), whose minimum, corresponding to the ground state energy, is found at the ground state density. Although the DFT theorem ensures the existence of the true EDF, it does not give any indication on how to build it. The DFT can be extended to nuclear systems [5–7] and the search of the elusive true one has given birth to several approximations, like the Skyrme, the Gogny, and the relativistic EDF [1, 8, 9], to cite the most famous, or the less employed Fayans [10]. These functionals have around ten-fifteen parameters, to be adjusted to reproduce experimental data. We will mainly focus on Skyrme, with a brief mention to Fayans.

Canonically, the first efforts tried to reproduce ground state properties of nuclei, like their binding energies and radii [1]. On the other hand, since several decades we also have several data on the response properties of nuclei, which are mainly probed through giant resonances [11]. These modes, which can be described as collective excitations where all the nucleons in the system participate, are yet another interesting property that can be described within the EDF framework. The parameters of the EDFs are fitted to these data to achieve the description of finite nuclei properties. Nevertheless, all this information also opens a window on the behaviour of the so-called nuclear matter [12]. Nuclear matter is an idealized system composed of neutrons and protons, where particles interact just through the nuclear force; its properties are abridged in the so-called nuclear equation of state (nEOS), i.e., the energy per particle as a function of the total baryon density of such system, whose functional form is derived from the EDFs. To a first approximation, nuclear matter is realized within the interior of nuclei, where surface effects do not play yet a predominant role, and nuclear experiments offer us insight on its features. For instance, in the giant monopole resonance [13] nuclei vibrate, expanding and compressing. The excitation energy of this mode is linked to the compressibility of nuclear matter which can be expressed as the second derivative of the nEOS. However, nuclei explore a limited set of densities, up around the so called saturation density n_{sat}, $n_{sat} \sim 0.16$ fm^{-3}, and are mainly composed of symmetric matter, i.e., with similar neutron and proton densities.

Cold neutron stars (NS), on the other hand, offer the opportunity to go beyond this density instead. These stars, one of the possible final stages of massive stars, have between 1 and 2 solar masses $M_\odot$, within a radius of the order of 10–15 km. Their internal densities may well be beyond n_{sat}, and, beside a thin crustal layer, they are composed by an admixture of neutrons, protons, electrons and muons to guarantee charge neutrality [14, 15]. The relative abundances are regulated by the $\beta-$equilibrium; in general, as the name suggests, NS are predominantly made of neutrons. Their macroscopic properties, like their mass [14, 16], radius [17, 18] and deformability [19, 20], depend uniquely on the star equation of state (EOS), which, in turn, depends on the nEOS, that summarizes the underlying assumption of the properties of nuclear matter, summarized in the nEOS. There is therefore a one to one connection between the nEOS and the observable properties of NSs and astronomical observations offer the unique opportunity of constraining nuclear matter properties at densities far beyond those achievable in terrestrial experiments.

Many existing works in the literature study the nEOS using input from both nuclear physics and astrophysics. However, often nuclear experiments are taken into account by simply inferring constraints on parameters of the nEOS, neither keeping track of the underlying correlations, nor controlling whether different nuclear observables can be reproduced simultaneously [21–26].

So, to overcome both these limitations, we will employ statistics techniques offered by the Bayesian inference framework. Bayesian inference [27, 28] offers detailed information on the probability distribution of the model parameters which best reproduce a particular set of experimental data. However, as it is a completely numerical method, it is feasible only if the computational model one is using requires negligible computational time. For this reason, we will employ extensively Gaussian Process emulators [29, 30] to speed up considerably our calculation, and keep the Bayesian process feasible time wise. Gaussian Process emulators are software that, given some representative results of the computer program in question, are able to mimic it at a fraction of the computational cost.

Our starting point will be the Skyrme EDF [31], which we use as a base model for a Bayesian inference with an comprehensive set of nuclear data from spherical nuclei, both doubly magic and open shell. Such data include both ground state properties (binding energies, radii, and spin-orbit splittings [32–34]) and collective excitations (polarizability, giant resonances [35–37]), all computed at the HF or RPA level. Furthermore, we include the much discussed parity-violating asymmetry in electron scattering [38, 39], which is a relatively model-independent probe of the leading parameters of the neutron distribution, thus entailing important consequences for NS [40, 41]. The result of this first analysis is a probability distribution of the Skyrme parametrization, all compatible with the data used in the inference. From this distribution, we infer statistical information on the behaviour of the nEOS in terms of its parameters, the so-called nuclear matter parameters (NMP).

Consequently, we can use this distribution as a base for a successive Bayesian inference, where this time the constraints come from astrophysical observations. Employing directly the Skyrme nEOS would be unwise, as its sub saturation density behaviour fixes the super saturation one. Instead we use a meta model (MM) representation [42, 43], which allows us to break this spurious correlation. The MM parameters are the NMP and the mapping between Skyrme and MM ensures the same behaviour of the nEOS below n_{sat}, thus maintaining the information from nuclear physics, but allows a radical different one above. The NS EOS is computed with this MM equivalent, and the relevant NS properties are compared with astronomical observations.

Approaching the problem in this way ensures that, on the one hand, the underlying correlation between parameters of the nEOS are exactly accounted for, and that, on the other hand, we do not compromise on the ability to reproduce nuclear observables. The final probability distribution on nEOS parameters is informed by both nuclear physics and astrophysics.

This Thesis is structured as follows. The first two chapters serve as an introduction to the nuclear DFT (Chapter 1) and to NSs (Chapter 2). Both contain all the basic information one needs to follow and appreciate the results presented later. Chapter 3 gives elementary information on Bayesian statistics, Bayesian inferences and emulator theory. It is devised to give the inexpert reader the essential facts of these techniques, that we employ extensively. In Chapter 4 we show the results on our nuclear inference. It dives into the methodology, and then offers a detailed discussion about the results, with a careful comparison with the literature. In Chapter 5 we present the results of the astrophysical inference, and explores the consequences the nuclear physics brings to the study of the NS EOS. Finally, in Chapter 6 we give the final conclusions and the outlook of the Thesis.

Ending the manuscript there will be a substantial *résumé* of the Thesis, in both Italian and French.

CHAPTER 1

Nuclear Theory

The challenge in describing nuclear systems is two-fold: on the one hand, the underlying nucleon-nucleon interaction is not known exactly; on the other hand, nuclei are many-body systems. Even if the actual Hamiltonian were known, the task would be extremely challenging, as it is in Coulomb systems, where the Hamiltonian is simpler.

Numerous research efforts have been devoted to tackling the nuclear many-body problem. The strategies employed are varied, and range from mean-field techniques within the energy density functional (EDF) framework to more sophisticated *ab-initio* computations.

An important part of this research focuses on optimising EDFs to describe nuclear properties. In this chapter, we will present the basics of density functional theory in Section 1.1, how it applies to nuclear systems, and how well it can reproduce experimental data (Sections 1.2 and 1.3). Then, we will proceed to develop the mathematical formalism behind the Skyrme functional in Sections 1.4. The final Section 1.5 is dedicated to an overview of nuclear matter.

1.1 Density functional theory

Density functional theory (DFT) lies on the Hohenberg-Kohn theorem [4], originally derived for electronic systems. Given a system in an external potential V_e, its energy E can be written as

$$E = \langle\Psi|\, T + V + V_e \,|\Psi\rangle \tag{1.1}$$

where T is the kinetic operator, V accounts for the interaction among electrons and $|\Psi\rangle$ is the ground state.

Now, in atoms and molecules, the total number of electrons N and the external potential V_e completely determine the physical problem, as the first fixes all electrical properties and the second the properties of the atomic nucleus [5]. The theorem states that the knowledge of the electronic density is sufficient to determine uniquely V_e and N

$$n(\boldsymbol{r}) \leftrightarrow V_e \leftrightarrow T + V + V_e \leftrightarrow \Psi \tag{1.2}$$

that is, there cannot be two different external potentials V_e and V_e' giving rise to the same density $n(\boldsymbol{r})$.

Then the energy of the system E can be written as a functional (i.e., a map from functions to real numbers) of the single-particle density $n(\boldsymbol{r})$,

$$E = E[n] = F[n] + \int v_e(\boldsymbol{r}) n(\boldsymbol{r}) d^3\boldsymbol{r} \tag{1.3}$$

and of the density profile $n_{GS}(\boldsymbol{r})$, which correspond to the minimum of E is the exact ground-state density. $F[n]$ is called again a functional of the particle density, and it accounts for the interactions among particles in the system. It is universal: it depends only on the properties of the interaction governing the system (the Coulomb interaction in the electronic case), and not on the external potential v_e. In the case of electronic systems, it is customary to divide $F[n]$ into three parts

$$F[n] = T + E_H[n] + E_{xc}[n] \tag{1.4}$$

where T accounts for the kinetic part, $E_H[n]$ is the direct term (akin to the Hartree term in the Hartree–Fock approximation; see Sec. 1.2) of the Coulomb interaction, and $E_{xc}[n]$ is the so-called exchange correlation term.

The DFT theorem (1.3) is incredibly powerful. The knowledge of the single-particle density $n(\boldsymbol{r})$, a three-coordinate function, is equivalent to the knowledge of the true many-body wave-function of the system (see Eq. (1.2)), and it is sufficient to describe the ground and excited states of the system. While originally proved for non-degenerate ground states, the DFT theorem can be extended to degenerate ground states, spin polarised systems, finite temperature and relativistic cases [44].

From Eq. (1.3) one can derive a mean field description of the system, i.e., treat the particles as if they were non-interacting and as if they just felt a field produced by the others. This is called the Kohn-Sham (KS) scheme [45]. Let's suppose that the density of the system can be written as a function of the single-particle wave-functions $\phi_i(\boldsymbol{r}, \sigma)$

$$n(\boldsymbol{r}) = \sum_{i,\sigma} |\phi_i(\boldsymbol{r}, \sigma)|^2 \tag{1.5}$$

where i is the particle index running over all particles and σ is the spin, and the kinetic term takes the form of Eq. (1.4) reads

$$T = \int -\frac{\hbar^2}{2m} \sum_i \phi_i^*(\boldsymbol{r}) \nabla^2 \phi_i(\boldsymbol{r}) = \int \frac{\hbar^2}{2m} \sum_i |\boldsymbol{\nabla} \phi_i(\boldsymbol{r})|^2 \tag{1.6}$$

The function $n_{GS}(\boldsymbol{r})$ minimizing the energy E (1.3) satisfies the condition of vanishing variation

$$\delta \left(E - \sum_{i,\sigma} \varepsilon_i \int \phi_i^*(\boldsymbol{r}, \sigma) \phi_i(\boldsymbol{r}, \sigma) \right) = 0 \tag{1.7}$$

where the constraint $\int \phi_i^*(\boldsymbol{r}, \sigma)\phi_i(\boldsymbol{r}, \sigma)$, with the Lagrangian multiplier ε_i, ensures the correct number of particles and requires the orthonormality between orbitals. Although counterintuitive, ε_i are not the actual single-particle levels.

Because E depends on the density n, which in turn depends on the single-particle wave functions through Eq. (1.5), using the composition rule for functional derivatives, one gets

$$\frac{\delta E}{\delta \phi_i^*} = \frac{\delta E}{\delta n} \frac{\delta n}{\delta \phi_i^*} = \frac{\delta E}{\delta n} \phi_i \tag{1.8}$$

Carrying out the variation with respect to ϕ_i^* (doing it with respect to ϕ_i would be the same), one finds a set of Schrödinger-like equations for each index i

$$\left(-\frac{\hbar^2}{2m} \nabla^2 + \frac{\delta E_H}{\delta n} + \frac{\delta E_{ex}}{\delta n} + v_e(\boldsymbol{r}) \right) \phi_i = \varepsilon_i \phi_i \tag{1.9}$$

where the two functional derivatives $\delta/\delta n$ play the role of a potential in the equation in the case of a local functional. Equations (1.9) are the so-called Kohn-Sham equations;

since the terms on the left-hand side depend on the density, they are solved iteratively: from an initial guess of the single-particle wave functions, one builds the $\delta F/\delta n$ and solves the equations. This leads to a new set of single-particle wave functions, from which one constructs a new potential, and the cycle restarts. The process continues until convergence is met.

Conceptually, the DFT theorem offers a powerful tool, as the knowledge of the true EDF contains all necessary information; on the other hand, it does not inform us on how to build such a functional, and one is left with the challenging task of finding it. The elusiveness of the EDF is the price to pay to access the simpler single-particle description. In electronic systems, E_H is known exactly since it comes from the direct Coulomb interaction, while the exchange-correlation potential turns out to be but a correction [5, 46]. On the other hand, in nuclear physics, the interaction among nucleons is unknown, which makes the search for the true EDF even more difficult. The very distinction between E_H and E_{xc}, as it will be shown, is not that meaningful either.

In conclusion, the effectiveness of DFT is limited by our ability to devise EDFs; below, in Section 1.4, we will focus on the particularly successful nuclear EDF Skyrme. But before, let's address the peculiarities of nuclear DFT.

1.2 Nuclear DFT

One may wonder whether Eq. (1.3) still holds for the nuclear case. The main difference between electronic and nuclear DFT lies in the fact that the external field v_e is 0 in the nuclear case, as nuclei are self-bound. The condition $v_e = 0$ is not of secondary importance, as it fixes a favourite reference frame: for example, in electronic systems, the frame that is at rest with the centre of mass of the ion(s). In the nuclear case, when one measures the density, one is measuring the intrinsic density of the system; in the lab frame, the density is practically vanishing at any point. DFT was proven for these laboratory densities, and it was not obvious that it held for the intrinsic one as well until it was shown in [47]. Furthermore, the original DFT formulation [4] leaves undetermined whether the relation chain in Eq. (1.2) holds for any given function; or, to restate equivalently, whether all well-behaved functions always correspond to some external potential v_e. This property is called v-representability. Levy [6] and Lieb [7] proved that indeed this is not the case. While this did not have any major implication for the practical applications of DFT [48], this led to an alternative and more general formulation of the theorems, the so-called constrained-search DFT (CSDFT) [5]. The minimization of the energy Eq. (1.3) is divided in two steps: first one minimises over all anti-symmetrised wave functions giving rise to a particular particle density, and then over all possible densities [49]. This equivalent formulation overcomes the representation problem, since it never explicitly assumes the link between the density $n(\boldsymbol{r})$ and the external potential v_e.

These nuances led to some debates among practitioners whether the nuclear case should be fully included in DFT [50–52]. This dispute, albeit interesting, goes beyond the scope of this thesis. Therefore, in the following, we will talk about nuclear EDF in the Levy-Lieb sense, assuming it is the correct way to tackle the nuclear problem, and not refer to nuclear DFT anymore.

Early experimental evidence hinted that the nucleons inside nuclei behave like independent particles in a field, the so-called mean-field, generated by all the other nucleons [53, 54]. The most important one is that nucleons in nuclei dispose themselves in shell-like energy levels, just like electrons in atoms do. The shell closures (called magic numbers in nuclear physics) remain pretty similar across the nuclear chart, as their atomic counterparts do in the periodic table [53, 54].

Due to the strong repulsive force nucleons feel at short distances, a mean-field description may seem counterintuitive. On the other hand, nucleon scattering experiments show that the nucleon mean free path within the nucleus is roughly the same as the nuclear radius [55, 56]. Hence, the nucleus is a diluted system, and interactions between two nucleons, i.e., correlation among particles, are rare events. In principle, this can be explained by invoking the Pauli blocking mechanism, as it prevents neutrons from getting too close to one another.

Therefore, in the beginning, theoretical efforts turned to the Hartree–Fock (HF) approximation to describe nuclear systems; later, it was realised that HF with effective interactions could be inscribed inside the EDF framework. First attempts focused on doubly magical nuclei like ^{208}Pb [1]; open shell nuclei show superfluid properties [11, 54] that require treatment of the pairing correlations; either a standard HF computation was coupled with the BCS method, or the more general Hartree–Fock–Bogoliubov (HFB) was employed directly [54].

In the HF approximation, the ground state wave function of a system with A particles (in our case, nucleons) $\Phi(\boldsymbol{r_1}, ..., \boldsymbol{r_A})$ can be expressed as a Slater determinant of single-particle wave functions $\phi_i = \phi_i(\boldsymbol{r}_i, \sigma_i)$

$$\Phi(\boldsymbol{r_1}, ..., \boldsymbol{r_A}) = \frac{1}{\sqrt{A}} \begin{vmatrix} \phi_1(\boldsymbol{r}_1) & \dots & \phi_A(\boldsymbol{r}_1) \\ \vdots & & \vdots \\ \phi_1(\boldsymbol{r}_A) & \dots & \phi_A(\boldsymbol{r}_A) \end{vmatrix} \tag{1.10}$$

It's worth pointing out that, unlike electronic systems, nuclei are composed of two species of particles, protons and neutrons; therefore, in nuclear systems, there are two types of single-particle wave functions, which give rise to two densities. Given a phenomenological interaction V, the energy of the system reads

$$E_{HF} = \langle\Phi|\, T + V \,|\Phi\rangle \tag{1.11}$$

Searching for the minimum of E_{HF} by imposing $\delta E_{HF} = 0$, one finds the equivalent of (1.7); the set ϕ_i which minimises E_{HF} satisfies

$$\left(-\frac{\hbar^2}{2m}\nabla^2 + U_H(\boldsymbol{r})\right)\phi_i(\boldsymbol{r}, \sigma) + \int U_F(\boldsymbol{r}, \boldsymbol{r'})\phi_i(\boldsymbol{r'}, \sigma) = \varepsilon_i \phi_i(\boldsymbol{r}, \sigma) \tag{1.12}$$

where the local Hartree potential (akin to E_H) reads[1]

$$U_H(\boldsymbol{r}) = \int v(\boldsymbol{r}, \boldsymbol{r'}) \sum_{j,\sigma} |\phi_j(\boldsymbol{r'}, \sigma)|^2 \, d^3\boldsymbol{r'} = \int v(\boldsymbol{r}, \boldsymbol{r'}) n(\boldsymbol{r'}) d^3\boldsymbol{r'} \tag{1.13}$$

and the Fock potential, which arises due to the anti-symmetrical nature of fermions, is

$$U_F(\boldsymbol{r}, \boldsymbol{r'}) = -v(\boldsymbol{r}, \boldsymbol{r'}) \sum_{j,\sigma} \phi_j^*(\boldsymbol{r'}, \sigma)\phi_j(\boldsymbol{r}, \sigma) \tag{1.14}$$

Like the KS equations (1.9), HF equations (1.12) are solved iteratively, since both U_H and U_F depend explicitly on the single-particle wave functions. The system ground state is then computed from Eq. (1.10) using the first A orbitals energy-wise.

[1]For simplicity, we are supposing spin degeneracy. Therefore, the spin degree of freedom in the potentials U_H and U_F disappears when the sum over the spin states is carried out.

Unfortunately, the HF approach described performs poorly when compared to experimental observables, if non-density-dependent interactions are used [3, 57, 58]. It was realised that these effective interactions were needed to reproduce both binding energies and the saturation behaviour of nuclear matter (for more details, see Sec. 1.5). If $v = v(\boldsymbol{r}, \boldsymbol{r'}; n)$, then a new term appears in Eqs. (1.13) and (1.14)

$$\begin{aligned} U_H^{DD}(\boldsymbol{r}) &= \int \left(v(\boldsymbol{r}, \boldsymbol{r'}) + n(\boldsymbol{r}) \frac{\partial v}{\partial n} \right) n(\boldsymbol{r'}) d^3\boldsymbol{r'} \\ U_F^{DD}(\boldsymbol{r}, \boldsymbol{r'}) &= - \left(v(\boldsymbol{r}, \boldsymbol{r'}) + n(\boldsymbol{r}) \frac{\partial v}{\partial n} \right) \sum_{j,\sigma} \phi_j^*(\boldsymbol{r'}, \sigma) \phi_j(\boldsymbol{r}, \sigma) \end{aligned} \tag{1.15}$$

due to its added dependence on the single-particle wave functions (see Eq. (1.5)). This new term $n(\boldsymbol{r})\partial v / \partial n$ is called "rearrangement" potential.

Indeed, all successful nuclear effective interactions present some density dependence. The first example was the Skyrme potential, proposed by Skyrme in the late '50s [31], and the first HF calculation using it was carried on in the seminal paper of Vautherin and Brink [1]. The Skyrme potential is zero range, i.e., the spatial dependence is proportional to a Dirac δ. This feature simplifies enormously the HF computations, as the Fock potential U_F becomes local. The Gogny force [8], although presenting finite range terms, still needs a density-dependent zero-range term, identical to Skyrme's. This testifies to its crucial role in the success of these phenomenological interactions.

In any case, a density-dependent force raises some perplexities from a theoretical point of view. This difficulty can be overcome if one interprets these potentials as generators of an EDF. In this way, from the theoretical point of view, one links HF to the DFT, thus making HF an approximation of an exact theory. In particular, rewriting Eq. (1.11)

$$E[n] = \langle \Phi | T + V | \Phi \rangle = \int \mathcal{E}(n, \boldsymbol{\nabla} n, ...) d^3\boldsymbol{r} d^3\boldsymbol{r'} \tag{1.16}$$

gives a particular form of functional, depending on the so-called density matrix $n = n(\boldsymbol{r}\sigma, \boldsymbol{r'}\sigma')$ and its gradients

$$n(\boldsymbol{r}\sigma, \boldsymbol{r'}\sigma') = \frac{1}{2} \left(n(\boldsymbol{r}, \boldsymbol{r'}) \delta_{\sigma,\sigma'} + \sum_{\nu} \langle \sigma | \sigma_\nu | \sigma' \rangle s_\nu(\boldsymbol{r}, \boldsymbol{r'}) \right) \tag{1.17}$$

where the vector $\boldsymbol{\sigma}$ is the vector composed of the Pauli matrices. A broader definition of the density is needed in the nuclear case because the nuclear interaction is richer than Coulomb's and depends both on the spin and isospin of the particles. In the density matrix expression (1.17), we define the generalised particle density $n_q(\boldsymbol{r}, \boldsymbol{r'})$

$$n_q(\boldsymbol{r}, \boldsymbol{r'}) = \sum_{i,\sigma} \phi_{iq}^*(\boldsymbol{r'}, \sigma) \phi_{iq}(\boldsymbol{r}, \sigma) \tag{1.18}$$

and the spin density $\boldsymbol{s}(\boldsymbol{r}, \boldsymbol{r'})$

$$\boldsymbol{s}_q(\boldsymbol{r}, \boldsymbol{r'}) = \sum_{i,\sigma,\sigma'} \phi_{iq}^*(\boldsymbol{r'}, \sigma') \phi_{iq}(\boldsymbol{r}, \sigma) \langle \sigma' | \boldsymbol{\sigma} | \sigma \rangle \tag{1.19}$$

In the expressions above, the subscript q stands for protons (p) or neutrons (n), since in the nuclear case we have two particle species. It is not unusual to find formulation of nuclear

EDF where one uses isoscalar and isovector densities, which are respectively the sum and difference of neutron and proton densities (see, for example, [59]). The generalised density (1.18) is obviously related to the particle density of the system $n_q(\boldsymbol{r}) = n_q(\boldsymbol{r}, \boldsymbol{r})$, and already appeared in the Fock potential (1.18).

With this prescription, one has an EDF in the form (1.3), and one can solve the KS Eqs. (1.9) to find the single-particle wave functions minimizing Eq. (1.16).

All scalar and time-even combination of the density matrix (1.17) and its gradients can be present in an EDF. Of course, keeping all orders of derivatives is inadvisable, as the number of parameters to fit would soar fast [60]. For this reason, it is customary to limit oneself to the second order, although works studying EDFs with further orders are present in the literature [61, 62]. The first derivative should be proportional to $(\boldsymbol{\nabla} - \boldsymbol{\nabla'})$, as the functional must be invariant under space translations. As a consequence, since $(\boldsymbol{\nabla} - \boldsymbol{\nabla'})^2 = (\boldsymbol{\nabla} + \boldsymbol{\nabla'})^2 - 4\boldsymbol{\nabla}\boldsymbol{\nabla'}$, the second derivative boils down to the action of the $\boldsymbol{\nabla}\boldsymbol{\nabla'}$ operator. All the derivatives are computed on the non-local quantities, and then are valued locally at $\boldsymbol{r} = \boldsymbol{r'}$. They are:

– the current $\boldsymbol{j}$:

$$\boldsymbol{j}(\boldsymbol{r}) = -i[\boldsymbol{\nabla} - \boldsymbol{\nabla'}]n(\boldsymbol{r}, \boldsymbol{r'})|_{\boldsymbol{r}=\boldsymbol{r'}}/2 \tag{1.20}$$

– the kinetic energy density τ:

$$\tau(\boldsymbol{r}) = \boldsymbol{\nabla}\boldsymbol{\nabla'}n(\boldsymbol{r}, \boldsymbol{r'})|_{\boldsymbol{r}=\boldsymbol{r'}} \tag{1.21}$$

– the spin current $\boldsymbol{J}_{\alpha\beta}$:

$$\boldsymbol{J}_{\alpha\beta}(\boldsymbol{r}) = -i[\boldsymbol{\nabla}_\alpha - \boldsymbol{\nabla}'_\alpha]s_\beta(\boldsymbol{r}, \boldsymbol{r'})|_{\boldsymbol{r}=\boldsymbol{r'}}/2 \tag{1.22}$$

– the spin kinetic density $\boldsymbol{T}$:

$$\boldsymbol{T}(\boldsymbol{r}) = \boldsymbol{\nabla}\boldsymbol{\nabla'}\boldsymbol{s}(\boldsymbol{r}, \boldsymbol{r'})|_{\boldsymbol{r}=\boldsymbol{r'}} \tag{1.23}$$

The time-parity descends from the generalised density n (1.18) and the spin density $\boldsymbol{s}$ (1.19). The first is time-even, while the second is time-odd [63, 64]. However, the action of the $\boldsymbol{\nabla}$ operator inverts the time-parity; so, for example, $\boldsymbol{j}$ is time-odd and τ is time-even. As will be shown below, this has an important effect on the explicit form of EDF for nuclei, as all time-odd terms can only appear in combination with other time-odd terms to respect the symmetries of the nuclear system [59]. In the remainder of this Thesis, we will work with even-even nuclei, for which all time-odd densities vanish identically. We will not encounter these terms anymore, which we mentioned above for completeness.

Once the link between EDF and the HF approximation was established, research efforts turned to writing directly EDFs, rather than going through an effective interaction first. A first step in this direction was taken in [65], where the authors added a term to the spin-orbit part of the Skyrme EDF that could not be derived from an existing effective potential. Then other efforts, like the Fayans EDF [10], started directly with an expression for the energy density $\mathcal{E}$.

A radically different strategy, which can still be included in the EDF framework, was proposed by Walecka [9, 66]. There, the authors wrote a relativistic Lagrangian with nucleonic and mesonic degrees of freedom. From this Lagrangian, one can compute the energy density $\mathcal{E}$ of the system, which again depends on the particle densities; just the nucleonic spinor fields play the role of orbitals within the non-relativistic EDF. For a compilation of different compilations, we refer to [67].

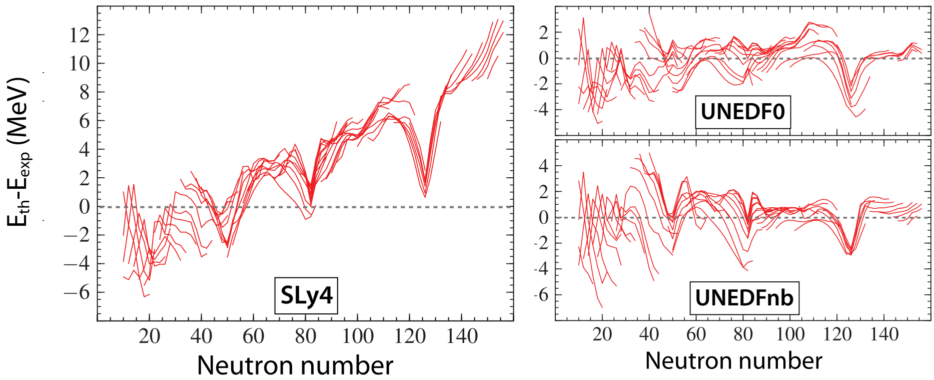

Figure 1.1: Binding energies across the nuclear chart for three Skyrme-like EDF: SLy4, UNEDF0, and UNEDFnb. We can appreciate the arch-like structure that forms around magical numbers. Plot taken and adapted from [74].

All the above approaches are phenomenological. Each has around ten to fifteen parameters to be fitted to experimental data; moreover, the EDFs ability to reproduce experimental results is more or less the same, regardless of the one employed (Skyrme, Gogny, relativistic...) [12].

The first observables EDFs are asked to reproduce are ground state properties, the most important of which is the binding energy. Usually, EDFs reproduce them with a root mean square deviation of about 1-2 MeV from experiment, with the best mass models achieving a deviation of about 0.5 MeV over the more than 2000 masses measured [68–71]. Although impressive, that is much greater than the experimental error, which usually is of the order of some keV, if not lower [32, 72]. On the other hand, the deviation is not normally distributed. Analysing the difference between theory and experiment over the nuclear chart reveals that EDFs behave differently close to magicity, and tend to overbind magical nuclei. In Figure 1.1 we can appreciate the arch-like plots that develop, for three different Skyrme interactions: the much studied SLy4 [73], and two UNEDF [74]. Even though the overall description for the nuclei is different, we see that the arches become quite recognisable at magic numbers 50, 82, and 126.

Since the HK theorem connects the ground state energy to the ground state density, one expects a good description of nuclear root mean square radii as well

$$\langle r_q^2 \rangle = \int d^3\boldsymbol{r} n_q(\boldsymbol{r}) \tag{1.24}$$

where the index q stands for either proton or neutron. While our knowledge of the neutron radius is limited due to the delicate nature of experiments trying to measure it, the proton radius can be deduced from the nucleus charge distribution, which can be measured in electron scattering experiments. Although there exists an exact relation involving the protons and neutrons form factors, one can relate the charge rms radius $\langle r_{\mathrm{ch}}^2 \rangle$ to the proton one through the empirical relation $\langle r_{\mathrm{ch}}^2 \rangle = \langle r_p^2 \rangle + 0.8^2$. As well as with the binding energies, EDFs do not reproduce the charge radii within experimental precision, which is ~ 0.001 fm, but rather they reach a rms deviation of about 0.02 fm [68, 71].

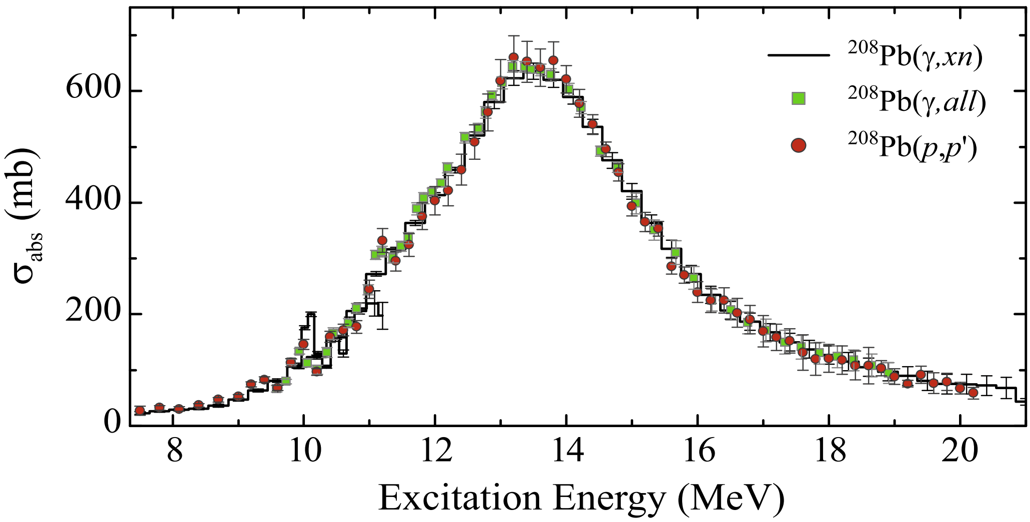

Figure 1.2: Experimental absorption cross section for the isovector giant dipole resonance ($L = 1$, $S = 0$, $T = 1$) in ^{208}Pb, with different probes. Plot taken and adapted from [12].

1.3 RPA

Although nuclei exhibit a rich variety of excitations, we restrict our attention to the so-called giant resonances, collective modes in which all the nucleons in the system participate [53, 54].

These excitations are very common in the nuclear landscape, and they have been widely studied. They are excited by different probes (photo-absorption or hadron scattering) and with excitation energies ranging between 10-30 MeV, although the peaks have widths of the order of some MeV [75]. It is customary to distinguish them by how much orbital angular momentum L they carry ($L = 0$ is called monopole, $L = 1$ dipole, $L = 2$ quadrupole and so on), spin S ($S = 0$ marks electric resonances, $S = 1$ magnetic) and isospin T ($T = 0$ isoscalar, neutrons and protons oscillate in phase, $T = 1$ isovector, neutrons and protons oscillate out of phase) [12, 13, 76]. Indeed, experimentally it has been observed that the excitation energy varies slowly with the number of nucleons A in the nucleus: for example, the empirical relation for the isovector giant dipole resonance (IVGDR) excitation energy E^{IV}_{GDR} is $E^{IV}_{GDR} \approx 80A^{-1/3}$ MeV. Figure 1.2 shows the photo-absorption cross section σ_{abs} for the IVGDR of ^{208}Pb. The peak is around 13.5 MeV, as suggested by the empirical relation, and the curve is 4-5 MeV wide.

Besides their obvious implications for nuclear structure, these collective states also probe the features of nuclear matter (see Section 1.5), and they will play a central role in our work.

The standard theoretical framework for describing these modes is called Random Phase Approximation (RPA) [54]. The equations governing RPA can be derived in two ways: either considering the excitation operator as a sum of all possible particle-hole and hole-particle excitations, or as the small perturbation limit of time-dependent DFT (TDDFT). Therefore, RPA is consistent with a mean field approach, consistent with the KS picture we described above.

As both derivations are equivalent, we will give some insights into the first one. The underlying hypothesis is that the operator $Q^\dagger_\nu$ which excites the ground state $|\Psi_0\rangle$ to an excited state $|\Psi_\nu\rangle$ can be written as

$$Q_\nu^\dagger = \sum_{p,h} X_{ph}^\nu a_p^\dagger a_h - Y_{hp}^\nu a_h^\dagger a_p \tag{1.25}$$

where p (h) refers to state above (below) the Fermi energy of the system, $a_i^{(\dagger)}$ is the destruction (creation) operator for a particle in state $|i\rangle$ and X_{ph}^ν, Y_{ph}^ν are the RPA amplitudes, which are real numbers. So, an excited state is the sum of all particle-holes ($a_p^\dagger a_h$) and holes-particle ($a_h^\dagger a_p$) excitations.

It is clear from Eq. (1.25) that if the ground state $|\Psi_0\rangle$ correspond to the HF/KS ground state $|\Phi_{HF}\rangle$, then

$$Q_\nu^\dagger |\Phi_{HF}\rangle = \sum_{p,h} X_{ph} a_p^\dagger a_h |\Phi_{HF}\rangle \tag{1.26}$$

since $|\Phi_{HF}\rangle$ is a Slater determinant with the first A state below the Fermi energy occupied (Eq. (1.10)), where A is the number of particles in the system, and by definition $a_p |\Phi_{HF}\rangle = 0$. This particular case is known as the Tamm–Dancoff Approximation (TDA), whose performance in nuclear physics is not always satisfactory [54].

This means that one has to consider a more general ground state, one where correlations among particles are taken into account through the presence of particle-hole states. In fact, the $|RPA\rangle$ ground state is defined from Eq. (1.25)

$$\begin{aligned} Q_\nu^\dagger |RPA\rangle &= |\Psi_\nu\rangle \\ Q_\nu |RPA\rangle &= 0 \end{aligned} \tag{1.27}$$

where for the excited state $|\Psi_\nu\rangle$ the relation $H|\Psi_\nu\rangle = E_\nu |\Psi_\nu\rangle$ holds.

The explicit expressions for the amplitudes X and Y are given by the eigenvalue problem

$$\begin{pmatrix} A & B \\ -B & -A \end{pmatrix} \begin{pmatrix} X^\nu \\ Y^\nu \end{pmatrix} = (E_\nu - E_0) \begin{pmatrix} X^\nu \\ Y^\nu \end{pmatrix} \tag{1.28}$$

where A, B are $n \times n$ matrices, where n is the number of possible particle–hole (and hole–particle) excitations considered in Eq. (1.25). Explicitly, they read

$$\begin{aligned} A_{ph,p'h'} &= \delta_{hh'}\delta_{pp'}(\varepsilon_p - \varepsilon_h) + \overline{v}_{ph'hp'} \\ B_{ph,p'h'} &= \overline{v}_{pp'hh'} \end{aligned} \tag{1.29}$$

where $\overline{v}_{ijkl}$ is the anti-symmetrised matrix element of the effective potential V and ε are the single-particle energies of Eq. (1.12). The derivation of Eqs. (1.28) and (1.29) can be found in many textbooks, like [54] or in a detailed monograph like [77]. Of course, as we said, nowadays there are EDFs which are written directly without starting from an underlying effective interaction V. For these, we can rewrite Eq. (1.29) within nuclear EDF formalism,

$$\begin{aligned} A_{ph,p'h'} &= \delta_{hh'}\delta_{pp'}(\varepsilon_p - \varepsilon_h) + \int \mathrm{d}^3r\, \mathrm{d}^3r' \phi_p^*(\boldsymbol{r})\phi_{h'}^*(\boldsymbol{r}') \frac{\delta^2 E}{\delta n(\boldsymbol{r}')\,\delta n(\boldsymbol{r})} \phi_h(\boldsymbol{r})\phi_{p'}(\boldsymbol{r}') \\ B_{ph,p'h'} &= \int \mathrm{d}^3r\, \mathrm{d}^3r' \phi_p^*(\boldsymbol{r})\phi_{p'}^*(\boldsymbol{r}') \frac{\delta^2 E}{\delta n(\boldsymbol{r}')\,\delta n(\boldsymbol{r})} \phi_h(\boldsymbol{r})\phi_{h'}(\boldsymbol{r}') \end{aligned} \tag{1.30}$$

where ϕ are the single-particles orbitals, and $E = E[n]$ is the energy density functional. The double functional derivative defines the so-called residual interaction $V_{\rm res}(\boldsymbol{r}, \boldsymbol{r'})$

$$V_{\rm res}(\boldsymbol{r}, \boldsymbol{r'}) = \frac{\delta^2 E}{\delta n(\boldsymbol{r'})\, \delta n(\boldsymbol{r})} \tag{1.31}$$

It takes into account the residual interaction between particles, which is neglected in the mean field approximation. Indeed, these expressions come out naturally, deriving the system (1.28) through TDDFT. RPA can be extended to open-shell nuclei, and it is called QRPA.

Once the amplitudes X and Y are known, one can compute the so-called strength function $S(E)$ of a one body, hermitian operator F corresponding to an external field

$$S(E) = \sum_\nu \delta(E - E_\nu + E_0) \left|\langle\nu|\, F\, |0\rangle\right|^2 \tag{1.32}$$

which quantifies which transitions to excited states ν are mostly favoured by the action of the field. Of particular interest are the moments of the strength function $m(k)$

$$m(k) = \int dE S(E) E^k = \sum_\nu (E_\nu - E_0)^k \left|\langle\nu|\, F\, |0\rangle\right|^2 \tag{1.33}$$

and their $k = 1$ ratios

$$\begin{aligned} E_1 &= \sqrt{\frac{m(1)}{m(-1)}} \\ \overline{E_1} &= \frac{m(1)}{m(0)} \end{aligned} \tag{1.34}$$

called, respectively, constrained and centroid energy, which can be linked to the excitation energies of the giant resonances [12].

Furthermore, within the linear approximation, the so-called dynamic polarizability $\alpha = \langle F\rangle/\lambda$, where λ is the strength of the external field, can be linked to the moments of the strength function. It can be explicitly written following perturbation theory as [78]

$$\alpha(E) = 2 \sum_\nu \frac{E_\nu - E_0}{(E_\nu - E_0)^2 - E^2} \left|\langle\nu|F|0\rangle\right|^2 . \tag{1.35}$$

In the limit of vanishing energy, $E \to 0$, Eq. (1.35) can be expanded in the strength function moments, Eq. (1.33), as

$$\frac{\alpha(E)|_{E\to 0}}{2} = m(-1) + E^2 m(-3) + \cdots \tag{1.36}$$

The first term of the expansion is the static polarizability α_D. In the case of the IVDGR, F is a dipole operator, then the static polarizability can be linked to the experimental cross section σ [12, 79]

$$\alpha_D = \frac{\hbar c}{2\pi^2 e^2} \int_0^\infty dE\, \frac{\sigma(E)}{E^2} \tag{1.37}$$

where e is the elemental charge. In the following, α_D will be central in our analyses, and we will refer to it simply as polarizability.

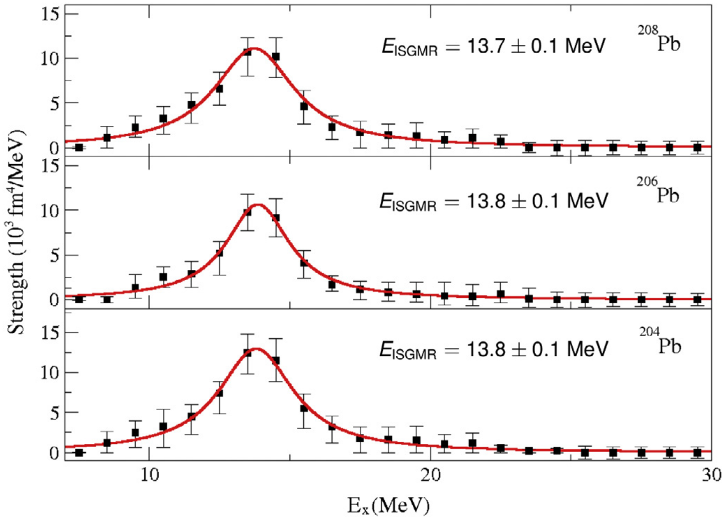

Figure 1.3: Experimental strength (black squares) of the ISGMR of three isotopes of Pb fitted with a Lorentzian (red line) for three Pb isotopes. The peak of the Lorentzian is the extrapolated excitation energy, reported in each subplot. Plot taken and adapted from [80].

RPA reproduces fairly well the excitation energy of these modes. Figure 1.3 shows the measured strength of the isoscalar giant monopole resonance of three isotopes of Pb (black squares), fitted with a Lorentzian (red line). The peak of the curve, which represents the excitation value of the resonance to be compared with RPA calculations, is reported in the Figure.

On the other hand, RPA is not as good in reproducing the resonance widths, the lifetime of the excited states or the fine structure of giant resonances, as one can appreciate by looking at the RPA width Γ_{RPA} against the experimental one Γ_{exp} in Figure 1.4, with RPA consistently underestimating the width by some MeV. This discrepancy stems from the RPA ansatz Eq. (1.25), which is quite crude, and neglects effects beyond particle-hole and hole-particle excitations.

To achieve a better description, one should keep track of beyond mean field effects and employ more sophisticated theories. Some examples are second RPA (so when considering $2p-2h$ excitations) [82] or particle-vibration-coupling (PVC) [83], which has recently been proven excellent to tackle the case of the low excitation energy of ^{120}Sn ISGMR [84, 85].

In this Thesis, the estimates of the centroid energies given by RPA will suffice, and we will not give more details about these more refined methods.

1.4 The Skyrme functional

We now turn our attention to the Skyrme interaction [31], one of the most successful and widely employed EDFs in nuclear physics. As said before, it was originally introduced as a zero-range phenomenological interaction between nucleons, and then was inserted in the broader framework of DFT. It has a two-body part $v_{ij}^{(2)}$ and a three-body term $v_{ijk}^{(3)}$ [1]

$$V_{sky} = \sum_{i<j} v_{ij}^{(2)} + \sum_{i<j<k} v_{ijk}^{(3)} \tag{1.38}$$

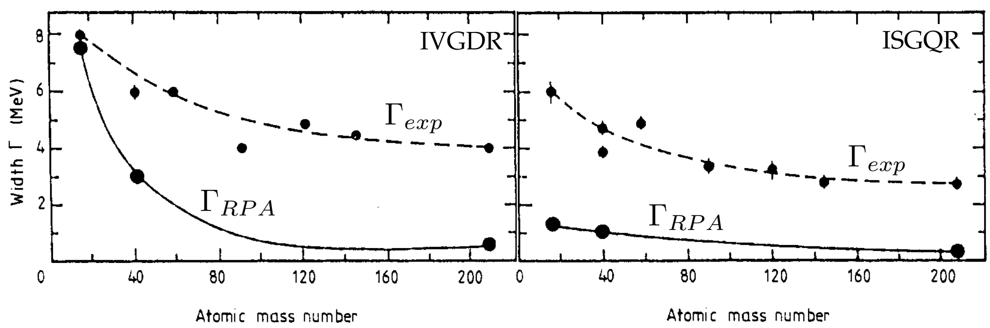

Figure 1.4: Experimental width Γ_{exp} (dotted line) and RPA width Γ_{RPA} (thick line) for the IVGDR (top) and ISGQR (bottom). Plot taken and adapted from [81].

Table 1.1: Skyrme parameters of some widely used interactions.

		SLy4 [86]	SkM* [87]	SLy5 [86]	SIII [88]
t_0	[MeV fm^3]	-2488.91	-2645.0	-2484.88	-1128.75
t_1	[MeV fm^5]	486.82	410.0	483.13	495.0
t_2	[MeV fm^5]	-546.39	-135.0	-549.40	-95.0
t_3	[MeV fm$^{3+3\sigma}$]	13777.0	15595.0	13763.0	14000.0
x_0	[-]	0.834	0.9	0.778	0.45
x_1	[-]	-0.344	0	-0.328	0.0
x_2	[-]	1.0	0	-1.0	0.0
x_3	[-]	1.354	0	1.267	1.0
σ	[-]	1/6	1/6	1/6	1.0
W_0	[MeV fm^5]	123.0	130.0	126.0	120.0

which explicitly reads in coordinate space

$$\begin{aligned} V(\boldsymbol{r},\boldsymbol{r'}) =& t_0\left(1+x_0P_\sigma\right)\delta(\boldsymbol{r}-\boldsymbol{r'}) \\ &+\frac{1}{2}t_1\left(1+x_1P_\sigma\right)\left[\boldsymbol{P}'^2\delta(\boldsymbol{r}-\boldsymbol{r'})+\delta(\boldsymbol{r}-\boldsymbol{r'})\boldsymbol{P}^2\right] \\ &+t_2\left(1+x_2P_\sigma\right)\boldsymbol{P}'\cdot\delta(\boldsymbol{r}-\boldsymbol{r'})\boldsymbol{P} \\ &+\frac{1}{6}t_3\left(1+x_3P_\sigma\right)\left[n\left(\frac{\boldsymbol{r}+\boldsymbol{r'}}{2}\right)\right]^\sigma\delta(\boldsymbol{r}-\boldsymbol{r'}) \\ &+iW_0(\boldsymbol{\sigma}_1+\boldsymbol{\sigma}_2)\cdot\left[\boldsymbol{P}'\times\delta(\boldsymbol{r}-\boldsymbol{r'})\boldsymbol{P}\right] \end{aligned} \tag{1.39}$$

where the operator P_σ is the spin-exchange, $\boldsymbol{P}$ corresponds to $\boldsymbol{P}=-i(\boldsymbol{\nabla}-\boldsymbol{\nabla'})/2$, while $\boldsymbol{P'}$ is its complex conjugate acting on the left. It can be shown that the three-body term in Eq. (1.38) is equivalent to the density-dependent term of Eq. (1.39) [1] if $\sigma=1$; we present here a more general formulation, with $\sigma\in\mathbb{R}^+$.

The Skyrme interaction, in the standard version presented in (1.39), has in total 10 parameters: the four t_is, the four x_is ($i=0,\ldots,3$), the exponent σ and the spin-orbit parameters W_0. In Table 1.1 we show their typical values.

The Skyrme EDF is found by means of Eq. (1.16). As mentioned above in Sec. 1.2, in this work we will devote attention to even-even nuclei, i.e., with the same number of neutrons and protons. This means that if there is a nucleon in a state $|i\rangle$, then its time-reversed counterpart $|\bar{i}\rangle$ is present as well [1]; thus the time-odd densities $\boldsymbol{s}$ (1.19), $\boldsymbol{j}$ (1.20) and $\boldsymbol{T}$ (1.23) vanish identically [63]. The Skyrme energy density functional thus takes the form [73]

$$E^{sky} = \int \mathcal{E}^{Sky}(\boldsymbol{r})d^3\boldsymbol{r} = \int (\mathcal{K}+\mathcal{E}_0^{sky}+\mathcal{E}_3^{sky}+\mathcal{E}_{\rm eff}^{sky}+\mathcal{E}_{\rm fin}^{sky}+\mathcal{E}_{\rm so}^{sky}+\mathcal{E}_{\rm sg}^{sky}+\mathcal{E}_{\rm Coul}^{sky})d^3\boldsymbol{r} \tag{1.40}$$

where

$$\begin{aligned}
\mathcal{K} =&\frac{\hbar^2}{2m}\tau, \\
\mathcal{E}_0^{Sky} =&\frac{1}{4}t_0\left[(2+x_0)\,n^2-(2x_0+1)\left(n_{\rm p}^2+n_{\rm n}^2\right)\right], \\
\mathcal{E}_3^{Sky} =&\frac{1}{24}t_3 n^\sigma\left[(2+x_3)\,n^2-(2x_3+1)\left(n_{\rm p}^2+n_{\rm n}^2\right)\right], \\
\mathcal{E}_{\rm eff}^{Sky} =&\frac{1}{8}\left[t_1\,(2+x_1)+t_2\,(2+x_2)\right]\tau n \\
&+\frac{1}{8}\left[t_2\,(2x_2+1)-t_1\,(2x_1+1)\right](\tau_{\rm p}n_{\rm p}+\tau_{\rm n}n_{\rm n}), \\
\mathcal{E}_{\rm fin}^{Sky} =&\frac{1}{32}\left[3t_1\,(2+x_1)-t_2\,(2+x_2)\right](\boldsymbol{\nabla}n)^2 \\
&-\frac{1}{32}\left[3t_1\,(2x_1+1)+t_2\,(2x_2+1)\right]\left[(\boldsymbol{\nabla}n_{\rm p})^2+(\boldsymbol{\nabla}n_{\rm n})^2\right], \\
\mathcal{E}_{\rm so}^{Sky} =&\frac{1}{2}W_0\left[\boldsymbol{J}\cdot\boldsymbol{\nabla}n+\boldsymbol{J}_{\rm p}\cdot\boldsymbol{\nabla}n_{\rm p}+\boldsymbol{J}_{\rm n}\cdot\boldsymbol{\nabla}n_{\rm n}\right], \\
\mathcal{E}_{\rm sg}^{Sky} =&-\frac{1}{16}\,(t_1x_1+t_2x_2)\,\boldsymbol{J}^2+\frac{1}{16}\,(t_1-t_2)\left[\boldsymbol{J}_{\rm p}^2+\boldsymbol{J}_{\rm n}^2\right].
\end{aligned} \tag{1.41}$$

where the densities subscripts n, p refer either to neutron or proton; if there is none, then it indicates the total density, i.e., the sum of the two. In Eq. (1.41), the contribution of $\boldsymbol{J}_{\alpha\beta}$ appears in its vector part $\boldsymbol{J} = -i[\boldsymbol{\nabla}-\boldsymbol{\nabla}']\times\boldsymbol{s}(\boldsymbol{r},\boldsymbol{r}')|_{\boldsymbol{r}=\boldsymbol{r}'}/2$. Explicitly, the three densities of interest are

$$\begin{aligned}
n_q(\boldsymbol{r}) &= \sum_{i,\sigma}|\phi_i^q(\boldsymbol{r},\sigma)|^2 \\
\tau_q(\boldsymbol{r}) &= \sum_{i,\sigma}|\boldsymbol{\nabla}\phi_i^q(\boldsymbol{r},\sigma)|^2 \\
\boldsymbol{J_q}(\boldsymbol{r}) &= \sum_{i,\sigma,\sigma'}|\phi_i^{q*}(\boldsymbol{r},\sigma')\boldsymbol{\nabla}\phi_i^q(\boldsymbol{r},\sigma)\times\langle\sigma'|\,\boldsymbol{\sigma}\,|\sigma\rangle\,|^2
\end{aligned} \tag{1.42}$$

Each term in Eq. (1.41) has a precise meaning. $\mathcal{K}$ is the kinetic energy density. $\mathcal{E}_0$ is a central attractive term; $\mathcal{E}_3$ is the density-dependent term which accounts for short-range repulsion. $\mathcal{E}_{\rm eff}$ instead is an effective mass term, while $\mathcal{E}_{\rm fin}$ mimics non local contribution to the nuclear force. Finally, $\mathcal{E}_{\rm so}$ considers the spin-orbit contribution to the total energy, and $\mathcal{E}_{\rm sg}$ is due to tensor coupling between spin and gradients. It is not unusual to neglect this term, as done for example in SLy4 parametrisation [86]. The Coulomb contribution is the direct Coulomb energy density, with the exchange term computed with the Slater approximation.

Following the Kohn-Sham scheme, minimizing (1.40) with respect to the single-particle wave function ϕ_i we get the Kohn-Sham equations (1.9)

$$\left[\boldsymbol{\nabla}\cdot\left(-\frac{\hbar^2}{2m_q^*(\boldsymbol{r})}\boldsymbol{\nabla}\right)+U_q(\boldsymbol{r})+V_{coul}(\boldsymbol{r})\delta_{q,p}-i\boldsymbol{W}_q\cdot(\boldsymbol{\nabla}\times\sigma)\right]\phi_i(\boldsymbol{r},\sigma)=\varepsilon_i\phi_i(\boldsymbol{r},\sigma) \tag{1.43}$$

where

$$\begin{aligned}\frac{\hbar^2}{2m_q^*(\boldsymbol{r})}=\frac{\delta E^{Sky}}{\delta\tau_q}=&\frac{\hbar^2}{2m}+\frac{1}{8}\left[t_1\left(2+x_1\right)+t_2\left(2+x_2\right)\right]n(\boldsymbol{r})\\&-\frac{1}{8}\left[t_1\left(1+2x_1\right)-t_2\left(1+2x_2\right)\right]n_q(\boldsymbol{r})\end{aligned} \tag{1.44}$$

is the effective mass,

$$\begin{aligned}U_q(\boldsymbol{r})=\frac{\delta E^{Sky}}{\delta n_q}=&\frac{1}{2}t_0\left[\left(2+x_0\right)n-\left(1+2x_0\right)n_q\right]\\&+\frac{1}{24}t_3\left\{\left(2+x_3\right)(2+\sigma)n^{\sigma+1}-\left(2x_3+1\right)\left[2n^\sigma n_q+\sigma n^{\sigma-1}\left(n_p^2+n_n^2\right)\right]\right\}\\&+\frac{1}{8}\left[t_1\left(2+x_1\right)+t_2\left(2+x_2\right)\right]\tau+\frac{1}{8}\left[t_2\left(2x_2+1\right)-t_1\left(2x_1+1\right)\right]\tau_q\\&+\frac{1}{16}\left[t_2\left(2+x_2\right)-3t_1\left(2+x_1\right)\right]\nabla^2 n\\&+\frac{1}{16}\left[3t_1\left(2x_1+1\right)+t_2\left(2x_2+1\right)\right]\nabla^2 n_q\\&-\frac{1}{2}W_0\left[\boldsymbol{\nabla}\cdot\boldsymbol{J}+\boldsymbol{\nabla}\cdot\boldsymbol{J}_q\right]\end{aligned} \tag{1.45}$$

is the mean field potential,

$$\boldsymbol{W}_q(\boldsymbol{r})=\frac{\delta E^{Sky}}{\delta\boldsymbol{J}_q}=\frac{1}{2}W_0\left(\boldsymbol{\nabla}n+\boldsymbol{\nabla}n_q\right)+\frac{1}{8}\left(t_1-t_2\right)\boldsymbol{J}_q-\frac{1}{8}\left(t_1x_1+t_2x_2\right)\boldsymbol{J} \tag{1.46}$$

is the spin potential, and

$$V_{\mathrm{coul}}(\boldsymbol{r})=\frac{e^2}{2}\int\frac{n_p\left(\boldsymbol{r}'\right)d^3r'}{\left|\boldsymbol{r}-\boldsymbol{r}'\right|}-\frac{e^2}{2}\left(\frac{3}{\pi}\right)^{1/3}n_p^{1/3} \tag{1.47}$$

is the Coulomb potential with the exchange term computed in the Slater approximation; the charge density is approximated with the proton density.

There are different ways to extend the Skyrme interaction. In [65] the authors proposed a simple modification to the $\mathcal{E}_{so}^{sky}$

$$\mathcal{E}_{\mathrm{so}}^{Sky}=\frac{1}{2}\left[W_0\boldsymbol{J}\cdot\boldsymbol{\nabla}n+W_0'\left(\boldsymbol{J}_{\mathrm{p}}\cdot\boldsymbol{\nabla}n_{\mathrm{p}}+\boldsymbol{J}_{\mathrm{n}}\cdot\boldsymbol{\nabla}n_{\mathrm{n}}\right)\right] \tag{1.48}$$

where now the spin-orbit interaction can have different behaviours in the isoscalar and isovector sectors. The relative relevance is given by the ratio W_0'/W_0, while the standard Skyrme picture is retrieved by putting $W_0'=W_0$.

Another possible strategy is to add density-dependent terms similar to t_1 and t_2 in

Eq. (1.39) (see, for example, [89])

$$\begin{aligned} V'(\boldsymbol{r},\boldsymbol{r}') &= V(\boldsymbol{r},\boldsymbol{r}') \\ &+ \frac{1}{2}t_4\left(1+x_4P_\sigma\right)\frac{1}{\hbar^2}\left[P'^2 n\left(\frac{\boldsymbol{r}+\boldsymbol{r}'}{2}\right)^\beta \delta\left(\boldsymbol{r}-\boldsymbol{r}'\right)\right. \\ &\left. + \delta\left(\boldsymbol{r}-\boldsymbol{r}'\right) n\left(\frac{\boldsymbol{r}+\boldsymbol{r}'}{2}\right)^\beta \boldsymbol{P}^2\right] \\ &+ t_5\left(1+x_5P_\sigma\right)\frac{1}{\hbar^2}\boldsymbol{P}\cdot n\left(\frac{\boldsymbol{r}+\boldsymbol{r}'}{2}\right)^\gamma \delta\left(\boldsymbol{r}-\boldsymbol{r}'\right)\boldsymbol{P} \end{aligned} \tag{1.49}$$

where there are now six extra parameters.

As mentioned above, nuclear pairing is needed to describe open-shell nuclei. To correctly account for this phenomenon, one needs to introduce a pairing potential in (1.39), which reads [90]

$$\begin{aligned} V\left(\boldsymbol{r},\boldsymbol{r}'\right) &= v_0\left[1+x\left(\frac{n\left(\frac{\boldsymbol{r}+\boldsymbol{r}'}{2}\right)}{n_{sat}}\right)\right]\delta\left(\boldsymbol{r}-\boldsymbol{r}'\right) \\ &\equiv V_{pair}(r)\delta\left(\boldsymbol{r}-\boldsymbol{r}'\right) \end{aligned} \tag{1.50}$$

where x can either be 0 for volume, 1 for surface, or 1/2 for mixed pairing, while $n_{sat} = 0.16\ \text{fm}^{-3}$. The parameter v_0 is the strength of the interaction, and is one additional parameter. In the following, we will only use volume pairing, $x = 0$.

We would like to conclude this Section mentioning an equivalent way of expressing the Skyrme EDF (1.40) used for the first time in [59], written as a function of the isoscalar and isovector densities n_0 and n_1

$$\begin{aligned} n_0 &= n_n + n_p \\ n_1 &= n_n - n_p \end{aligned} \tag{1.51}$$

and the analogous kinetic and spin densities τ_t and J_t, $t = 0, 1$. The energy density reads

$$\mathcal{E} = \frac{\hbar^2}{2m}\tau_0 + \sum_{t=0,1}\left[C_t^n(n_0)n_t^2 + C_t^{\nabla^2 n}n_t\nabla^2 n_t + C_t^\tau n_t\tau_t + C_t^J J_t^2 + C_t^{\nabla J}n_t\boldsymbol{\nabla}\cdot J_t\right] \tag{1.52}$$

where the coefficient C are, as a function of the t_is and x_is

$$\begin{aligned} C_0^n &= \frac{1}{8}\left(3t_0\right) + \frac{1}{48}\left(3t_0\right)n_0^\sigma; & C_1^n &= -\frac{1}{8}\left(t_0+2t_0x_0\right) - \frac{1}{48}\left(t_0+2t_3x_3\right)n_0^\sigma \\ C_0^{\nabla^2 n} &= \frac{1}{64}\left(-9t_1+5t_2+4t_2x_2\right); & C_1^{\nabla^2 n} &\frac{1}{64}\left(3t_1+6t_1x_1+t_2+2t_2x_2\right); \\ C_0^\tau &= \frac{1}{64}\left(12t_1+20t_2+16t_2x_2\right); & C_1^\tau &= \frac{1}{64}\left(-4t_1-8t_1x_1+4t_2+8t_2x_2\right); \\ C_0^J &= \frac{1}{64}\left(4t_1-8t_1x_1-4t_2-8t_2x_2\right); & C_1^J &= \frac{1}{64}\left(4t_1-4t_2\right) \\ C_0^{\nabla J} &= -\frac{W_0}{2}-\frac{W_0'}{4}; & C_1^{\nabla J} &= -\frac{W_0'}{4} \end{aligned} \tag{1.53}$$

We will use both formulations of the Skyrme EDF in the following.

1.5 Nuclear matter and the nuclear Equation of State

Nuclear matter is defined as a uniform infinite system composed of neutrons and protons at zero temperature interacting only through the nuclear force [12, 91–93]. The Coulomb interaction among protons is neglected, as its energy in an infinite system would be divergent.

Clearly, nuclear matter is an idealisation. On the other hand, it is achieved, to a good extent, in the interior of nuclei, where the density is roughly constant and the interaction is dominated by the nuclear force, and in neutron stars, where the high densities in their interior exceed the nuclear ones (see Chapter 2) [12]. Finite nuclei deliver information only on symmetric or quasi-symmetric matter, i.e., when the proton and neutron densities are similar; neutron stars deliver information on highly asymmetric matter instead, since they are mostly composed of neutrons.

Of particular interest is the so-called nuclear equation of state (nEOS), the energy per particle e of nuclear matter, as a function of the total baryon density n_B and the neutron-proton asymmetry δ

$$\begin{aligned} n_B &= n_n + n_p \\ \delta &= \frac{n_n - n_p}{n_n + n_p} \end{aligned} \tag{1.54}$$

For instance, $e(n_B, 0)$ represents the energy per particle of symmetric nuclear matter, while $e(n_B, 1)$ represents the energy of pure neutron matter.

As it is known [53, 54] the nuclear force displays a saturation mechanism. This can be seen in electron scattering experiments [94], where the measured density in the interior of nuclei is approximately 0.16 fm^{-3}, regardless of the nucleus, and roughly constant away from the nuclear surface [53, 54]. This suggests that the pressure in the nuclear interior vanishes. Rephrased in the nEOS formalism, given that the pressure P reads [73]

$$P(n_B, \delta) = n_B^2 \left. \frac{de}{dn} \right|_{(n_B, \delta)} \tag{1.55}$$

this indicates that $e(n_B, 0)$ presents a well-defined minimum, since the nuclear interior is approximately symmetric. The density at which this minimum appears is called the saturation density n_{sat}.

It is customary to expand $e(n, \delta)$ in powers of δ around 0

$$e(n_B, \delta) \approx e(n_B, 0) + S(n_B)\delta^2 + o(\delta^4) \tag{1.56}$$

where we only retain the even powers due to the isospin symmetry of the nuclear interaction. We define the symmetry energy $S(n_B)$

$$S(n_B) = \frac{1}{2} \left. \frac{\partial^2 e}{\partial \delta^2} \right|_{\delta=0} \tag{1.57}$$

which represents the energy required to venture into asymmetric matter. Although Eqs. (1.56) and (1.57) have meaning in the proximity of $\delta = 0$, one remarkably finds that $S(n_{sat}) \approx e(n_{sat}, 1) - e(n_{sat}, 0)$; so one could interpret (1.57) as the energy cost of transmuting all protons into neutrons.

Expanding $e(n_B, 0)$ and $S(n_B)$ around n_{sat} leads to[2]

$$e(n_B, 0) = \sum_{k=0}^{4} \frac{1}{k!} \left(\frac{n_B - n_{sat}}{3n_{sat}} \right)^k X_{sat}^k + o(n_B - n_{sat})^5 \tag{1.58}$$

$$S(n_B) = \sum_{k=0}^{4} \frac{1}{k!} \left(\frac{n_B - n_{sat}}{3n_{sat}} \right)^k X_{sym}^k + o(n_B - n_{sat})^5 \tag{1.59}$$

where the coefficient of the expansion

$$\begin{aligned} X_{sat}^k &= (3n_{sat})^k \frac{\partial^k e(n_B, 0)}{\partial n^k} \bigg|_{n_B = n_{sat}} \\ X_{sym}^k &= (3n_{sat})^k \frac{\partial^k S(n_B)}{\partial n^k} \bigg|_{n_B = n_{sat}} \end{aligned} \tag{1.60}$$

are called nuclear matter parameters (NMP), and their value is strictly tied to the results of nuclear experiments and neutron star observations [12]. In particular, for the saturation parameters (the coefficients of the $e(n_B, 0)$ expansion)

- $\boldsymbol{X_{sat}^0 = E_{sat}}$: the energy per particle of symmetric matter at saturation;
- $\boldsymbol{X_{sat}^1 = L_{sat} = 0}$: the slope of the energy of symmetric matter at saturation. Since we know that $e(n_{sat}, 0)$ is a minimum of $e(n_B, 0)$, then L_{sat} vanishes. The condition $L_{sat} = 0$ actually determines the nuclear saturation density, and it is why one considers n_{sat} a NMP;
- $\boldsymbol{X_{sat}^2 = K_{sat}}$: the incompressibility of symmetric matter.

For the high order coefficients $\boldsymbol{X_{sat}^3 = Q_{sat}}$ and $\boldsymbol{X_{sat}^4 = Z_{sat}}$ very little is known, as their influence on the properties of nuclear system is very difficult to probe; this is not surprising, since nuclei have densities around saturation, and such high derivatives should not have a great impact.

Similarly, for the symmetry parameters (the coefficients of the $S(n_B)$ expansion)

- $\boldsymbol{X_{sym}^0 = E_{sym}}$: the symmetry energy at saturation;
- $\boldsymbol{X_{sym}^1 = L_{sym}}$: the slope of the symmetry energy at saturation. Since $L_{sat} = 0$, L_{sym} is linked to the pressure of neutron matter at saturation;
- $\boldsymbol{X_{sym}^2 = K_{sym}}$: the curvature of symmetry energy, deeply connected to L_{sym}, but quite difficult to constrain.

For the high order coefficients $\boldsymbol{X_{sym}^3 = Q_{sym}}$ and $\boldsymbol{X_{sym}^4 = Z_{sym}}$ the same holds as for their *sat* counterparts.

Experiments on nuclei and astronomical observations of neutron stars further our knowledge of the properties of nuclear matter, constraining the NMPs. As mentioned above, experiments on nuclear radii measure the internal densities of nuclei, which turn out to be approximately constant across the nuclear chart. As that density is n_{sat}, nuclear radii measurements constrain n_{sat}. Nuclear binding energies bring information about the

[2] The presence of the denominator $3n_{sat}$ is reminiscence of an expansion in k_F, since $dk_F/k_F = 1/3\, dn_B/n_B$.

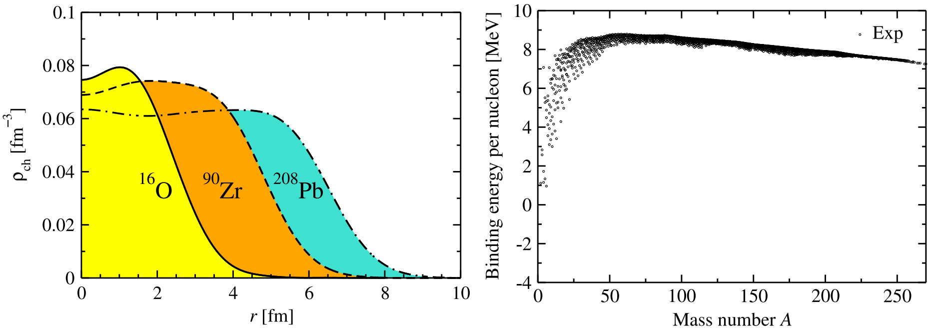

Figure 1.5: Experimental charge density for three different nuclei (left), and binding energy per nucleon across the nuclear chart (right). Images taken and adapted from [12].

value of $e(n_{sat}, 0)$. Since in symmetric matter, Coulomb, finite size, and asymmetry effects are not to be considered, its value corresponds to the volume term of the liquid drop model [54]; therefore, $E_{sat} \approx -16$ MeV. Both these constraints are a manifestation of the saturation property of the nuclear force, and we show in Figure 1.5 the experimental data supporting it: on the left, there is the charge density, akin to the proton density, which is roughly constant in the nucleus interior, and approximately the same for different nuclear species; on the right, there is the binding energy per nucleon, which saturates at approximately 8 MeV once nuclei are heavy enough, more or less, since they have at least of 50 nucleons.

When the number of neutrons exceeds that of protons in nuclei, the neutron density extends farther out than the proton one. The resulting external layer, called neutron skin, is therefore composed of highly asymmetric matter. The neutron skin thickness is defined as the difference between neutron and proton root mean square radii, Eq. (1.24), and it is a source of information on the density dependence of the symmetry energy [95].

Neutron distributions are very difficult to measure [12]: neutrons have null electric charge, so electric probes cannot be employed, while hadronic ones suffer from model dependency stemming from the uncertainties in the nuclear force. However, the neutron weak charge is much greater than the proton one, and weak probes offer a model-independent way of studying the neutron distribution. Recently, parity-violating elastic electron scattering experiments measured the so-called parity-violating asymmetry A_{PV} for ^{208}Pb and ^{48}Ca [38, 39]. The A_{PV} quantifies the difference between the cross section of left- and right-handed electrons scattering on the target nucleus. From the measured A_{PV} one can infer the neutron distribution, and, consequently, the neutron skin thickness. To a greater skin thickness corresponds a greater neutron pressure, which, as we mentioned above, is linked to the NMP L_{sym}.

Giant resonances are another source of information on the nEOS parameters [12, 13, 75, 96]: isoscalar modes, where protons and neutrons are excited in phase, explore how nuclear matter can be compressed and deformed; isovector modes, where instead protons and neutrons are excited out of phase, shed light on properties of highly asymmetric matter (so δ different from 0), which are otherwise quite difficult to probe. Of particular importance for the parameter K_{sat} is the isoscalar giant monopole resonance, also called breathing mode, where the nucleus vibrates, compressing and expanding. The excitation energy of this mode constrains this parameter, since, following its definition Eq. (1.60), it can be interpreted as the compressibility of symmetric nuclear matter. On the isovector side, the dipole polarizability α_D Eq. (1.37) can be linked, in simplified liquid drop

Table 1.2: Summary for the Nuclear Matter parameters. We list credible intervals for their value, as presented in [12]. the question mark denotes the fact that present experimental information cannot constrain the value of the parameter. In the second column, we state the observation sources from which we can infer them. The list is not comprehensive, but instead is limited to the sources we will use in the following. For the sake of compactness, we use this legend: BE = binding energies, ISGMR = IsoScalar Giant Monopole Resonance, IVGDR = IsoVector Giant Dipole Resonance, A_{PV} = Parity-Violating scattering, NS = Neutron star.

		Range	Experiments
n_{sat}	[fm^{-3}]	[0.154,0.159]	Charge and nuclear densities
E_{sat}	[MeV]	[-16.2,-15.6]	BE
K_{sat}	[MeV]	[220,260]	ISGMR
Q_{sat}	[MeV]	?	-
Z_{sat}	[MeV]	?	-
E_{sym}	[MeV]	[28,36]	BE, IVGDR, NS
L_{sym}	[MeV]	[20,120]	BE, IVGDR, A_{PV}, NS
K_{sym}	[MeV]	?	Possibly NS
Q_{sym}	[MeV]	?	-
Z_{sym}	[MeV]	?	-

models, to the neutron skin thickness and the symmetry energy at saturation; therefore it represent an important constraint the parameters E_{sym} and L_{sym} [97, 98].

Neutron stars also offer a precious insight into the behaviour of neutron-rich matter, well beyond the densities explored by nuclei [92]. All their properties, from masses and radii to tidal deformability, depend intimately on the stellar equation of state, which is built upon the nEOS.

In Table 1.2, the reader can find a summary of the typical ranges for the nuclear matter parameters and what kind of experiments constrain them. We did not include the constraints coming from Heavy Ion Collision (HIC) experiments, because we will not employ these results in the following. For a review of the topic, we refer to [99, 100].

1.5.1 Nuclear equation of state from EDF

Deriving the nEOS from the EDFs is rather simple. One needs to take the functional term of the EDF and disregard all terms that concern finite-size effects (i.e., density gradients) and spin-orbit contributions [73]. So, for Skyrme, one must retain only the $\mathcal{E}_0^{Sky}$, $\mathcal{E}_3^{Sky}$ and $\mathcal{E}_{\rm eff}^{Sky}$ terms of Eq. (1.40). If we express it in terms of total baryon density n_B and neutron-proton asymmetry δ Eq. (1.54), it reads

$$\begin{aligned} e^{Sky}(n_B,\delta) =& \frac{3}{5}\frac{\hbar^2}{2m}\left(\frac{3\pi^2}{2}\right)^{2/3} n_B^{2/3} F_{5/3}(\delta) + \frac{1}{8} t_0 n_B \left[2\left(x_0+2\right) - \left(2x_0+1\right) F_2(\delta)\right] \\ &+ \frac{1}{48} t_3 n_B^{\sigma+1} \left[2\left(x_3+2\right) - \left(2x_3+1\right) F_2(\delta)\right] \\ &+ \frac{3}{40}\left(\frac{3\pi^2}{2}\right)^{2/3} n_B^{5/3} \Big\{\left[t_1\left(x_1+2\right) + t_2\left(x_2+2\right)\right] F_{5/3}(\delta) \\ &+ \frac{1}{2}\left[t_2\left(2x_2+1\right) - t_1\left(2x_1+1\right)\right] F_{8/3}(\delta)\Big\} \end{aligned} \tag{1.61}$$

where the function $F_m(\delta)$ is defined as $F_m(\delta) = [(1+\delta)^m + (1-\delta)^m]/2$.

From the expressions (1.61) one can derive the relation between the parameters of the interaction and the nuclear matter parameters through Eq. (1.60).

It is worth noting that, in principle, not all NMPs are independent from one another. For example, standard Skyrme like (1.41) have too few parameters, and only n_{sat}, E_{sat}, K_{sat}, E_{sym} and L_{sym} are truly independent; the others will be heavily correlated to them [101]. Although such high derivatives of the nEOS are not as relevant for the properties of nuclei, they play a significant role in determining the behaviour of nuclear matter at super-saturation densities, which is crucial for the modelling of neutron stars (see below, Chapter 2). Extended Skyrme-like those proposed in Eq. (1.49) can increase the functional flexibility and relax at least some of these restrictions, although the present experimental information from nuclear physics and astrophysics is not sufficient to constrain the higher-order NMPs like $Q_{sat,sym}$ and $Z_{sat,sym}$. However, as it is argued in [101], there is still merit to employ more sophisticated functional forms to avoid these model-induced, spurious correlations reverberating onto the free parameters. We relied on a standard Skyrme interaction and therefore we are subject to this inherent systematics. We will revisit this issue in the relevant points of this Thesis and in the Conclusions.

There are present in the literature a handful of EDFs that are more flexible than Skyrme, like the KIDS functional [102–104], where the parameters K_{sym} and Q_{sat} are free, and the already mentioned Fayans [10], that has K_{sym} independent, whose main features we will discuss about in Appendix A.

Chapter 2

Neutron stars

We now turn our attention to neutron stars (NS). They are among the most compact objects in the universe: their mass is approximately between one and two solar masses ($M_\odot$) and their radius between 10 and 15 km [14, 15]. If the star were a homogeneous sphere, its density would be around the nuclear saturation density, $\overline{n}_{NS} \approx n_{sat}$. That said, the density is maximum in the interior and it surpasses n_{sat}, with some theoretical models reaching even ten times saturation density [105]. Newtonian gravity is not valid in their proximity, and general relativity is needed instead.

NS matter is so dense that the very concept of a nucleus loses its meaning. Indeed, besides the external layers, NSs are composed of a fluid of neutrons and protons, with electrons and, eventually, muons, to guarantee electrical neutrality [106]. More exotic degrees of freedom, like hyperons or even deconfined quark matter, may appear in the innermost regions [107, 108], although the present observational indications cannot confirm or rule out this conjecture [109]. In this work, we will assume that the interior of NSs is constituted by nucleonic matter (see Sec. 1.5), and we will not delve into these interesting possibilities.

The nuclear equation of state (nEOS), in particular that of pure neutron matter (PNM), is one of the fundamental tools to study NS equation of state (EOS) [92, 108, 110], which determines their structure and deeply influences their observational properties, like masses, radii, and tidal deformability. Therefore, one can use NS astronomical observations as a benchmark to test EOS candidates and to study the nuclear matter behaviour at densities well beyond those attainable on Earth in nuclear experiments.

This Chapter is structured as follows. In Section 2.1 we will present a concise overview of the properties of NS, and the theoretical means to compute all the observational properties. Then, in Section 2.2, we will go through the most constraining observational data for the study of the EOS. We will move on to Section 2.3 where we will focus on how to build the equation of state of the star from a particular nuclear model, and we will conclude with Section 2.4 where we will present the meta-model (MM), that is the nEOS formalism we used in this work as an extension of the Skyrme nEOS to study the NS core.

2.1 Phenomenology of Neutron Stars

The idea of NSs precedes their discovery greatly. Indeed, the first proposal of a "dense star, which looks like a giant nucleus" is to be attributed to Lev Landau in the early 1930s, just before Chadwick's discovery of the neutron in 1932 (see [111] for an interesting historical reconstruction). In 1934, Baade and Zwicky advanced the idea of *neutron stars*, and proposed that they are the remnants of supernova explosions [112, 113]. Remarkably, after almost 100 years, the scientific community still agrees that NSs are born in core-collapse supernovae. We will present in the following a schematic overview of NS formation, while more information can be found in detailed reviews [114–117].

As it is widely known, stars counterbalance the gravitational pressure with the energy released by fusion reactions in their interior [118, 119]. Protons are converted into helium, helium into carbon, and so on, until the fusion chain reaches ^{56}Fe, the most stable nuclear species (^{56}Fe has one of the highest binding energies per nucleon; see Fig. 1.5); afterwards, fusion becomes energetically disfavoured and halts. Only sufficiently massive stars ($M \geq 8M_{\odot}$) can reach this stadium [114]; lighter ones usually stop somewhere in the chain, and their destiny is to become white dwarfs.

Once iron starts being produced, it falls in the star's core, which is supported solely by the degeneracy pressure of the electrons [14]. However, this pressure can sustain masses up to the Chandrasekhar limit $M_C \simeq 1.44\, M_{\odot}$ [120]; heavier objects will collapse. Such is the fate of the iron core: as matter continues falling inside it, its mass surpasses the Chandrasekhar limit and starts collapsing, quickly followed by the rest of the star. The density in the iron core increases drastically in this process, with the electrons pushed into the nuclei, neutronizing matter. Their disappearance accelerates the collapse, as their degeneracy pressure, which was still opposing the implosion, rapidly plummets. When the core density exceeds the nuclear saturation n_{sat}, matter rapidly stiffens due to the short-range nuclear repulsive force and the core bounces back [114]. If the star is too massive ($M \geq 25M_{\odot}$), then this bounce cannot halt the gravitational collapse, and eventually a black hole will be formed; otherwise, the rebound scatters the stellar material away in a supernova explosion. The whole process is incredibly fast, taking approximately one second [114].

The iron core remnant becomes a proto-neutron star (PNS), whose matter is heated considerably during the violent process of the core-collapse, with temperatures reaching up to $T \sim 10^{11-12}$, $K \sim 10 - 100$ MeV. Nonetheless, in a short time (a matter of days), much of this heat is carried away by neutrinos escaping the star [121, 122]: the outer layers of the NS solidify into a lattice of neutron-rich nuclei (the so-called crust), which will take some centuries to radiate away its residual heat [108], while the nuclear matter inside (the core) becomes isothermal when the temperature drops to $\sim 10^8\, K \sim 0.01$ MeV [123]. A neutron star is born.

The considerable shrinkage of the dying star core results in sizeable rotation frequencies and magnetic fields of NSs. Their period is typically below 10 s, with the fastest rotating ones arriving at ≈ 1 ms [124], while their magnetic fields reach 10^{10-11} G, with the so-called "magnetars" NSs reaching 10^{15} G [125]. NSs emit radiation beams from their magnetic poles. If their spin axis is misaligned from its magnetic axis, and if this pulse is emitted towards Earth, it acts like a lighthouse in the sky, and we call the NS a pulsar. They were observed for the first time in 1968 by Hewish and Bell[1] [126]. The pulsating electromagnetic emission is extremely stable in time [14], and this remarkable precision led to the measurements of small irregularities, sudden spin-ups called glitches [127]. They entail interesting consequences for NS structure, in particular for their crust, and are the subject of thorough investigations [128].

All these objects, which emit across the electromagnetic spectrum, are indeed all the same, NSs [129], of different ages and magnetic fields; their internal structure is the same. Since the density spans several orders of magnitude, stellar matter widely differs, and several layers, with different properties and characteristics, can be identified descending from the surface to the center [14]. In Figure 2.1, we show a schematic representation of the typical layering.

[1] Actually, pulsars were the first NSs ever observed.

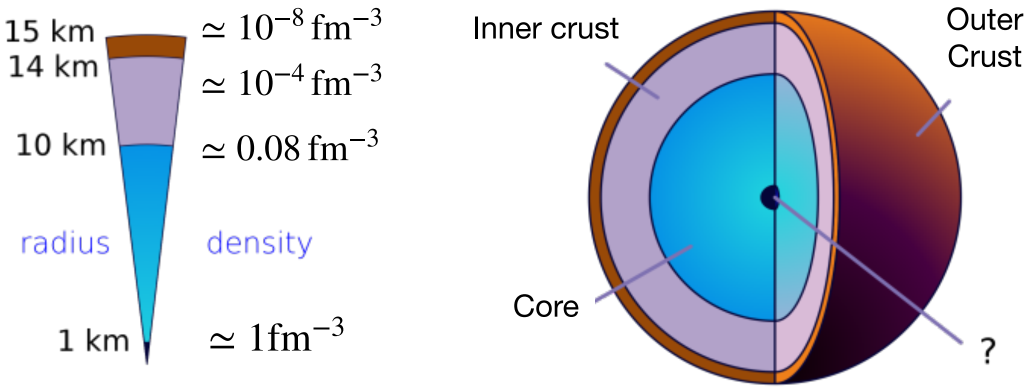

Figure 2.1: Layering of a NS. Image by, and adapted from, Wikipedia user Brews Ohare. CC BY-SA 3.0.

The outermost layer is a thin (just some millimeters thick) and relatively diluted atmosphere, where density is lower $n \leq 10{-}8$ fm^{-3} and the thermal and magnetic effects cannot be disregarded [130]. Although crucial for the study of the emission spectra of NSs, this zone is not important for the modelling of their structure, and we will not study it in our work.

The outer crust lies below. It is composed of a solid lattice of completely ionized atoms immersed in a homogeneous electron fluid. As the density increases going deeper, matter neutronization progresses and the ions become richer and richer in neutrons [131–134]. Once the density is sufficiently high, $n \approx 2 \times 10^{-4}$ fm^{-3}, the nuclei reach their drip-line and neutrons start leaking out, filling the space among lattice points [132]. Since ions are not isolated anymore, but are instead part of a continuous, although inhomogeneous, nuclear medium, one usually refers to them as nuclear clusters, or, simply, clusters. The so-called neutron drip density n_d marks the end of the outer crust and the beginning of the inner crust. As the density of the neutron sea keeps rising as the depth increases, the free neutrons form a macroscopic superfluid [135]; its presence entails profound consequences for several astrophysical phenomena, like for NSs cooling or pulsar glitches [136]. In the very bottom layers of the inner crust, the neutron sea becomes so dense that nuclear clusters may get deformed into exotic shapes, like rods, slabs, or hollow cylinders. These shapes are generally referred to as the pasta-phase [137].

Once the free neutron gas density reaches approximately half saturation density, i.e., $n_{sat}/2 \approx 0.08$ fm^{-3}, then the very concept of nucleus loses its meaning, clusters disappear, and star matter becomes homogeneous. This point marks the transition from the crust to the core of the star, and the density at which it happens is the so-called crust-core transition density n_{cc}. It is a very delicate quantity to determine, and, as we will show below, is affected by model-dependency.

The core accounts for $\sim 90\%$ of the star radius and more than 95% of its mass, and its matter is composed of free neutrons, protons, electrons, and, eventually, muons [14, 106]. Protons as well are superfluid in this region, and neutrons may show the more exotic $^3\mathrm{P}_2$ pairing. There is much speculation about whether more exotic degrees of freedom, like hyperons, deconfined quark matter, or even dark matter, could appear in the deepest part of NS [108, 138, 139]. If one accounts for these possibilities, then an additional layer should be added, the so-called inner core (opposed to the outer core composed of normal nuclear matter). As mentioned in the introduction of this chapter, we will not explore this possibility and will work under the nucleonic hypothesis.

NSs are, obviously, in hydrostatic equilibrium. Due to their compactness, the usual Newtonian hydrostatic equilibrium equations do not hold; one needs to use their relativistic counterpart, the so-called Tolman–Oppenheimer–Volkoff (TOV) equations [140, 141]

$$\begin{aligned} \frac{dP}{dr} &= -\frac{G\rho(r)\,m(r)}{r^2}\left(1+\frac{P(r)}{\rho(r)c^2}\right)\left(1+\frac{4\pi P(r)r^3}{m(r)c^2}\right)\left(1-\frac{2Gm(r)}{rc^2}\right)^{-1} \\ \frac{dm}{dr} &= 4\pi r^2\rho(r) \end{aligned} \tag{2.1}$$

where G is the universal gravitational constant, $P(r)$ is the pressure profile, $\rho(r)$ is the mass density profile and $m(r)$ is the enclosed mass within a radius r, linked to the density $\rho(r)$ through the second equation. The boundary conditions are

$$\begin{cases} m(r=0) & = 0 \\ \rho(r=0) & = \rho_c \\ P(r=R) & = 0, \end{cases} \tag{2.2}$$

where ρ_c is the central density of the star and R its radius.

The TOV Eqs. (2.1) were published in 1939, and hold in the case of a spherical symmetric and static space time. They are not a closed system, since there are three unknown functions (m, ρ, and P), but only two equations. The relation between pressure and density is not known *a priori*; that is, one needs to know the EOS of stellar matter to solve the system. Since the star is composed of different constituents in its various layers, in principle, the pressure is a function of all the different densities ρ_i as well as of the temperature, that is, $P = P(\rho_i, \ldots, T)$. As we will discuss later (see Sec. 2.3), it turns out that for the description of sufficiently old NS the pressure depends only on the baryon density ρ_B, i.e., $P = P(\rho_B)$.

The solution of the TOV Eqs. (2.1) for different central densities ρ_c gives rise to the so-called $M-R$ relation, a curve in the mass-radius plane where one reads the radius corresponding to a given mass. It is one of the EOS most distinctive fingerprints. Indeed, the NSs EOS is the sole element missing from the TOV Eqs. (2.1), and thus it determines the $M-R$ relation completely: simultaneous measurements of masses and radii of a single NS can help discriminate between realistic and unrealistic models. For a central density $\rho_{c,max}$, the $M-R$ curve reaches its maximum, i.e., the maximum mass M_{max} a NS can support. If it is lower than the largest observed mass, $M_{max} < M_{max}^{obs}$, then again the EOS in question is unrealistic and should be discarded. As an example, we show in Figure 2.2 the $M-R$ relation for different Skyrme-derived EOS (the details on how to derive the stellar EOS from an EDF will be given below in Sec. 2.3). The yellow and purple points represent the simultaneous mass-radius measurements of the NICER mission [142, 143], while the two coloured stripes are the largest NS mass observed with the Shapiro delay technique [14] (a concise description of observational constraints will be given below, in Sec. 2.2). EOSs that do not reach the maximum mass, or whose $M-R$ relation is inconsistent with the NICER results, should be ruled out. In this example, the authors chose EOSs that are at least marginally compatible with observational data; as newer measurements arrive, the hope is that constraints on the EOS grow tighter and tighter. In general, stiffer EOSs, i.e., those whose pressure is greater, correspond to larger radii, given the same mass, than softer EOS.

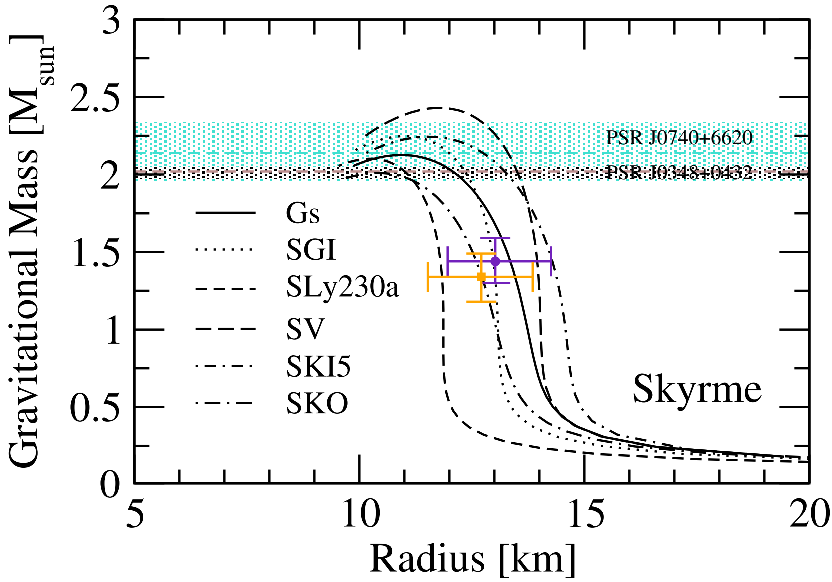

Figure 2.2: Mass–Radius relation for different Skyrme-like EOSs. The constraints from the NICER mission (yellow and purple dots) [17, 18] and the maximum mass criterion from PSR J0740+6620 and PSR J0348+0432 (dotted horizontal bands) are shown as well [16, 144], to assess the compatibility of each EOS with the astronomical observations. Plot taken and adapted from [145].

Another interesting quantity of the star is its moment of inertia. In the slow rotating approximation, the moment of inertia I can be written as [146]

$$I = \frac{8\pi}{3} \int_0^R dr\, r^4\, e^{-\Phi(r)+\Lambda(r)} \left(\rho(r) + \frac{P(r)}{c^2} \right) \frac{\bar{\omega}(r)}{\Omega} \tag{2.3}$$

where Ω is the angular velocity of the star, Φ and Λ are metric functions and $\varpi(r)$ encodes the dragging of the inertial frame. Remarkably, the ratio $\bar{\omega}(r)/\Omega$ depends entirely on the EOS [147]. By changing the integral limits in Eq. (2.3), one can compute the moment of inertia of the crust, which is of interest for different astrophysical phenomena, like glitches and NSs cooling [148–150].

Another purely EOS-dependent property of NSs is the so-called tidal deformability, which can be measured in binary NS systems [151]. These systems emit gravitational waves, which carry away energy and cause the stars to orbit closer and closer. As the distance decreases, they become progressively deformed due to the tidal field of the companion. This deformation is quantified by the induced quadrupole moment Q, which is proportional to the tidal field $\mathcal{G}$

$$Q = -\lambda \mathcal{G} \tag{2.4}$$

where the proportionality factor is the tidal deformability λ, which encodes how much an object is deformable. We are actually interested in the adimensional tidal deformability Λ, which reads

$$\Lambda = \frac{\lambda}{M^5} = \frac{2}{3} k_2 \beta^{-5} \tag{2.5}$$

where M is the mass of the star, k_2 is the tidal Love number and $\beta = GM/(Rc^2)$. In the following, if we refer to the tidal deformability, we are referring to the adimensional one

Eq. (2.5). In the slow rotation approximation, k_2 is a function of pressure and density

$$k_2 = \frac{8}{5}\beta^5(1-2\beta)^2[2-y(R)+2\beta(y(R)-1)]/a \tag{2.6}$$

with

$$\begin{aligned} a &= 6\beta[2-y(R)+\beta(5y(R)-8)] \\ &\quad + 4\beta^3\left[13-11y(R)+\beta(3y(R)-2)+2\beta^2(1+y(R))\right] \\ &\quad + 3(1-2\beta)^2[2-y(R)+2\beta(y(R)-1)]\ln(1-2\beta) \end{aligned} \tag{2.7}$$

and

$$\begin{aligned} \frac{dy}{dr} =& -\frac{y^2}{r} - \frac{y-6}{r-2Gm/c^2} \\ & - \frac{4\pi G}{c^2} r^2 \frac{(5-y)\rho + (9+y)P/c^2 + \left(P+\rho c^2\right)/c_s^2}{r-2Gm/c^2} \\ & + \frac{1}{r}\left[\frac{2G}{c^2}\frac{\left(m+4\pi P r^3/c^2\right)}{r-2Gm/c^2}\right]^2 \end{aligned} \tag{2.8}$$

with the boundary condition for $y(r)$ being $y(0) = 2$. In the above, c_s is the speed of sound of matter. Once again, the only information missing from computing Eq. (2.8) and thus the tidal deformability Λ (2.5) is the relation $P(\rho)$. At equal mass, stiffer EOS translates into a larger Λ than softer EOS.

The gravitational waves produced by the binary system can be detected by gravitational telescopes like LIGO and VIRGO. In particular, as we will see below in Sec. 2.2, the phase of the wave signal depends on a combination of both Λ, $\tilde{\Lambda}$

$$\begin{aligned} \tilde{\Lambda} &= \frac{16}{13}\frac{(M_1+12M_2)\,M_1^4\Lambda_1 + (M_2+12M_1)\,M_2^4\Lambda_2}{(M_1+M_2)^{1/5}} \\ &= \frac{16}{13}\frac{(1+12q)\,\Lambda_1 + (q+12)\,q^4\Lambda_2}{(1+q)^5} \end{aligned} \tag{2.9}$$

and the frequency on a combination of both masses, the so-called chirp mass $\mathcal{M}$ [110]

$$\mathcal{M} = \frac{(M_1 M_2)^{3/5}}{(M_1+M_2)^{1/5}} \tag{2.10}$$

where the subscripts 1 and 2 indicate the mass or the tidal deformability of the stars in the system. In the second row of Eq. (2.9), we wrote $\tilde{\Lambda}$ as a function of the mass ratio $q = M_2/M_1$ of the lighter star and the heavier.

Information from gravitational waves offers another precious, model-independent constraint on the NS EOS.

2.2 Observations

As explained in the previous section, observations of mass, radius, and tidal deformability constrain the EOS of NSs. In this Section, we review the most important measurements available today.

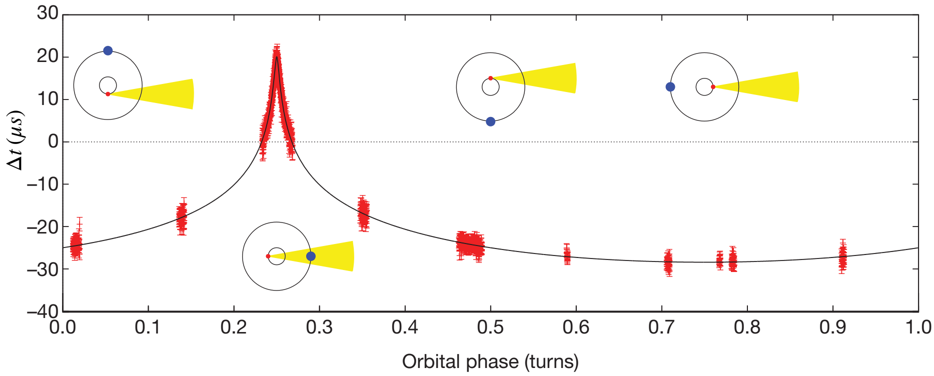

Figure 2.3: Shapiro delay measurement for a pulsar in a binary system, as a function of the orbital phase. The black line is the delay predicted, and the red line is the one measured. The cartoons show particular orbit positions, with the red dot being the pulsar, the blue one its companion, and the yellow cone the pulse emitted towards Earth. Plot taken and adapted from [154].

2.2.1 Mass measurements and maximum mass

As illustrated before in Sec. 2.1, one critical aspects of $M - R$ plots is the concept of maximum mass M_{max}: if it is lower than the most massive neutron star observed, then the EOS is unrealistic. From this important constraint on the EOS stems our interest in mass measurements. As a reference, most NSs have 1.4 $M_{\odot}$, while the heaviest confirmed stars are slightly above 2 $M_{\odot}$.

One of the most precise and clean techniques to measure neutron star masses is the so-called Shapiro delay [152], which exploits the fact that light takes more time to reach an observer traveling near a massive object than it would need traveling in a flat time-space. In particular, Shapiro delay is well-suited to study the mass of pulsar companions in binary systems [153]. Given the extreme regularity of pulsar emission, the arrival time delay of the pulse, caused by the companion orbiting in front of the line of sight of the telescope, can be measured with great accuracy. In Figure 2.3, we show the measurement of the Shapiro delay Δt of the pulse of pulsar J1614-2230 [154], as a function of the orbital phase. The black line is the theoretical Shapiro delay, while the red points are the measurements. The cartoons help localize the relative position of the objects during the orbit: when the delay is greatest, the companion (blue dot) is directly in front of the pulse (yellow cone) emitted by the pulsar (red dot). From the time delay, one can measure with great precision the mass of the companion, from which, in turn, one can derive the mass of the pulsar from the Keplerian orbit [155]. It turns out that J1614-2230 is quite massive, $M = (1.97 \pm 0.04)\, M_{\odot}$.

Shapiro delay is a very clean measure of the NS masses, as its only assumption is the validity of general relativity. Beside J1614-2230, other notable measurements are the pulsars J0348+0432, with $M = (2.01 \pm 0.04)\, M_{\odot}$ [16], and J0740+6620, with $M = (2.08 \pm 0.07)\, M_{\odot}$ [144].

Due to its lack of model dependence, we decided to include only mass measurements done with Shapiro delay in our analysis on the stellar EOS (see Sec. 5.4). Other mass measurements, performed with other techniques, like the extremely massive pulsar J0952-0607 ($M = (2.37 \pm 0.17)\, M_{\odot}$) [156], will not be taken into account.

However clean it may be, Shapiro delay cannot probe the star radius; so only heavier and heavier masses can put new constraints on the EOS. Instead, the NASA NICER mission can perform such delicate measurements. We will illustrate its properties in the next subsection.

2.2.2 Mass and radius measurements

The Neutron star Interior Composition ExploreR (NICER) [142, 143] aims to measure pulsar masses and radii simultaneously. The telescope picks up soft X-ray emissions from the so-called hot-spots, surface regions with a higher temperature than their surroundings.

In particular, as the NS revolves, NICER can follow the intensity of the hot-spot emissions. Due to the intense curvature of space-time in the proximity of the star, some light emitted from its far side not facing the telescope can still be detected, as sketched in Figure 2.4a. This effect is more appreciable the more compact the pulsar is.

From the study of these pulses, one can, through a Bayesian analysis, infer the properties of the emitting object. In particular, four mass-radius measurements were reported: PSR J0030+0451 [17, 18], PSR J0740+6620 [157, 160], PSR J0437+4715 [158], and PSR J0614–3329 [159], though the systematics of this last analysis are still debated. The probability distributions for these four measurements are shown in Figure 2.4b.

Unlike the Shapiro delay, the analysis of NICER data is more model-dependent. The composition of the atmosphere, as well as the complexity added by the strong magnetic fields, makes the modelling of the hot-spot and its emission particularly challenging [142]. As a consequence, the error bars are large. Therefore, many EOS candidates are compatible with the NICER observations.

2.2.3 Gravitational waves observations

As mentioned earlier, NSs in binary systems are a source of gravitational waves. As this emission carries away energy from the system, NSs spiral closer and closer, getting deformed by the tidal field of the companion, until eventually they merge. The combined deformability $\tilde{\Lambda}$ Eq. (2.9) affects the wave phase, while its frequency is essentially determined by the chirp mass $\mathcal{M}$ Eq. (2.10) [110, 161, 162].

The importance of the tidal deformability can be seen in Figure 2.5, which shows a simulation of the gravitational signal of two $1.4\,M_\odot$ objects, for different values of $\tilde{\Lambda}$, 0 (which corresponds to undeformable objects, i.e., black holes), 300 and 600 [163]. Long before the merging, the three signals are almost indistinguishable. On the other hand, both the wave frequency and the amplitude grow as the distance between the star decreases, and this effect is more evident the bigger $\tilde{\Lambda}$ is.

Signals like this are detectable here on Earth by the gravitational wave telescopes. On August 17$^{\text{th}}$ 2017, the LIGO gravitational wave detectors of the LIGO-VIRGO collaboration picked up the distinctive signal of two compact objects merging [19, 164]. They measured a chirp mass (2.10) $\mathcal{M} = (1.186 \pm 0.001)M_\odot$, which clearly shows that the two objects were indeed NS. On the right of Figure 2.5, we can see the signals they detected show the distinctive increase in frequency and amplitude as the time to the merger approaches.

From the analysis of these data, they were able to extract information on the joint probability distribution of $\tilde{\Lambda}$ and the mass ratio M_2/M_1 [20]. The result of their analysis is in Figure 2.6.

Although gravitational wave measurements present some small systematics due to the modelling of the waveform, the connection between observation and the star EOS is general relativity (see Sec. 2.1). This connection is more direct and cleaner than NICER's,

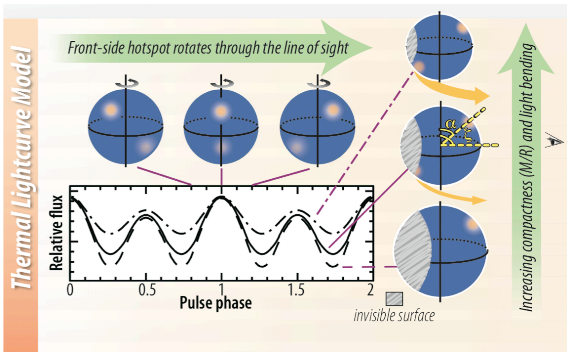

(a) Basic measurement of NICER telescope. By looking at the flux intensity of the hot-spot (red dot) as a function of the revolution, one can study the compactness property of the pulsar. For more compact stars, hot spots on the far side are more visible. Plot taken and adapted from [142].

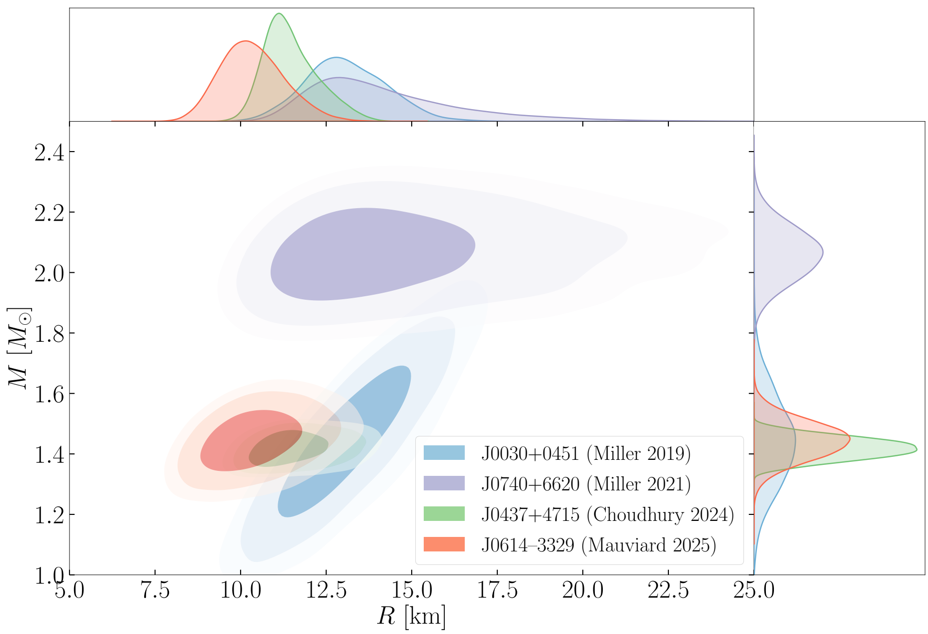

(b) NICER posteriors for the four measurements [18, 157–159]. The shaded areas identifies the 68%, 95% and 99% confidence intervals.

Figure 2.4: Concept of NICER functioning and results for the four pulsar masses and radii.

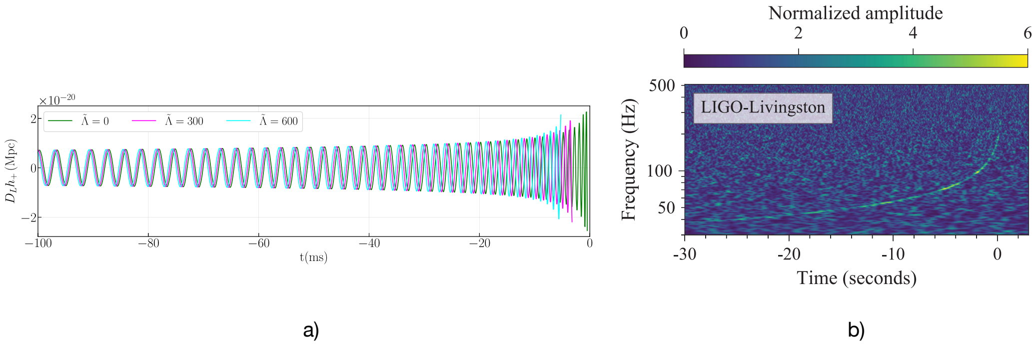

Figure 2.5: (a) Simulation of a gravitational wave signal coming from a binary system of two objects with $M = 1.4\, M_{\odot}$ as a function of time before merger, for three different $\tilde{\Lambda}$. (b) Signals detected by the LIGO-Virgo telescopes. Plots taken and adapted from [19] and [163].

and, up to date, gravitational wave signals from BNS mergers offer the potentially most powerful constraint on NSs EOS.

2.3 Equation of state

All the NS observables we discussed in Section 2.2 are uniquely determined by the stellar EOS. We will now turn our attention to how to compute it.

As mentioned earlier, the EOS is the relation between pressure P, the temperature T, and the (number n or mass ρ) densities of the different constituents like neutrons, protons, electrons, and muons, $P = P(T, n_n, n_p, n_e, n_\mu, \ldots)$.

Very shortly after NSs become neutrino-transparent (a matter of days), the temperature drops to $\approx 10^8 K$, which is much lower than the Fermi temperature of the stellar matter, in the order of $T \sim 10^{12}\, K$ [128, 165]. The temperature can be treated as null, $T = 0$, simplifying greatly the EOS. Indeed, this is not a valid assumption for PNS or for the study of BNS systems remnant; in these cases, the temperature dependence is relevant [92].

Though fast on the human scale, the cooling of the PNS is orders of magnitude slower than the timescale of both strong and weak reactions, which are therefore all in equilibrium. NS matter is therefore catalysed, i.e., it is in its absolute ground state [106]. This means that the EOS can only depend on the conserved charges of the strong and weak interaction, namely the baryonic, leptonic, and electric charge density, and the densities of the different species are determined by the chemical equilibrium relations. Moreover, except in the very first phase of the collapse and bounce of the SN, neutrinos freely escape the star, meaning that the lepton number is not conserved, and n_{lep} is determined by the weak equilibrium. Finally, the charge number is not only conserved but also constant $n_{ch} = 0$ because the star is neutral. So finally, whatever the constituents, $P = P(n_B)$, where n_B is the total baryonic density. In the specific case of a nucleonic composition, we have $n_e + n_\mu = n_p$ (charge neutrality), $\mu_n = \mu_p + \mu_e$ (again weak equilibrium with no neutrinos), with $\mu_\mu = \mu_e$. This defines an (EOS dependent) relation between n_n and n_p, or if we define $\delta = (n_n - n_p)/(n_n + n_p)$, a relation $\delta(n_B)$ (more details below, Subsec. 2.3.4).

Since we are interested in cold NS, $T = 0$ and fixed baryon density n_B, the thermo-

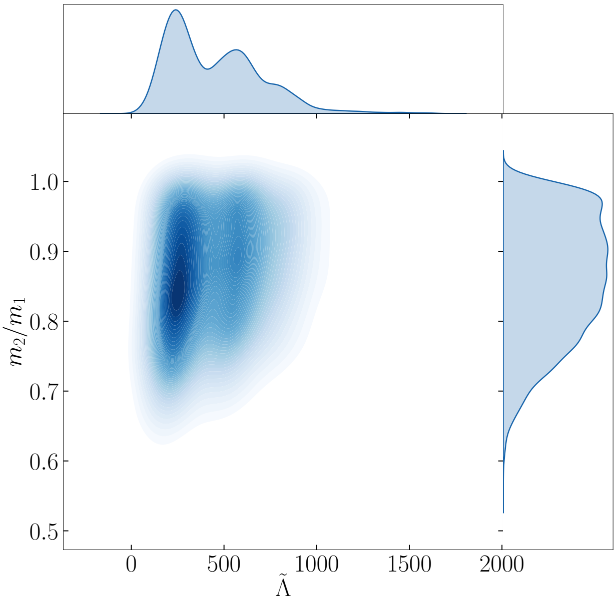

Figure 2.6: Posterior distribution of $\tilde{\Lambda}$ and mass ratio m_2/m_1 inferred from the analysis of the GW data [20].

dynamic potential corresponds to the energy per baryon $\mathcal{E}/n = e$ of the system [2]. In the nucleonic hypothesis, that is considering a (n, p, e, μ) composition, it reads:

$$\mathcal{E}(n_B) = \mathcal{E}_l(n_l) + \mathcal{E}_B(n_B, \delta(n_B)) \tag{2.11}$$

$P = n_B \partial\mathcal{E}/\partial n_B - \mathcal{E}$. The prescription is quite straightforward: one starts from a given baryon density n_B (usually below the neutron drip density n_d), computes the $\beta-$equilibrium, equivalent to the minimization of the energy function with respect to the composition under the constraint of zero net charge density[3], and finds the relevant thermodynamic quantities; then repeats this process for the successive density $n_B + \Delta n$ and so on [106].

The challenge is, therefore, finding the appropriate expression of Eq. (2.11) to minimize. Two observations are in order. First, $\mathcal{E}$ in Eq. (2.11) should reflect the layering of NSs discussed in Sec. 2.1. Second, and most important, some assumptions on nuclear interactions lie at the base of $\mathcal{E}$ [92, 108, 110]. The notion of nuclear matter and the concept of nEOS, developed in Sec. 1.5, will be very useful; in the following, we will use interchangeably the phrasing nEOS and energy density of nuclear matter, since the simple relation $\mathcal{E}/n_B = e$ links the two, and the leptonic component is fully determined as a function of the proton density n_p. It is important that the nEOS remains consistent throughout the computation of the whole EOS, so as to obtain a so-called unified EOS. As we will see, computing the EOS in the crust is significantly more complicated than in the core, and, since the crust is just a small portion of NSs, one might be tempted to use already existent crust EOS (like [166–168]) for its own core EOS. Although one might

[2] Since the Helmholtz free energy per particle $f = \mathcal{E}/n_B - Ts = \mathcal{E}/n_B$ at zero temperature.

[3] The equivalence between the equilibrium of particle (strong, weak and electromagnetic) reactions and the energy density minimization holds for all star layers and will be apparent in the simple derivation for homogeneous matter in Section 2.3.4.

assume the error introduced this way would be small, it turns out that it is not [169]: it could be of about 30% in the crust thickness estimation, and 4% in the total radius of the star. As the astrophysical constraints will become tighter and tighter in the future, one should avoid introducing such inconsistencies.

With this purpose in mind, in the next subsection 2.3.1 we will present the leptonic part of the EOS, and subsequently discuss the EOS in the crust (Subsec. 2.3.2) and in the core (Subsec. 2.3.4). A small note on the crust-core transition, and how to handle it, will be given in subsec. 2.3.3.

2.3.1 Lepton EOS

Everywhere in the star, leptons can be modelled as homogeneous [15], and their kinetic energy is that of a free relativistic Fermi gas. The interaction with the protons will be accounted for in the crust EOS and described in Subsec. 2.3.2, while in the core, the interaction gives rise to no energy contribution due to the protons being homogeneous as well.

As shown in [14], the energy density of a relativistic Fermi gas of species l reads

$$\mathcal{E}_l = \frac{c}{\pi^2}\int_0^{k_{F_l}} dk k^2 \sqrt{\hbar^2 k^2 + m_l^2 c^2} \tag{2.12}$$

where the Fermi momentum k_{F_l} is linked to the density through $k_{F_l} = (3\pi^2 n_l)^{1/3}$. From Eq. (2.12), one can derive the pressure of the gas

$$\begin{aligned} P_l(n_l) &= n_l \frac{\partial \mathcal{E}_l}{\partial n_l} - \mathcal{E}_l \\ &= \frac{P_r}{8\pi^2}\left[x_r\left(\frac{2}{3}x_r^2 - 1\right)\gamma_r + \ln\left(x_r + \gamma_r\right)\right] \end{aligned} \tag{2.13}$$

with $x_r = \hbar k_{F_l}/(m_l c)$, $P_r = m_l^4 c^5/\hbar^3$ and $\gamma_r = \sqrt{x_r^2 + 1}$. Finally, the chemical potential reads

$$\mu_l(n_l) = \frac{\partial \mathcal{E}_l}{\partial n_l} = \frac{P_l + \mathcal{E}_l}{n_l} \tag{2.14}$$

These equations hold for any relativistic Fermi gas, given the appropriate rest mass m_l of the species. In particular, they hold for electrons and muons, and we will use them extensively in the following; as we will show below, due to the weak equilibrium condition, the respective fraction is found by imposing $\mu_e(n_e) = \mu_\mu(n_\mu)$.

2.3.2 EOS in the crust

As discussed in Sec. 2.1, NS crusts are composed of a lattice of neutron-rich ions and a uniform[4] cloud of electrons (outer crust), supplemented by a uniform gas of free neutrons surrounding the nuclear clusters once the baryon density surpasses the drip point (inner crust). At the edge of the core, the density is so high that non-spherical shapes become energetically convenient for the ions, the so-called pasta phases [137]. Albeit very interesting, in the following, we will not account for these degrees of freedom, and we will only consider spherical clusters.

A simple way to approach the problem is to use the Wigner-Seitz (WS) approximation. The lattice is broken down into unit spherical cells, the so-called WS cells, at whose center

[4]Screening effects can be neglected at these densities [**131**].

sits a nuclear cluster and whose radius R_{WS} is determined by the requirement of charge neutrality. The optimal configuration would be a body-centered cubic (BCC) lattice, whose difference with the WS approximation lies in the Coulomb contribution to the energy, a difference that can be evaluated analytically and added [14, 132]. Actually, the energy density Eq. (2.11) would lead to the correct EOS only if, for all n_B, the same species of nuclear cluster is present, i.e., there is just one possible proton number Z. It turns out that this is not true, and the optimal cluster solution changes with n_B. Then, one should use the Gibbs energy per particle g at constant pressure to avoid artificial pressure discontinuities [131, 170]. However, on the one hand, the numerical errors introduced in this way are negligible [170], while on the other, the minimization of $\mathcal{E}$ at constant density is a much simpler task than that of g at constant pressure, as one would need to invert the PNM EOS. Therefore, we will continue our discussion with $\mathcal{E}$ as thermodynamic potential.

That being said, there are different strategies to model the energy density within the cell, which range from simple models, like the compressible liquid drop, to mean-field quantum approaches. While the quantum route obviously yields more reliable results, it is much more delicate to implement and much more expensive computationally. Furthermore, many different works [171, 172] showed that the EOS of the star is barely affected by the strategy one employs, and what is affected the most is the composition of the crust. However, the composition matters mostly for the NS transport properties, while it is practically irrelevant for the static properties like masses, radii, and tidal deformability, which are the only ones that interest us. In the following, we will go through those strategies relevant to this work.

Compressible Liquid Drop Model

A simple approach is the so-called Compressible Liquid Drop Model (CLDM) [131], for which the cluster is treated as a compressible liquid drop of nuclear matter. The energy density reads

$$\mathcal{E}_{WS} = \frac{E_{cl}}{V_{WS}} + \mathcal{E}_e + [\overline{n}_p m_p + (n_B - \overline{n}_p) m_n]c^2 + (1-u)\mathcal{E}_{NM}(n_g, \delta = 1) \tag{2.15}$$

where E_{cl} is the energy of the cluster, $\mathcal{E}_e$ is the energy density of the relativistic electron[5] gas Eq. (2.12), $\overline{n}_p$ is the mean proton density in the cell, $u = V_{cl}/V_{WS}$ is the fraction of the cell volume occupied by the cluster, and $\mathcal{E}_{NM}$ is the energy density of the uniform neutron gas (only in the inner crust), i.e., the nEOS of (see Sec. 1.5).

The cluster energy can be further subdivided into a volume term E_V, an interface term E_I, and a Coulomb term E_C

$$E_V = \mathcal{E}_{NM}(n_{cl}, \delta_{cl}) V_{cl} \tag{2.16}$$

$$E_I = 4\pi r_0^2 A^{2/3} \sigma + r_0 A^{1/3} \sigma_c \tag{2.17}$$

$$E_C = \frac{3}{5}\left(\frac{1-I}{2}\right)^2 \frac{A^2 e^2}{R_{cl}} \left(1 - \frac{3}{2}u^{1/3} + \frac{1}{2}u\right) \tag{2.18}$$

E_V is modelled as a sphere of homogeneous nuclear matter at density n_{cl} and neutron-proton asymmetry δ_{cl} occupying the volume $V_{cl} = A_{cl}/n_{cl}$, where A_{cl} is the number of nucleons in the cluster. Clearly, the energy density $\mathcal{E}_B$ should be consistent with that

[5] Due to the weak equilibrium condition, $\mu_e = \mu_\mu$ and to the fact that $m_\mu >> m_e$, muons appear only at densities well above those typical of the crust and can therefore be neglected here.

of the neutron gas. E_I instead models the interface layer between the nuclear drop and the neutron gas, and accounts for non-uniformity effects affecting both. It is modelled as the sum of a surface tension σ, multiplied by the cluster surface $4\pi r_0^2 A^{2/3}$ and a curvature tension σ_c multiplied by the radius of the cluster $r_0 A^{1/3}$. σ and σ_c are functions themselves, depending on the cluster properties and some internal parameters; some examples can be found in [173–176] and references therein. Finally, E_C is the Coulomb energy, which sums the contributions from the spherical cluster, the lattice, and the interaction with the electron cloud; I is the global asymmetry of the cluster, linked to the number of protons Z by

$$Z = \frac{1-I}{2} A \tag{2.19}$$

and R_{cl} is the cluster radius.

We aim to determine the EOS in the crust as a function of the total baryon density n_B. The composition of the WS cell is determined uniquely by the parameter set ϑ

$$\vartheta = \{A_{cl},\, I,\, n_{cl},\, n_g,\, R_{WS}\} \tag{2.20}$$

Indeed, the first three fix the properties of the cluster, n_g of the neutron gas (only in the inner crust), and R_{WS} sets the dimension of the cell.

So, for a fixed n_B, first one must search the optimal value A_{cl}, I, n_{cl}, n_g and R_{WS} which minimize the energy density Eq. (2.15), under the constraints of charge neutrality and fixed baryon density

$$\begin{cases} n_B = \dfrac{A_{cl}}{V_{cl}} + n_g(1-u) = \text{const.} \\ \overline{n}_p = \dfrac{3Z}{4\pi R_{WS}^3} = \dfrac{3(1-I)A_{cl}}{8\pi R_{WS}^3} = n_e \end{cases} \tag{2.21}$$

Once the optimal set $\vartheta_{min} = \vartheta_{min}(n_B)$ is found, we have access to the EOS

$$\begin{aligned} \mathcal{E}_{WS}(n_B) &= \left[\frac{E_{cl}}{V_{WS}} + \mathcal{E}_e + [\overline{n}_p m_p + (n_B - \overline{n}_p) m_n]c^2 + (1-u)\mathcal{E}_{NM}(n_g, \delta = 1)\right]_{\vartheta_{min}} \\ P(n_B) &= -\left.\frac{\partial E_{WS}}{\partial V_{WS}}\right|_{\vartheta_{min}} = \Big[P_g + P_e + P_L\Big]_{\vartheta_{min}} \\ c_s(n_B)^2 &= \frac{n_B c^2}{P + \mathcal{E}_{WS}} \left(\frac{\mathrm{d}P}{\mathrm{d}n_B}\right)\bigg|_{\vartheta_{min}} \end{aligned} \tag{2.22}$$

where the pressure is made up of three contributions: one from the neutron gas, one from the electron gas, and one from the lattice, which originates from the variation of the Coulomb energy due to the variation of the cell dimension. The optimal set ϑ_{min} solves the following system of equations

$$\begin{cases} \dfrac{\partial\left(E_{cl}/A\right)}{\partial A}=0 \\ \dfrac{n_{cl}^2}{A}\dfrac{\partial E_{cl}}{\partial n_{cl}}=P_g\left(n_g\right) \\ \dfrac{E_{cl}}{A}+\dfrac{1-I}{A}\dfrac{\partial E_{cl}}{\partial I}+\dfrac{P_g\left(n_g\right)}{n_{cl}}=\mu_g\left(n_g\right)-m_nc^2 \\ \dfrac{2}{A}\left(\dfrac{\partial E_{cl}}{\partial I}-\dfrac{\overline{n}_p}{1-I}\dfrac{\partial E_{cl}}{\partial \overline{n}_p}\right)-\Delta m_{pn}c^2=\mu_e\left(\overline{n}_p\right) \\ \mu_g(n_g)=\dfrac{\partial\mathcal{E}_{NM}(n_g,\delta=1)}{\partial n_g}+m_nc^2 \end{cases} \tag{2.23}$$

where $P_g = n_g(\mu_g - m_nc^2) + \mathcal{E}_{NM}(n_g, \delta = 1)$ is the neutron gas pressure, and $\Delta m_{pn} = m_p - m_n$. The full derivation can be found in [174, 176, 177].

Quantum mean-field approaches

A more refined approach is to abandon the artificial distinction between cluster and gas, and rather focus on the neutron and proton density profiles $n_n(r)$ and $n_p(r)$. In this framework, the energy density of the cell $\mathcal{E}_{WS}$ reads

$$\mathcal{E}_{WS}=\frac{1}{V_{WS}}\int_0^{R_{WS}}4\pi r^2dr\,\mathcal{E}_B(n_n(r),n_p(r))+\mathcal{E}_{Coul}+\mathcal{E}_e+[\overline{n}_pm_p+(n_B-\overline{n}_p)m_n]c^2 \tag{2.24}$$

There are three energy densities in play in Eq. (2.24). The Coulomb energy density reads, neglecting the exchange contribution

$$\begin{aligned} \mathcal{E}_{Coul}=&\frac{1}{V_{WS}}\int_{V_{WS}}\frac{e^2}{2}V_C(\boldsymbol{r})(n_p(\boldsymbol{r})-n_e) \\ =&\frac{8\pi e^2}{V_{WS}}\int_0^{R_{WS}}\frac{dr}{r^2}\left(\int_0^r\left(n_p\left(r'\right)-n_e\right)r'^2dr'\right)^2 \end{aligned} \tag{2.25}$$

where e^2 is the electric charge squared, n_e is the background uniform electron gas density and V_C is the electrostatic potential satisfying the Poisson equation

$$\nabla^2V_C=-4\pi e(n_p(r)-n_e) \tag{2.26}$$

The second equality in Eq. (2.25) is shown to hold for spherical geometries [178]. The kinetic energy of the electrons is expressed by Eq. (2.12). Finally, $\mathcal{E}_B$ gives the nuclear contribution, to be integrated over the cell volume. This term is not a simple function of the local densities $n_n(r), n_p(r)$ but the complete EDF, with kinetic, surface, and spin-orbit contributions (e.g., if one works with the Skyrme EDF, it has all the terms in Eqs. (1.41)).

Analogously to the CLDM crust, the composition of the WS cell is found minimizing Eq. (2.24), under the constraints of fixed baryon density n_B and charge neutrality

$$\begin{cases} n_B=\dfrac{1}{V_{WS}}\displaystyle\int_0^{R_{WS}}4\pi r^2dr\left(n_n(r)+n_p(r)\right)=\text{const.} \\ \overline{n}_p=\dfrac{1}{V_{WS}}\displaystyle\int_0^{R_{WS}}4\pi r^2dr\,n_p(r)=n_e \end{cases} \tag{2.27}$$

There are two strategies to find the optimal Wigner-Seitz energy density. One can go the full quantum route: starting by specifying a given number of neutrons N and protons Z in the cell, as well as a given cell radius R_{WS}, one can find the neutron and proton wave-functions through the solution of the appropriate Kohn-Sham equations (1.9). Then, searching over the combinations of N, Z, and R_{WS}, which respect the constraints (2.27), one finds the optimal configuration of the cell corresponding to the minimum of $\mathcal{E}_{WS}$. This strategy was pioneered in the early seventies by the seminal work of Negele and Vautherin [166], where they used the Skyrme interaction as the nuclear model. Further improvements account for the neutron superfluidity using more sophisticated techniques like HFB/HF+BCS, see [179–181].

On the other hand, microscopic calculations typically employ a limited set of nuclear models, due to being computationally expensive, and are ill-equipped to be used in ample statistical studies, like in Bayesian inferences. Indeed, the interest in simpler models, like the CLDM, stems from the facility and rapidness they can be employed in statistical analysis [21, 177, 182, 183]. Still, the astrophysical community approached the problem with semi-classical methods, which we will employ extensively in the following. It is the Thomas-Fermi (TF) [184] or extended Thomas-Fermi (ETF) approximation [185]. In this approximation, all the generalized densities that appear in $\mathcal{E}_B$ are functions of the particle density; so, if $\mathcal{E}_B = \mathcal{E}^{Sky}$, see Eq. (1.41), then $\tau_q(r) = \tau_q(n(r))$, $J_q = J_q(n(r))$. Again, once N, Z, and R_{WS} are specified, one must minimize Eq. (2.24) to find the optimal density profiles. Although this minimization turns out to be as computationally expensive as solving the full HF problem, a widely employed simplification greatly reduces its numerical cost. In fact, imposing a peculiar functional form on the densities, as a Woods-Saxon function [186–189]

$$n_q(r) = \frac{n_{cl_q}}{1+\exp\left(\frac{r-R_q}{a_q}\right)} + \frac{n_{g_q}}{1+\exp\left(-\frac{r-R_q}{a_q}\right)} \tag{2.28}$$

and minimizing Eq. (2.24) with respect to the density profiles parameters $n_{cl_q}, n_{g_q}, R_q, a_q$, $q = n, p$, rather than to the value of the densities at each spatial point, speeds up the computation considerably. In Eq. (2.28), the first term determines the cluster density, while the second governs the rise of the free neutron gas. Some more refined profiles can be used; see [170]. Typically, as all protons are bound in the ion, $n_{g_p} = 0$.

Once the optimal cell configuration $n_q^{min}(r)$, $q = n, p$ for a given baryon density n_B is found, $n_q^{min}(r) = n_q^{min}(r; n_B)$, we can write the EOS of the crust as

$$\begin{aligned}
\mathcal{E}_{WS}(n_B) &= \Bigg[\frac{1}{V_{WS}}\int_0^{R_{WS}} 4\pi r^2 dr\, \mathcal{E}_B(n_n(r), n_p(r)) + \mathcal{E}_{Coul} + \mathcal{E}_e \\
&\qquad\qquad \overline{n}_p m_p + (n_B - \overline{n}_p) m_n\Big] c^2 \Bigg]_{n_q^{min}(r),\, q=n,p} \\
P(n_B) &= -\left.\frac{\partial E_{WS}}{\partial V_{WS}}\right|_{n_q^{min}(r),\, q=n,p} = \Big[P_n + P_e\Big]_{n_q^{min}(r),\, q=n,p} \\
c_s(n_B)^2 &= \frac{n_B c^2}{P+\mathcal{E}_{WS}}\left.\left(\frac{\mathrm{d}P}{\mathrm{d}n_B}\right)\right|_{n_q^{min}(r), q=n,p}
\end{aligned} \tag{2.29}$$

where the pressure has three contributions: a nuclear one [170]

$$P_n = -\mathcal{E}_B(n_n^{min}(R_{WS}), n_p^{min}(R_{WS})) + \sum_{q=n,p} n_q^{min}(R_{WS}) \left.\frac{\partial \mathcal{E}_B}{\partial n_q}\right|_{r=R_{WS}} \tag{2.30}$$

and the electron one P_e, Eq. (2.13). The direct Coulomb interaction does not give any contribution to the pressure [170].

2.3.3 Interlude: the crust-core transition

At a certain baryon density n_{cc}, the inner crust configuration (cluster plus free neutron gas) becomes energetically unfavourable, and the homogeneous phase (a liquid of protons and neutrons) becomes more convenient. That particular density is called the crust-core transition density. It ranges between 0.06 and 0.10 fm^{-3} [190], which corresponds approximately to the density of the nuclear clusters. It is important to remark that, even if the variance of n_{cc} and the associated pressure P_{cc} is relatively small, it can have a great impact on the properties of the crust, like its radius, its moment of inertia, and so on (see Sec. 5.5). The actual value of n_{cc} depends on the many-body method used for the crust modelling, the model for the nuclear matter energy density $\mathcal{E}_B$, as well as the definition itself of the transition point.

There are different strategies to find n_{cc}. One way is from the core, i.e., starting from homogeneous matter and progressively reducing the baryon density to see whether it becomes unstable against density fluctuations. If these fluctuations are global, the instability corresponds to the point of liquid-gas phase transition of neutral nuclear matter, and it is called thermodynamic spinodal instability; if instead they are local, it corresponds to the onset of cluster formation, and the associated phenomenon is called dynamical spinodal instability [191]. It is reasonable to expect that these instabilities take place around densities close to the crust-transition. However, the crystalization time scales of NSs crusts are much longer than those of spinodal separation (of the order of some 10^{-22} s) [192, 193]. Rather, they serve as a useful estimation (for the thermodynamic) or lower limit (for the dynamical) for the actual n_{cc} (see also the discussion in Sec. 5.2).

In principle, a more reliable approach would be to compute the transition from the crust, i.e., comparing, at increasing baryon density n_B, the energy density of the clusterized phase ($\mathcal{E}_{WS}$ Eq. (2.15) or Eq. (2.24)) with that of the homogeneous phase ($\mathcal{E}_{npe\mu}$, see Sec. 2.3.4). The crust-core transition density is defined by[6]

$$\mathcal{E}_{npe\mu}(n_{cc}) < \mathcal{E}_{WS}(n_{cc}) \tag{2.31}$$

However, a word of caution is in order. One should recall that the modelling of the crust is more complex than the modelling of the core, meaning that the hypotheses and approximations employed might create biases in the determination of the transition point using the technique "from the crust". In particular, allowing the cluster to become deformed in the pasta phases might increase the value of n_{cc} [194–196].

2.3.4 EOS in the core

As already mentioned, we assume that only nuclear matter exists in NS cores, and exotic degrees of freedom do not emerge; in other words, we work under the nucleonic hypothesis. We therefore do not make any distinction between the outer and the alleged inner core: core matter is composed of a neutral gas of neutrons, protons, electrons, and, eventually, muons, the so-called *npe*(μ) gas [106], where all components are supposed to be homogeneous.

Its energy density $\mathcal{E}_{npe\mu}$ can be written as the sum of the energy density of its constituents, $\mathcal{E}_{npe\mu} = \mathcal{E}_B + \mathcal{E}_e + \mathcal{E}_\mu$, plus the appropriate rest masses. As for the crust, we

[6] We are supposing that the phase transition is continuous, i.e., nuclei melt progressively into the homogeneous matter.

want to find the optimal value of $\mathcal{E}_{npe\mu}$ as a function of the baryon density n_B; that is, finding the asymmetry δ which minimizes the thermodynamic potential, as implied by the condition of equilibrium of the weak interactions. Once again, beside the fixed baryon density, there is the additional constraint of charge neutrality; it can be encoded in the auxiliary energy density $\Omega_{npe\mu}$ through the Lagrangian multiplier λ_c

$$\begin{aligned}\Omega_{npe\mu}(n_B,\delta) =&\mathcal{E}_{npe\mu}(n_B,\delta)+\lambda_c\left(n_B\frac{1-\delta}{2}-n_e-n_\mu\right)\\ =&\mathcal{E}_B\left(n_B,\delta\right)+\mathcal{E}_e\left(n_e\right)+\mathcal{E}_\mu\left(n_\mu\right)+n_B\left(\frac{1-\delta}{2}m_p+\frac{1+\delta}{2}m_n\right)c^2\\ &+\lambda_c\left(n_B\frac{1-\delta}{2}-n_e-n_\mu\right)\end{aligned} \tag{2.32}$$

where $\mathcal{E}_B$ is the nEOS, $\mathcal{E}_e$, $\mathcal{E}_\mu$ are the energy densities of the electrons and muon gas defined in Eq. (2.12). From Eq. (2.32), we recognize the proton and neutron fractions

$$\begin{aligned}x_p &= \frac{n_p}{n_B}=\frac{1-\delta}{2}\\ x_n &= \frac{n_n}{n_B}=\frac{1+\delta}{2}\end{aligned} \tag{2.33}$$

The optimal composition δ_β minimizes Eq. (2.34). From the derivative with respect to the electron and muon densities to zero, we get

$$\begin{aligned}\lambda_c &= -\frac{\partial\Omega_{npe\mu}}{\partial n_e}=\frac{\partial\mathcal{E}_e}{\partial n_e}=\mu_e\\ \lambda_c &= -\frac{\partial\Omega_{npe\mu}}{\partial n_\mu}=\frac{\partial\mathcal{E}_\mu}{\partial n_\mu}=\mu_\mu\end{aligned} \tag{2.34}$$

which leads to the equality $\mu_e=\mu_\mu$. Now, putting the derivative with respect to δ to zero

$$\left.\frac{\partial\Omega_{npe\mu}}{\partial\delta}\right|_{n_e,n_\mu}=0 \tag{2.35}$$

one gets the β-equilibrium condition for homogeneous matter

$$\mu_n=\mu_p+\mu_e \tag{2.36}$$

where the proton and neutron chemical potentials are defined through

$$\mu_q=\left.\frac{\partial\mathcal{E}_B}{\partial n_q}\right|_{n'_q}+m_qc^2 \tag{2.37}$$

and μ_e comes from Eq. (2.14)[7]. Eq. (2.36) corresponds to the detailed balance for the (inverse)$\beta-$decay reactions, for which neutrons transforms into protons and vice-versa

$$\begin{aligned}&p+e^-\to n+\nu_e\\ &n\to p+e^-+\overline{\nu}_e\end{aligned} \tag{2.38}$$

[7]Note that Eq. (2.14) does not contain explicitly the rest mass since it is already included in the energy density $\mathcal{E}_l$ Eq. (2.12).

These reactions also give rise to muons in NS cores once the electron chemical potential surpasses the muon rest mass,

$$\mu_e \geq m_\mu c^2 = 105.66 \text{ MeV} \tag{2.39}$$

if, on the other hand, $\mu_e < m_\mu c^2$, then there is no muon gas.

β-equilibrium (2.36) determines the neutron-proton asymmetry δ_β which minimizes the energy density $\mathcal{E}_{npe\mu}$ (2.32) for a given baryon density n_B, $\delta_\beta = \delta_\beta(n_B)$. From that, one can compute the EOS of NS core matter at baryon density n_B

$$\begin{aligned}
\mathcal{E}_{npe\mu}(n_B) &= \mathcal{E}_B\left(n_B, \delta_\beta\right) + \mathcal{E}_e\left(n_e\right) + \mathcal{E}_\mu\left(n_\mu\right) + n_B\left(\frac{1-\delta_\beta}{2}m_p + \frac{1+\delta_\beta}{2}m_n\right)c^2 \\
P(n_B) &= P_B(n_B, \delta_\beta) + P_e(n_B, \delta_\beta) + P_\mu(n_B, \delta_\beta) \\
c_s(n_B)^2 &= \frac{n_B c^2}{P + \mathcal{E}_{npe\mu}}\left(\frac{\partial P}{\partial n_B}\right)
\end{aligned} \tag{2.40}$$

In the above relations, the pressure of nuclear matter P_B is given by

$$P_B(n_B, \delta) = \sum_{q=n,p} n_q(\mu_q - m_q c^2) - \mathcal{E}_B(n_B, \delta) \tag{2.41}$$

that of the lepton gases by Eq. (2.13), and the electrons and muons densities satisfy the system

$$\begin{cases} \mu_e(n_e) = \mu_\mu(n_\mu) \\ n_e + n_\mu = \dfrac{1-\delta_\beta}{2} n_B \end{cases} \tag{2.42}$$

Note that if muons are not present, the system (2.42) reduces to $n_e = n_p$.

Finding $\delta_\beta(n_B)$ for different values of the baryon density gives access to the EOS of the core of the star, from which one can solve the structure equations (2.1), (2.5) and (2.3) (TOV, tidal deformability, moment of inertia).

It is left to determine which is the appropriate expression for the energy density of homogeneous nuclear matter $\mathcal{E}_B$, which encodes our assumptions on the nuclear interaction, and it is pivotal in determining the stellar EOS, both in the crust and in the core. In other words, the appropriate expression of the nEOS. Relativistic mean-field (RMF) models are one of the most common strategies to describe $\mathcal{E}_B$ [197, 198].

Alternatively, one could employ non-relativistic EDF like Skyrme and Fayans, and use the derived nEOS (see Eqs. (1.61) and (A.2.1)). On the other hand, these functionals were built to describe finite nuclei, and they could not be as good at describing high-density nuclear matter. One could go the totally agnostic route and use completely agnostic models, i.e., those that do not make assumptions on the nuclear interaction, and fit them to some astrophysical and nuclear data. Some examples are piece-wise polytropes [199] and Gaussian processes EOS [200]. Alternatively, one could follow the strategy proposed in [42, 43], where the so-called meta model (MM) nEOS was developed. The MM is a semi-agnostic model, able to reproduce existing nEOS (like Skyrmes, RMFs, and so on), but at the same time being more flexible for matter at higher densities, those relevant for NS. For this reason, the MM will be our tool for the second part of this work, and the next Section is dedicated to it.

2.4 The Meta-Model

The MM [42, 43] is a flexible tool conceived to describe nuclear matter from sub- to supra-saturation densities. The main motivation that brought it to its creation is that nuclear EDFs like Skyrme (see Sec. 1.4) were designed to model nuclei and their properties, rather than homogeneous nuclear matter ranging from sub to many times saturation density. Therefore, spurious correlation imposed by their functional form, which plays little to no role in nuclei, could fully manifest and hinder nuclear EDF capabilities of describing NS matter. As an example, we bring the fact that the K_{sym} NMP, Eq. (1.60), is not free for Skyrme (see below, Sec. 4.1): while no nuclear experiments are sensitive to this parameter, it is crucial for the description of NS phenomenology.

The MM aims to overcome these limitations. It is built upon the Taylor expansion around saturation of the nEOS, Eq. (1.56). Rather than using Eq. (1.56), the strategy is to break the energy density into two terms, a kinetic and a potential one

$$\mathcal{E}_{MM}(n,\delta) = \mathcal{T}(n,\delta) + \mathcal{V}(n,\delta) \tag{2.43}$$

As the MM was conceived as an extension of nEOS from EDF, it retains the mean-field framework, i.e., nucleons in homogeneous matter behave as independent particles. Therefore, the kinetic term $\mathcal{T}$ should be that of a non-relativistic Fermi gas composed of two particle species, corrected by their effective mass to account for in-medium effects

$$\mathcal{T}\,(n,\delta) = n\frac{t_{\rm sat}^{FG}}{2}\left(\frac{n}{n_{\rm sat}}\right)^{2/3}\left[(1+\delta)^{5/3}\frac{m}{m_n^*} + (1-\delta)^{5/3}\frac{m}{m_p^*}\right] \tag{2.44}$$

where $t_{sat}^{FG} = 3\hbar^2/(10m)(3\pi^2/2)^{2/3}n_{sat}^{2/3}$ is the kinetic energy of SNM, and $m = (m_n + m_p)/2$ is the mean nucleon mass. The two effective masses depend on the density and asymmetry Eq. (1.44). It is useful to write them as a function of two parameters κ_{sat} and κ_{sym}

$$\frac{m}{m_q^*(n,\delta)} = 1 + (\kappa_{sat} + \tau_3\kappa_{sym}\delta)\left(1 + \frac{n-n_{sat}}{n_{sat}}\right) \tag{2.45}$$

where $\tau_3 = 1$ ($\tau_3 = -1$) for neutrons (protons). The two κ parameters are linked to the definition of Landau effective masses for nucleons in homogeneous matter, given by

$$\begin{aligned}\kappa_{sat} &= \frac{m}{m_{sat}^*} - 1\\ \kappa_{sym} &= \frac{1}{2}\left(\frac{m}{m_n^*} - \frac{m}{m_p^*}\right)\end{aligned} \tag{2.46}$$

The kinetic term of the MM is identical to Skyrme's, Eq. (1.61) (the terms proportional to $n^{2/3}$ and $n^{5/3}$). On the other hand, the parameter σ, dominant at high density, is replaced with a polynomial of order 4. This decouples the high-density behaviour from the low-density one, avoiding biases induced by the Skyrme functional in its extrapolation to super-saturation densities. The potential part of the MM $\mathcal{V}$ reads

$$\sum_{k=0}^{4}(v_k^{is} + v_k^{iv}\delta^2)\frac{n}{k!}\left(\frac{n-n_{sat}}{n}\right)^k u_k(n) \tag{2.47}$$

where the function $u_k(n)$

$$1 - \exp\left(-b\frac{n}{n_{sat}}\right)\left(\frac{n-n_{sat}}{n_{sat}}\right)^{4-(k-1)} \tag{2.48}$$

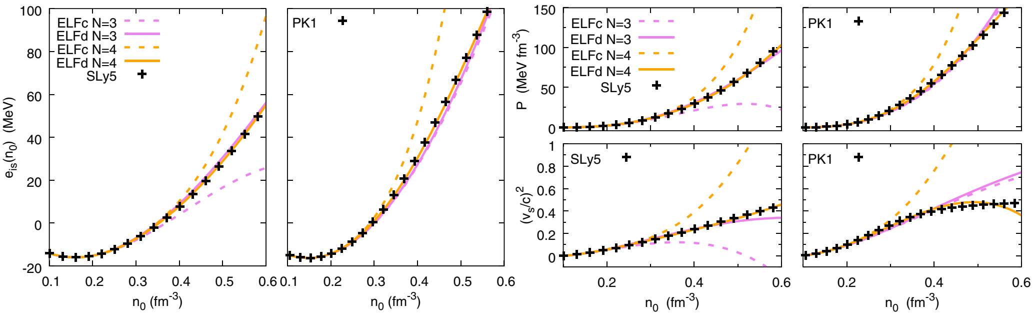

Figure 2.7: MM representation of SLy5 [73] and PK1 [201] of SNM energy per particle, pressure, and sound speed. The index N refers to the maximum order to be considered in the expansion Eq. (2.47). The ELFc model works (dotted line) until 2-3 times the saturation density, and then diverges from the original model. In the ELFd choice shown in the figure, the high-order parameters are not high-order derivatives at saturation, but they are fixed to reproduce the high-density behaviour of the original model. Plot taken and adapted from [42].

ensures that $\mathcal{V}(n=0,\delta)=0$. The extra parameter b, which dominates the rapidity with which u_k goes to zero, will be set at $10\ln(2)$, as suggested by the authors in [42]. The isoscalar and isovector coefficients v_k^{is} and v_k^{iv} depend explicitly on the NMP (1.60); they explicitly read

$$\begin{aligned} v_0^{is} &= E_{sat} - t_{sat}^{FG}\left(1+\kappa_{sat}\right) \\ v_1^{is} &= -t_{sat}^{FG}\left(2+5\kappa_{sat}\right) \\ v_2^{is} &= K_{sat} - 2t_{sat}^{FG}\left(-1+5\kappa_{sat}\right) \\ v_3^{is} &= Q_{sat} - 2t_{sat}^{FG}\left(4-5\kappa_{sat}\right) \\ v_4^{is} &= Z_{sat} - 8t_{sat}^{FG}\left(-7+5\kappa_{sat}\right) \end{aligned} \tag{2.49}$$

and

$$\begin{aligned} v_0^{iv} &= E_{sym} - \frac{5}{9}t_{sat}^{FG}\left[1+\left(\kappa_{sat}+3\kappa_{sym}\right)\right] \\ v_1^{iv} &= L_{sym} - \frac{5}{9}t_{sat}^{FG}\left[2+5\left(\kappa_{sat}+3\kappa_{sym}\right)\right] \\ v_2^{iv} &= K_{sym} - \frac{10}{9}t_{sat}^{FG}\left[-1+5\left(\kappa_{sat}+3\kappa_{sym}\right)\right] \\ v_3^{iv} &= Q_{sym} - \frac{10}{9}t_{sat}^{FG}\left[4-5\left(\kappa_{sat}+3\kappa_{sym}\right)\right] \\ v_4^{iv} &= Z_{sym} - \frac{40}{9}t_{sat}^{FG}\left[-7+5\left(\kappa_{sat}+3\kappa_{sym}\right)\right] \end{aligned} \tag{2.50}$$

Stopping the Taylor expansion at order 4, the MM reproduces satisfactorily the behaviour of Skyrme functionals up to 2-3 n_{sat}, after which it becomes poor (the so-called ELFc in [42]). [8] The authors of [42] point out that an arbitrarily chosen behaviour at high density can be obtained, keeping an almost unchanged behaviour at subsaturation, if the third and fourth order parameters $v_{3,4}^{is,iv}$ are not taken from Eqs.(2.49),(2.50), but rather fixed to reproduce a given value of energy and pressure at some chose super-saturation density point. This strategy of parameter fixing is referred to as ELFd in [42]; see discussion there. In Figure 2.7, the reader finds the MM representation of the SLy5 Skyrme

[8] In fact, different non-Skyrme models, such as ab-initio or RMF nEOS, are also well reproduced by an appropriate fit of the parameters of the Taylor expansion [42].

interaction [86] and the PK1 RMF [201], as well as the corresponding pressure and sound speed, for the two fitting strategies, ELFc and ELFd.

The MM Eq. (2.43) can emulate existing nuclear models quite well. On the other hand, all its parameters are independent of each other, and so it can freely explore the parameter space to best capture the behaviour of high-density nuclear matter. The excellent mapping to the Skyrme nEOS given by Eqs.(2.49),(2.50), and the possibility of decoupling the low and high density behaviour of the EOS by an appropriate change of the high order parameters, will be very useful in the following.

Chapter 3

Bayesian background and emulators

Throughout this Thesis, we made great use of the tools offered by Bayesian statistics. In this brief Chapter, we will give basic principles of Bayesian statistics in Section 3.1, with a quick overview of the computational methods for inference in Section 3.2. As these two Sections cover elementary notions, we drew from well-established textbooks, mainly "Information theory, Inference, and Learning algorithm" [27] a "Bayesian data analysis" [28]. Section 3.3 treats Gaussian process-based emulators, central in our work to perform otherwise too-lengthy Bayesian inferences.

3.1 Elementary Bayesian statistics

Bayesian statistics is based on Bayes' Theorem. Let $p(x, y)$ be the joint probability distribution function of two random variables x, y. One defines the marginalized probability distribution of x over y, $p(x)$, as

$$p(x) = \int p(x, y)\mathrm{d}y, \tag{3.1}$$

which is the probability distribution of x regardless of y, and the conditional probability distribution of x given y, $p(x|y)$, as

$$p(x|y) = p(x, y)/p(y) \tag{3.2}$$

which is the probability distribution of x given a particular y (with an analogous definition for $p(y|x)$).

Bayes' theorem follows from the conditional probability definition (3.2) of $p(x|y)$ and $p(y|x)$

$$p(x|y) = \frac{p(y|x)p(x)}{p(y)} \tag{3.3}$$

This simple equality is very powerful for situations where one wants to infer probability distributions of non-observable quantities (like those of model parameters) from some observable ones (like those of experimental results). Let us suppose that we acquire a set of experimental data X; let us say also that there is a model M, with parameters θ, that we want to test against these observations. We are then interested in the joint probability $p(\theta, X)$ and, in particular, in the probability distribution of parameters given the data. Then with Bayes' theorem (3.3) we write

$$p(\theta|X) = \frac{p(X|\theta)p(\theta)}{p(X)} \tag{3.4}$$

In Bayesian language, each term in (3.4) has a precise name.

- $p(\theta|X)$ is called the posterior probability distribution (also known simply as *posterior*);
- $p(X|\theta)$ is called the *likelihood* (sometimes indicated with the symbol $\mathcal{L}$);
- $p(\theta)$ is the prior probability distribution (also simply referred to as *prior*);
- $p(X)$, called *evidence*, is the normalization factor, as it is θ-independent.

The main object of interest is the posterior, the (multivariate) parameter probability distribution. It is worth stressing that it contains all the information about parameter distributions, like correlations and so on; it does not simply give an estimate of the best value of the parameters. It is the final result of each Bayesian analysis, from which one can build robust prediction bands for unobserved quantities.

The likelihood $\mathcal{L}$ quantifies how accurately the results obtained with a parameter set θ reproduce the experimental result X. Its expression depends on the experimental observable and differs from case to case. A common choice is a Gaussian likelihood (see below, Eq. (4.7)). On the other hand, we also used non-Gaussian likelihoods, like the one for the maximum neutron star mass, which is a cumulative distribution function, or the LVC or NICER results, which are based on inferred probability distributions from astronomical observations (see Sec. 5.4).

The prior distribution reflects the prior knowledge about the parameters before including any (new) experimental information and encodes all the assumptions an investigator makes in their analysis. It is a critical choice, as it clearly influences deeply the posterior distribution. One of the most common priors is a uniform (or flat) distribution within an interval, sometimes ambiguously called an uninformative prior. Indeed, it is uninformative only if the posterior falls to zero within its boundaries; otherwise it induces a truncation in the posterior, which is not wrong *per se*, but rather reflects a decision taken by the statistician. Alternatively, another option for prior distribution is a previous posterior distribution. This is particularly useful when a new set of data $\tilde{X}$ becomes available and one wants an updated posterior distribution. This procedure, called Bayesian updating, is equivalent to repeating the inference from the ground up using the complete set of data (the combination of the "old" X and the "new" $\tilde{X}$).

Finally, the evidence does not have a simple interpretation, and it is usually regarded as a normalisation factor. One could interpret it as the probability of getting X as an experimental value given your model M. It is particularly useful when one wants to compare different models: the ratio $p_{M_1}(X)/p_{M_2}(X)$ determines which model suits better the data. Usually, it is very hard to compute because it involves an integral of the posterior, which (usually) is a multidimensional function. Furthermore, besides model comparison, it is not really of great importance, as one can get the confidence interval and the shape of the distribution from the non-normalised posterior itself.

3.2 Sampling the posterior

The main drawback of the Bayesian approach is that it is computationally expensive. The posterior (3.4) can be computed exactly seldomly; in almost all practical situations, one resorts to posterior sampling, usually through Monte-Carlo methods.

One of the most used techniques is the Metropolis-Hastings (MH) algorithm [202]. This algorithm is a Markov-Chain random walk in parameter space, where the new proposed point is accepted with a probability P. It proceeds like this: from last point in the chain θ_n a candidate θ^* is individuated through a random walk step. The probability that θ^* will be the next point in the chain is P

$$P = \frac{p(\theta^*|X)}{p(\theta_n|X)} = \frac{p(X|\theta^*)p(\theta^*)}{p(X|\theta_n)p(\theta_n)} \tag{3.5}$$

If P is greater than a randomly extracted number r between 0 and 1, $P \geq r$, then the step is accepted and θ^* becomes the new point in the random walk ($\theta_{n+1} = \theta^*$), otherwise it is refused and the new point is the same as before, $\theta_{n+1} = \theta_n$. In principle, an infinite chain can sample exactly the posterior. In practice, one stops after a certain number of iterations (usually in the order of millions or tens of millions, although each situation is different). The Monte Carlo chain is the sampling of the posterior probability distribution.

P is the ratio of their posterior probability distributions (Eq. (3.4)) computed respectively in θ^* and θ_n. Note that the normalisation $p(X)$ gets simplified away. Furthermore, if the prior is a flat distribution, then $p(\theta^*) = p(\theta_n)$, and so P corresponds to the likelihood ratio.

The MH algorithm is devised to explore the regions in parameter space where the posterior is greatest, while having the possibility to explore low posterior zones. Other algorithms (like Hamiltonian Monte Carlo or the No-U-Turn-Sampler) can explore the parameter space more efficiently, but still require many evaluations of the likelihood. Therefore, Monte Carlo methods are feasible if the computational cost of the model is low. If not, one must resort to other techniques to evaluate the likelihood, like employing software emulators.

3.3 Gaussian process emulators

For our results in Chapter 4, we employed extensively a Gaussian Process (GP) based emulator. In this brief section, we will give the key ideas on what a GP is and how it works.

Following [29], a Gaussian process is defined as *"a collection of random variables, any finite number of which have a joint Gaussian distribution"*. While the formal definition is a bit obscure, the idea behind it is strikingly simple and stems from the fact that marginalised and conditioned Gaussian distributions are still Gaussian. We will present the core concepts following [29] and [30].

The core concept is that the outputs of a function f, which represents the computer program one wants to emulate, are actually distributed following a multivariate Gaussian. Let us suppose we have a training set $T = \{(\theta_i, f_i),\ i = 1, \ldots, N\}$, where $f_i = f(\theta_i)$, of points where we know the value of our function. Let us suppose also that we are interested in the values of f over the set $E = \{\theta^*_i,\ i = 1, \ldots, N^*\}$, which we will refer to as f^*. Then, all the outputs of f follow a multivariate normal distribution $\mathcal{N}$

$$\begin{pmatrix} f \\ f^* \end{pmatrix} \sim \mathcal{N}\left(\overline{\boldsymbol{\mu}}, \boldsymbol{\Sigma}\right) = \frac{1}{(2\pi)^{k/2}\det(\boldsymbol{\Sigma})^{1/2}} \exp\left(-\frac{1}{2}(\mathbf{x} - \overline{\boldsymbol{\mu}})^{\mathrm{T}}\boldsymbol{\Sigma}^{-1}(\mathbf{x} - \overline{\boldsymbol{\mu}})\right) \tag{3.6}$$

where the vector $\overline{\boldsymbol{\mu}}(\theta)$ is the mean function of the GP, and the covariance matrix $\boldsymbol{\Sigma}$ can be decomposed into sub-matrices

$$\boldsymbol{\Sigma} = \begin{bmatrix} K & K_* \\ K_*^T & K_{**} \end{bmatrix} \tag{3.7}$$

These matrices are a function of the covariance, or kernel, function κ, $K = \kappa(\theta, \theta)$ $(N \times N)$, $K_* = \kappa(\theta, \theta^*)$ $(N \times N^*)$, and $K_{**} = \kappa(\theta^*, \theta^*)$ $(N^* \times N^*)$. κ determines the scale at which

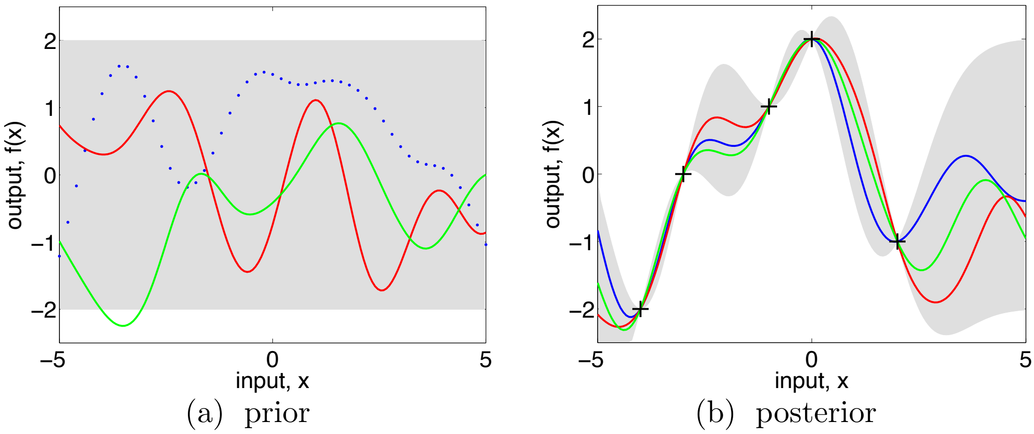

Figure 3.1: f values extracted from a GP before (a) and after (b) considering data from the training data set T. Plot taken from [29].

the value of $f(\theta_a)$ influences the value of $f(\theta_b)$. One of the most used kernels is the so-called squared exponential

$$\kappa(\theta_a, \theta_b) = \sigma^2 \exp\left(-\frac{||\theta_a - \theta_b||^2}{2l^2}\right) \tag{3.8}$$

where σ and l are hyper-parameters, and $||\cdot||$ is the euclidean norm. That is, the idea is that if two points are close, then the respective outputs of f will be close as well; on the other hand, one does not expect two faraway points to have a great impact on each other. The choice of the covariance functions deeply influences the performance of the emulator, and different functions are employed in practice.

Without loss of generality, we can set $\overline{\boldsymbol{\mu}} = 0$. Then, one gets the probability distribution of f^* by conditioning on f

$$p(f^*|f) = \mathcal{N}\left(K_*^T K^{-1} f,\, K_{**} - K_*^T K^{-1} K_*\right) \tag{3.9}$$

An example of the procedure is given in Figure 3.1. Panel (a) shows three extractions without condition on the training set T. All three oscillate around the mean (zero) and close-by points have similar values, and mostly stay within the 95% interval, shown in grey. One of these three is shown by a dotted line to remember that, with GPs, we can extract only samples of a function, and cannot capture its true continuous behaviour. On panel (b), there are three other extractions, after conditioning over the training set $f(\theta)$, represented by the black crosses. All three pass through the values of $f(\theta)$, and the 2σ interval is much reduced even for values between data points. Finally, it is interesting to observe that after the last training point, the GP starts behaving again as if no data were present (after four, the grey band occupies again the region (-2,2)). The emulator programs need as input the training set T, which now is the set of the computer program results over a representative sample of the parameter space, and then optimise the hyperparameters of the kernel function κ to find the best interpolator.

Ground state properties of nuclei, like binding energies and charge radii, are relatively fast to compute. On the other hand, RPA calculations for the collective excitation are way longer and are too slow to be used in a Bayesian inference. All the Bayesian analyses we will present in the following would not have been possible without the emulators. We did not develop our own, but rather used the MADAI software [203], a published emulator built for Bayesian inferences (see below, Sec. 4.2). As our analysis depends intimately on the performance of the emulators, we took particular care in assessing their performance (Figure 4.2).

Chapter 4

Bayesian inference with Skyrme EDF

The present chapter is based on, and expands some aspects presented in, the paper 'Impact of ground-state properties and collective excitations on the Skyrme ansatz: a Bayesian study' by Pietro Klausner, Gianluca Colò, Xavier Roca-Maza and Enrico Vigezzi, published by Physical Review C [204].

As discussed in Chapter 1, EDFs are one of the most successful frameworks for describing nuclear systems. However, as we mentioned there, the current experimental precision with which many nuclear properties are determined is unreachable for current theory [12]. While advances in developing new EDFs with better capabilities, accuracy, and predictive power have been reported in the last decade [205], there exist indications that current EDFs have reached their limits, and cannot be improved much further. Such a claim, in the case of the Skyrme EDFs, has been made when the UNEDF set has been built [206]. Within the same Skyrme framework, it has been shown that extending the form of the EDF, namely including fourth-order derivative terms on top of the usual second-order ones, does not lead to very significant improvements [207]. A symptom of the obstacles in further improving functionals can be found in the difficulty of reproducing new, different observables. For example, the prediction of binding energies of recently measured exotic nuclei: the predictions of different Skyrme parametrizations vary considerably, although their results on stable nuclei are close to experiment [208]. Another recent example that has attracted considerable interest [209–212] is the tension among the two parity-violating asymmetries A_{PV} measured for ^{48}Ca in the CREX experiment [38] and for ^{208}Pb in the PREX-II experiment [39]. The two measurements are in tension, as no parametrization can describe both simultaneously, although this is a problem common to all EDFs, not only Skyrme. Some examples of current problems can be found in the literature (see, e.g., [213, 214]).

At this stage, we want to assess the limits of the EDFs, at least in the Skyrme case, with a technique that is as unbiased and as statistically meaningful as possible. A suitable tool for such a goal is to perform a Bayesian inference (see Chapter 3). The use of Bayesian inference allows estimating the entire probability distributions of the parameter values, while the more traditional χ^2-test only provides point-like estimates for these parameters, assuming that they are normally distributed. In this way, we have access to the probability distribution of new experimental observables not used in the fit, and therefore assess the limitations of our model. In recent years, Bayesian inference has taken the lead in different fields in physics, and among them also in nuclear physics (see, e.g., [215]).

The results of the Bayesian inference will depend on the pool of selected data that we wish to reproduce. Analysing the sensitivity of the results to this pool is part of our purpose. At the same time, we would like to design a methodology based on transparent logic, being well aware that this can be improved in future works. Therefore, we try to define a representative set of observables that are known to encode reliable information on the different terms of EDFs. Many existing EDFs, although not all, have been fitted to masses and radii of a few magic nuclei. We will first perform an analysis, limiting ourselves to magic nuclei, including some properties of excited states. In a second step, we will also add data from open-shell nuclei. In this way, we hope to be able to test more extensively the different terms of a local functional that depend on the time-even densities and spot possible limitations of the Skyrme ansatz.

Our first step is to relate, whenever possible, the EDF parameters to properties of the nuclear Equation of State (nEOS) at saturation density n_{sat}, the nuclear matter parameters NMPs, Eq. (1.60). On some of these parameters, empirical information is available [12] (see also Sec. 1.5, Table 1.2), and, in addition, they appear to be physically meaningful. This strategy has already been used in the literature by different authors (see, e.g., [216]), and we use a variant of this idea by following the scheme that has been proposed in [217, 218]. This step will help us in the choice of the prior distribution in the Bayesian analysis.

Model parameters related to nuclear surface effects, or the spin-orbit interaction, do not have a counterpart in nEOS parameters; consequently, those must be treated differently. For the latter, there exist slightly different strategies in the literature to fix the values of the spin-orbit parameters. In the present work, we will adopt the simplest approach, that is, to use two spin-orbit splittings to determine one spin-orbit parameter, possibly introducing a bias with this restricted selection. For the former, the situation is more delicate. Although nuclear observables such as masses, radii, or collective excitations are very sensitive to surface effects, it is not possible to easily isolate them from bulk contributions; our prior will be large enough to contain the most common values of these parameters present in published Skyrme. For a recent compilation, we refer to [219].

We will perform several subsequent Bayesian inferences, using a larger set of observables each time. In this way, we will be able to assess more clearly the ability of the employed experimental data, and in particular of those associated with collective excitations, to constrain the posterior distributions of our selected parameters.

This Chapter is structured as follows. In Section 4.1 we present the mapping between the usual Skyrme parameters t_i and x_i and a combination of NMPs and surface. This transformation will be crucial for our analysis. Then, in Section 4.2, we discuss in detail our methodology and specify the characteristics of our Bayesian inference: prior distribution, observables and errors, likelihood, and sampling method. In Section 4.3, we present the result of the first Bayesian inference, where we consider data from double-magic nuclei. We analyse in detail the parameter posterior distribution, studying in detail the effect of each observable, and compare our results with other analyses present in the literature. In Section 4.4, we investigate the sensitivity of our model to E_{sym}- and L_{sym}-correlated observables, and justify the second Bayesian inference, presented below in Section 4.5, where we included data from open-shell nuclei.

4.1 Mapping of Skyrme parameters into NMP

As mentioned above, it is wise, in a Bayesian framework, to express Skyrme parameters in terms of the NMPs whenever possible, since information on their values can sometimes be inferred from experiments (see Table 1.2). Therefore, it is easier to devise a suitable prior distribution for them rather than Skyrme parameters, which, on the other hand, span a huge range of values (see Table 1.1), and do not have a clear physical meaning.

With a large prior distribution, one can easily find unphysical parametrizations, i.e., for which the Hartree-Fock (HF) computation does not reach convergence.

Following the scheme proposed in [217, 218], Skyrme parameters can be put in a one-to-one relation with the following set θ of parameters

$$\theta = \{n_{sat},\, E_{sat},\, K_{sat},\, E_{sym},\, L_{sym},\, m_0^*/m,\, m_1^*/m,\, G_0,\, G_1,\, W_0\} \tag{4.1}$$

where n_{sat}, E_{sat}, K_{sat}, E_{sym}, L_{sym} are five NMPs (Eq. (1.60)), m_0^*/m, m_1^*/m are the isoscalar and isovector effective masses,

$$\begin{aligned}
\frac{m_0^*}{m} &= \left(1 + \frac{2m}{\hbar^2} n_{sat} C_0^\tau\right)^{-1} = \left(1 + \frac{m}{8\hbar^2} n_{sat}(3t_1 + 5t_2 + 4t_2 x_2)\right)^{-1} \\
\frac{m_1^*}{m} &= \left(1 + \frac{2m}{\hbar^2} n_{sat}\left(C_0^\tau - C_1^\tau\right)\right)^{-1} = \left(1 + \frac{m}{4\hbar^2} n_{sat}\left(2t_1 + x_1 + 2t_2 + t_2 x_2\right)\right)^{-1}
\end{aligned} \tag{4.2}$$

G_0 and G_1 govern the gradient terms of the interaction, as the surface properties are not related to the NMPs,

$$\begin{aligned}
G_0 &= -\frac{C_0^{\nabla^2 n}}{2} = \frac{1}{32}(9t_1 - 5t_2 - 4t_2 x_2) \\
G_1 &= -\frac{C_1^{\nabla^2 n}}{2} = \frac{1}{32}(3t_1 + t_1 x_1 + 6t_2 + 2t_2 x_2)
\end{aligned} \tag{4.3}$$

and W_0 is the spin-orbit parameter.

From the set θ, we can write the usual Skyrme parameters as

$$\begin{aligned}
t_0 &= \frac{4\alpha}{3n_{sat}}, \\
x_0 &= (y-1)\frac{3E_{sym}^{\rm loc}}{\alpha} - \frac{1}{2}, \\
t_3 &= \frac{16\beta}{n_{sat}^\gamma(\gamma+1)}, \\
x_3 &= -3y(\gamma+1)\frac{E_{sym}^{\rm loc}}{2\beta} - \frac{1}{2}, \\
t_1 &= \frac{20C}{9n_{sat}k_F^2} + \frac{8G_0}{3}, \\
t_2 &= \frac{4(25C - 18D)}{9n_{sat}k_F^2} - \frac{8\left(G_0 + 2G_1\right)}{3}, \\
x_1 &= \left(12G_1 - 4G_0 - \frac{6D}{n_{sat}k_F^2}\right)\left(\frac{1}{3t_1}\right), \\
x_2 &= \left(20G_1 + 4G_0 - \frac{5(16C - 18D)}{3n_{sat}k_F^2}\right)\left(\frac{1}{3t_2}\right), \\
\sigma &= \gamma - 1,
\end{aligned} \tag{4.4}$$

where

$$C = \left(\frac{m}{m_0^*} - 1\right) E_{kin}^0$$

$$\begin{aligned}
D =& \frac{5}{9} E^0_{kin} \left(4\frac{m}{m^*_0} - 3\frac{m}{m^*_1} - 1 \right) \\
\alpha =& -\frac{4}{3} E^0_{kin} - \frac{10}{3} C - \frac{2}{3} \left(E^0_{kin} - 3E_{sat} - 2C \right) \\
& \times \frac{K_{sat} + 2E^0_{kin} - 10C}{K_{sat} + 9E_{sat} - E^0_{kin} - 4C} \\
\beta =& \left(\frac{E^0_{kin}}{3} - E_{sat} - \frac{2}{3} C \right) \\
& \times \frac{K_{sat} - 9E_{sat} + 5E^0_{kin} - 16C}{K_{sat} + 9E_{sat} - E^0_{kin} - 4C} \\
\gamma =& \frac{K_{sat} + 2E^0_{kin} - 10C}{3E^0_{kin} - 9E_{sat} - 6C} \\
E^{loc}_{sym} =& E_{sym} - E^{kin}_{sym} - D \\
y =& \frac{L_{sym} - 3E_{sym} + E^{kin}_{sym} - 2D}{3(\gamma - 1) E^{loc}_{sym}} \\
k_F =& \left(\frac{3\pi^2}{2} \right)^{1/3} n^{1/3}_{sat} \\
E^0_{kin} =& \frac{3\hbar^2}{10m} \left(\frac{3\pi^2}{2} \right)^{2/3} n^{2/3}_{sat} \\
E^{kin}_{sym} =& \frac{\hbar^2}{6m} \left(\frac{3\pi^2}{2} \right)^{2/3} n^{2/3}_{sat}
\end{aligned} \tag{4.5}$$

The explicit expression of NMPs for the Skyrme functional, following the definition Eq. (1.60), can be found in Appendix B.

4.2 Bayesian setup

Before diving into the results, we have to specify the characteristics of our Bayesian setup. As mentioned in the beginning, we performed two inferences, one with only data from double-magic nuclei and one with data from double-magic and open-shell nuclei. The difference between the two is solely in the choice of observables; the rest of the setup is identical. In the following discussion, therefore, we present the details of the first inference. When we move to the second, we will highlight the differences in the setup before turning to the results.

According to Eq. (3.4), the probability distribution of the parameters θ, the so-called posterior, depends on their likelihood $\mathcal{L}(\theta)$ and their prior distribution $p(\theta)$. As we know, with different degrees of confidence, the interval in which these parameters reside, but we have no clear indication of a preferred value, we assumed a uniform, or flat, prior for the parameters

$$p(\theta) = \prod_i \begin{cases} \frac{1}{b_i - a_i} & \theta_i \in (a_i, b_i) \\ 0 & \theta_i \notin (a_i, b_i) \end{cases} \tag{4.6}$$

where θ is our parameter set Eq. (4.1). The limits (a, b) for each parameter are listed in Table 4.1, and are based on a large set of available Skyrme parametrizations (see [219] for a detailed compilation). We have tried to keep the ranges as large as possible to avoid

Table 4.1: Delimiting intervals of the uniform prior distribution.

	Units	Lower limit	Upper limit
n_{sat}	[fm^{-3}]	0.150	0.175
E_{sat}	[MeV]	-16.50	-15.50
K_{sat}	[MeV]	180.00	260.00
E_{sym}	[MeV]	24.00	40.00
L_{sym}	[MeV]	-20.00	120.00
G_0	[MeV fm^5]	90.00	170.00
G_1	[MeV fm^5]	-90.00	70.00
W_0	[MeV fm^5]	60.00	190.00
m_0^*/m	[-]	0.70	1.10
m_1^*/m	[-]	0.60	0.90

truncation in the posterior (see further discussions below in Sec. 4.3).

As for the likelihood, we opted for a product of Gaussians

$$\mathcal{L}(\theta) = \prod_i^N \exp\left(-\frac{(X_i - M_i(\theta))^2}{2\sigma_i^2}\right) \tag{4.7}$$

where the index i runs over all the N observables, X_i and σ_i are, respectively, the observable value and uncertainty, and $M_i(\theta)$ is the model prediction for the parameters θ. Our functional choice for $\mathcal{L}$ derives from the hypothesis that all the observables are uncorrelated.

In Table 4.2, we show the list of observables X, alongside their uncertainties σ. We selected a variety of ground-state and excited properties of double-magic nuclei. In the first part of the Table, we put the ground-state properties: the binding energies $B.E.$, charge radii R_{ch}, and spin-orbit splittings ΔE_{SO}. The binding energies have been taken from the AME2020 mass table [32, 72], while the radii from Ref. [33]. As we mentioned in Sec. 1.2, binding energies and charge radii are measured to a level of precision far greater than the accuracy of current EDFs capabilities. Using directly the experimental errors is not advisable. Otherwise, we risk the Bayesian process warping the model parameters in the attempt to reproduce data to a degree of precision that we already know is not attainable. This would artificially bias our results and conceal the physical information derived from the experiments. Therefore, we adopted the errors typical of EDF calculations instead: 2 MeV for binding energies and 0.05 fm for charge radii. Setting the same error for all masses means that we are asking for a smaller relative error for the heaviest ones. However, since our aim is achieving a description of the $B.E.$ in line with the known capabilities of the Skyrme interaction ($\lesssim$ 1 MeV of the experimental result for the best mass models), we opted for a flat error for the sake of simplicity. Assuming different errors would change the relative weights of the $B.E.$ only of a few parts per thousand, and will not affect the result much. The spin-orbit splittings are the $\nu 2p$ splitting of ^{48}Ca and $\pi 2f$ of ^{208}Pb (from [34], Tab. III; if more than one value is present, we took the arithmetic mean). We assigned a theoretical error of 0.5 MeV. In the second part of the Table, we list the giant isoscalar resonance excitation energies we considered. We opted for two monopole E^{IS}_{GMR}s and one quadrupole E^{IS}_{GQR}: for the former, we took ^{208}Pb [37], and ^{90}Zr, [220] (both constrained energy); for the latter, we took ^{208}Pb (centroid energy) [221]. With similar reasoning as above, we have assigned

Table 4.2: Observables and initial adopted errors. See text for details.

Ground-state properties			
	$B.E.$ [MeV] [32]	R_{ch} [fm] [33]	ΔE_{SO} [MeV] [34]
^{208}Pb	1636.4 $\pm$ 2.0	5.50 $\pm$ 0.05	2.02 $\pm$ 0.50
^{48}Ca	416.0 $\pm$ 2.0	3.48 $\pm$ 0.05	1.72 $\pm$ 0.50
^{40}Ca	342.1 $\pm$ 2.0	3.48 $\pm$ 0.05	-
^{56}Ni	484.0 $\pm$ 2.0	-	-
^{68}Ni	590.4 $\pm$ 2.0	-	-
^{100}Sn	825.2 $\pm$ 2.0	-	-
^{132}Sn	1102.8 $\pm$ 2.0	4.71 $\pm$ 0.05	-
^{90}Zr	783.9 $\pm$ 2.0	4.27 $\pm$ 0.05	-

Isoscalar resonances		
	E^{IS}_{GMR} [MeV] [37, 220]	E^{IS}_{GQR} [MeV] [221]
^{208}Pb	13.5 $\pm$ 0.5	10.9 $\pm$ 0.5
^{90}Zr	17.7 $\pm$ 0.5	-

Isovector properties			
	α_D [fm^3] [35, 36]	$m(1)$ [MeV fm^2] [35]	A_{PV} (ppb) [38, 39]
^{208}Pb	19.60 $\pm$ 0.60	961 $\pm$ 22	550 $\pm$ 18
^{48}Ca	2.07 $\pm$ 0.22	-	2668 $\pm$ 113

an error of 0.5 MeV to each one of them. Finally, in the third part of the Table, we have listed three isovector properties, which are the dipole polarizability α_D Eq. (1.37) of ^{208}Pb [35] and ^{48}Ca [36], the energy-weighted sum (EWSR) rule $m(1)$ Eq. (1.33) of the IVGDR of ^{208}Pb (from [35, 79]) and the parity-violating asymmetry A_{PV} of ^{208}Pb and ^{48}Ca (from [38, 39]). Unlike the other observables, for these we will employ the experimental errors, as they are in line with the predictive power of standard nuclear techniques. All these observables help constraining the Skyrme parameters θ (4.1), as we also discussed in Section 2.3. Below, presenting the results, we will carefully analyse which observable constrains which parameter.

The posterior distribution of the parameters Eq. (3.4) cannot be computed analytically, but rather is sampled through the Metropolis-Hastings (MH) algorithm [202]. This is a Markov chain Monte Carlo method frequently employed in Bayesian inferences, devised to explore the parameter space, focusing on regions with high likelihood. It requires several likelihood evaluations (of the order of $\sim 10^6 - 10^7$ points in parameter space [29, 30]) to reach a representative sampling of the posterior. This means that the MH algorithm is serviceable only if $M(\theta)$ requires negligible computational time.

Different published codes could serve as $M(\theta)$. An example is the `hfbcs-qrpa` code [222] (see also Ref. [223]), where the ground-state properties are obtained by solving the nuclear Kohn-Sham equations (1.43), while nuclear excited states are calculated based on the same Skyrme EDF through RPA Eq. (1.28) (see, e.g., Ref. [57], and Ref. [223] for the details of our implementation). For the A_{PV}, we computed it using a strategy similar to those in Ref. [95, 209, 211]. We employ the code ELSEPA [224] to calculate the elastic scattering cross section of right- and left-handed electrons. The scattering potential is derived from the point-like neutron and proton densities, which are an output of the `hfbcs-qrpa` ground state computation, convoluted with the weak and electromagnetic form factors. The A_{PV} is then the difference between the right-handed and left-handed

Figure 4.1: Workflow for the Bayesian inferences.

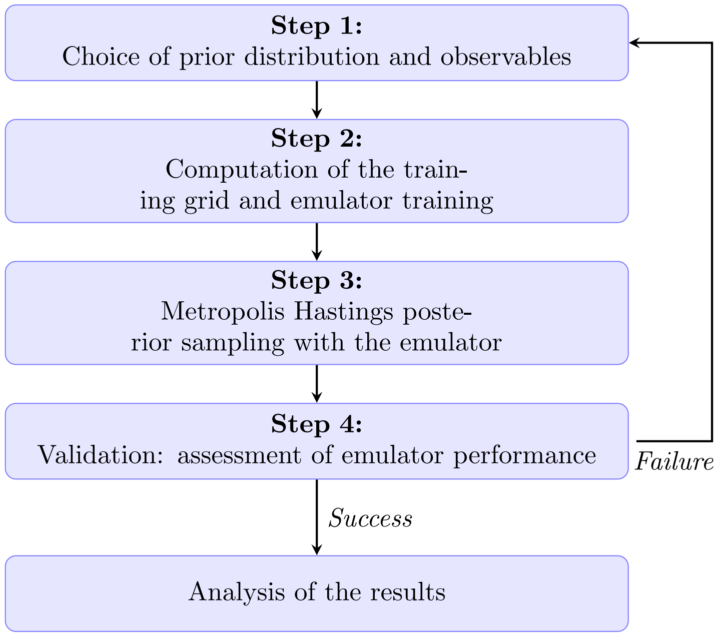

cross sections, normalized over the sum of the two [39].

While the computations for ground-state properties are almost instantaneous, the RPA calculations for the parity-violating asymmetry and especially the excited states are much more demanding: the complete set of observables requires approximately two hours. A direct employment of the `hfbcs-qrpa` code in the MH algorithm is therefore unfeasible time-wise. Instead, we resorted to an emulator software, which mimics the program, resulting in negligible computational time. We employed the MADAI package, developed by the MADAI collaboration [203], a Gaussian Processes emulator (see Sec. 3.3) built for Bayesian inferences with slow models. This software requires as input a training grid, i.e., the program results computed on representative points in parameter space. The emulator, once trained, can predict the `hfbcs-qrpa` code results in no computational time. Therefore, the emulated model is suitable for the MH algorithm.

We summarize in Figure 4.1 our workflow. Once the parameters prior distribution, the observables, and their errors are specified (Step 1), we build the training grid (Step 2): the MADAI software itself proposes a Latin hypercube (see appendix of [225]) which covers uniformly the parameter space, and we compute the values of the observables at each point of the hypercube with the `hfbcs-qrpa` code. Employing the parameter set θ of Eq. (4.1) is extremely convenient when building the grid. When using directly the standard Skyrme parameters, even with seemingly reasonable parameter priors, many parametrizations in the training grid will be pathological, i.e., parametrizations for which the Hartree-Fock computation does not converge for some observables. Resorting to the NMPs drastically decreases the number of these occurrences. A sensible choice of the prior intervals (Tab. 4.1) excludes most, but not all, unphysical parameterizations; those remaining must be removed from the grid to allow the MADAI software to run. We found that we can discard up to $\sim$10% of the initial grid points without compromising the quality of the emulation.

Once the training grid is ready, the emulator is trained, and we sample the parameter posterior through the MH algorithm (Step 3). As the sampling clearly depends on the emulator capacity of correctly emulating the model, it is imperative to assess if it is working properly. We test its performance through what we call validation (Step 4): if the validation is not successful, the inference is rejected, and the process must start from the beginning, addressing the causes of the emulator poor performance. In our experience, a faulty emulation is due to too many discarded points in the original training grid. This is usually caused by a prior too large that allows too many pathological parametrizations. The limits in Table 4.1 are the most generous we found that are compatible with a satisfying emulator performance.

The validation is performed on some randomly extracted points from the posterior. One could, in principle, perform the validation on some uniformly selected points in parameter space, rather than on the posterior samples. On the other hand, doing it on the posterior offers the possibility of studying the emulator performance on the regions of highest $\mathcal{L}$, i.e., the most frequently sampled by the MH algorithm. An imperfect emulation there would be more devastating than in the regions of low likelihood, which are sampled less often.

For each of these points, we compare the emulator guess with the actual `hfbcs-qrpa` result. In Fig. 4.2, we show a graphic representation of this analysis for the observables of ^{208}Pb, for one of the inferences we will describe below. The x-coordinate of each red point corresponds to the model result, while the y-coordinate to its emulator's counterpart. The blue line is $x = y$, which represents perfect emulation, while the two dotted blue lines that delimit the shaded yellow region are $x = y \pm \Delta$, where Δ is the error associated with each observable (Tab. 4.2). We are satisfied with the emulator if at least 90% of the points fall between the two lines. In the example, there are no points outside the accepted boundaries except for E^{IS}_{GQR}, where only 2 points out of 250 lie outside the allowed region. We also observe that the emulator tends to consistently overestimate the polarizability. This is, of course, an undesirable behaviour. However, the induced bias is minimal: in this case, the mean overestimation is of ~ 0.1 fm^3, which corresponds to 0.5% of the experimental value; by contrast, the error is 3%. We decided not to look into the MADAI software to investigate further the origin of this behaviour. Although this might affect the cleanness of our results, the effect on the posterior distribution is limited. As we will argue below in Sec. 4.4, the dependence of α_D on the isovector parameters E_{sym} and L_{sym} is so steep that such a small deviation cannot have great consequences on the likelihood computation, and cannot produce significant biases in the Monte-Carlo exploration of the parameter space.

We perform the validation on the posterior rather than on randomly selected points in parameter space because that is where the MH algorithm finds the most probable parameters.

All the inferences we present in this work passed the validation step. The validation for each one of them is summarized in Appendix C.

4.3 Results with double-magic nuclei

In the first Bayesian inference, we focused on observables of double-magic nuclei, both ground-state and collective excitations. The isovector sector of the interaction is much less constrained than the isoscalar, and is of great importance for the study of neutron stars; for this reason, we included different observables sensitive to the isovector part, among which the highly debated A_{PV} of ^{208}Pb and ^{48}Ca. As these observables constrain different parameters, we actually performed several inferences, adding progressively each

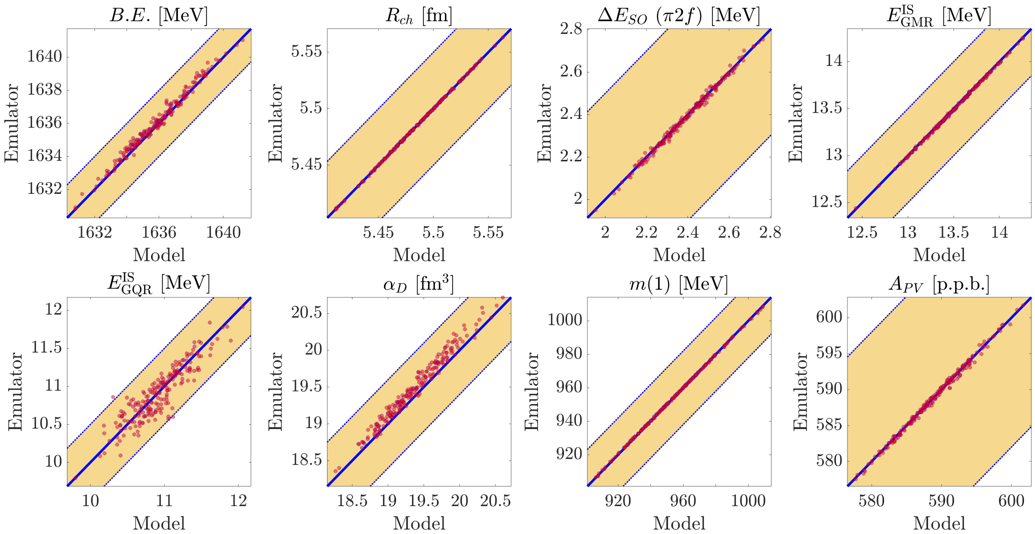

Figure 4.2: Emulator vs. our model (the `hfbcs-qrpa` program) for the ^{208}Pb observables. The diagonal marks the $x = y$ line, so perfect accordance between emulator and model. The yellow region, delimited by two dashed blue lines, is our acceptance region, where the emulated value and the program result difference is lower than the error used for the inference.

type of observable, one at a time, to assess their impact on the posterior distributions. In total, we performed seven inferences, all with the same prior distribution (Tab. 4.1), following the sequent scheme:

1. $B.E.$, R_{ch}: only nuclear masses and radii;

2. $+\Delta E_{SO}$: masses and radii plus the two spin-orbit splittings (i.e., all the ground-state properties);

3. $+\alpha_D$: the ground-state properties plus the nuclear polarizability;

4. $+GR$: the ground-state properties, the nuclear polarizability, the excitation energy of the Isoscalar Monopole and Quadrupole Giant Resonances (E^{IS}_{GMR}, E^{IS}_{GQR}) and the EWSR of the Isovector Giant Dipole Resonance;

The isovector part of the nEOS, crucial for the description of NSs, is troubled by many uncertainties [40, 41, 226]. In our observable pool, there are two that can probe this sector are the α_D and the A_{PV}. As it is known, there is tension between the PREX and CREX results, as no nuclear model can reproduce their results simultaneously [209, 211]. Therefore, we added the parity violation asymmetries first individually, and then together:

5. $+A_{PV}$ (^{48}Ca only): the ground-state properties, the nuclear polarizability, the Giant Resonances, and the parity-violating asymmetry of ^{48}Ca;

6. $+A_{PV}$ (^{208}Pb only): the ground-state properties, the nuclear polarizability, the Giant Resonances, and the parity-violating asymmetry of ^{208}Pb;

7. $+A_{PV}$ (^{208}Pb and ^{48}Ca): all the observables.

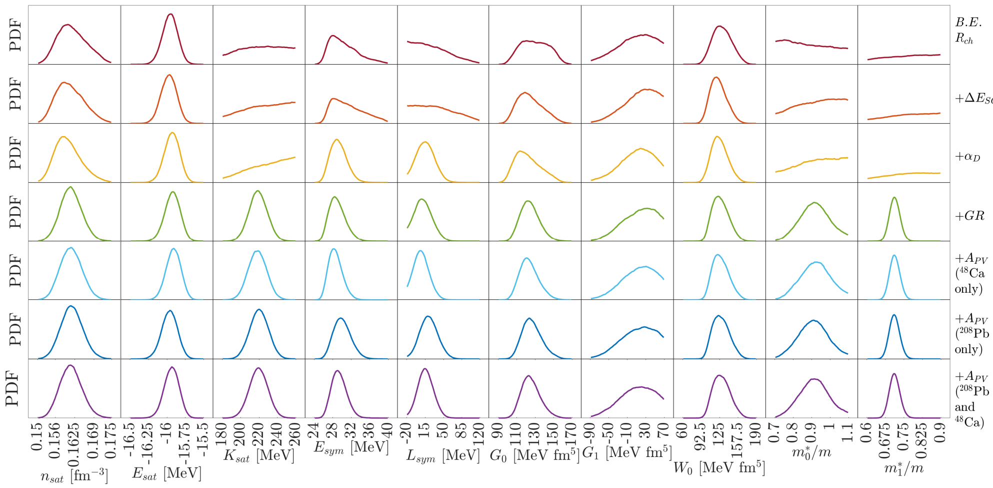

Figure 4.3: Marginalized posterior distributions of parameters for the seven inferences.

In Figure 4.3, we show the posterior distribution marginalized over all but one of our ten parameters, also called the marginalized posterior for brevity. Each of the seven rows of the figure corresponds to one of the seven inferences listed above, going from top to bottom. In each of the ten columns, we display the sampled marginalized probability distribution function (PDF) associated with the entire prior interval of the corresponding parameter. For the sake of illustration, the means and standard deviations of each distribution are reported in Table 4.3. However, they are of limited or no significance when the distributions tend to be flat over the prior interval.

In the first row, we can observe that the masses constrain the energy at saturation E_{sat} and the spin-orbit parameter W_0, while the charge radii constrain the saturation density n_{sat}. Adding the spin-orbit constraint in the second row lowers a little the mean value and the width of the W_0 distribution, and has a small influence on the other parameters. It is worth noting that our choice of spin-orbit splittings seems to slightly favour values of m_0^* in the upper part of the prior interval. The posterior distributions are instead almost flat for K_{sat} and the isoscalar and isovector effective masses. Other experimental data are needed to constrain them.

The G_1 parameter distribution, which remains fairly identical in all seven inferences, peaks within the boundaries of the prior interval, but does not have enough room to develop its tail. We tried to enlarge the prior interval, but this created several pathological points in the emulator training grid, well above the empirical 10% "safety limit" that we had set (see the discussion above in Sec. 4.2). We checked that the vast majority of these points had $G_1 > 70$ MeV fm^5; therefore we cannot but accept this truncation of the posterior. The isoscalar surface parameter G_0 displays a broad distribution that becomes sharper once more observables are added.

The distribution of the E_{sym} and L_{sym} parameters appears to be weakly constrained by these two first inferences. The E_{sym} distribution peaks slightly below 28 MeV, and has a mean value of about 31 MeV and a standard deviation of 3 MeV, displaying a long tail which explores the full prior interval up to 40 MeV. The L_{sym} distribution is rather flat, although it starts decreasing after 50 MeV. This behaviour may seem puzzling at first,

Table 4.3: Means μ and standard deviations σ of the marginalized posterior distributions for all the seven inferences. Their units are: fm^{-3} for n_{sat}; MeV for E_{sat}, K_{sat}, E_{sym}, and L_{sym}; MeV·fm^5 for G_0, G_1, and W_0. The isoscalar and isovector effective masses $m^*_{0,1}/m$ are numbers.

		$B.E.$ R_{ch}	$+\Delta E_{SO}$	$+\alpha_D$	$+GR$	$+A_{PV}$ (^{48}Ca only)	$+A_{PV}$ (^{208}Pb only)	$+A_{PV}$ (^{208}Pb and ^{48}Ca)
n_{sat}	μ	0.162	0.161	0.160	0.161	0.161	0.162	0.161
	σ	0.005	0.005	0.004	0.004	0.004	0.004	0.004
E_{sat}	μ	−15.96	−15.97	−15.93	−15.93	−15.91	−15.96	−15.94
	σ	0.10	0.11	0.10	0.11	0.10	0.11	0.10
K_{sat}	μ	223	226	229	219	218	220	219
	σ	22	22	21	10	10	10	10
E_{sym}	μ	30.5	31.3	29.2	29.0	28.6	30.1	29.4
	σ	3.1	3.4	1.8	1.8	1.5	1.9	1.6
L_{sym}	μ	28.4	36.1	15.8	11.8	8.2	22.2	16.1
	σ	33.1	35.8	17.2	16.5	14.4	16.9	14.7
G_0	μ	130	125	122	124	124	127	125
	σ	15	14	14	10	10	11	10
G_1	μ	8	16	10	14	13	12	9
	σ	38	35	35	35	34	36	36
W_0	μ	130	123	125	127	127	128	129
	σ	17	15	15	14	14	15	15
m^*_0/m	μ	0.88	0.93	0.93	0.92	0.92	0.91	0.91
	σ	0.12	0.11	0.11	0.08	0.08	0.08	0.08
m^*_1/m	μ	0.76	0.77	0.77	0.71	0.71	0.71	0.71
	σ	0.08	0.08	0.08	0.02	0.02	0.02	0.02

since usually ground-state properties only impose a positive correlation between E_{sym} and L_{sym}, and do not point to some preferred values. On the other hand, this feature has already been observed in classic χ^2 fits on the Skyrme interaction. If we look at Table I and II of [227], we see that, consistently, to lower E_{sym} and L_{sym} values corresponded lower χ^2; that is equivalent, translated in a Bayesian setup, to the plots we observe in the first two rows of Figure 4.3. Broadening the observable pool and including also open-shell nuclei will quench this effect (see below, Sec. 4.5). We do observe, anyway, the strong correlation between E_{sym} and L_{sym}, which is well documented in the literature (see, for example, [228]). In fact, in the second inference, the two parameters have a correlation coefficient of 0.96, in line with other works. We will be back to this point when commenting on Figure 4.5.

Our distributions can be compared with other investigations in which only ground-state constraints have been considered. A word of caution is needed: although we have provided values for the mean μ and standard deviation σ of the distributions in Table 4.3, those of E_{sym} and L_{sym} are still quite flat, and so these quantities do not have the same meaning as in Gaussian distributions. In [229], a set of binding energies and charge radii from 72 nuclei, both closed-shell and open-shell, and both spherical and deformed, was used in the analysis. The optimal value found for E_{sym} in the case of the UNEDF0 functional (30.54 ± 3.06 MeV) is very similar to ours, while L_{sym} was poorly constrained. In [69], the full AME2003 mass table was analysed with the finite-range droplet model (FRDM), obtaining an error of $\sigma = 0.57$ MeV on the masses and the optimal values $E_{sym} = 32.5 \pm 0.5$ MeV and $L_{sym} = 70 \pm 15$ MeV. These values are compatible with those obtained in our ΔE_{SO} inference, but are determined with a much smaller error, hinting again that including more binding energies and charge radii may be helpful in future Bayesian analysis.

Their posterior changes drastically when we added the nuclear polarizability α_D in the observable pool: now E_{sym} and L_{sym} are well constrained, as we can clearly see comparing the second and third rows of Figure 4.3. The means μ decrease respectively by 1.5 and 20 MeV, while the standard deviations σ are practically halved. In the literature, the correlation between L_{sym}, E_{sym} and α_D is amply documented. For example, in [97] the authors have found a strong correlation between the slope L_{sym} and the product $\alpha_D E_{sym}$. Furthermore, in [98], the authors expanded their work by adding the experimental data of ^{68}Ni and ^{120}Sn α_D as well, and wrote explicitly a linear relation between L_{sym} and E_{sym} using the experimental values. They also remarked that the functionals able to reproduce the experimental values of $\alpha_D E_{sym}$ in ^{68}Ni, ^{120}Sn and ^{208}Pb within 1 σ have $E_{sym} \in [30, 35]$ MeV and $L_{sym} \in [20, 66]$ MeV, although their analysis considered a handful of Skyrme parametrizations, and it was not a full statistical study.

The observables introduced with the *GR* inference (fourth row of Fig. 4.3, green lines) have multiple effects: the excitation energies of the GMR constrains K_{sat} as seen in Section 1.5, that of GQR and the $m(1)$ value for the IVGDR constrain the isoscalar and effective masses m_0^*/m and m_1^*/m, respectively.

Let us analyse the impact of the monopole constraint. We find that the mean value of K_{sat} is approximately 220 MeV, with a standard deviation of 10 MeV. These values are not affected by the addition of further observables (Tab. 4.3). Our result is compatible with previous analyses, which deduced a value $K_{sat} = 240 \pm 20$ MeV [230] by comparing with the ISGMR experimental results, taking into account the fact that Skyrme EDFs may have different density dependences (cf. also [227]), and also considering relativistic EDFs. While such analyses have been mainly based on ^{208}Pb, other nuclei may point to slightly lower values of K_{sat} [13]. Other studies [231] pointed out that medium-heavy nuclei have a mean density that is lower than saturation (typically, around $\rho \approx 0.1$ fm^{-3}): by analysing the giant monopole resonance data from this perspective, they predicted a less stringent interval of $K_{sat} = 230 \pm 40$ MeV.

The isoscalar effective mass m_0^*/m is constrained once we include the excitation energy of the E_{GQR}^{IS} in ^{208}Pb, leading to relatively high values ($m_0^*/m \approx 0.9$). This confirms previous findings, starting from the pioneering work of [96]. More recently [232], it was shown that models with lower values of the effective mass tend to predict too high excitation energies for this collective mode. The link between the ISGQR and the isoscalar effective mass m_0^*/m can be understood with a simple harmonic oscillator model [78, 96]. The vibration restoring force, following the quadrupole perturbation, is proportional to $\sqrt{m/m_0^*}$.

The EWSR of the IVGDR instead constrains the isovector effective mass m_1^*/m because both quantities are connected with the so-called isovector enhancement factor κ [12, 73]. It can be shown [53, 54] that the enhancement factor, on the one hand, is connected to the isovector effective mass $m_1^*/m = (1+\kappa)^{-1}$, and on the other hand that it is connected to the EWSR $m(1) = (1+\kappa)m_{TRK}$, where m_{TRK} is the classical sum rule (also called Thomas–Reiche–Kuhn, TRK).

The dipole polarizability and the energy of the ISGMR in ^{208}Pb were also used in [233] to fit a relativistic energy density functional, in addition to the ground-state properties of many nuclei, including open-shell nuclei with their pairing correlations. The resulting DD-PCX functional yields $E_{sym} = 31.13 \pm 0.32$ MeV and $L_{sym} = 46.32 \pm 1.68$ MeV. As already mentioned, having a larger pool of nuclei is certainly an asset; at the same time, we cannot directly compare the latter errors with ours, as the fit was performed with a different EDF. We will show nonetheless below, in Section 4.5, that including data from open-shell nuclei will bring the results closer to this analysis.

We included the parity-violating asymmetries in the last three inferences. As we can observe in Fig. 4.3, adding the $A_{PV}(^{48}\mathrm{Ca})$ (light blue lines) or the $A_{PV}(^{208}\mathrm{Pb})$ (blue lines) has opposite effects on the E_{sym}, L_{sym} distributions, shifting them towards slightly lower or slightly higher values, respectively. This tendency becomes much more pronounced if the polarizability is excluded from the pool of observables. This can be clearly seen

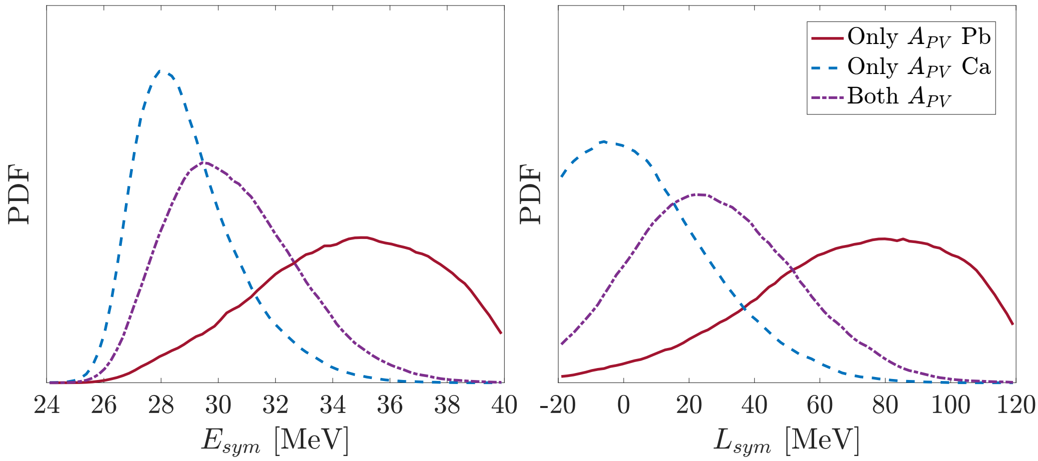

Figure 4.4: Effect of the A_{PV} on the posterior distributions of E_{sym} and L_{sym}, if α_D is not in the observables pool. We can observe the tension between the experimental results in ^{48}Ca and ^{208}Pb.

in Fig. 4.4, where we show the posterior distributions associated with E_{sym} and L_{sym}, obtained by excluding α_D from the inference. Including only the ^{208}Pb A_{PV}, the E_{sym}-distribution peaks around 36 MeV while the L_{sym}-distribution peaks around 85 MeV. This is consistent with previous works showing that a high L_{sym} value is needed to explain the PREX-II results [39, 209]. On the other hand, including only the ^{48}Ca A_{PV} the E_{sym}-distribution peaks around 28 MeV while the L_{sym}-distribution peaks around 0 MeV.

This is the manifestation of the known tension between the two measurements in ^{48}Ca and ^{208}Pb [211, 212]. It must be pointed out, anyway, that the distributions are quite broad, and they overlap over a rather extended region of the parameter space. Including both A_{PV}'s, one obtains distributions that are intermediate between the two extreme cases that we have discussed, with E_{sym} and L_{sym} peaked around 30 MeV and 20 MeV, respectively. These values are not far from those obtained in the final $+A_{PV}$ inference including all our observables, shown in Fig. 4.3, which, however, displays smaller widths, due to the polarizability constraint.

In a recent work [234], the authors performed a Bayesian analysis similar in spirit to ours, also based on Skyrme interactions but including a less diversified set of observables. Their constraints include ground-state properties of double-magic nuclei, and the excitation energy of the ^{208}Pb monopole giant resonance; they also introduced the PREX-II and CREX results in the form of the deduced weak form factors, and not directly with the experimental observable A_{PV}. On the other hand, α_D, the IVGDR energy weighted sum rule, and the excitation energy of the ISGQR were not included in the inference. Their resulting posterior distributions for E_{sym} and L_{sym} are similar to those we obtain neglecting α_D, shown above in Fig. 4.4. They find $E_{sym} = 29.1\pm^{2.1}_{1.8}$ MeV and $L_{sym} = 17.1\pm^{23.8}_{22.3}$ MeV (68.3% credible intervals). Their values for K_{sat} lie in the interval $225\pm^{2.9}_{2.8}$ MeV (68.3% credible interval), which is compatible with our result. They also produced a representative Skyrme interaction, SkREx, whose parameters lie well within our posterior distributions, except for $G_1 = 55$ MeV fm^5, a value which is slightly disfavoured by our findings. This interaction predicts values of α_D lying within 1σ of the experimental results for both ^{48}Ca and ^{208}Pb.

Another Bayesian study was performed in [101], based on previous exploratory studies [235–237], both with the traditional Skyrme interaction and with KIDS functional [102–104]. If we focus on their results on the traditional Skyrme, we see that the isovector parameters, namely E_{sym} and L_{sym}, differ from our findings (Figure 15 of [101]). Their analysis of the traditional Skyrme seems to favour high values of $E_{sym} \gtrsim 35$ MeV, although their posterior distribution is truncated by the prior limits. Instead, L_{sym} peaks at around 60 MeV, plummeting abruptly afterward, although it is difficult to estimate if this sudden decrease is due to the correlation with E_{sym} (see below, Figure 4.5). As for the KIDS results, their E_{sym} is identical, while L_{sym} has a quite broad and somewhat flat distribution between 0 and 90 MeV, after which it falls off. Again, the truncation in E_{sym} may play a role. These differences can be traced back to two different aspects. First, their fitting protocol is different from ours: the authors fixed some parameters (E_{sat}, n_{sat}, G_0, G_1, W_0 and m_0^*/m); they perform inferences with observables from either ^{208}Pb or ^{120}Sn; they do not use a Gaussian likelihood for the binding energies $B.E.$ and the charge radii R_{ch} of the aforementioned nuclei, but rather they accept any combination of parameters that predicts them within 3% of the experimental value; they use the data of the PREX-II experiment in terms of inferred neutron skin and not of the experimental observable A_{PV}; finally, they use a different dataset (i.e., photoabsorption data) for the ^{208}Pb IVGDR EWSR. The different choice of likelihood for the ground-state properties entails great consequences. Asking the model to reproduce binding energies with great precision greatly reduces the region of parameter space allowed for simultaneously describing the excited properties like the polarizability; we will elaborate more on this point below, commenting on Figures 4.8a and 4.8b. Second, and valid only for the KIDS part of their analysis, they use a more flexible functional: for them, the NMP K_{sym} and Q_{sat} are free, and, unlike the traditional Skyrme, not determined by the other NMPs, as we observed in Section 1.5. This extra flexibility appears, in their case, to allow a broader posterior distribution of L_{sym} compared to ours, which is linked to the freedom of K_{sym}. Using an extended Skyrme EDF (like that used in [238]) could make our findings more similar to theirs.

In [219], the authors compiled the parameters and nuclear matter properties of 255 published Skyrme interactions. Thus, it is interesting to compare our parameter marginalized posterior distributions with those of published parametrizations, even though the statistical meaning of the latter is not as clear as ours: rather than a true probabilistic sampling of parameter space, it collects many analyses on the Skyrme interaction, thus reflecting modeler bias and different fit protocols. We start with the saturation density n_{sat}. The distributions are quite similar, even though most Skyrme have $n_{sat} \approx 0.16$ fm^{-3}, whereas ours is slightly shifted to higher values. On the other hand, we find that E_{sat} is in line with what is published, with most Skyrme EDFs having values in the interval $(-16.3, -15.5)$ MeV. Instead, K_{sat} is lower than commonly given values, peaking around 220 MeV and having tails below 200 MeV, while most Skyrme interactions have K_{sat} values around $235 - 240$ MeV. Similarly, but more markedly, we find lower values than previously reported for E_{sym} and especially for L_{sym}. We find that E_{sym} peaks at around 29 MeV, and values over 32 MeV are heavily disfavored, while most Skyrme have E_{sym} between 31 and 33 MeV. For L_{sym}, we find a peak at around 15 MeV, while values over 45 MeV are highly unlikely; instead, published Skyrme shows a much wider interval, which ranges from 0 MeV to more than 100 MeV, with those around 50 MeV particularly frequent. As for the surface parameters, we find published G_0 values ranging from 0 to 200 MeV fm^5, even though the most frequent are those where our distribution peaks. Instead, our G_1 distribution and the published one are very similar, which is quite reassuring given the fact that we should, but could not, expand its prior interval. For both effective masses m_t^*/m we find a much tighter spread in values. Both of the published ones span from 0.5 to slightly more than 1. Finally, the authors of Ref. [219] did not report the values of the spin-orbit parameter. On the other hand, given our experience, our results, which are centered around 130 MeV fm^5, are in line with the most common parametrizations.

There is also a compilation of existing RMF parametrizations [67]. They selected those models that agree with various constraints on NMP and on the behaviour of symmetry energy and PNM (we refer to the paper for the details). They predict in general a stiffer EOS, with larger values of E_{sym} (around 37 MeV) and L_{sym} (around 80 MeV). However, the comparison with our results is not as straightforward, due to the difference in EDF.

We show the corner plot associated with our final $+A_{PV}$ inference in Figure 4.5. The single-parameter marginalized posterior distributions are shown on the diagonal, while the other panels contain the bivariate marginalized distributions. This plot is useful to identify the strongest correlations among the observables. In particular, one can notice the strong correlation between E_{sym} and L_{sym} already discussed above. This correlation stems from the fact that $B.E.$s constrain the symmetry energy at $n \sim 0.1$ fm^{-3}: $S(0.1\,\mathrm{fm}^{-3}) \approx 25$ MeV [227, 239]. Therefore, at saturation, if a parametrization has a high E_{sym}, then it requires a high L_{sym} to meet the constraint at 0.1 fm $^{-3}$; if, on the other hand, it has a low E_{sym}, it needs a low L_{sym} to satisfy the same condition. The correlation between m_0^*/m and G_0 results from the fact that they are different combinations of the same Skyrme parameters t_1, t_2, and x_2 (see Eqs. (4.2) and (4.3)). Other important correlations are observed between E_{sym}, and E_{sat}, still due to the constraint of the symmetry energy at $n \sim 0.1$ fm^{-3}, and between W_0 and G_1, whose physical meaning eludes us at the present moment.

An interesting consistency check is to investigate how well Skyrme parametrizations extracted from the posterior distribution reproduce the observables used for the fit. For this analysis, we extracted 100'000 posterior samples and used the emulator to get the model results, obtaining as a result a probability distribution for each observable. From this, we computed the arithmetic mean and standard deviation of observables along the samples. The results are collected in Tab. 4.4.

We find that almost all our results lie within $1\sigma_c$ from the experimental data, where σ_c

$$\sigma_c = \sqrt{\sigma_{inf}^2 + \sigma_{exp}^2} \tag{4.8}$$

and σ_{inf} is the standard deviation of the resulting posterior distribution while σ_{exp} is the experimental error (so $\sigma_{exp} = 0$ for those observables with a theoretical error).

The only exceptions are the binding energies of ^{56}Ni and ^{48}Ca, the charge radii of both Ca isotopes, and the spin-orbit splitting of ^{48}Ca, which are between 1 and $2\sigma_c$ (highlighted in orange), and the ^{208}Pb A_{PV} and spin-orbit splitting (highlighted in red), that lie at slightly more than $2\sigma_c$. The binding energies and charge radii are still satisfactory even if coloured in orange, as the inference results are still within the theoretical error we assigned. The fact that both spin-orbit splittings are not as precisely reproduced as the other observables may indicate that the spin-orbit sector should be treated with greater precision, while we kept it simple in our work, on purpose, by including just one spin-orbit parameter. Finally, the fact that ^{208}Pb A_{PV} is badly reproduced is another aspect of the above discussion (see Fig. 4.4 and comments) about the tension between ^{208}Pb A_{PV} and ^{48}Ca A_{PV} and the dominant effect of α_D which leads to low values for E_{sym} and L_{sym}.

It is also interesting to see the performance of our models on the α_D of ^{68}Ni, following the example set by [233] for the DD-PCX relativistic functional. We performed a similar test by computing the posterior distribution of ^{68}Ni α_D from the same 100'000 posterior samples from which we derived Table 4.4. ^{68}Ni α_D was not in the observable pool of

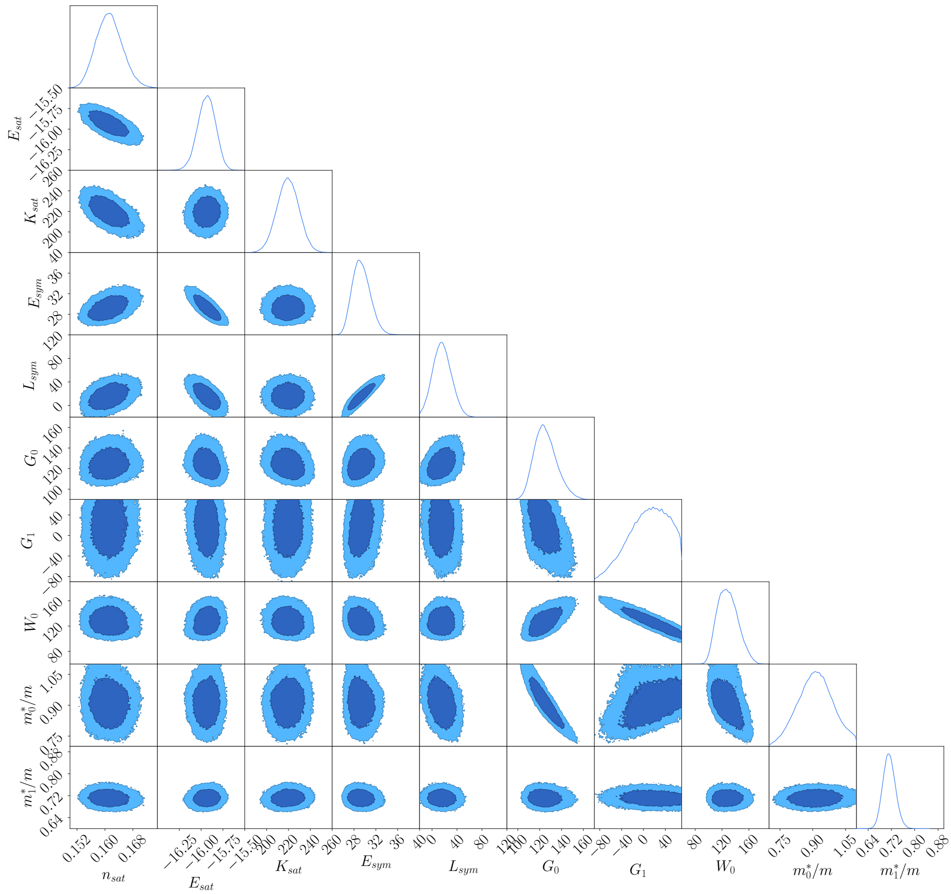

Figure 4.5: Corner plot when using all observables.

Table 4.4: Mean and standard deviation of the observables posterior distributions. If a number the result is coloured in orange, it means that its distance from the experimental value is between 1 and $2\sigma_c$ (Eq. (4.8)), if in red, more than two.

Ground-state properties			
	$B.E.$ [MeV]	R_{ch} [fm]	ΔE_{SO} [MeV]
^{208}Pb	1636 ± 1.8	5.49 ± 0.03	2.34 ± 0.16 (red)
^{48}Ca	417 ± 1.2 (orange)	3.51 ± 0.02 (orange)	1.92 ± 0.20 (orange)
^{40}Ca	342 ± 1.6	3.50 ± 0.02 (orange)	-
^{56}Ni	482 ± 1.4 (orange)	-	-
^{68}Ni	590 ± 1.0	-	-
^{100}Sn	826 ± 1.6	-	-
^{132}Sn	1103 ± 1.7	4.71 ± 0.03	-
^{90}Zr	784 ± 1.3	4.27 ± 0.02	-

Isoscalar resonances		
	$E^{\mathrm{IS}}_{\mathrm{GMR}}$ [MeV]	$E^{\mathrm{IS}}_{\mathrm{GQR}}$ [MeV]
^{208}Pb	13.5 ± 0.3	10.8 ± 0.4
^{90}Zr	17.8 ± 0.4	-

Isovector properties			
	α_D [fm^3]	$m(1)$ [MeV fm^2]	A_{PV} [p.p.b.]
^{208}Pb	19.5 ± 0.5	958 ± 22	589 ± 5 (red)
^{48}Ca	2.30 ± 0.08	-	2591 ± 54

the inference, and comparing it with the posterior distribution of ^{208}Pb and ^{48}Ca is a good check for the predictive power of our fit. The results are shown in Figure 4.6. The experimental values are marked either with a thick red line (on-diagonal plots) or with a red dot (off-diagonal plots); the 1σ regions are coloured in red (on-diagonal plots), or hatched (off-diagonal plots). The experimental data for ^{68}Ni is taken from [98, 240]. Looking at the marginalized posterior on the diagonal, we see that the distributions of ^{68}Ni and ^{208}Pb α_D are compatible at the 1σ level with the experiment, while that of ^{48}Ca is at slightly more than 1σ, which we already observed discussing Table 4.4. Furthermore, from the bivariate distribution, we observe that no particular problem arises when describing simultaneously any two of the three α_D, with ^{68}Ni and ^{208}Pb α_D distribution being contained almost entirely in the 1σ hatched region. This control shows that, even if E_{sym} and L_{sym} values are somewhat low in our analysis, it does not affect the model ability to reproduce experimental data (Table 4.4), not even in the case of a new, isovector-sensitive observable (Figure 4.6).

Another check of the performance of our parametrizations is controlling their consistency with PNM χEFT computations [241]. We will make such a comparison in the following chapter, commenting on Figure 5.8. We anticipate here that approximately 20% of the models in our posterior are completely compatible with these calculations.

Finally, we turn to the correlations between the model parameters and the observables. To study those, we took the model results over the training grid, which spans the whole parameter space, and computed the Pearson correlation factors of all possible combinations of observable and parameter; we thus find a correlation matrix, which we show in Fig. 4.7. The observables are along the columns, grouped by their type and

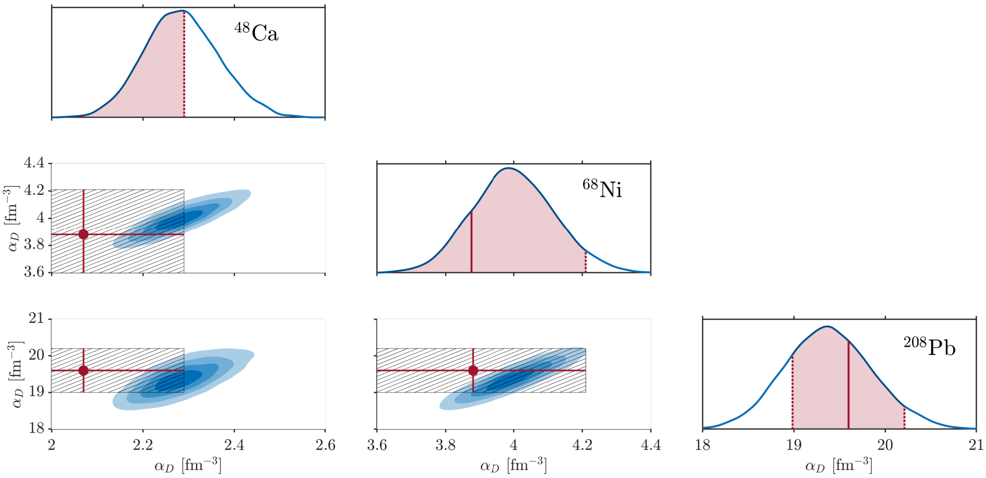

Figure 4.6: Corner plot of the α_D posteriors of ^{48}Ca, ^{68}Ni and ^{208}Pb. The experimental values are marked either with a thick red line (marginalized distribution) or with a red dot (bivariate distribution); the 1σ regions are coloured in red (marginalized distribution), or hatched (bivariate distribution).

ordered from the lightest to the heaviest nucleus, while the parameters are on the rows, divided into isoscalar, isovector, and spin-orbit. The value of the correlation coefficient is in a coloured scale, going from dark blue (-1, total anti-correlation) to dark red (1, total correlation). 0, no correlation, is mapped in white.

The energy at saturation E_{sat} is mainly anti-correlated with the binding energies, and very little with the charge radii. On the other hand, the saturation density n_{sat} is anti-correlated with the charge radii (and especially with that of ^{208}Pb). These correlations can be expected on quite general grounds. If one increases E_{sat}, nuclei are over-bound and the "anti-"correlation is merely a result of the sign convention on the binding energy; at the same time, a higher (lower) saturation density leads to more compact (more dilute) nuclei. The compressibility K_{sat} is highly correlated with both E^{IS}_{GMR}'s, as is well known and has already been discussed. The isoscalar surface parameter G_0 is well correlated with the ground-state observables (slightly more to those of lighter nuclei, where the surface plays a stronger role), while the isoscalar effective mass m_0^*/m is mainly correlated to $E^{\mathrm{IS}}_{\mathrm{GQR}}$ as expected. As for the isovector parameters, E_{sym} is slightly anti-correlated with the polarizabilities α_D; on the other hand, L_{sym} is strongly correlated with α_D [97, 98, 242] and anti-correlated with A_{PV} [95]. These correlations have, of course, a secondary effect on the distribution of E_{sym}. For the isovector surface parameter G_1, no single observable acts as a stringent constraint, which explains its rather wide distribution. The situation is the opposite for the isovector effective mass m_1^*/m, which is specifically affected by the EWSR $m(1)$ of the ^{208}Pb IVGDR. Finally, the spin-orbit parameter W_0 is highly correlated to the spin-orbit splittings, but with the binding energies as well.

4.4 The combined effect of binding energies and polarizabilities

An interesting question is why our analysis finds E_{sym} and L_{sym} values that are lower than those usually reported in the literature. To investigate this aspect, we studied the

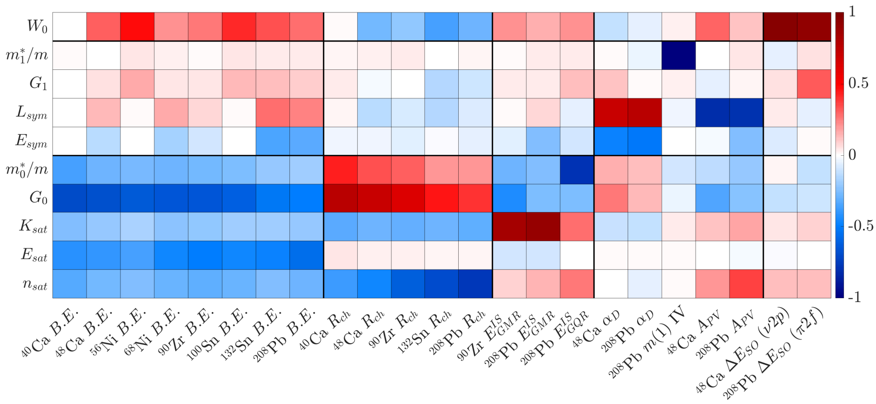

Figure 4.7: Correlations between parameters and observables. The two thick horizontal lines divide the spin-orbit, isoscalar, and isovector parameters, while the thick vertical lines separate the different groups of observables included in our analysis according to their type.

dependence of some selected observables on L_{sym}, fixing all the parameters to their best $\log(\mathcal{L})$ value, except for E_{sym}, which we varied from 28 MeV to 38 MeV, in steps of 2 MeV, and of course L_{sym}, which remained free.

In Figure 4.8a we study the `hfbcs-qrpa` code results as a function of L_{sym}. On the $x-$axis we have the full prior interval of L_{sym}, while on the $y-$axis the result of the `hfbcs-qrpa` code, expressed as a percentage of the experimental value. 100%, perfect accordance with the experiment, is highlighted with a black horizontal line. The orange lines are the binding energies $B.E.$s of ^{208}Pb (darker) and ^{48}Ca (lighter), representative of the $B.E.$s we use. We can observe the expected correlation induced on $E_{sym} - L_{sym}$: with increasing E_{sym}, the program needs a progressively higher value of L_{sym} to match the experimental result. Overall, the $B.E.$s vary by about 5% of the experimental value over the L_{sym} range.

The dashed lines are the polarizability α_D of ^{208}Pb (dark blue) and ^{48}Ca (light blue), while the dotted ones are the parity-violating asymmetries A_{PV} of ^{208}Pb (dark green) and ^{48}Ca (light green). As expected, the A_{PV} [211] decreases as L_{sym} grows, while the polarizabilities grow with L_{sym} [97, 98]. The A_{PV} changes rather slowly, spanning $\sim 10 - 15\%$ of the experimental value across the L_{sym} prior interval, while the α_D has a quite steep gradient, varying significantly in an interval of $\sim$ 40 MeV. If we look at the observables uncertainties in Table 4.2, we see that, while A_{PV} and α_D have a relative error of ∼3% (∼10% for the^{48}Ca α_D), the $B.E.$s impose a much tighter constraint, as they have an error of some parts per thousand. This brings us to the main argument: the Metropolis-Hastings algorithm will always favour zones where the model prediction for the $B.E.$s is close to the experimental value; otherwise the likelihood Eq. (4.7) would rapidly fall to zero. In $E_{sym} - L_{sym}$ terms, it means that it follows the correlation imposed by the masses. On that correlation, the MH algorithm can either land on high $E_{sym} - L_{sym}$ zones, where one can describe fairly well the $B.E.$s together with the ^{208}Pb A_{PV}, or on low $E_{sym} - L_{sym}$ regions, where one can describe the $B.E.$s and α_D simultaneously. Since α_D has a much steeper dependence on L_{sym} than A_{PV}, and their relative error is similar, the likelihood will fall off much more rapidly than the A_{PV} one when moving away from the regions where the model reproduces the experimental results. Therefore, the Bayesian process will prefer regions where the masses and the α_D are simultaneously well reproduced, which happens when $E_{sym} \in (28, 30)$ MeV, where the posterior probability density is concentrated in Figure 4.3.

This becomes even clearer if we look directly at the likelihood $\mathcal{L}_i$ for each observable, i.e., we single out the terms in the product in Eq. (4.7). Figure 4.8b is the same as 4.8a, but instead of showing the model results as a function of L_{sym}, it shows directly the $\mathcal{L}_i$ relative to each observable. The thick black line is the total likelihood $\mathcal{L}_{tot}$, i.e., the product of the single likelihoods of the selected observables. It is in logarithmic scale, as can be appreciated by looking at the right $y-$axis. We see that for $E_{sym} =$ 30 MeV the $\log(\mathcal{L}_{tot})$ reaches its highest value; at $E_{sym} = 28$ MeV its peak decreases approximately 70%. For $E_{sym} \geq 32$ MeV, $\mathcal{L}_{tot}$ plummets: in the bottom row, where we had to change the scale, we can observe it is several orders of magnitude lower than at $E_{sym} = 30$ MeV. Therefore, the reason we find such low values of E_{sym} and L_{sym} lies in the request of simultaneously describing the polarizabilities and the binding energies within the experimental error and 2 MeV, respectively. This also explains the difference with works which are similar in the general spirit but different in practice, because they give much less weight to masses, like [101].

One might rightly wonder whether the experimental errors we are employing are too tight, and if the demands on $B.E.$s and on α_Ds should be relaxed. On the one hand, EDFs were primarily developed to reproduce masses (and radii), so now accepting a less precise description of such important observables seems unsatisfactory. On the other hand, we do not have any independent indication that the α_D should require a more generous uncertainty.

Alternatively, we could expand our pool of observables, in particular the $B.E.$s. As mentioned in Sec. 1.2, double-magic nuclei are particular, and EDFs tend to over-bind them. Furthermore, we have three symmetric nuclei, which are even more delicate and require special treatment to account for possible proton-neutron pairing effects or other effects that are often mocked up by the so-called Wigner term [243–245]. We get all our ground-state information from double-magic nuclei, and this could create unwanted biases. For this reason, in the next Section, we will report the results of updated inferences, where we expanded our observables pool, including binding energies of open-shell nuclei.

4.5 Results with open-shell nuclei

The updated set of observables is in Table 4.5, and was inspired by looking at previous analysis, like [229]. Following up with the previous Section, we included the $B.E.$s of open-shell Ca, Sn, and Pb isotopes, as well as the charge radius of ^{50}Ca and the neutron pairing gap Δ_n of ^{120}Sn, and removed all observables linked to $N = Z$ nuclei. In total, we added ten new observables; we checked that adding a few more $B.E.$ or R_{ch} did not significantly alter the final results. As mentioned in Sec. 1.2, open-shell nuclei present superfluid properties. Therefore, we add the volume pairing term in the Skyrme interaction, Eq. (1.50), with the pairing strength v_0 acting as a new parameter, to account for these pairing correlations. The binding energies are taken from the AME2020 mass collection [32, 72], the radius from [33], while the pairing gap is derived by the odd-even-staggering three-points mass difference formula [53, 246]

$$\Delta(A; Z) = \frac{(-1)^A}{2}[B.E.(A-1; Z) + B.E.(A+1; Z) - 2B.E.(A; Z)] \tag{4.9}$$

where A is the number of nucleons, Z the number of protons, and $B.E.$ is the binding energy.

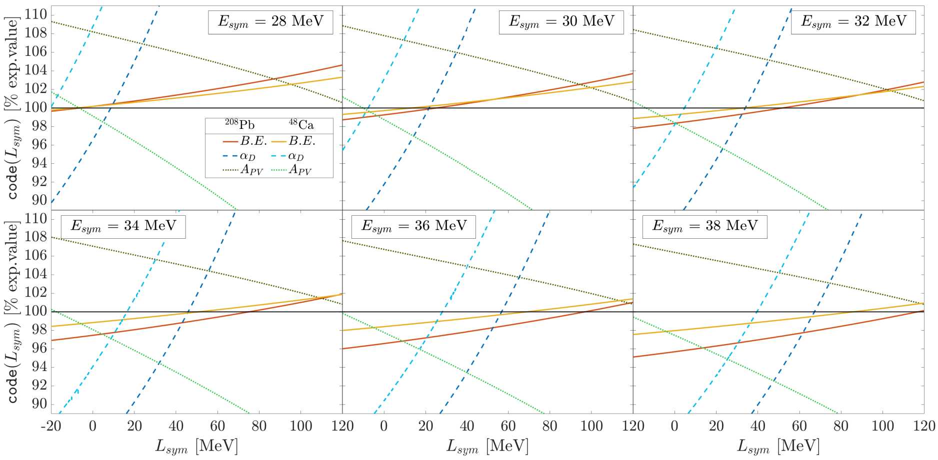

(a) Model results (training grid) as a function of L_{sym}

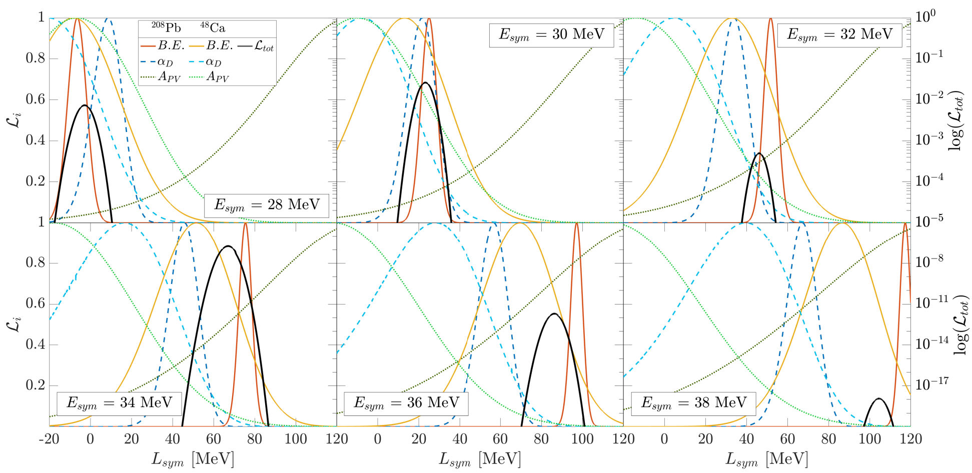

(b) Likelihood $\mathcal{L}$ as a function of L_{sym}.

Figure 4.8: Model results and Likelihood $\mathcal{L}$ at varying L_{sym}. E_{sym} it has been fixed to 6 values, from 28 to 38 MeV in steps of 2 MeV, while all the other parameters have been fixed at the best likelihood model of the complete inference.

Table 4.5: Observable used for the new set of inferences. The new open shell data is are in the fourth part of the Table, while the updated data for ^{90}Zr E^{IS}_{GMR} and both A_{PV} are highlighted in bold font.

Ground-state properties			
	$B.E.$ [MeV]	R_{ch} [fm]	ΔE_{SO} [MeV]
^{208}Pb	1636.4 ± 2.0	5.50 ± 0.05	2.02 ± 0.50
^{48}Ca	416.0 ± 2.0	3.48 ± 0.05	1.72 ± 0.50
^{68}Ni	590.4 ± 2.0	-	-
^{132}Sn	1102.8 ± 2.0	4.71 ± 0.05	-
^{90}Zr	783.9 ± 2.0	4.27 ± 0.05	-

Isoscalar resonances		
	$E^{\mathrm{IS}}_{\mathrm{GMR}}$ [MeV]	$E^{\mathrm{IS}}_{\mathrm{GQR}}$ [MeV]
^{208}Pb	13.5 ± 0.5	10.9 ± 0.5
^{90}Zr	$\mathbf{18.7 \pm 0.5}$	-

Isovector properties			
	α_{D} [fm^3]	$m(1)$ [MeV fm^2]	A_{PV} (ppb)
^{208}Pb	19.60 ± 0.60	961 ± 22	$\mathbf{528 \pm 18}$
^{48}Ca	2.07 ± 0.22	-	$\mathbf{2550 \pm 113}$

New Data from open shell nuclei			
	$B.E.$ [MeV]	R_{ch} [fm]	Δ_n [MeV]
^{50}Ca	427.5 ± 2.0	3.52 ± 0.05	-
^{46}Ca	398.8 ± 2.0	-	-
^{44}Ca	381.0 ± 2.0	-	-
^{42}Ca	361.9 ± 2.0	-	-
^{120}Sn	1020.5 ± 2.0	4.65 ± 0.05	1.3 ± 0.2
^{112}Sn	953.5 ± 2.0	-	-
^{124}Sn	1050.0 ± 2.0	-	-

Besides the inclusion of open-shell nuclei, we also updated the experimental values of the ^{90}Zr giant monopole resonance excitation energy and of both A_{PV}. For the former, newer analysis of the raw data found a higher value for the excitation energy, $E^{IS}_{GMR} =$ 18.7 MeV [247]. The new E^{IS}_{GMR} will mainly shift the distribution of K_{sat} to larger values, and to lower ones that of n_{sat}, leaving mostly untouched the other parameters, whose correlation with E^{IS}_{GMR} is feeble (see Figure 4.7). For the latter, it was pointed out that the theoretical calculations needed a QED correction to be compared with the experimental results [248], which increases the value of the computed A_{PV}. However, as these corrections are essentially model-independent, we can take them into account by lowering the value of the experimental A_{PV} instead. As L_{sym} and A_{PV} are anti-correlated (Figure 4.7), this will push L_{sym} to larger values. [209, 211].

The prior distribution is the same as the previous analysis, with the above-mentioned addition of the pairing parameter v_0, to have a cleaner comparison with the previous inferences. Its prior distribution will be uniform within the interval $v_0 \in (150, 350)$ MeV fm^3. For the rest, the inferences will proceed as in Sec. 4.3, following the scheme 4.1.

We first start by assessing the effects on the posterior distribution of the new ground-state observables. We performed an inference with just the ground-state properties

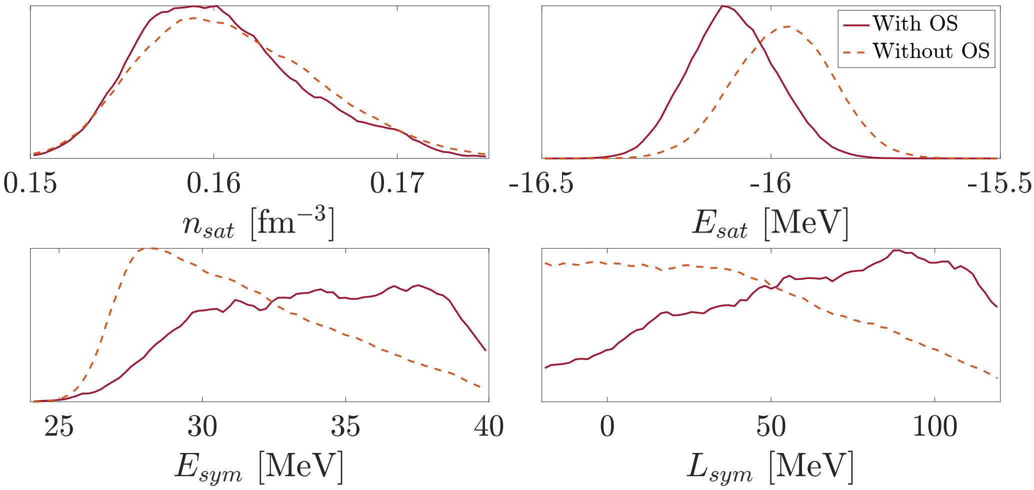

Figure 4.9: Marginalized posterior distributions of n_{sat}, E_{sat}, E_{sym}, and L_{sym} when considering only ground-state properties. The orange dashed line corresponds to the results of the second row of Figure 4.3, while the red line corresponds to the equivalent when adding the open-shell data and removing the $N = Z$ nuclei from the observable pool.

($B.E.$s, R_{ch}, ΔE_{SO}, and Δ_n), and compared it with its counterpart without open-shell nuclei (second row of Figure 4.3). In Figure 4.9, we show such a comparison, focusing on the most affected parameters: n_{sat} and E_{sat}, E_{sym} and L_{sym}. The red line represents the new results, while the dashed orange line represents the previous results.

The addition of the new data and the removal of $N = Z$ nuclei leaves n_{sat} pretty much uneffected, while shifts E_{sat} distribution towards lower values: the pairing interaction impacts mostly the binding energy of the nucleus, whilst leaving unaltered the spatial dependence of the wave functions, and, therefore, the density profiles. On the other hand, E_{sym} and L_{sym} distributions changed considerably. The first lacks that puzzling peak around 29 MeV that characterized the "without open-shell" case, now growing from 25 MeV to 30 MeV, plateauing until ~ 38 MeV, and then dropping. It is much closer to what one would expect from an analysis with just $B.E.$s, as no clear value of E_{sym} is preferred, since $B.E.$s constrain the symmetry energy at $n_B \sim 0.1$ fm^{-3}, thus leaving its value at saturation undetermined [227, 239]. The second one, although very low L_{sym} values seem disfavoured, is all in all flatter than the "without open-shell" case, and does not show the same drop after 50 MeV. To illustrate further this point, in Figure 4.10 we show the posterior distribution of the symmetry energy S at $n_B \sim 0.1$ fm^{-3}, the posterior of the parameter K_{sym} (which, we remind, is not a free parameter in the Skyrme interaction) and the posterior of the symmetry energy from 0.08 to 0.18 fm^{-3} as a confidence interval band, for the two inferences. The posterior of $S(n_B = 0.1$ fm$^{-3})$ is almost identical with or without the open shell nuclei binding energies, as expected. However, we see that there is a clear shift in the parameter K_{sym}: since in the "With OS" analysis E_{sym} is larger, it needs a larger K_{sym} to connect it to $S(n_B = 0.1$ fm$^{-3})$. This translates to an overall stiffer symmetry energy, as it is shown in the bottom panel.

We now turn to the study of the posterior when adding all the observables in Table 4.5. We performed three different inferences, all with the new open-shell data:

1. "With OS, New E^{IS}_{GMR}", where we updated only the experimental value of E^{IS}_{GMR};

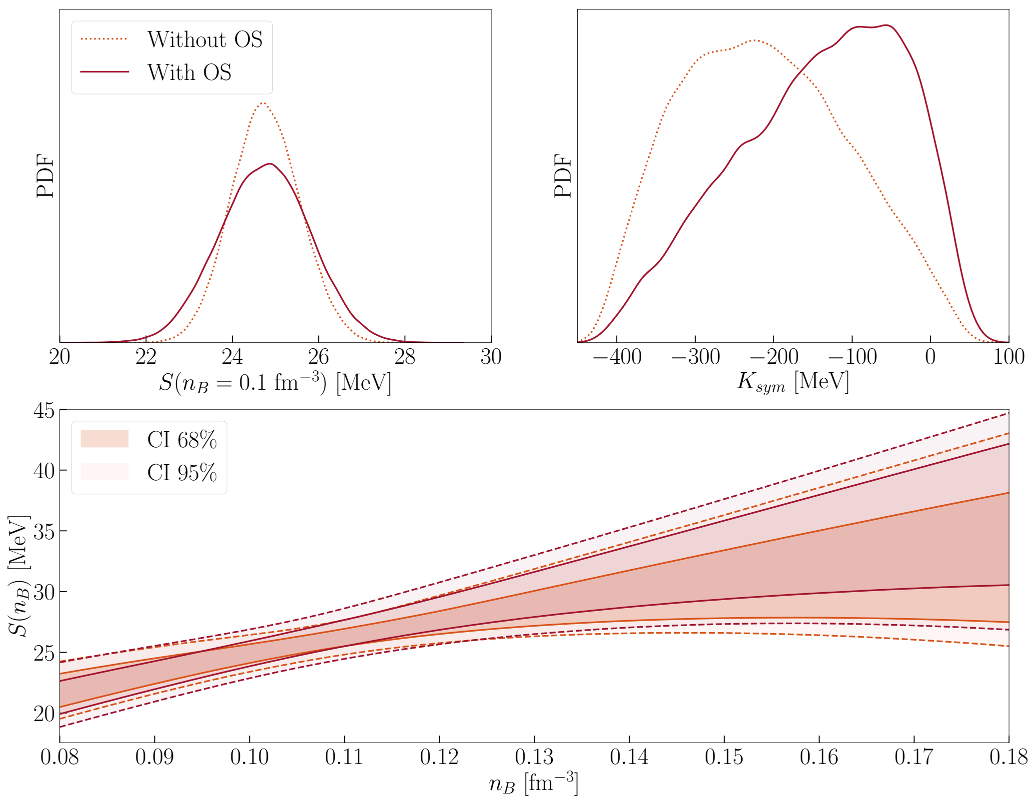

Figure 4.10: Posterior distribution of the symmetry energy S at $n_B \sim 0.1\ \mathrm{fm}^{-3}$, the posterior of the parameter K_{sym}, and the posterior of the symmetry energy from 0.08 to 0.18 fm^{-3} as a confidence interval band, for the two inferences. In orange is “Without OS”, and in red “With OS”; the colour scheme is maintained throughout the plots. In the bottom panel, the darker areas, delimited by full lines, enclose the 68% confidence interval; the lighter ones, delimited by dotted lines, enclose the 95% interval.

2. "With OS, New E^{IS}_{GMR} and A_{PV}", where we updated the E^{IS}_{GMR} and both A_{PV};
3. "With OS, New E^{IS}_{GMR} and ^{48}Ca A_{PV}", where we updated the E^{IS}_{GMR} and just the ^{48}Ca A_{PV}.

The reasoning behind the last inference is that a corrected experimental value of $A_{PV} =$ 528 p.p.b. pushes L_{sym} towards extreme values, $L_{sym} \gtrsim 160$ MeV, as can be verified by looking at Figure 4.8a. This exacerbates the tension between A_{PV} and α_D, making them even less compatible. Using an observable in such tension with the others risks heavily biasing our results. The Bayesian inference will find a compromise that minimizes the total likelihood; however, if the measurements we use are in tension, as it is in our case, then the compromise might be a mediocre description of all the experimental data. Therefore, to isolate and assess the impact of the corrected ^{208}Pb A_{PV} on the results, we performed an inference removing it, and just keeping the ^{48}Ca one.

In Figure 4.11 we show the marginalized posterior distributions of the three new inferences alongside the results of Sec. 4.3 (last row of Figure 4.3), while in Table 4.6 we list the mean μ and the standard deviation σ of each marginalized distribution.

The distributions of n_{sat} and E_{sat} exhibit similar shifts as those in the analysis with just ground-state properties, Figure 4.9, although the n_{sat} one is more prominent than before. This is linked to the marked increase in K_{sat}, to which n_{sat} is anti-correlated, due to the new E^{IS}_{GMR}: its peak increased by about 20 MeV, due to the addition of the new E^{IS}_{GMR}. E_{sym} and L_{sym} both increased as well. When considering all the data, we see that E_{sym} peaks at around 32 MeV, while without ^{208}Pb A_{PV} peaks at around 30 MeV. The L_{sym} peak, on the other hand, shifts to 40 MeV when using all the data, and to 25 MeV otherwise. Interestingly, using the old A_{PV} data, or using just the corrected ^{48}Ca, gives similar results. The reason is that with the corrected value, lower than the original, ^{48}Ca A_{PV} favours L_{sym} values that are similar to those required by the α_D. The distributions of G_0, G_1, W_0, and both effective masses are not affected appreciably.

While adding the open-shell $B.E.$s gave the freedom to E_{sym} and L_{sym} to explore higher values, the general picture was not altered significantly. We still find L_{sym} values which can be, all in all, considered low; and it is not surprising, since the constraint imposed by the α_Ds, investigated in Sec. 4.4, is still present.

We now turn to the posterior on the experimental observables in Table 4.7. By comparing with Table 4.4, we see that, globally, the quality of the reproduction has not changed much. Although there is a slight worsening in the description of ^{68}Ni $B.E.$ and the ^{48}Ca radius, they are still similar to the previous results. On the other hand, the addition of the new E^{IS}_{GMR} decreased the quality of the description of the ^{208}Pb one, which is now more than $1\sigma_c$ away. Also, the ^{48}Ca α_D grew further away from the experimental data, due to the increase in the E_{sym} and L_{sym} distributions.

Other measurements of A_{PV} or of the neutron skin thickness Δr_{np} would prove undoubtedly useful for strengthening our results. As we explained above (see Section 2.3), the neutron skin thickness is an excellent probe to constrain the L_{sym} parameter [95]. Different measurements of this quantity are available for different nuclei, including several Sn isotopes, which have been used in other studies to constrain the symmetry energy (see, for example, [249, 250]). However, these other attempts lack the cleanness and the systematic treatment of uncertainties that characterize the PREX-II and CREX experiments; therefore, even if we do have access to these measurements, we decided not to include them in the fit. Nonetheless, we made a sensitivity study for ^{120}Sn, where we computed its posterior distribution from a posterior sample, in the same way we computed ^{68}Ni α_D above, in Section 4.3. We show the results in Figure 4.12 for the "With OS, New E^{IS}_{GMR} New A_{PV}" and "With OS, New E^{IS}_{GMR} New ^{48}Ca A_{PV}" inferences, in

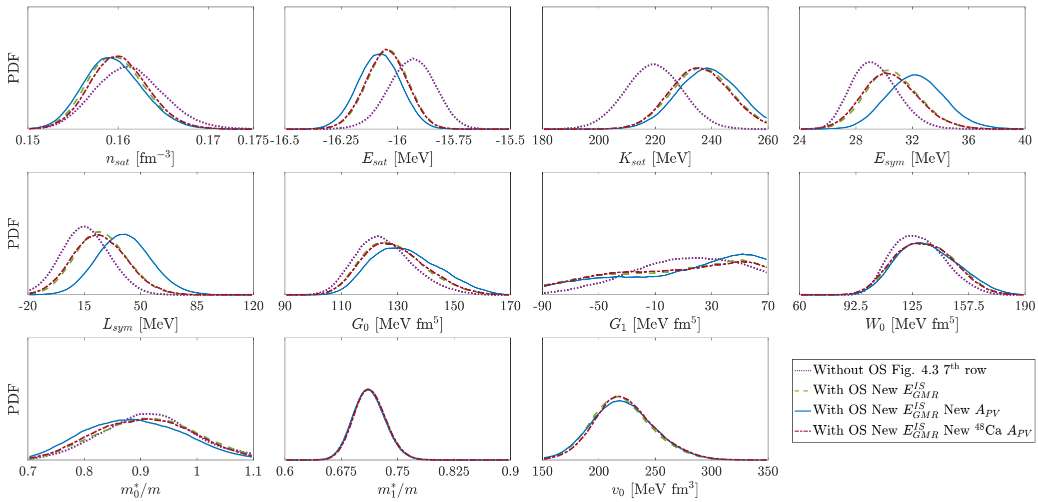

Figure 4.11: Marginalized posterior distributions of n_{sat}, E_{sat}, E_{sym}, and L_{sym} when considering only ground-state properties. The red line corresponds to the results of the second row of Figure 4.3, while the dotted green line to the equivalent when adding the open-shell data and removing the $N = Z$ nuclei from the observable pool.

Table 4.6: Means μ and standard deviations σ of the marginalized posterior distributions for all the advanced inferences. Their units are: fm^{-3} for n_{sat}; MeV for E_{sat}, K_{sat}, E_{sym}, and L_{sym}; MeV$\cdot$fm^5 for G_0, G_1, and W_0. The isoscalar and isovector effective masses $m^*_{0,1}/m$ are numbers.

		With OS New E^{IS}_{GMR}	With OS New E^{IS}_{GMR} New A_{PV}	With OS New E^{IS}_{GMR} New ^{48}Ca A_{PV}	Without OS Fig. 4.3 7$^{\text{th}}$ row
n_{sat}	μ	0.160	0.160	0.160	0.161
	σ	0.003	0.003	0.003	0.004
E_{sat}	μ	−16.05	−16.08	−16.05	−15.94
	σ	0.09	0.09	0.09	0.10
K_{sat}	μ	236	238	236	219
	σ	10	10	10	10
E_{sym}	μ	30.6	32.3	30.5	29.4
	σ	1.9	2.0	2.0	1.6
L_{sym}	μ	25.7	39.8	24.9	16.1
	σ	16.0	16.6	16.7	14.7
G_0	μ	129	133	129	125
	σ	11	12	11	10
G_1	μ	3	8	2	9
	σ	44	44	44	36
W_0	μ	133	134	132	129
	σ	17	17	17	15
m_0^*/m	μ	0.91	0.89	0.91	0.91
	σ	0.08	0.08	0.08	0.08
m_1^*/m	μ	0.71	0.71	0.71	0.71
	σ	0.02	0.02	0.02	0.02
v_0	μ	220	222	223	-
	σ	27	28	27	-

Table 4.7: Mean and standard deviation of the observables posterior distributions. If a number the result is coloured in orange, it means that its distance from the experimental value is between 1 and $2\sigma_c$ (Eq. (4.8)), if in red, more than two.

Ground-state properties			
	$B.E.$ [MeV]	$R_{\rm ch}$ [fm]	$\Delta E_{\rm SO}$ [MeV]
^{208}Pb	1637 ± 1.8	5.49 ± 0.03	2.41 ± 0.23
^{48}Ca	416 ± 1.0	3.50 ± 0.02	1.95 ± 0.21
^{68}Ni	589 ± 0.9	-	-
^{132}Sn	1101 ± 1.7	4.71 ± 0.02	-
^{90}Zr	784 ± 1.2	4.27 ± 0.02	-

Isoscalar resonances		
	E^{IS}_{GMR} [MeV]	E^{IS}_{GQR} [MeV]
^{208}Pb	14.0 ± 0.3	10.9 ± 0.4
^{90}Zr	18.4 ± 0.4	-

Isovector properties			
	α_D [fm^3]	$m(1)$ [MeV fm^2]	A_{PV} [p.p.b.]
^{208}Pb	19.9 ± 0.5	958 ± 22	579 ± 6
^{48}Ca	2.36 ± 0.08	-	2499 ± 57

New Data from open shell nuclei			
	$B.E.$ [MeV]	$R_{\rm ch}$ [fm]	Δ_n [MeV]
^{50}Ca	428 ± 1.0	3.52 ± 0.02	-
^{46}Ca	400 ± 0.8	-	-
^{44}Ca	382 ± 0.9	-	-
^{42}Ca	362 ± 1.2	-	-
^{120}Sn	1020 ± 1.0	4.63 ± 0.02	1.26 ± 0.18
^{112}Sn	954 ± 1.6	-	-
^{124}Sn	1050 ± 0.9	-	-

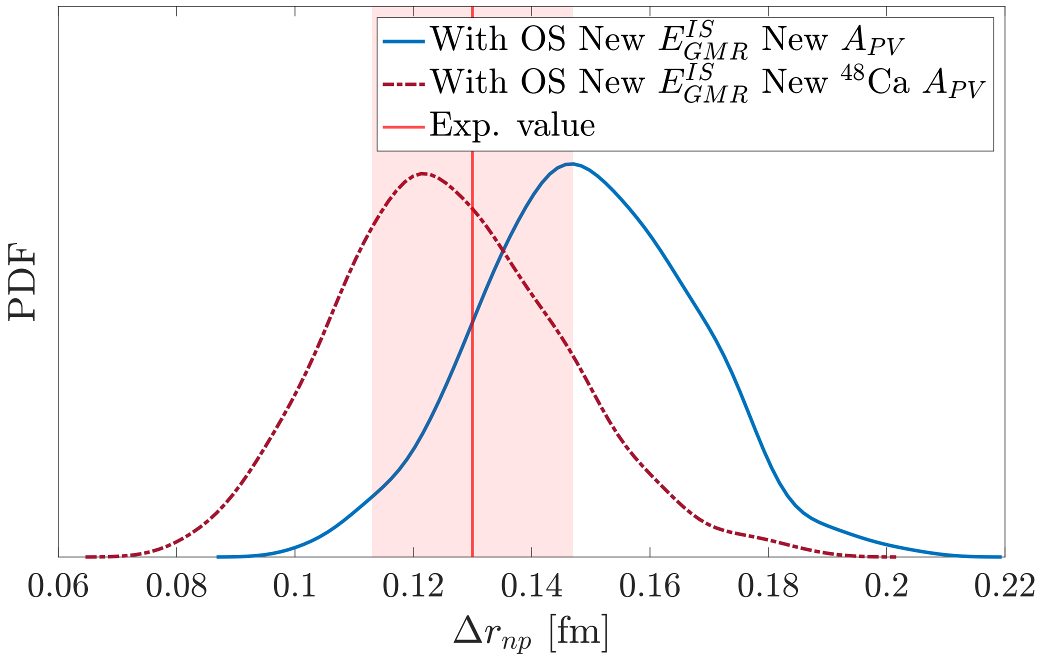

Figure 4.12: Posterior distribution of ^{120}Sn neutron skin thickness Δr_{np}, computed from posterior samples of the 'With OS, New E^{IS}_{GMR} New A_{PV}" and "With OS, New E^{IS}_{GMR} New ^{48}Ca A_{PV}" inferences, in full blue and dot-dashed red respectively. The weighted mean value of the experimental results is marked with a vertical red line, and the shaded area marks the $1-\sigma$ region. It combines the data from [252–254].

blue and red respectively. The experimental result $\Delta r_{np} = 0.13 \pm 0.017$ fm, taken from [251], is a weighted mean of three different experiments: one from elastic p scattering [252] obtaining $\Delta r_{np} = 0.147 \pm 0.033$ fm, one from spin-dipole resonance (^{3}He-t) [253] obtaining $\Delta r_{np} = 0.18 \pm 0.07$ fm, and the last from $\overline{p}$ annihilation [254] obtaining $\Delta r_{np} = 0.12 \pm 0.02$ fm. Overall, both distributions are compatible with the combined mean, although the blue one, informed by the corrected ^{208}Pb A_{PV}, is further away from the mean than the red one. This seems to indicate again that the ^{208}Pb A_{PV} measurement is in tension with the other isovector-sensible observables. However, the three measurements are quite spread, the gap between the smallest and the largest amounting to almost 30%. If the true value is closer to 0.18 fm, both distributions would not be in agreement with the experiment, and Δr_{np} of ^{120}Sn would push for higher values of L_{sym}, going in the direction of ^{208}Pb A_{PV}. A future "SREX" experiment measuring the A_{PV} of ^{120}Sn would therefore be a great source of information.

Chapter 5

Bayesian Inferences on Neutron star Properties

The present chapter is based on, and expands some aspects presented in, the paper 'Neutron Star crust informed by nuclear structure data' by Pietro Klausner, Marco Antonelli, and Francesca Gulminelli, in the phase of peer-review by Physical Review C [255].

The EOS of NSs remains a major uncertainty in nuclear astrophysics, as a wide range of baryonic densities must be covered, which cannot be accessed by a single theory or experimental approach. While the high-density behaviour of dense matter is mostly probed by astrophysical observations, nuclear physics experiments provide robust constraints at sub-saturation densities. A key challenge is to ensure that nuclear uncertainties are properly accounted for when extrapolating empirical information on finite nuclei to deduce the bulk behaviour of matter.

Unlike traditional studies that impose nuclear matter parameter priors in an ad hoc manner [22], our approach starts from the full posterior distribution of Skyrme functionals derived in Section 4.3 (thus, without the open shell nuclei) [1]. This distribution is consistent with a large set of static and dynamical nuclear experimental observables. In particular, in the observable pool are present α_D and A_{PV}, both deeply linked to the symmetry energy and the EOS of pure neutron matter [98, 211], which are thought to entail relevant consequences for NSs [40, 41, 226]. Deriving the prior from an experiment-informed posterior enables an exact treatment of correlations among nuclear matter parameters [98] and surface terms, both of which play a crucial role in the construction of the NS crust, while preserving the information content of the nuclear observables and providing a more physically grounded prior for the NS EOS.

From these Skyrme functionals, we construct unified EOSs for $npe\mu$ matter, where the inner crust is treated using an extended Thomas-Fermi method that makes full use of the nuclear-physics-informed finite-size terms of the energy functional (see Sec. 2.3). The extension to densities above saturation is achieved using the meta-modeling technique (Sec. 2.4), while maintaining consistency with the underlying functional form. We then perform a Bayesian inference to determine which of these unified EOSs satisfy astrophysical constraints, including NS mass measurements, tidal deformability constraints from GW170817, and NICER mass-radius observations (Sec. 2.2). Additionally, we explore key NS observables, such as the crustal moment of inertia, which plays a crucial role in pulsar glitch models [256].

The chapter is structured as follows. In Section 5.1, we go through how we computed the NS EOS starting from a posterior Skyrme parametrization. We detail how we found the MM equivalent of this parametrization in Section 5.3, and how we computed the crust EOS and composition in the ETF approximation in Section 5.2. We then present

[1] The analysis with the posterior derived in Sec. 4.5 is still in progress as we are writing this manuscript.

the details of our Bayesian inference in Section 5.4 and finally we move on to the results discussion in Section 5.5.

5.1 Computation of the NS EOS

In the Bayesian framework, updating a previous inference with new experimental data is a swift operation: one needs to use as a prior distribution the previous posterior distribution.

Still, the analysis in Chapter 4 employed a standard Skyrme interaction as the base model for the nuclear EOS. Using the same model for the NS EOS would be unwise, as its lack of flexibility at super-saturation densities would hinder our ability to describe neutron star properties, due to the artificial correlation among the low-density nEOS and the high-density one (see discussion in Sec. 1.5). Passing to the MM nEOS Eq. (2.43) solves this problem, since we can decouple the high-order parameters from the lower-order ones and remove the limitations imposed by the Skyrme functional form. We devised a procedure to map a Skyrme parametrization into a MM equivalent, so that the nEOS behaviour at sub-saturation densities is almost identical, but at super-saturation can be radically different; more details will be given below in Section 5.3. This is in line with our philosophy of work. Nuclear experiments probe the nEOS around saturation, and have little consequences for the super-saturation part, which NS observations probe instead. As we approach the problem in a Bayesian framework, we want to allow maximum flexibility in the high-density sector, while retaining all possible information from low-density experiments.

At the same time, the MM is a nEOS, not an EDF capable of describing finite nuclear systems; therefore it can be employed for the study of NS crusts only within the framework of simple techniques like the CLDM (Subsec. 2.3.2). Instead, the Skyrme functional is better equipped in this regard: full-quantum approaches or approximations like the extended Thomas Fermi (ETF) have been widely employed to tackle the problem [168, 257]. Especially since crustal densities are similar to those of nuclei, we can also leverage the information coming from nuclear inferences on Skyrme surface and spin-orbit terms; otherwise it would be lost, as it entails no consequence for nuclear matter behaviour.

We proceed as follows: starting from a Skyrme parametrization from the nuclear posterior, we compute the crust EOS and composition with an approximated ETF technique, detailed in Section 5.2. We start from $n_B = 2.66 \times 10^{-4}$ fm^{-3}, the neutron drip density for the BSk24 functional. We do not compute the composition nor the EOS of the outer crust, but rather use those of the BSk24 energy density functional [2] [71]. The outer crust is composed of neutron-rich nuclei, and, in principle, one could leverage the information coming from our previous nuclear inferences. However, the shell effects, which are predominant there due to the absence of the free neutron gas, cannot be accounted for by the ETF formalism, and one should use full quantum approaches like HFB instead. As we mentioned in Subsec. 2.3.2, these methods are more precise, but come at a heavier computational cost, which is not compatible with a Bayesian approach like ours. The extended Skyrme BSk24 was fit to a comprehensive data set spanning the whole nuclear chart, and, therefore, we expect it to be the best likelihood model of a hypothetical Bayesian analysis constrained by that data set. Furthermore, the uncertainty in the EOS of the outer crust due to the uncertainty of the EDF is too small to have a noticeable effect on the global star observables we will compute [168]. That is why we feel confident that using BSk24 outer crust EOS will not appreciably affect our results.

Once the crust core transition density n_{cc} Eq. (2.31) is found, if the EOS in the crust is stable, i.e., there is no pressure drop with increasing density, and causal, i.e., the speed

[2] The outer crust data were taken from the CompOSE online repository [258].

Figure 5.1: Schematization of our procedure for computing the NSs EOS.

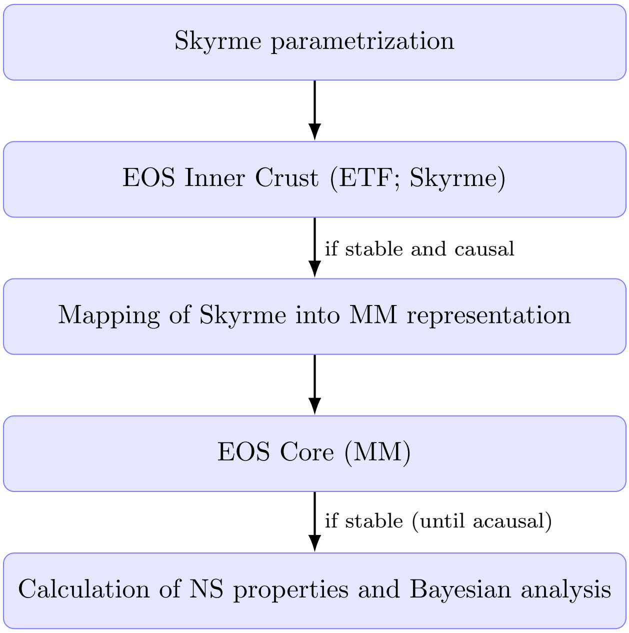

of sound is lower than the speed of light, we pass to the $npe(\mu)$ core EOS computation, described in Subsecs. 2.3.4. The core is treated with the MM representation of the Skyrme, described below in Section 5.3, to allow, as mentioned, more freedom in the high-density behaviour. The EOS computation proceeds until the model eventually becomes acausal, i.e., until the speed of sound overcomes that of light; only if it is also stable, we compute all relevant properties of NSs ($M - R$ relation, $\Lambda(M)$, crustal properties, and so on), used later to calculate the likelihoods for the Bayesian analysis, described below in Section 5.4. We summarize these steps in Figure 5.1.

5.2 Computation of the crust: an ETF approximation

Following our discussion in Subsec. 2.3.2, the energy density of the spherical Wigner-Seitz cell, $\mathcal{E}_{WS}$ is given by (2.24), which we rewrite below for clarity

$$\mathcal{E}_{WS} = \frac{1}{V_{WS}} \int_0^{R_{WS}} 4\pi r^2 dr\, \mathcal{E}_B(n(r), n_p(r)) + \mathcal{E}_{Coul} + \mathcal{E}_e + [\overline{n}_p m_p + (n_B - \overline{n}_p) m_n] c^2 \quad (5.1)$$

We focus here on the baryonic contribution $\mathcal{E}_B$, while the Coulomb and the electron gas kinetic contributions are those reported in Eq.s (2.25) and (2.12). The expression of $\mathcal{E}_B$, for the Skyrme EOS, is given by Eq. (1.52).

As explained above, in the ETF approximation [185, 189] one writes the kinetic and spin densities τ and J Eq.s (1.42) as a function of the single particle densities n. The kinetic density reads

$$\tau = \sum_{q=n,p} \frac{3}{5} \left(3\pi^2\right)^{2/3} n_q^{5/3} + \tau_{q,2}^{L} + \tau_{q,2}^{NL} \quad (5.2)$$

where the local and non local contributions $\tau_{q,2}^{L}$ and $\tau_{q,2}^{NL}$ are

$$\begin{aligned}\tau_{q,2}^{L} =& \frac{1}{36}\frac{(\nabla n_q)^2}{n_q} + \frac{1}{3}\Delta n_q,\\ \tau_{q,2}^{NL} =& \frac{1}{6}\frac{\nabla n_q \cdot \nabla f_q}{f_q} + \frac{1}{6}n_q\frac{\Delta f_q}{f_q} - \frac{1}{12}n_q\left(\frac{\nabla f_q}{f_q}\right)^2\\ &+ \frac{1}{2}\left(\frac{2m}{\hbar^2}\right)^2 n_q \left(\frac{W_q}{f_q}\right)^2\end{aligned} \tag{5.3}$$

and the effective mass $f_q = m/m_q^*$ is given by Eq. (1.44). The spin density reads

$$J_q = -\frac{2m}{\hbar^2 f_q} n_q W_q, \tag{5.4}$$

where the spin-orbit potential W_q

$$\begin{aligned}W_q =& -\left(C_0^{\nabla J} + C_1^{\nabla J}\right)\nabla n_q - \left(C_0^{\nabla J} - C_1^{\nabla J}\right)\nabla n_{\bar{q}}\\ &+ \left(C_0^{J} + C_1^{J}\right) J_q + \left(C_0^{J} - C_1^{J}\right) J_{\bar{q}}\end{aligned} \tag{5.5}$$

where $\overline{q}$ is the opposite nucleonic species. The relation between the spin currents J_n and J_p and the gradient of the densities is thus given by the solution of the 2×2 system of linear equations

$$\begin{aligned}&\left(\frac{\hbar^2}{2m}f_q + \left(C_0^{J} + C_1^{J}\right) n_q\right) J_q + \left(C_0^{J} - C_1^{J}\right) n_q J_{\bar{q}}\\ &= \left(C_0^{\nabla J} + C_1^{\nabla J}\right) n_q \nabla n_q + \left(C_0^{\nabla J} - C_1^{\nabla J}\right) n_q \nabla n_{\bar{q}}.\end{aligned} \tag{5.6}$$

We do not solve the full variational problem in r-space since it would be too lengthy to implement in a Bayesian framework; instead, we use parametrized Woods-Saxon profiles for the local total baryonic and proton densities:

$$\begin{aligned}n(r) =& \frac{n_{cl}}{1 + \exp\left(\frac{r-R}{a}\right)} + \frac{n_g}{1 + \exp\left(-\frac{r-R}{a}\right)}\\ n_p(r) =& \frac{n_{cl,\,p}}{1 + \exp\left(\frac{r-R_p}{a_p}\right)}\end{aligned} \tag{5.7}$$

The ETF problem amounts to minimizing the energy density Eq. (5.1) with respect to 8 independent variables: $n_g, n_{cl}, n_{cl,p}, R, R_p, a, a_p, R_{WS}$. Such a minimization problem is still very numerically demanding for the Bayesian study of this work, where the crust has to be computed typically for some 10^4 different models to get convergent results. The number of independent variables can be reduced if we assume that the bulk isospin asymmetry $\delta = (n_{cl} - 2n_{cl,p})/n_{cl}$, i.e., the asymmetry at the center of the cluster, can be obtained from the pressure equilibrium condition between bulk matter at density n_{cl} and a homogeneous neutron gas at density n_g. Such a condition reads:

$$n^2 \left.\frac{\partial(\mathcal{E}_B(n,\delta)/n)}{\partial n}\right|_{n_{cl}} = P_g(n_g, \delta = 1) \tag{5.8}$$

where $\mathcal{E}_B$ is the energy density of homogeneous nuclear matter, and P_g is the pressure of the pure neutron gas. Since the equilibrium bulk density n_{cl} is expected to be close to the saturation density n_{sat} of symmetric nuclear matter [195], in Eq.(5.8) the function $\mathcal{E}_B$ can be expanded around this point giving an analytical expression of δ as a function of the nuclear matter parameters $K_{sat}, L_{sym}, K_{sym}$:

$$\delta = \sqrt{\frac{(n_{sat} - n_{cl})K_{sat} + (3n_{sat}/n_{cl})^2 P_g}{3L_{sym}n_{sat} - K_{sym}(n_{sat} - n_{cl})}} \tag{5.9}$$

From this, we immediately find the central proton density $n_{cl,p}$

$$n_{cl,p} = \frac{1-\delta}{2} n_{cl} \tag{5.10}$$

An extra reduction of the computational effort can be achieved by using the results of [188], where the authors performed extensive Woods-Saxon fits of Hartree-Fock (HF) profiles in the density and asymmetry conditions typical of the inner crust. They showed that the diffuseness parameters a, a_p follow an approximate quadratic law with the bulk asymmetry, and proposed a quasi-universal parametrization with an optimal fit:

$$\begin{aligned} a &= 0.54 + 1.04 \times \delta^2 \\ a_p &= 0.53 + 0.33 \times \delta^2 \end{aligned} \tag{5.11}$$

Using Eqs. (5.9), (5.10), and (5.11), the ETF variational problem is reduced to a dimensionality $N = 5$, which is the same numerical cost as the CLDM minimization. Moreover, a one-to-one mapping can be established between the ETF residual variational variables (n_{cl}, n_g, R, R_p, R_{WS}) and the CLDM variational variables θ Eq. (2.20) (A_{cl}, I, n_{cl}, n_g, R_{WS}) used in [21].

The minimization of the energy density Eq. (5.1) with respect to the reduced variable set (n_{cl}, n_g, R, R_p, R_{WS}) (or the equivalent CLDM-like parameters (A_{cl}, I, n_{cl}, n_g, R_{WS})) leads to the optimal ETF profile only if the ansatz Eq.s (5.9), (5.10), and (5.11) are good approximations of the optimal values of $n_{cl,p}, a, a_p$. If indeed that is the case, then this mapping between CLDM and ETF variables allows us to use the same numerical code to compute the crust both in the CLDM and ETF formalisms, thus minimizing the technical problems that arise when different numerical structures are interfaced.

R_{WS}, n_{cl} and n_g are mapped identically into their ETF counterparts. The average proton density relates to the cell volume and the average cluster baryon number A and asymmetry I via $\overline{n}_p = Z/V_{WS} = A(1-I)/2/V_{WS}$. Concerning the radius parameters, they are mapped into effective CLDM-like variational variables through the following relations [259]:

$$R_{(p)} = R_{HS(,\mathrm{p})} \left(1 - \frac{\pi^2}{3} \left(\frac{a_{(\mathrm{p})}}{R_{HS(,\mathrm{p})}} \right)^2 \right), \tag{5.12}$$

where the hard-sphere radii are defined as [3]

$$\begin{aligned} R_{HS} &= \left(\frac{3}{4\pi} \frac{A}{n_{cl}} \right)^{1/3}, \\ R_{HS,\,p} &= \left(\frac{3}{4\pi} \frac{(1-I)A}{2n_{0,\,p}} \right)^{1/3}. \end{aligned} \tag{5.13}$$

[3]These radii define uniform spheres containing the same number of nucleons (or protons) as the diffused distribution and with the corresponding central density.

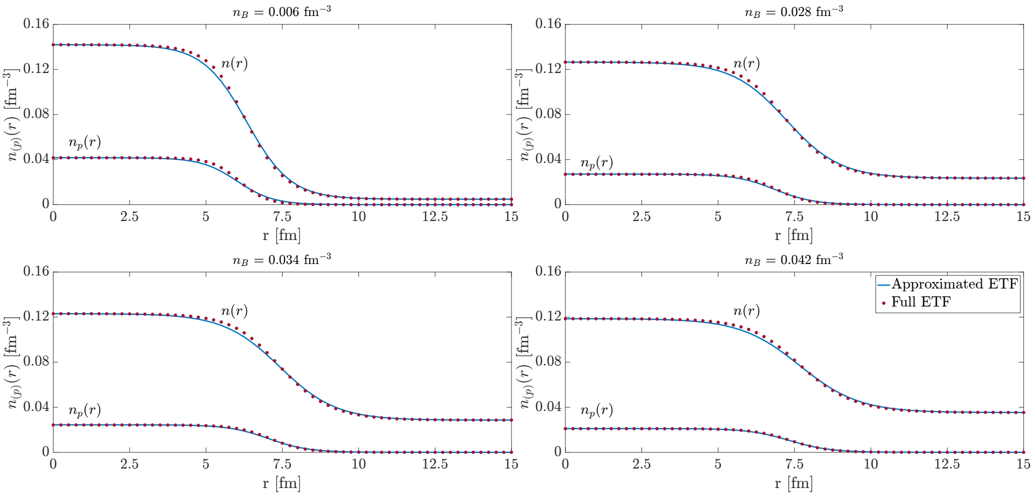

Figure 5.2: Comparison of the optimal Sly4 density profiles in the full ETF variation of Ref. [168] and the ones using approximate values for $n_{0\mathrm{p}}, a, a_\mathrm{p}$ from Eqs.(5.9),(5.11).

The crust computation thus follows the CLDM procedure described in Subsec. 2.3.2, with the energy density computed with Eq. (2.24).

We verified the validity of these approximations, Eq.s (5.9), (5.10), and (5.11) in two ways, employing as a benchmark the vastly tested SLy4 parametrization. First, we used the optimal profiles at various baryon densities from a well-tested ETF code for the crust [168], which minimizes the energy of the cell using exactly our same ansatz for the parametrized density profiles Eq. (5.7). From these profiles, we computed the correspondent values of the CLDM variables (A_{cl}, I, n_{cl}, n_g, R_{WS}), from which in turn we derived our estimation of the density profiles Eq. (5.7) parameters, following the prescriptions described above. The results for the SLy4 interaction at some representative densities in the inner crust are shown in Figure 5.2. The agreement is overall satisfactory, which shows that Eq.s (5.9), (5.11) give good estimations of $n_{0\mathrm{p}}, a, a_\mathrm{p}$ in the case of the optimal profile.

A stronger validation test consists of the direct comparison of the crust composition, found by our ETF approximation, with that of the full ETF [168]. Owing to the different numerical methods involved, larger discrepancies are expected than with the density profiles; nonetheless, a general satisfactory consistency is observed. Figure 5.3 shows the resulting optimal cell compositions, including A_{cl}, I, and related quantities, again for the benchmark comparison of the SLy4 model.

The crust computation starts at $n_B = 2.66 \times 10^{-4}$ fm^{-3}, the neutron drip density of the BSk24 interaction, and stops when the crust-core transition density n_{cc} Eq. (2.31) is found. Unfortunately, in the random generation of the EOS model for the Bayesian inference, the algorithm often encounters numerical instabilities and cannot find a solution to the system of equations at densities of about 0.06 fm^{-3}, where we still have $\Delta\mathcal{E} < 0$. It is possible to mitigate this problem by tuning the initial guesses for the minimisation procedure, refining the mesh in baryon densities, or implementing ad hoc back-stepping conditions. However, we have not been able to devise a model-independent solution that can be implemented in an automated procedure for our Bayesian study, namely a robust minimization procedure that works for all baryon densities and all instances of nuclear models we need to sample. We instead resorted to a linear extrapolation of the

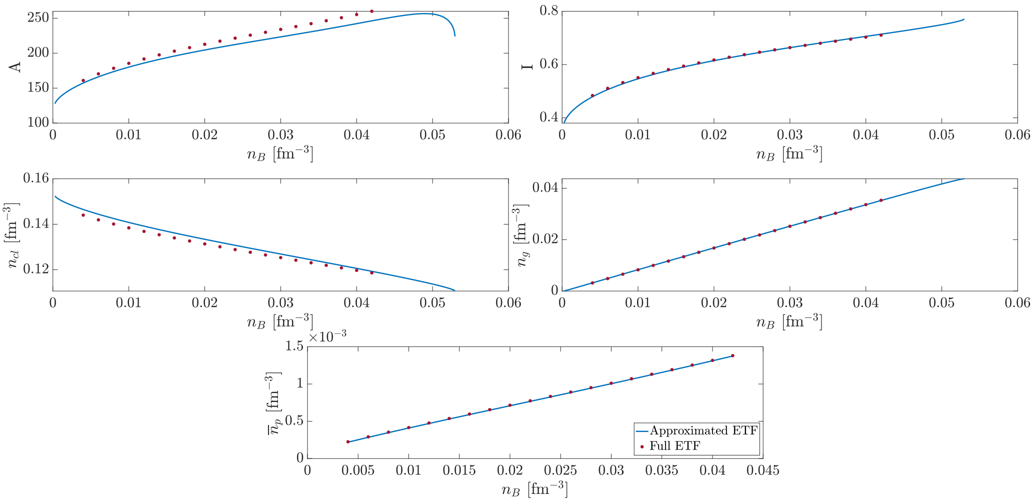

Figure 5.3: Comparison of the cell variational parameters obtained in this work, with the ones from ref.[168], in the case of the Sly4 interaction.

quantity $\Delta\mathcal{E}(n_B)$ to estimate the value of the CC transition density n_{cc}. The validity and limitations of this extrapolation are further discussed below and in Section 5.5.2. Once n_{cc} is determined, we can interpolate the energy density $\mathcal{E}$, the pressure P, the proton fraction y_p, and the free neutron gas density n_g. The first two are interpolated with a third-order polynomial, ensuring the continuity of $\mathcal{E}$ and P. On the other hand, y_p shows an almost linear relation with the baryon density, and so we interpolated it linearly. Finally, n_g, which at n_{cc} coincides with the total neutron density, is interpolated between the last five points of the crust and the first five of the core with a third-order polynomial. More details are given in Appendix D.2.

The extrapolation procedure is illustrated in Figure 5.4 for a representative model example (SkmSmpl2; see Appendix D.1 for details). In the figure, the blue line shows the energy density difference $\Delta\mathcal{E}$ as a function of the baryon density n_B from the ETF calculation: in this typical case, the computation stops slightly above 0.06 fm^{-3} (red point), while the dotted line represents the extrapolation, and the red star marks the estimated n_{cc}. For comparison, the dashed grey line shows $\Delta\mathcal{E}$ computed using the CLDM[4]. The ETF curve closely resembles the CLDM one in shape, and the trend appears approximately linear in the region where the ETF calculation breaks down, which supports the validity of the extrapolation procedure.

Another validation test is presented in Table 5.1, which reports different n_{cc} calculations for the widely employed Skyrme functional SLy4 [73], and compares them with our estimated value. We can see that the linear extrapolation leads to an agreement with the full ETF result of [194, 262, 263] within $\approx 2\%$. We can also see that the CLDM predictions are affected by a considerable dispersion, due to the different possible surface energy representations in that classical approach. Even within this dispersion, in the case of the Sly4 model, the more microscopically funded ETF formalism tends to produce slightly higher values for the CC transition point. The dependence on the nuclear model will be studied in detail in Section 5.5.2.

[4]All CLDM calculations in this work are performed using the code developed in [21], to which we refer for implementation details.

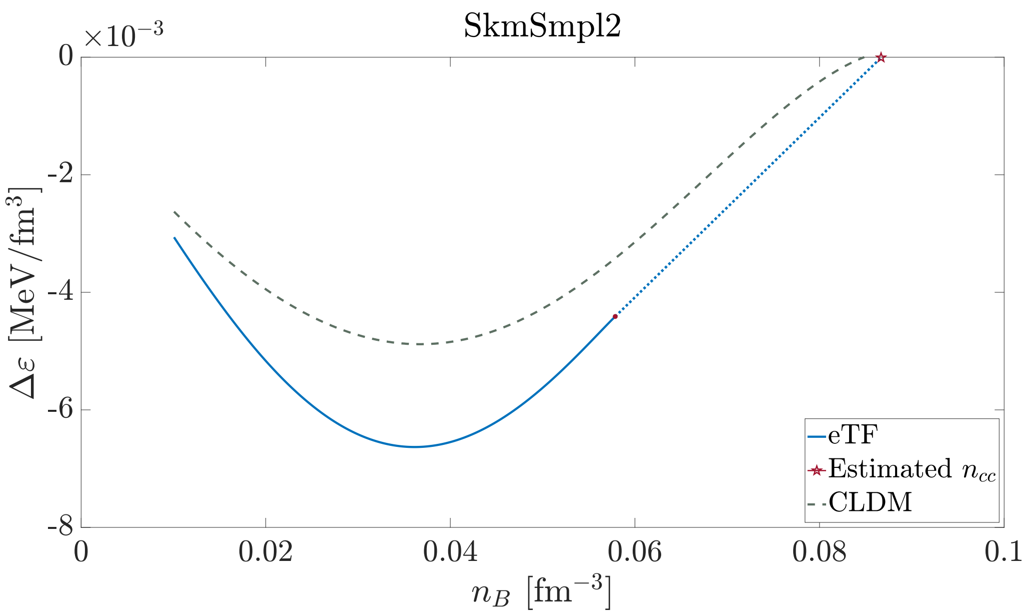

Figure 5.4: Difference in energy density $\Delta\mathcal{E}$ between the homogenous and clusterized phase, as a function of the baryon density n_B, for the sampled Skyrme interactions SkmSmpl2. The blue line is the ETF computation, while the grey dashed one is its CLDM counterpart. The red dot marks when the ETF computations fail; the linearly guessed n_{cc} is marked with a red star.

Table 5.1: Crust-Core transition for SLy4 interaction with different computational strategies.

Strategy	Source	n_{cc} [fm^{-3}]
CLDM	[177]	0.073-0.083
CLDM	[260]	0.072
CLDM	[261]	0.076
CLDM	[21]	0.081
Spinodal (thermodynamical)	[190]	0.089
Spinodal (dynamical)	[190]	0.080
Full ETF	[194]	0.081
Full ETF	[262, 263]	0.082
ETF	this work	0.083

Table 5.1 also reports the CC transition density obtained with two other methods widely employed in the literature, the thermodynamical and dynamical spinodal instability boundaries [190]:

- The thermodynamical spinodal corresponds to the instability point of neutral nuclear matter undergoing the nuclear liquid-gas phase transition. It provides an upper bound to the physical instability of homogeneous $npe\mu$ matter to cluster formation, due to the absence of finite-size (surface and Coulomb) effects [123]. These effects are included in the dynamical spinodal calculation, which determines when matter becomes unstable against finite-size density fluctuations, that is, against the clusterization of matter in the presence of a uniform electron background [190, 193].

- The dynamical spinodal can be considered a lower limit to the CC transition point, since in a first-order phase transition, the unstable region is systematically contained within the coexistence region, and the crust formation timescale is expected to be sufficiently long for metastable homogeneous fluid matter to evolve into solid crustal matter [15].

As seen in Table 5.1, in the case of Sly4, our extrapolated ETF result aligns with these qualitative considerations. Among the various methods used in the literature to define the crustal EOS and the CC transition point, explicit crust modelling with microscopic many-body approaches (HFB [257] or its semi-classical counterpart, ETF) is considered the most accurate. However, concerning the determination of the CC point, we cannot exclude a possible bias introduced by the linear extrapolation of our ETF results. For this reason, we adopt the ETF method to compute the crust and its EOS, but also consider the CLDM and the spinodal definition in determining the crustal properties in Section 5.5.

5.3 Mapping of Skyrme into the meta-model

As far as homogeneous EOS properties are concerned, the Skyrme parameter set allows to independently vary only five NMPs (n_{sat}, E_{sat}, K_{sat}, E_{sym}, and L_{sym}) (see above Sec. 4.1). The higher order derivatives $Q_{sat,sym}$, $Z_{sat,sym}$, and K_{sym}, crucial for describing nuclear matter at high-density, are therefore not free parameters but rather a function of those five. On the other hand, the MM Eq. (2.43) parameters are the ten NMPs up to fourth order, the effective isoscalar and isovector masses, and the b parameter.

The five free NMPs (n_{sat}, E_{sat}, K_{sat}, E_{sym}, and L_{sym}), as well as the two effective masses m_0^* and m_1^* (isoscalar and isovector), are mapped exactly in their MM counterparts; K_{sym}, pivotal for the sound speed, will be computed following the Skyrme formulae (see Appendix B). While this does not decouple K_{sym} from the other parameters, it ensures the continuity of the sound speed in the star medium. As for $Q_{sat,sym}$ and $Z_{sat,sym}$, we use the Skyrme ones if the baryon density is below saturation; otherwise, we employ randomly picked values, which we will mark with a *. This way, we keep the behaviour of the Skyrme equations of state at low densities, where they were fitted, while allowing more freedom at high densities. A word of caution: although we bridge all the information coming from nuclear experiments on the nEOS, we also introduce the limitations imposed by Skyrme lack of flexibility for the description of PNM at subsaturation densities, which is pivotal for the modeling of NS crusts.

To illustrate the procedure, Figure 5.5 shows three possible MM representations for a randomly selected Skyrme interaction from the final result of Section 4.3, which we call "SkmSmpl1". Its parameters are given in Appendix D.1. The solid line represents

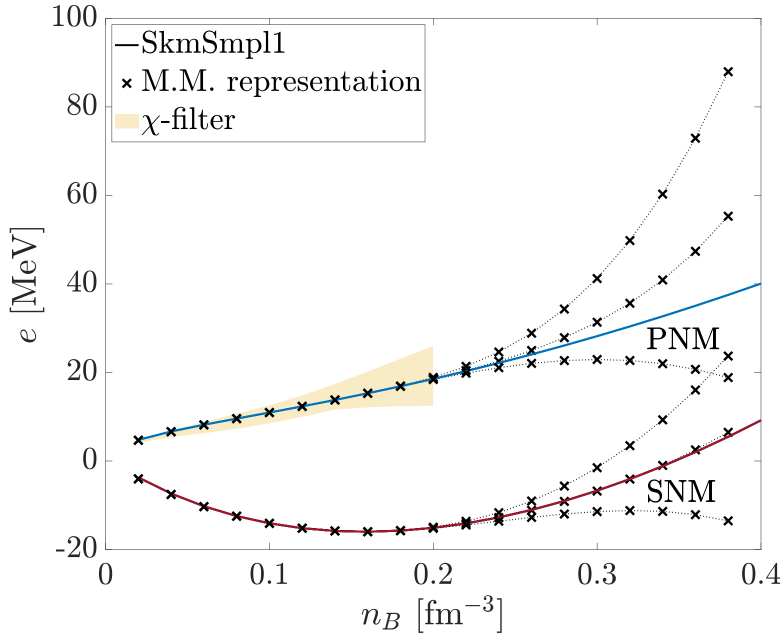

Figure 5.5: Mapping of SkmSmpl1 EOS (line) into three different possible realizations of the MM (black crosses) for symmetric nuclear matter (SNM, in red) and pure neutron matter (PNM, in blue); see text for details. The yellow region delimits the 90% interval of the region predicted by ab-initio calculations employing chiral interactions, taken from [241].

the Skyrme nuclear EOS, in red for symmetric nuclear matter (SNM) and blue for pure neutron matter (PNM). The black crosses are the corresponding quantities computed with the three MM representations of SkmSmpl1, as prescribed above. Up until 0.2 fm^{-3} they are almost identical (indeed, they are the same below n_{sat} as we employ SkmSmpl1 $Q_{sat,sym}$ and $Z_{sat,sym}$) and faithfully reproduce the Skyrme EOS; at higher densities, they diverge due to the different $Q_{sat,sym}$ and $Z_{sat,sym}$ parameters.

5.4 Bayesian setup

Similarly to Section 4.2, we now turn to the details of our Bayesian inference: the prior distribution and the likelihood.

As mentioned above, the former is the posterior displayed in Figure 4.5, complemented with flat priors for the high-density parameters $Q^*_{sat,sym}$ ans $Z^*_{sat,sym}$, which were not present in the first analysis (see Table 5.2 for a summary).

For the latter, we assigned to the parameter extraction θ a likelihood $\mathcal{L}_{tot}(\theta)$, which is the product of four independent likelihoods, $\mathcal{L}_{tot} = \prod_i \mathcal{L}_i$. The $\mathcal{L}_i$s encode the information from different independent physical constraints:

1. $\mathcal{L}_{\mathrm{J0740}}$ is informed by the largest NS masses measured with high precision; we use that of pulsar PSR J0740+6620 from [16], $M_{max} = (2.08 \pm 0.07)M_\odot$;

2. $\mathcal{L}_{\mathrm{LVC}}$ concerns the Ligo-Virgo collaboration tidal deformability measurement from the GW170817 event[5] [20];

[5] We employ $\tilde{\Lambda}$ and q posteriors found with the PhenomPNRT waveform.

Table 5.2: Prior distribution for the parameters. We marked with a * those parameters whose prior comes from the posterior distribution depicted in Figure 4.5. For the others, we give the limits of this interval are shown.

n_{sat}	[fm^{-3}]	*
E_{sat}	[MeV]	*
K_{sat}	[MeV]	*
Q_{sat}	[MeV]	*
Z_{sat}	[MeV]	*
Q^*_{sat}	[MeV]	[-2000,2000]
Z^*_{sat}	[MeV]	[-3000,3000]
E_{sym}	[MeV]	*
L_{sym}	[MeV]	*
K_{sym}	[MeV]	*
Q_{sym}	[MeV]	*
Z_{sym}	[MeV]	*
Q^*_{sym}	[MeV]	[-4000,4000]
Z^*_{sym}	[MeV]	[-5000,5000]
m^*_0	[-]	*
m^*_1	[-]	*
W_0	[MeV fm^5]	*
G_0	[MeV fm^5]	*
G_1	[MeV fm^5]	*

3. $\mathcal{L}_{\text{NICER}}$ includes the joint inferences of the mass and radius of a NS by the NICER mission [18, 157–159];

4. $\mathcal{L}_\chi$ measures the consistency between the energy per nucleon of neutron matter of the sampled model with the χ-EFT chiral band presented in [241] from a compilation of different ab-initio calculations, a band which is considered as a 90% confidence interval. It is depicted as the yellow region in Figure 5.5.

Due to the nature of these constraints, a simple Gaussian likelihood, like the one we employed for our previous Bayesian inference, Eq. (4.7), would not be appropriate.

For the maximum mass, we impose a cumulative distribution function of a normal distribution

$$\mathcal{L}_{J0740}(\theta) = \frac{1}{0.07\sqrt{2\pi}} \int_{-\infty}^{M_{\max}(\theta)/M_\odot} \exp\left(-\frac{1}{2}\frac{(x-2.08)^2}{0.07^2}\right) dx \tag{5.14}$$

With this formulation, we do not impose a hard cut on the maximum mass, but rather allow for models that almost reach the observed M_{max} to stay in the analysis.

The information from GW170817 comes from the inferred joint probability distribution p_{LVC} of $(\tilde{\Lambda}, q)$ depicted in Figure 2.6. We chose the likelihood as the integral

$$\mathcal{L}_{LVC}(\theta) = \int_{0.73}^{1} p_{LVC}(\tilde{\Lambda}(q), q)\, dq \simeq \sum_{q_i=0.73}^{1} p_{LVC}\left(\tilde{\Lambda}\left(q_i\right), q_i\right) \tag{5.15}$$

where the relation $\tilde{\Lambda}(q_i)$ is determined by the solution of Eq. (2.5), which depends on the EOS. As q is the ratio of the lighter star mass to the heavier, it naturally is lower than 1, while 90% of the distribution is contained above 0.73 [20].

Table 5.3: Values of $e_m^\chi(n)$ and $e_M^\chi(n)$ for the $\mathcal{L}_\chi$.

n_B [fm^{-3}]	$e_m^\chi(n)$ [MeV]	$e_M^\chi(n)$ [MeV]
0.02	4.10	4.69
0.04	5.37	6.92
0.06	6.28	8.83
0.08	7.24	10.65
0.10	8.51	12.57
0.12	9.97	14.84
0.14	11.61	17.44
0.16	12.11	20.22
0.18	12.38	23.13
0.20	12.43	26.00

The information from the NICER mass radius measurements is incorporated similarly in the respective likelihood

$$\mathcal{L}_{NICER}(\theta) = \prod_N \int p_N\left(M, R(M)\right) dM \simeq \prod_N \sum_{M_i} p_N\left(M_i, R(M_i)\right) \tag{5.16}$$

where p_N are the $M - R$ probability distributions depicted in Figure 2.4b, and N runs over all four measurements available. The relation $R(M_i)$ is found by solving the TOV equations Eq. (2.1), and depends strictly on the EOS.

Finally, the χ filter is implemented as a trapezoidal Gaussian. It reads

$$\mathcal{L}_\chi(\theta) = \prod_n \begin{cases} \exp\left(-\dfrac{(e(n) - e_m^\chi(n))^2}{2\sigma_\chi(n)^2}\right) & e(n) \in (-\infty, e_m^\chi(n)) \\ 1 & e(n) \in (e_m^\chi(n), e_M^\chi(n)) \\ \exp\left(-\dfrac{(e(n) - e_M^\chi(n))^2}{2\sigma_\chi(n)^2}\right) & e(n) \in (e_M^\chi(n), \infty) \end{cases} \tag{5.17}$$

where the product runs over 10 baryon densities $n = 0.02, \ldots, 0.20$ fm^{-3}, $e_m^\chi(n)$ is the lower limit of the allowed region at baryon density n, $e_M^\chi(n)$ is the upper limit, and $e(n)$ is the model energy per particle of neutron matter. The error $\sigma_\chi(n)$ ensure that the under the tails lies 10% of the total probability

$$\sigma_\chi(n) = \frac{e_M^\chi(n) - e_m^\chi(n)}{9\sqrt{2\pi}} \tag{5.18}$$

The values of $e_m^\chi(n)$ and $e_M^\chi(n)$ are reported in Table 5.3.

Instead of resorting to the Metropolis-Hastings algorithm, we compute the posterior distribution with a different sampling technique. We extract 10^5 models from the prior distribution, assigning to each Skyrme a single random set of $Q^*_{sat,sym}$ and $Z^*_{sat,sym}$. We then calculate $\mathcal{L}_\chi$, as it is much faster to compute than the other likelihoods. For all those models whose $\mathcal{L}_\chi > 10^{-10}$, we compute the relative neutron star EOS. We discard all the models for which the computation is unsuccessful, i.e., those for which the EOS is unstable and acausal. The distribution of successful models, weighted with the total likelihood $\mathcal{L}_{tot}$, will be our final result, the posterior distribution [6].

[6] For those models whose $\mathcal{L}_\chi < 10^{-10}$, we simply put $\mathcal{L}_{tot} = 0$.

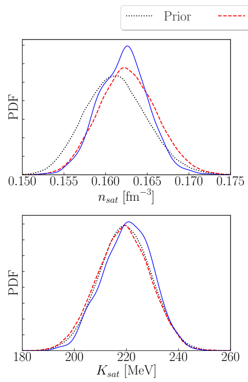

(a) Isoscalar parameters

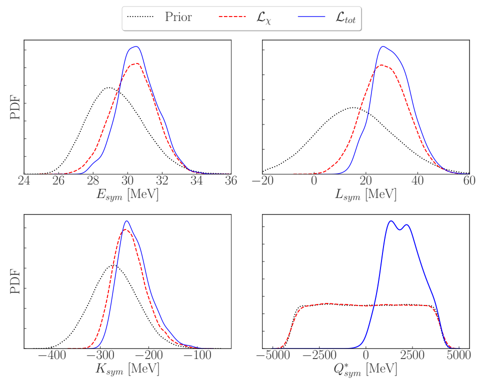

(b) Isovector parameters

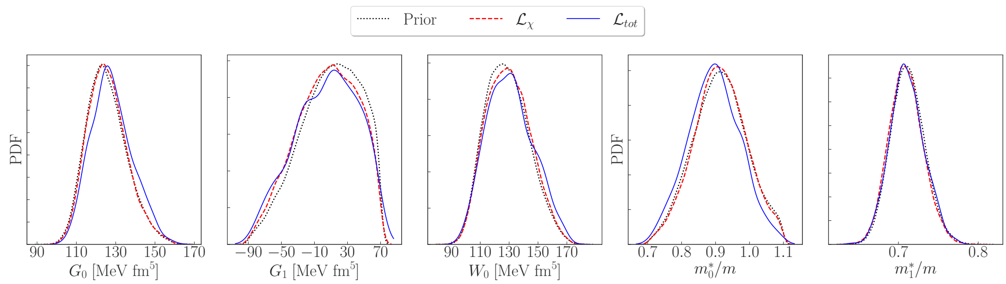

(c) Surface parameters

(d) Effective mass parameters

Figure 5.6: Nuclear matter parameters marginalized priors and posteriors. Bulk isoscalar (a), bulk isovector (b), surface and spin-orbit (c), and effective masses (d) parameters are shown.

5.5 Results

5.5.1 Nuclear matter parameters

In Figure 5.6, we show the marginalized posterior distributions of the different parameters of the Skyrme-metamodel. The current constraints bear no information on the fourth-order parameters $Z^*_{sat,sym}$, so we omitted them in the figure. The dotted black lines correspond to the marginalized prior informed by nuclear experiments, last row of Figure 4.3, while the dotted red ones represent the prior weighted only with $\mathcal{L}_\chi$, which is additionally informed by the chiral calculations; finally, the solid blue line shows the marginalized full posteriors that also includes the astrophysical information.

Looking at the isoscalar parameters in the upper left part, we see that prior and posterior distributions are very similar, except for Q^*_{sat}, which is shifted by the astrophysical constraints toward the positive side of its agnostic prior distribution. This indicates that the isoscalar sector is already well constrained by nuclear physics data, except at high densities, where the requirement to support the gravitational pressure of very massive NSs leads to a stiffening of the EOS, and consequently to positive values for both Q^*_{sat} and Q^*_{sym}.

The complementarity of the information provided by nuclear theory and nuclear experiments is clearly visible in the low-order isovector bulk parameters (upper right panels of Figure 5.6). While the information from nuclear experiments is compatible with the

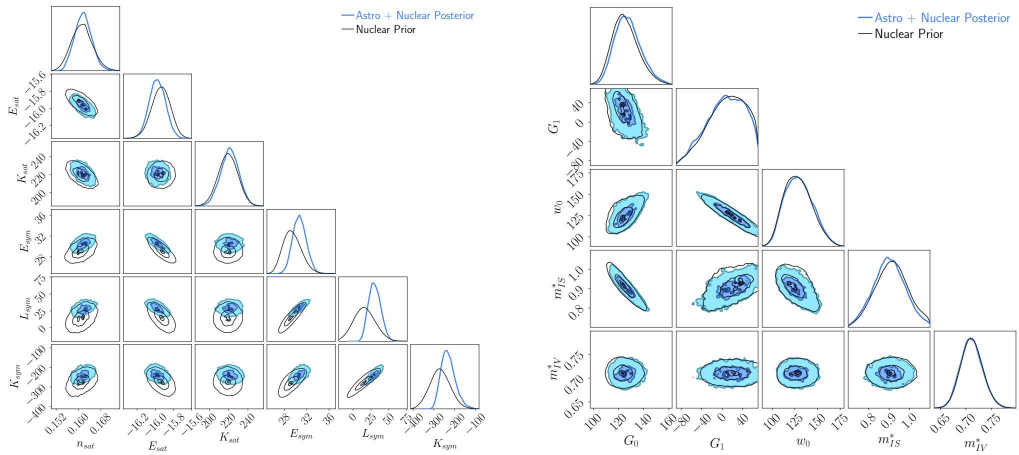

(a) Bulk parameters **(b)** Surface and effective mass parameters

Figure 5.7: Corner subplots of the bulk (left part) and surface and effective mass (right part) parameters. Black lines and contours: prior. Blue lines and contours: posterior including both nuclear and astrophysical constraints. Other possible correlations were not significant and are therefore not shown.

chiral constraint, the latter leads to a sharper definition of the parameters and an average shift toward higher values. The peak of the E_{sym} distribution increases from 29 MeV to almost 31 MeV, while the L_{sym} most probable value shifts from ~ 15 MeV to ~ 30 MeV. Interestingly, the application of the astrophysical constraints only induces minor modifications to these distributions, highlighting the strong predictive power of nuclear theory for extremely neutron-rich matter. The posterior distribution of K_{sym} is also shifted to higher values compared to the nuclear experiments informed prior, but little can be concluded from this, since K_{sym} is not an independent parameter in Skyrme interactions (see the discussion above in Section 5.3).

The lower part of Figure 5.6 shows the isoscalar and isovector surface parameters of the Skyrme interaction, G_0 and G_1, the spin-orbit coupling W_0, and the two effective masses m_0^*, m_1^*. These parameters are already well constrained by the nuclear structure inference ("prior" curves in Figure 5.6, which are the same as Figure 4.5), and we observe that none of the additional constraints modifies their distributions. This indicates that the requirement of supporting the crust does not impose further constraints on the nuclear models.

Unfortunately, at the present time, we are not able to disentangle the effects of the astrophysical constraints from those of the chiral filter. As mentioned in Section 5.4, $\mathcal{L}_\chi$, defined in Eq. (5.17), is much faster to compute than the astrophysical likelihoods. For this reason, we only computed the NS EOS of those models whose $\mathcal{L}_\chi$ was larger than 10^{-10}, and not for the rest. In this way, we gave up singling out the effect of the astrophysical constraints on the results in order to considerably improve the efficiency of the computation. However, in a recent Bayesian study whose methodology is very similar to ours [21], the effects of the astrophysical constraints were studied independently from the chiral filter. From their investigation, it can be seen that the astrophysical constraints have little effect on E_{sym} and L_{sym}, opposed to the chiral computations; K_{sym}, on the other hand, is impacted by both.

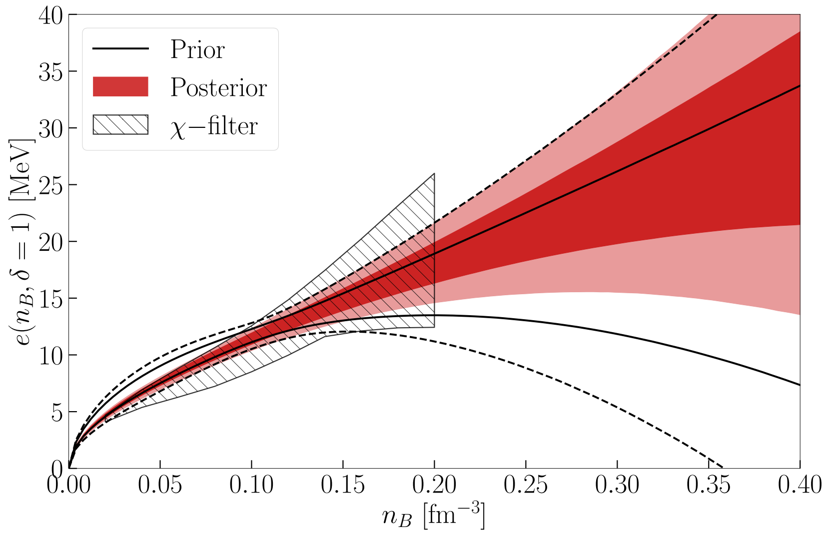

Figure 5.8: Posterior of the energy per particle of PNM, $e(n_B, \delta = 1)$. The full (dotted) black lines enclose the 68% (95%) confidence interval of the energy computed on the prior, which corresponds to the nuclear posterior of Chapter 4. The red band is the posterior, i.e., the prior distribution weighted with $\mathcal{L}_\chi$ Eq. (5.17). The darker red corresponds to the 68% confidence interval, while the lighter red to the 95%. The hatched region delimits the 90% interval of the region predicted by ab-initio calculations employing chiral interactions, taken from [241].

In Figure 5.7, we show selected corner plots illustrating the most relevant correlations among the bulk and surface model parameters. The additional information preserves all correlations imposed in the prior by experimental nuclear observables from ab-initio calculations and observational constraints, but the parameter estimation is significantly narrowed in the isovector sector.

We can also control whether the χEFT theoretical computations are in tension with our nuclear prior. We illustrate our analysis in Figure 5.8. To do it, we compute the PNM energy per particle $e(n_B, \delta = 1)$ for each prior sample: the full (dotted) black lines enclose the 68% (95%) confidence interval for the PNM EOS as a function of the baryon density n_B. Weighing this distribution with the χEFT likelihood Eq. (5.17), we get the posterior, in red: the darkest region corresponds to the 68% confidence interval, while the lighter to the 95%. The hatched region is the depiction of the 90% confidence interval of the χEFT computations presented in [241]. It is important to specify that, for this case only, the PNM EOS was computed entirely with the Skyrme nEOS Eq. (1.61), and not with its MM equivalent. At the prior level, there is a significant superposition with the $\chi-$band around saturation, although at low densities, $n_B < 0.1$ fm^{-3}, where the χEFT calculations are more reliable and thus the hatched region is narrower, the Skyrme models tend to overestimate the energy per particle. This confirms that the experimental constraints are partially compatible with the theoretical predictions. In our case, the value of $\mathcal{L}_\chi$ is maximum, i.e., the nEOS of PNM is always within the chiral band, for approximately 20% of our models. The posterior distribution is instead squashed into the hatched region, thus becoming highly compatible with [241].

Table 5.4: Median value and 68% confidence interval limits of the crust-core transition density n_{cc} and the pressure at transition P_{cc}, for the three different estimation methods.

	ETF	CLDM	Spinodal
n_{cc} [fm^{-3}]	$0.092^{+0.010}_{-0.009}$	$0.095^{+0.009}_{-0.008}$	$0.082^{+0.006}_{-0.006}$
P_{cc} [MeV fm^{-3}]	$0.525^{+0.079}_{-0.083}$	$0.533^{+0.054}_{-0.067}$	$0.418^{+0.044}_{-0.054}$

5.5.2 Crust-Core transition point

The Bayesian posterior for the CC transition point is shown in Figure 5.9, where we show the joint probability distribution of the CC transition density n_{cc} and the corresponding pressure P_{cc}, along with the marginalized distributions obtained using the different methods (ETF, CLDM, and dynamical spinodal) described in Section 5.2. In Table 5.4 we report the median value and 68% confidence interval of the distributions.

The ETF estimation exhibits a tail at high transition densities, $n_{cc} \gtrapprox 0.11$ fm^{-3}, as well as some outliers corresponding to values of n_{cc} significantly higher than those from CLDM or the spinodal. This is a spurious effect caused by the linear extrapolation used in the ETF to determine the transition point. This interpretation is justified by the fact that, for a minority of sampled models, the numerical solution of the ETF variational equations fails near the minimum of $\Delta\mathcal{E}$ (see Figure 5.4), leading the extrapolation to overestimate the transition density, sometimes substantially.

Apart from this bias, the distributions obtained with CLDM and ETF, and shown in the left part of Figure 5.9 are very similar. It might seem surprising that a simple approach like the CLDM yields results in reasonable agreement with ETF. However, it is important to recall that:

- The CLDM is informed by the same bulk parameter distributions as the ETF.

- Some level of consistency between surface and bulk parameters is ensured in our version of the CLDM, since its surface parameters are optimized on experimental nuclear masses [21].

- The CLDM method is affected by important uncertainties due to the different possible modelings of the surface energy (see Table 5.1). However, in the version used in the present paper and taken from [21], the parameter p governing the behavior of the surface energy at extreme isospin ratios is fixed to $p = 3$, a value suggested in the seminal CLDM papers [264, 265] to better comply with Thomas-Fermi calculations in slab geometry.

The right part of Figure 5.9 compares the ETF estimation of the CC transition point with that obtained from the dynamical spinodal instability [193]. Before comparing the CC transition obtained with the spinodal and ETF methods, we first comment on our results for the dynamical spinodal. A previous Bayesian study based on the spinodal criterion [266] reported significantly lower values, $n_{cc} = (0.071 \pm 0.011)$ fm^{-3} and $P_{CC} = (0.294 \pm 0.102)$ MeV fm^{-3}. That study incorporated the chiral constraint, but the surface parameters were constrained solely by a global fit to experimental masses using a classical approach. As a result, the posterior values reported in [266], $G_0 = 30 \pm 9$ and $G_1 = 115 \pm 143$, are in tension with the more robust estimates of Table 4.3, namely $G_0 = 125 \pm 10$ and $G_1 = 9 \pm 36$. This discrepancy underscores the importance of accurately determining the surface parameters when predicting the CC transition point.

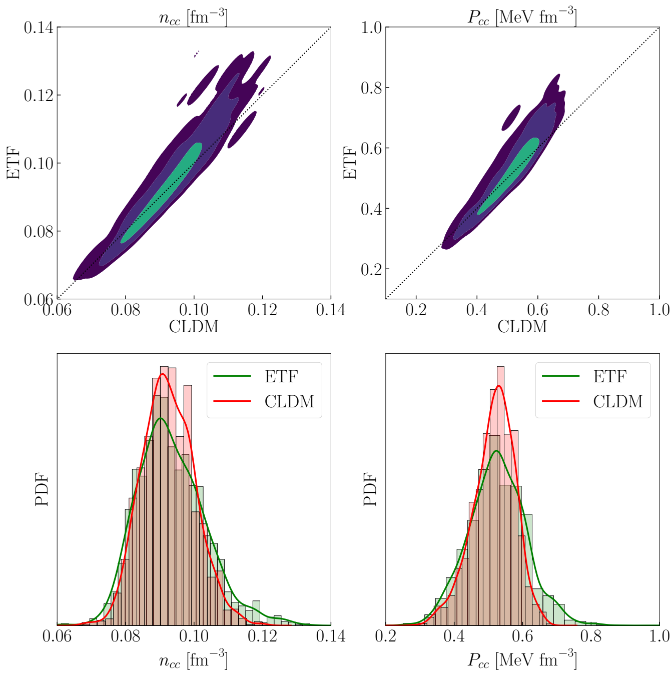

(a) ETF vs. CLDM

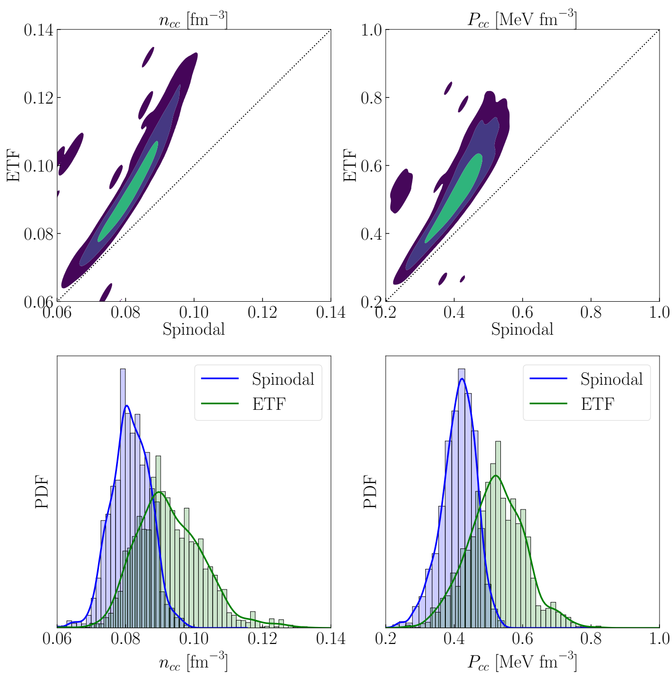

(b) ETF vs. Spinodal

Figure 5.9: Posterior of the CC density and pressure transition point obtained with different estimation methods. Upper panels: comparison between ETF (with linear extrapolation, see text) and CLDM. Lower panels: comparison with the dynamical spinodal definition.

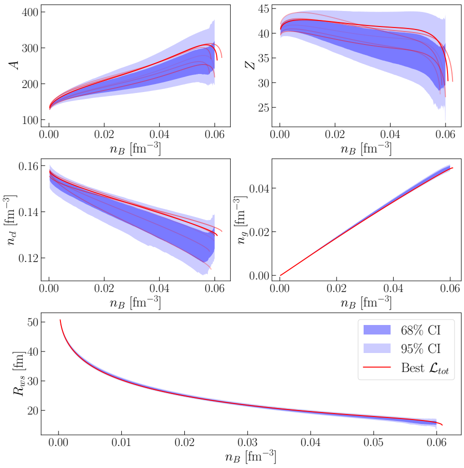

(a) Cluster mass number A_{cl} (upper left), atomic number Z (upper right), central density n_{cl} (middle left), gas density n_g (middle right), and Wigner-Seitz cell radius R_{WS} (lower panel).

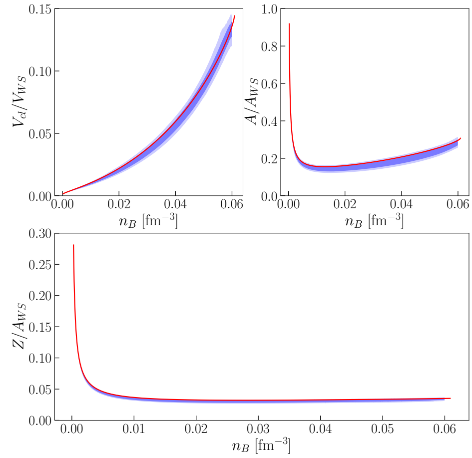

(b) Volume fraction occupied by the cluster in the cell (upper left), fraction of nucleons (upper right), and protons (lower panel).

Figure 5.10: Posterior distribution of the crust composition. At each baryon density n_B, the blue bands indicate the 68% and 95% confidence intervals. The red lines correspond to models with the highest $\mathcal{L}_{tot}$; opacity increases with increasing $\mathcal{L}_{tot}$.

Turning to the comparison between spinodal and ETF results, we observe that even with optimized surface parameters, the spinodal estimate underestimates both the dispersion and the mean values of the n_{cc} and P_{cc} posteriors. This is in qualitative agreement with the expectation that the spinodal criterion provides a lower bound to the transition point, as discussed in Section 5.2. We attribute the observed discrepancy to intrinsic physical differences rather than to the extrapolation of n_{cc}. The CLDM distributions of n_{cc} and P_{cc} are much closer to those of the ETF than to those of the spinodal instability. These findings highlight the need for a unified treatment of the EOS and explicit modelling of the inhomogeneous crust to determine the CC transition and related crustal properties reliably.

Finally, a validation of our approximation comes from another study [267], where the crust-core transition properties were investigated. There, the authors used extended Skyrme interactions to compute the energy of PNM, and employed the CLDM approach to model the NS crust, fitting its surface parameters to quantum 3D Hartree–Fock computations of the nuclei in the crust. They found for the transition density $n_{cc} = 0.092^{+0.018}_{-0.01}$ fm^{-3}, and for the pressure $P_{cc} = 0.48^{+0.27}_{-0.28}$ MeV fm^{-3}. They also investigated the crust-core transition under the lenses of the dynamical spinodal and found, again, similar results.

5.5.3 Crust properties

In Figure 5.10a, we present our results for the crust composition, obtained using the ETF variational method. We focus on five quantities that are sufficient to characterize the crust composition: the number of nucleons in the cluster A_{cl}, the number of protons Z, the nuclear density at the cluster center n_{cl}, the neutron gas density n_g, and the radius of the Wigner-Seitz cell R_{WS}. The plots are truncated at $n_B = 0.06$ fm^{-3}, as the information at $n_B > 0.06$ fm^{-3} is affected by a lack of statistics due to numerical issues in solving the system of variational equations.

It is interesting to observe that the best model lies at the edge of the 95% region for both A_{cl} and Z. While this may seem counterintuitive, we recall that $\mathcal{L}_{tot}$ is the product of four terms (see Section 5.4), none of which explicitly involves the crust. This explains why high-likelihood models are broadly distributed across the posterior and not clustered around their central region.

The crust composition's qualitative behavior as a density function is consistent with previous studies based on a more limited set of models and constraints [177, 268]. The progressive melting of clusters toward the core is indicated by an increasing cluster mass number A_{cl} and a decreasing central density n_{cl}, while the decrease in atomic number Z reflects the increasing neutron richness at higher densities imposed by beta equilibrium.

The specificity of our work lies in the ability to assess, from the Bayesian posterior, the residual model dependence of the crust composition after incorporating all available information from nuclear theory and experiment into the ETF formalism. In particular, we observe that the steadily increasing neutron gas density and the steadily decreasing linear size of the WS cell are quasi-universal features. Their predicted values closely match those obtained with the more sophisticated ETFSI formalism [168, 269], which accounts for proton shell effects within the Strutinsky approach.

A much stronger model dependence is instead observed for the cluster properties A_{cl}, Z, and n_{cl}. This is not surprising, given that the number of protons (nucleons) in the cluster accounts for no more than $\approx 3\%$ ($\approx 30\%$) of the total baryon number in the Wigner-Seitz cell, as we can appreciate in Figure 5.10b. This, combined with the nuclear physics uncertainties associated with neutron-rich nuclei, results in a high dispersion of the predictions. The smooth behavior of Z reflects the semiclassical nature of the ETF approximation, which does not account for shell effects. In contrast, the more microscopic ETFSI approach is known to stabilize specific Z numbers corresponding to shell closures over broad regions of the inner crust (typically $Z = 40$ [168]). Nevertheless, the dispersion arising from model dependence exceeds the impact of shell effects that are here neglected [172].

From an astrophysical perspective, the quantities of greatest interest are the crustal radius R_c and the crustal moment of inertia I_c, which are key parameters in simulations of NS cooling [150]. Both are linked to the crust-core transition properties: the first is mainly connected to the chemical potential, while the second to the pressure P_{cc}. The posterior distributions of these quantities are shown in Figure 5.11, based on the different definitions of the CC transition point introduced in Section 5.2 and for various NS masses. We focus in particular on relatively low masses, where the crust plays a more significant role.

We observe that the radius predictions from ETF and CLDM are very close, consistent with the compatible CC transition point values obtained in the two approaches, as shown in Figure 5.9. Conversely, the spinodal definition systematically yields lower values for both R_c and I_c, again due to the shift in the transition point.

Finally, the differences between the methods tend to diminish as the stellar mass increases, due to the reduced importance of the crust. The median value and 68% confidence interval of the distributions are reported in Table 5.5.

5.5.4 Glitch activity and moment of inertia of the inner crust

To account for the large glitch activity of the Vela pulsar (PSR J0835–4510), a substantial amount of angular momentum must be stored in the neutron star crust in the form of a

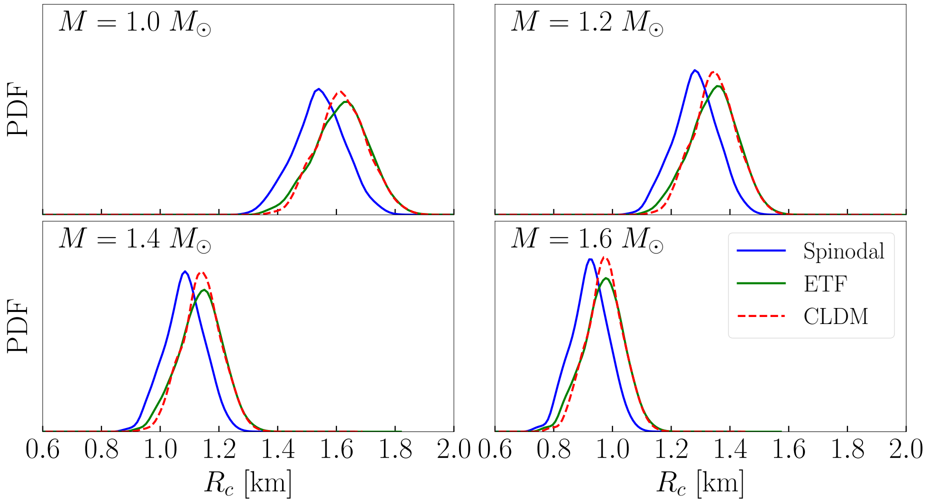

(a) Radius

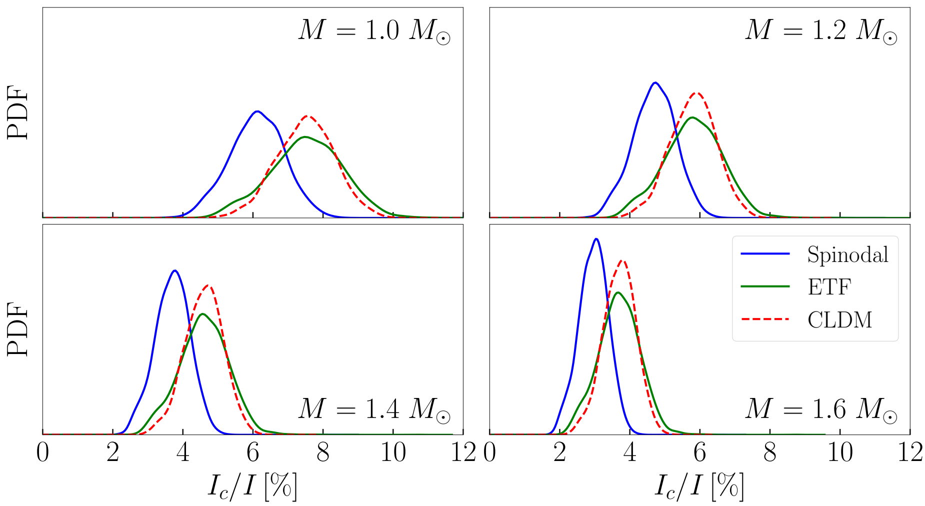

(b) Crust Moment of inertia

Figure 5.11: Posterior distributions of the crustal radius (left) and moment of inertia (right) for four different NS masses, using different definitions of the CC transition point: ETF (green), dynamical spinodal (blue), and the CLDM (dashed red).

Table 5.5: Median value and 68% confidence interval limits of the crust radius R_c and the fraction of the moment of inertia of the crust over the total I_c/I, for four different NS masses.

	M $[M\odot]$	ETF	CLDM	Spinodal
R_c [km]	1.0	$1.622^{+0.087}_{-0.095}$	$1.619^{+0.085}_{-0.088}$	$1.542^{+0.086}_{-0.084}$
	1.2	$1.349^{+0.077}_{-0.083}$	$1.349^{+0.074}_{-0.078}$	$1.282^{+0.076}_{-0.076}$
	1.4	$1.141^{+0.068}_{-0.079}$	$1.141^{+0.067}_{-0.071}$	$1.084^{+0.067}_{-0.069}$
	1.6	$0.973^{+0.062}_{-0.074}$	$0.974^{+0.061}_{-0.066}$	$0.924^{+0.060}_{-0.065}$
I_c/I [%]	1.0	$7.5^{+1.0}_{-1.0}$	$7.5^{+0.8}_{-0.9}$	$6.1^{+0.7}_{-0.8}$
	1.2	$5.8^{+0.8}_{-0.8}$	$5.8^{+0.6}_{-0.7}$	$4.7^{+0.6}_{-0.6}$
	1.4	$4.6^{+0.7}_{-0.7}$	$4.6^{+0.5}_{-0.6}$	$3.7^{+0.5}_{-0.5}$
	1.6	$3.7^{+0.6}_{-0.5}$	$3.7^{+0.4}_{-0.5}$	$3.0^{+0.4}_{-0.4}$

superfluid neutron current [256]. This is possible only if the superfluid component in the crust carries a sufficiently large fraction of the star's moment of inertia [149, 270–272]. The estimated minimum required fractional moment of inertia strongly depends on the proportion of neutrons entrained by the normal component, represented by the ion lattice [273]; see also [256] for a review. The strength of this entrainment phenomenon, which is an input for the hydrodynamic description of the inner crust [256, 274], remains a subject of debate, as it depends on the nuclear interaction, subtle neutron band structure, and pairing effects [273]. While a precise quantitative evaluation of the entrainment parameter is still under discussion (see [275–279] for recent developments) a minimal hypothesis is to assume that all and only the neutrons bound to the cluster are entrained, i.e., are locked to the normal component in the crust.

This hypothesis closely resembles the negligible entrainment scenario suggested by the recent revision of the entrainment strength in the inner crust by [279]. The number of unbound neutrons in each Wigner-Seitz cell can be estimated from the neutron gas density n_g as $N_{\text{unbound}} = n_g V_{WS}$, where V_{WS} is the cell volume [188, 280]. This assumption, which we refer to as "minimal entrainment", defines an upper bound on the moment of inertia I_n of the superfluid neutrons available to explain the large glitch activity of the Vela pulsar. It corresponds, essentially, to the early estimate of the moment of inertia fraction relevant for glitches proposed in the work of [270].

The dimensionless glitch activity parameter $\mathcal{G}$ quantifies, on average, the fraction of the star's spin-down that is reversed by glitches over long timescales [256]. For the Vela pulsar, different statistical methods yield a value of approximately $\mathcal{G}_{\text{Vela}} = 0.016 \pm 0.002$; see Table 1 in [149]. It can be shown that the moment of inertia I_n of the superfluid neutrons in the region responsible for glitches (assumed to be the inner crust) must satisfy

$$\frac{I_n}{I - I_n} > \mathcal{G}\,, \tag{5.19}$$

where I is the total moment of inertia of the star; see [256] for a discussion on how to include entrainment corrections in I_n.

In Figure 5.12 we show the posterior distribution of the quantity $I_n/(I - I_n)$ for different values of the star mass. If the zero entrainment hypothesis is retained, the glitch activity of the Vela pulsar is compatible with a crustal origin unless Vela's mass exceeds $\approx 2\,M_\odot$. Hence, Figure 5.12 can be seen as a Bayesian extension of the early result of [270].

For comparison, in Figure 5.12 we also include the case corresponding to a scenario with strong entrainment, which can be approximated by multiplying the value of $\mathcal{G}_{\text{Vela}}$

by a prefactor[7] of ~ 4.6. This value reflects the effect of strong entrainment on the fraction of neutrons available to store angular momentum during a glitch, as previously considered in [271, 272]. In this strong entrainment case, the constraint (5.19) can be satisfied only under the ETF definition of the CC transition point (panel b of Figure 5.12), and only if the mass of the Vela pulsar is very low ($M \lesssim 1.1\, M_\odot$), in accordance with [149]. Interestingly, under the less sophisticated crustal definition based on the spinodal instability criterion, the hypothesis of a crustal origin would be entirely ruled out in this case of strong entrainment.

5.5.5 EOS and Mass-Radius relation

We now turn to the posterior of the EOS and energy density of the star, shown in the left panel of Figures 5.14 (energy density) and 5.13 (pressure) as a function of the mass density ρ. The darker shades mark the 68% confidence region and the lighter shade the 95%.

Overall, the energy density $\mathcal{E}$ exhibits very weak dependence on the nuclear interaction, as evident from the narrow width of the distribution. At approximately four times n_{sat}, the spread increases, although, due to the scarcity of the models able to sustain those densities, the statistic is weaker.

For the pressure P, we plotted the model yielding the highest $\mathcal{L}_{tot}$, indicated by the red line, and the agnostic 90% confidence interval from the GW170817 tidal polarizability measurement by the LVC [164], indicated by dashed lines. The overall distribution is in good agreement with the agnostic LVC posterior but considerably thinner, thus highlighting the important information brought by nuclear physics theory and experiments. In the present work, only results from ab-initio nuclear theory and nuclear structure experiments are considered, which limits the laboratory information to relatively low densities. A more precise determination of the high-density behavior $n_B \gtrsim 2n_{sat}$ would require constraints from heavy-ion collision data [100]. The specific information brought by nuclear structure data can be appreciated from the right panel of Figure 5.13, which shows a zoom of the EOS and a comparison with the posterior probability distribution found in [21], whose methodology is very similar to ours, as explained above. The comparison between the two posterior distributions thus quantifies how the nuclear data information propagates into the knowledge of the neutron star EOS. We can see that in the present work, star matter is considerably soft near saturation, reflecting the overall low L_{sym} values predicted by the analysis (see Figure 5.6). Beyond n_{sat}, the EOS stiffens rapidly to support the maximum observed mass, and then softens again to coincide with the results of [21] at higher densities, where only general physical constraints such as stability and causality govern the MM predictions. The right panel of Figure 5.13 focuses on the pressure posterior in the star core. This time, we compare our findings with the results of [21], whose 68% and 95% confidence intervals are delimited with dashed and continuous black lines. The stiffening of the equation of state is evident between one and two saturation densities.

In general, we can observe concavities in the EOS when there are mild tensions among different experimental data. For instance, in [210] one can observe a peculiar behaviour of the function $P(\rho)$, which is quite steep until saturation, and softens afterwards. It is worth noting that in their work, they give much weight to the PREX-II data, which demands a high L_{sym} parameter, incompatible with both GW170817 [41] and the two more recent

[7] Multiplying $\mathcal{G}$ by a prefactor (equal to 1 in the case of zero entrainment) is a simple and practical approximation to estimate the potential impact of entrainment. However, this prefactor is not universal in principle: it can vary across different nuclear models and stellar masses. More accurate treatments, and the basis for this approximation, are discussed in [149, 256, 281].

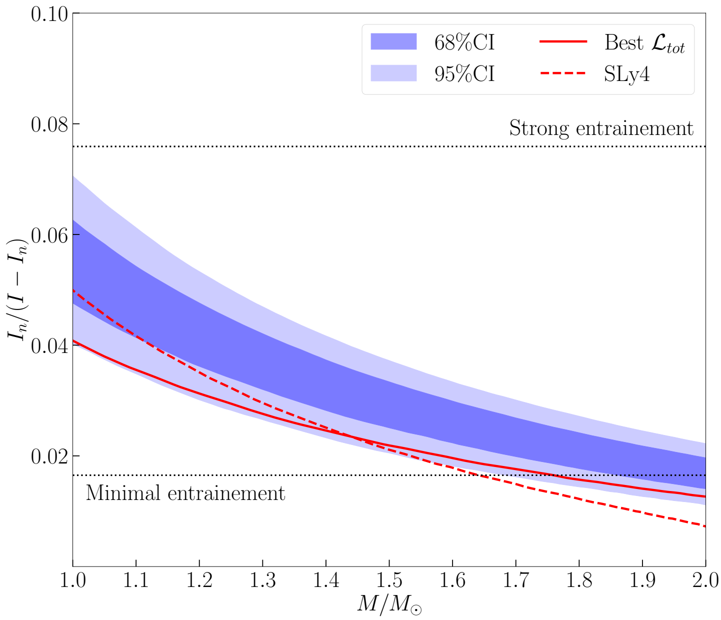

(a) Spinodal

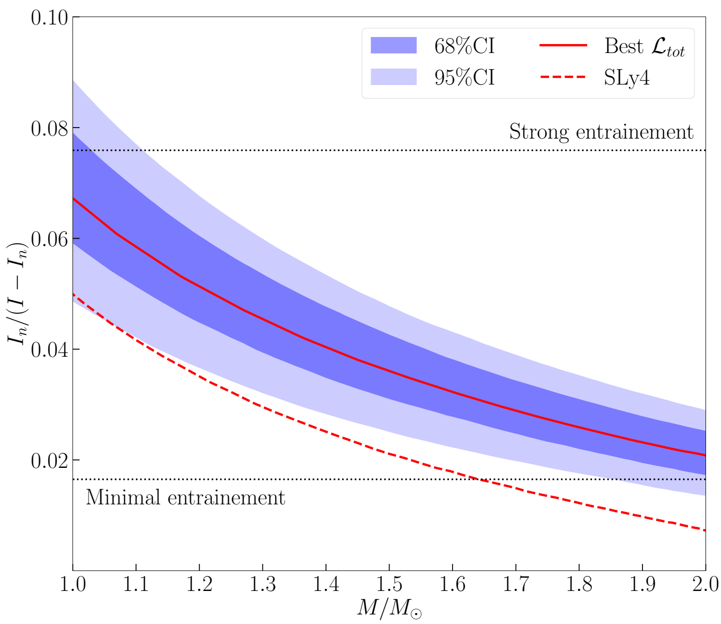

(b) Linear

Figure 5.12: Posterior of the ratio in (5.19) as a function of the stellar mass, using the CC transition point defined via the dynamical spinodal (left) or the ETF crust calculation (right). The darker (lighter) blue bands represent the 68% (95%) confidence intervals. The solid (dashed) red line corresponds to the model with the highest $\mathcal{L}_{tot}$ (the Sly4 model [73]). For comparison, the value $\mathcal{G}_{\rm Vela}$ of Vela's glitch activity is shown with horizontal lines, in the cases of minimal [270] and strong [149, 271, 272] entrainment.

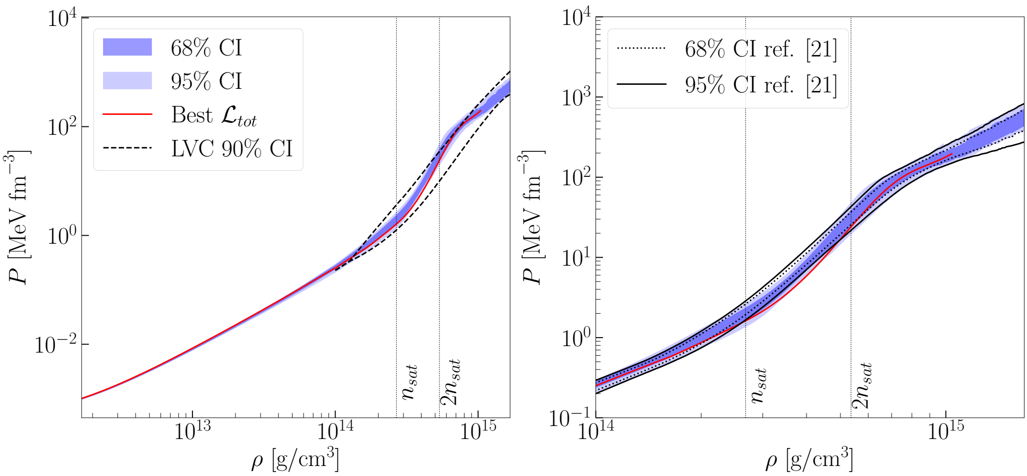

Figure 5.13: The posterior of the pressure P as function of the mass density ρ. The darker shade indicates the 68% confidence intervals, while the lighter one corresponds to the 95%. For comparison, the pressure of the best-fit model (highest $\mathcal{L}_{tot}$) is shown as a red line, and the dashed black region denotes the 90% confidence interval from the GW170817 analysis [164]. On the right, a zoom of the pressure posterior around saturation. This time, the black (dotted) line represents the (68%) 95% confidence interval of [21].

NICER measurements [282]. By contrast, our nuclear prior, which is incompatible with PREX-II, predicts quite soft neutron matter, not able to support $2M_\odot$. The effect on the NS EOS is thus similar, but reversed: while in our case we have soft matter around saturation, with a following stiffening to reach the two solar masses, they have quite stiff neutron matter due to the PREX data, and after the EOS softens to comply with astronomical observations.

In Figure 5.15 we show the squared sound speed$(c_s/c)^2$, computed with Eqs. (2.29) and (2.40), again comparing it to the results of [21] [8] . We observe that $(c_s/c)^2$ increases rapidly between one and two n_{sat} c_s: this rapid growth corresponds to the stiffening of the equation of state in this density region. In [284], it was demonstrated through pQCD calculations that $(c_s/c)^2$ approaches 1/3 at $n_B \approx 40n_{sat}$, corresponding to the so-called conformal limit. The authors further argued that extrapolating the EOS towards this limit, just by demanding causality and mechanical stability, imposes significant constraints on the behaviour of baryonic matter well below the regime of pQCD validity. This approach, they claimed, excludes a wide range of EOS candidates in a model-independent and analytical manner. However, in a follow-up study [285], it was shown that this extrapolation technique remains highly constraining only when initiated at densities around $n_B \sim 10n_{sat}$; below this threshold, the constraining power diminishes rapidly with decreasing starting density. Given that our models cannot be considered reliable at such high baryonic densities, we have chosen not to adopt this strategy in our present analysis.

Figure 5.16 displays the posterior of the symmetry energy. As before, the distribution is narrow up to n_{sat}, and broadens significantly at higher densities. The distribution is

[8] To keep the comparison with [21], we consider the barotropic sound speed rather than the adiabatic (or frozen) one [26]: since the barotropic sound speed coincides with the one calculated by considering the TOV energy-pressure profile, this is the quantity that measures the stiffness of the chemically equilibrated EOS; see, e.g., the discussion in [283].

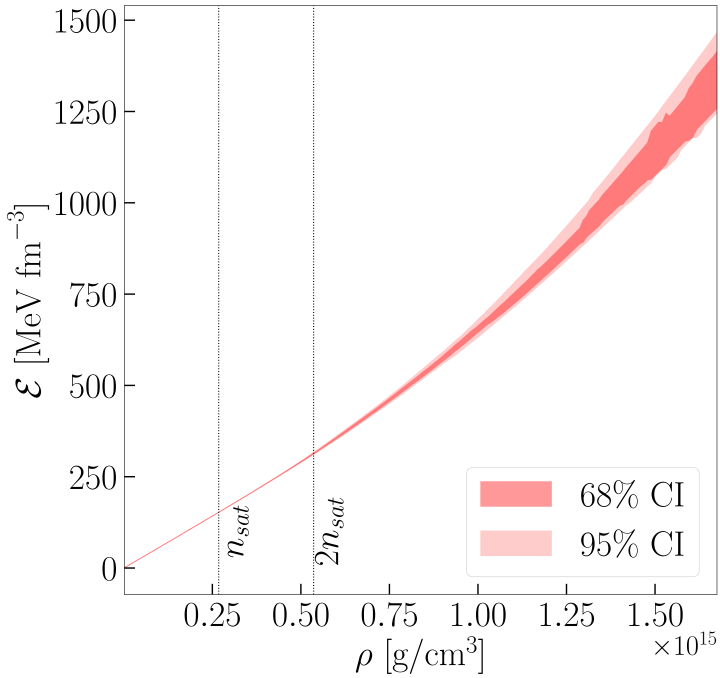

Figure 5.14: The posteriors energy density $\mathcal{E}$ as functions of the mass density ρ. The darker red shade indicates the 68% confidence intervals, while the lighter one corresponds to the 95%.

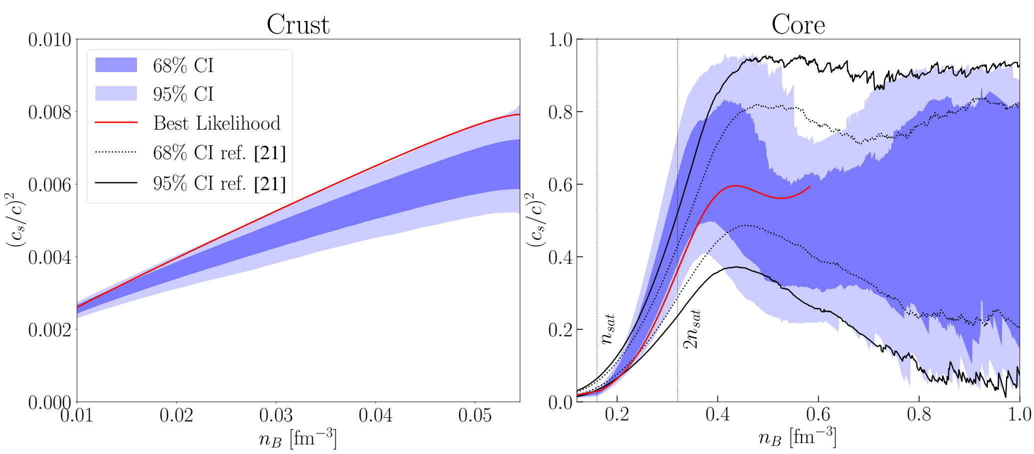

Figure 5.15: Posterior of the sound speed inside the star. The darker shades indicate the 68% confidence intervals, while the lighter shades correspond to the 95%. The dotted and solid black lines delimit the same intervals for the result of [21]. For comparison, the pressure of the best-fit model (highest $\mathcal{L}_{tot}$) is shown as a red line. The left subplot focuses on the inner crust, while the right on the core.

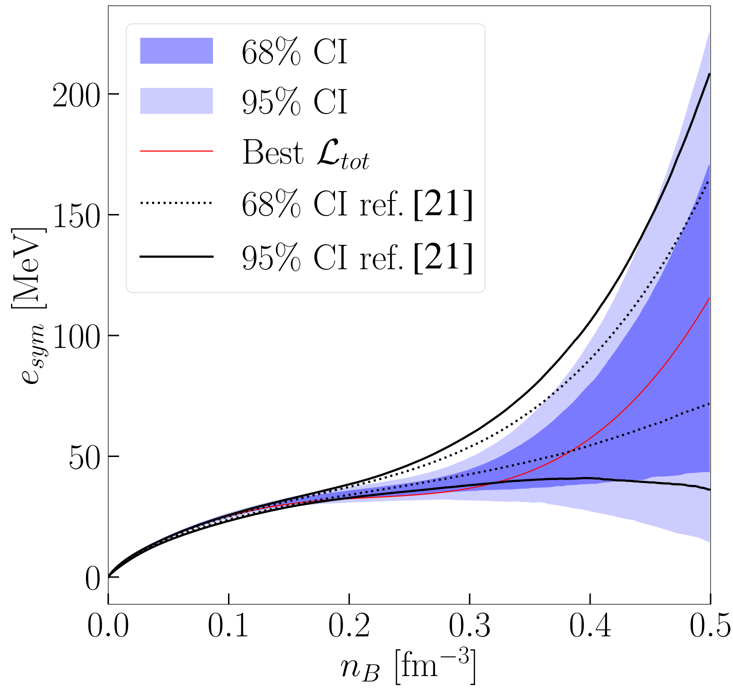

Figure 5.16: Symmetry energy posterior. The darker shades indicate the 68% confidence intervals, while the lighter shades correspond to the 95%. The symmetry energy of the best-fit model is in red. The black (dotted) line represents the (68%) 95% confidence interval of [21].

again compatible with the results of [21], but we can again appreciate the softening of the symmetry energy as imposed by the nuclear structure-informed prior used in this work. At very high density, where no nuclear physics information is available, our predictions are slightly more spread than in [21]. This might be because we use independent high-order parameters ($Q_{sat,sym}$ and $Z_{sat,sym}$) above saturation, thus completely decoupling the low-density information from the one at high-density, where additional degrees of freedom might pop up and the Taylor expansion becomes meaningless.

We conclude our results section with the mass-radius plot shown in Figure 5.17. For reference, the five models corresponding to the highest values of $\mathcal{L}_{tot}$ are displayed. The two black contours indicate the 68% confidence regions of the NICER inferences included in our analysis. Instead, the orange-shaded regions represent the posterior probability distribution found in [21]. The different colours delimit the regions containing, from darker to lighter, 68% and 95% of the distribution. The results are compatible, especially at high NS masses ($M \sim 2M_\odot$), where our results are well within the 68% region. On the other hand, at low NS masses ($M < 1.5M_\odot$), our analysis predicts thinner distributions and a non-negligible shift towards smaller radii, as a clear consequence of the softer symmetry energy.

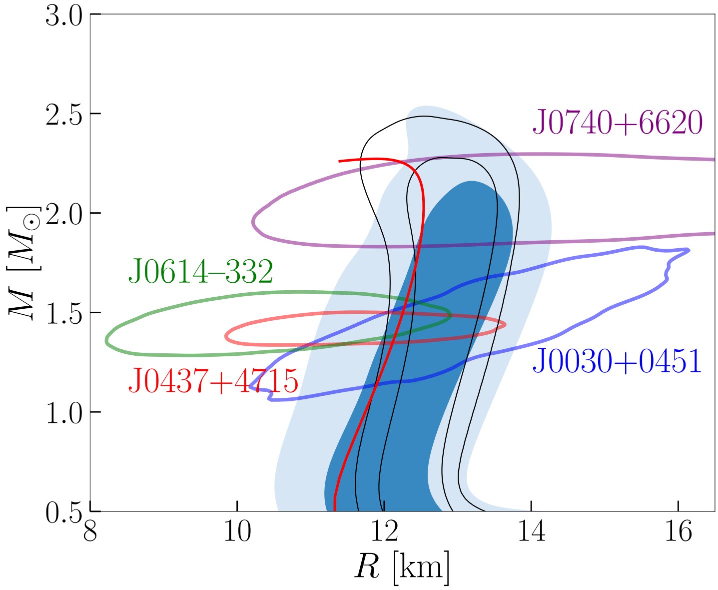

Figure 5.17: Posterior of the MR relation. The darker blue encloses the 68% probability region, while the lighter blue encloses the 95%. The best model is highlighted in red. The four coloured contours enclose the 95% probability regions of the four NICER measurements used in our analysis, see Figure 2.4b. The regions in the dark lines represent the posterior probability distribution found in [21] (68% the smallest, 95% the biggest).

Chapter 6

Conclusions and outlook

In this Thesis, we investigated the properties of the nuclear equation of state. Our work consists of two parts: a first Bayesian statistical analysis based on data from nuclear experiments, and a second Bayesian analysis, built on the results of the first, this time using data from NS observations.

First, we investigated the traditional Skyrme EDF ansatz [73] within a Bayesian inference framework, employing several nuclear properties, both in the ground state (binding energies, charge radii, spin-orbit splitting) and in excited states (isoscalar and isovector giant resonances). Among them, we included the parity-violating asymmetry A_{PV} [38, 39] and the dipole polarizability α_D [35, 36], both measured for ^{48}Ca and ^{208}Pb. It has been argued that these observables have notable consequences for asymmetric matter and the study of NSs [40, 41, 98, 226]. At the present time, however, no model can reproduce simultaneously the ^{208}Pb A_{PV} and the other three observables at the 1σ level. This tension is well documented in the literature [209, 211] and it is sometimes referred to as the PREX-CREX puzzle.

Bayesian techniques offer us a reliable statistical strategy to study the chosen model and assess its uncertainties. On the other hand, these methods are purely numerical and require the model evaluation on millions of points in parameter space. RPA calculations for computing giant resonance excitation energies are too time-consuming for direct use: a single inference, even on a supercomputer, would require months. To bypass this problem, we employed Gaussian-process emulators [29]. These emulators can mimic a computer program results in negligible time, learning from a limited sample of its results. We opted for the publicly available MADAI package [203], designed for Bayesian analyses.

We first focused on a data set containing only doubly magic nuclei. We performed a sequence of inferences, gradually adding different types of constraints and therefore clarifying the role that each observable plays in shaping the posterior distributions. The final result is a multidimensional probability distribution of the Skyrme parameters, expressed in terms of NMPs and the EDF surface and spin–orbit parameters. The marginalized posterior distributions, i.e., the distribution after having integrated over all but one parameter, are compatible with previous results in the literature [228, 229, 231, 234], except for L_{sym} and, to some extent, E_{sym}, for which we found instead lower values, $L_{sym} = 16.1 \pm 14.7$ MeV and $E_{sym} = 29.4 \pm 1.6$ MeV. Although unexpected, the Skyrme parametrisations we find are still compatible at the 1σ level with all the experimental data we chose for the fit, as well as with other isovector-sensitive observables we did not use, like ^{68}Ni α_D. The only exception is ^{208}Pb A_{PV}, for which we find significant evidence ($> 2\sigma$) that its measurement is in tension with the other observables.

Through a sensitivity analysis of the model, we discovered that the low $E_{sym} - L_{sym}$ values originate from the requirement of simultaneously reproducing the nuclear binding energies within 2 MeV of experiment and the dipole polarizabilities within their experimental uncertainties. The presence of ^{208}Pb A_{PV}, which instead demands much larger L_{sym} values, is not sufficient to counterbalance this effect.

In view of this realisation, we refined our choice of observables, mainly focusing on the binding energies. Our initial choice of binding energies was limited to doubly magic nuclei, including several symmetric nuclei, which are notoriously difficult for EDFs to describe without *ad hoc* terms [243–245]. These terms, often called Wigner terms, account for peculiar phenomena that are more pronounced in $N = Z$ nuclei, like proton–neutron pairing. This motivated the inclusion of binding energies of open-shell nuclei in our observable pool, and the removal of the $N = Z$ nuclei. Furthermore, a recent work [248] argued that QED corrections are needed to compare A_{PV} theoretical computations with the experimental results. As these corrections are from QED, they are essentially model-independent, and one can account for them by modifying the A_{PV} experimental values, which become lowered by $\sim 5\%$.

The resulting posteriors of E_{sym} and L_{sym} are shifted to larger values: $E_{sym} = 32.3 \pm 2.0$ MeV and $L_{sym} = 39.8 \pm 16.6$ MeV. However, these results are distorted by the extremely low value of ^{208}Pb A_{PV}, which our model is still not able to reproduce and exacerbates the already present tension with the other observables. For this reason, we also performed an inference without ^{208}Pb A_{PV}, which yielded $E_{sym} = 30.5 \pm 2.0$ MeV and $L_{sym} = 24.9 \pm 16.6$ MeV, still a significant increase from the original results, but much more contained. As of now, we are uncertain if it is acceptable to use such a measurement in analyses like ours. New experiments on the neutron skin thickness, such as the upcoming MREX measurement [286] which will measure again ^{208}Pb A_{PV}, or additional A_{PV} measurements in other nuclei, are much needed to shed light on the PREX–CREX tension and guide theoretical analyses.

The second part of the Thesis uses the nuclear posteriors from the first part as input. We performed a Bayesian analysis of the NS EOS, combining constraints from the maximum observed NS mass [144], the tidal deformability from GW170817 [20], and simultaneous mass–radius inferences from NICER [18, 157–159]. To refine the treatment of the inner crust and outer core, where the neutron gas plays a crucial role, we incorporated constraints from ab initio calculations of low-density neutron matter, specifically the energy band predicted in [241]. The strength of our approach lies in the correct integration of the nuclear physics posterior, which is included directly at the level of the prior. This ensures that our final results genuinely reflect the combined influence of terrestrial nuclear measurements, as opposed to previous studies [21–26], where nuclear matter parameters were sampled independently. By using the nuclear posterior as the prior, we incorporate the effect of nuclear surface properties on the nuclear matter parameters and capture all their mutual correlations. A further improvement relative to previous studies is the unified, nuclear-structure-informed Bayesian modelling of the crust, incorporating the correlated bulk and surface posteriors to improve the estimate of the crust–core transition point. This transition is computed both from the onset of the dynamical spinodal instability and from a more microscopic ETF variational method, though with some simplifications due to numerical complexity. We find that the ETF method increases the average crust–core transition pressure by 12% relative to the spinodal estimate, which significantly affects predictions for the crustal radius and moment of inertia. We believe these results are relevant for crust modelling and for assessing uncertainties in its composition and structure, where microphysical input consistent with both laboratory experiments and ab initio calculations is essential. The most important effect of the nuclear-structure-informed prior is an increased softness of the NS EOS around saturation, leading to a pronounced concavity in the region $n_{sat} \lesssim n_B \lesssim 2n_{sat}$, observable, for instance, in the smaller radii of lighter NSs compared to other studies [21]. This behaviour is strongly correlated with the soft symmetry energy implied by the nuclear inference. While this very soft symmetry energy is still compatible at 2σ with terrestrial systematics [287], further work is required to assess the influence of the specific nuclear data used in the first part. Sensitivity studies on the prior distributions would help evaluate the robustness of these conclusions. From a nuclear physics perspective, our findings highlight the non-negligible impact of astrophysical constraints on the saturation properties of nuclear matter, providing information complementary to laboratory experiments. The most affected parameters are E_{sym} and L_{sym}. Negative L_{sym} values, which remain compatible with terrestrial data alone, are incompatible with χEFT calculations and are therefore ruled out. Both E_{sym} and L_{sym} distributions are shifted toward higher values, both now peaking around 30 MeV. The construction of next-generation gravitational-wave detectors (Einstein Telescope in Europe [288] and Cosmic Explorer in the US [289]) will enable the detection of many more BNS mergers. Future X-ray missions such as STROBE-X [290] and eXTP [291] are expected to obtain simultaneous mass–radius measurements with uncertainties $\lesssim 0.5$ km. Such data will tighten constraints on the NS EOS and therefore on the nEOS, hopefully on the less constrained parameters like K_{sym}, Q_{sat} and Q_{sym}. They may even reach the precision needed to confirm or rule out the presence of hyperons or quark matter [292], which we did not consider here and which are believed to cause significant softening of the NS EOS.

The findings of this work are a foundation for further analyses. Our inferences favour a soft equation of state for PNM. However, the degree of this softness, i.e., the precise values of E_{sym} and L_{sym}, is quantified only within the standard Skyrme EDF, whose flexibility in the symmetry energy sector is limited, with K_{sym} strongly correlated with E_{sym} and L_{sym} [101]. This limitation influences our findings, and our results are affected by this systematic uncertainty. It would be interesting to repeat the same analysis with the same protocol employing other EDFs. For instance, there are different available codes for Gogny or RMF functionals. Interfacing them with our computational tools is quite straightforward, and a comparison with the Skyrme results would provide much insight. In this regard, we carried out some exploratory work in this direction with the Fayans functional (see Appendix A), although we are not yet able to perform complete inferences. The Fayans functional has a more flexible density dependence than Skyrme and could thus achieve a better description of asymmetric matter. More flexible EDFs are generally advantageous, as demonstrated with the KIDS functional in [101]. Although due to current observational limitations this extra flexibility does not translate into tight constraints on all higher-order NMPs, it nonetheless preserves the freedom of the lower-order ones, such as L_{sym}, thereby reducing the systematic uncertainties linked to model choice. Ultimately, the goal would be to average among all these results to extract a probability distribution of nuclear matter parameters which is as model-independent as possible. Advanced Bayesian methods, such as Bayesian model mixing, could be used for this purpose; some preliminary steps exist in the literature [293, 294].

In Section 4.4, we highlighted the importance of the choice of nuclear observables in our analyses. A key issue to address, parallel to the model-dependencies, is: what is the minimal set of nuclear observables necessary to constrain the behaviour of nuclear matter? What are the appropriate uncertainties? Which measurements should be excluded because they either do not provide meaningful information on nuclear matter or cannot be consistently described by our models? There is, of course, no definitive answer; however, such investigations would help establish a protocol for future studies, especially since different choices of observables can make comparisons across statistical analyses ambiguous. Furthermore, as mentioned at the beginning, we did not include data from Heavy-Ion

Collision (HIC) experiments. These constraints usually come in the form of inferred values of the symmetry energy at sub- and supra-saturation density [295, 296]. They could be, in principle, easily incorporated similarly to our treatment of χEFT calculations. At the same time, it should be emphasised that practitioners are still striving to assess the convergence of results of different transport models [297].

If these nuclear choices are propagated to the study of NSs, their impact could help connect specific nuclear observables to particular NS properties. Although we do not expect any single observable to strongly affect global stellar properties, it may be relevant for certain crustal features. To fully assess this, we should improve our crust modelling. One could envision an improved ETF algorithm or even more refined quantum methods, such as HFB, combined with Gaussian-process emulation to make Bayesian analyses feasible [257]. It would also be desirable to construct a truly unified MM EDF suitable for both nuclear and astrophysical regimes, removing the need for mapping between the sub- and supersaturation nEOS. Finally, access to new nuclear posteriors based on different EDFs could have significant implications for NS EOS studies as well. As we expect NS to be sensitive to the higher-order NMPs, using functionals in which they are free to vary and are not constrained by the functional form would result in an undeniable benefit.

Appendix A

Fayans functional and functional derivatives

A.1 The Fayans functional

The Fayans energy density functional E^{Fay} [10] is a relatively new approach in nuclear physics, and, to our knowledge, only a few works are present in the literature that propose analysis with it [298, 299]. In the following, we follow the notation employed in [300].

Unlike Skyrme, it does not stem from an underlying effective interaction, but exists only in its EDF formulation. It is divided into different contributions

$$E^{Fay} = \int \mathcal{E}^{Fay} d^3\boldsymbol{r} = \int (\mathcal{K} + \mathcal{E}^{Fay}_{nuc} + \mathcal{E}^{Fay}_{so} + \mathcal{E}^{Fay}_{Coul}) d^3\boldsymbol{r} \tag{A.1.1}$$

$\mathcal{K}$ is the kinetic energy density, and it has the same functional form as in Eq. (1.41)). $\mathcal{E}^{Fay}_{nuc}$ concerns the nuclear part of the interaction, and can be further subdivided into a volume and a surface term

$$\begin{aligned}\mathcal{E}^{Fay}_{nuc} &= \mathcal{E}^{Fay}_{nuc,v} + \mathcal{E}^{Fay}_{nuc,s} \\ &= \frac{2}{3}\varepsilon^0_F \hat{n}_{sat}\left[a^v_\alpha f_\alpha(\alpha)\alpha^2 + a^v_\beta f_\beta(\alpha)\beta^2\right] \\ &+ \frac{2}{3}\varepsilon^0_F \hat{n}_{sat} r_0^2 \left[a^s_\alpha g_\alpha(\alpha, \boldsymbol{\nabla}\alpha)(\boldsymbol{\nabla}\alpha)^2 + a^s_\beta g_\beta(\alpha, \boldsymbol{\nabla}\alpha)(\boldsymbol{\nabla}\beta)^2\right]\end{aligned} \tag{A.1.2}$$

where ε^0_F is the Fermi energy at saturation and the radius parameter r_0 is defined as $r_0 = (3/(8\pi\hat{n}_{sat}))^{1/3}$, $\hat{n}_{sat} = 0.08$ fm^{-3} $= n_{sat}/2$ is half the saturation density. α and β are adimensional functions of proton and neutron densities

$$\begin{aligned}\alpha &= \frac{n_n + n_p}{2\hat{n}_{sat}} \\ \beta &= \frac{n_n - n_p}{2\hat{n}_{sat}}\end{aligned} \tag{A.1.3}$$

and the volume function f and the surface function g in Eq. (A.1.2) read

$$f_t = \frac{1 - b^v_t \alpha^{\sigma^v_t}}{1 + c^v_t \alpha^{\sigma^v_t}} \tag{A.1.4}$$

$$g_t = \frac{1}{1 + c^s_t \alpha^{\sigma^s_t} + d^s_t r_0^2 (\boldsymbol{\nabla}\alpha)^2} \tag{A.1.5}$$

The nuclear part of the EDF has 16 parameters, although in the original Fayans paper, the parameter a^s_β is set to 0, $\sigma^s_\beta = \sigma^v_\beta = 1$, $\sigma^v_\alpha = \sigma^s_\alpha = \sigma$, and $c^v_\alpha = c^s_\alpha$.

As for the Coulomb part, the EDF reads (already in spherical symmetry)

$$\begin{aligned}\mathcal{E}^{Fay}_{Coul} = \mathcal{E}^{Fay}_{Coul,d} + \mathcal{E}^{Fay}_{Coul,ex} = 2\pi e^2 n_p(r)\left(\frac{1}{r}\int_0^r n_p(r')r'^2 dr' + \int_r^\infty n_p(r')r'dr'\right)\\ -\frac{3}{4}\left(\frac{3}{\pi}\right)^{\frac{1}{3}} e^2 n_p^{\frac{4}{3}}(1 - h_C\alpha^{\sigma^C_\alpha})\end{aligned} \tag{A.1.6}$$

where e is the electric charge, and the charge density has been approximated with the proton density. The term proportional to h_C accounts for beyond mean field, in particular, to the Coulomb-nuclear correlation [10, 301].

As for the spin-orbit, the EDF term reads

$$\mathcal{E}^{Fay}_{so} = \frac{4}{3}\varepsilon^0_F r_0^2\left(\kappa_\alpha\alpha\boldsymbol{\nabla}\cdot\boldsymbol{J} + \kappa_\beta\beta\boldsymbol{\nabla}\cdot(\boldsymbol{J}_n - \boldsymbol{J}_p)\right), \tag{A.1.7}$$

The $\kappa_{\alpha/\beta}$ parameters are linked to the Skyrme's W_0 and W_0' by the equivalence

$$\begin{aligned}W_0 &= -\frac{8}{3}\frac{\varepsilon^0_F r_0^2}{2\hat{n}_{sat}}(\kappa_\alpha - \kappa_\beta)\\ W_0' &= -\frac{16}{3}\frac{\varepsilon^0_F r_0^2}{2\hat{n}_{sat}}\kappa_\beta\end{aligned} \tag{A.1.8}$$

Although the Fayans functional has not known the same success as Skyrme, its richer functional form could lead to an improved description of nuclear properties. In Table A.1 the reader can find the values of two published parameterisations.

Unlike Skyrme, the Fayans functional does not have an effective mass term. Thus the KS equations (1.9) have a simpler form

$$\left(-\frac{\hbar^2}{2m}\nabla^2 + U_q(\boldsymbol{r}) + V_{coul,q}(\boldsymbol{r}) - i\boldsymbol{W}_q\cdot(\boldsymbol{\nabla}\times\sigma)\right)\phi_i(\boldsymbol{r},\sigma) = \varepsilon_i\phi_i(\boldsymbol{r},\sigma) \tag{A.1.9}$$

where the corresponding neutron and proton mean fields U_q are

$$U_q = \frac{\delta E}{\delta n_q} = \frac{1}{2\hat{n}_{sat}}\left(\frac{\delta E}{\delta\alpha} \pm \frac{\delta E}{\delta\beta}\right) \tag{A.1.10}$$

where + (−) is for the neutrons (protons) mean field.

Following the division of the various EDF components, for the volume part, we have

$$U^v_q = \frac{\varepsilon^0_F}{3}\left[a^v_\alpha\left(\alpha^2\frac{\partial f_\alpha}{\partial\alpha} + 2\alpha f_\alpha(\alpha)\right) + a^v_\beta\left(\beta^2\frac{\partial f_\beta}{\partial\alpha} \pm 2\beta f_\beta(\alpha)\right)\right] \tag{A.1.11}$$

As for the surface term, we give the expression of the functional derivatives with respect to α and β, from which one can derive the mean field following (A.1.10)

$$\begin{aligned}\frac{\delta E^{Fay}_{nuc,s}}{\delta\alpha} = \frac{2}{3}\varepsilon^0_F\hat{n}_{sat}a^s_\alpha r_0^2 g_\alpha\Bigg\{\\ 2\nabla^2\alpha\left(d^s_\alpha r_0^2 g_\alpha\left(\frac{\partial\alpha}{\partial r}\right)^2 - 1\right) + g_\alpha c^s_\alpha\sigma^s_\alpha\alpha^{\sigma^s_\alpha - 1}\left(\frac{\partial\alpha}{\partial r}\right)^2\left(1 - 4d^s_\alpha r_0^2\left(\frac{\partial\alpha}{\partial r}\right)^2 g_\alpha\right)\end{aligned}$$

Table A.1: Fayans parameters of some published parameterizations interactions.

	FaNDF^0 [10]	Fy (std) [298]
a^v_α	-9.559	-9.496
b^v_α	0.633	0.627
c^v_α	0.131	0.145
a^v_β	4.428	12.47
b^v_β	0.250	-1.388
c^v_β	1.300	19.380
σ^v_α	1/3	1/3
σ^v_β	1	1
a^s_α	0.600	0.524
c^s_α	0.131	0
d^s_α	0.440	0.099
a^s_β	0	0
c^s_β	0	0
d^s_β	0	0
σ^s_α	1/3	1/3
σ^s_β	1	1
h_C	0.941	0
κ	0.19	0.19
κ'	0	0.025

$$+ 8 g_\alpha d_\alpha^s r_0^2 \left[\frac{\partial^2 \alpha}{\partial r^2} \left(\frac{\partial \alpha}{\partial r} \right)^2 \right] \left(1 - d_\alpha^s r_0^2 g_\alpha \left(\frac{\partial \alpha}{\partial r} \right)^2 \right) \Bigg\}$$

$$+ \frac{2}{3} \varepsilon_F^0 \hat{n}_{sat} a_\beta^s r_0^2 g_\beta \Bigg\{ 2 \nabla^2 \alpha \left[d_\beta^s r_0^2 g_\beta \left(\frac{\partial \beta}{\partial r} \right)^2 \right]$$

$$- g_\beta c_\beta^s \sigma_\beta^s \alpha^{\sigma_\beta^s - 1} \left(\frac{\partial \beta}{\partial r} \right)^2 \left(1 + 4 d_\beta^s r_0^2 \left(\frac{\partial \alpha}{\partial r} \right)^2 g_\beta \right) +$$

$$+ 4 g_\beta d_\beta^s r_0^2 \left(\left[\left(\frac{\partial^2 \beta}{\partial r^2} \frac{\partial \beta}{\partial r} \right) \frac{\partial \alpha}{\partial r} \right] - 2 d_\beta^s r_0^2 g_\beta \left[\frac{\partial^2 \alpha}{\partial r^2} \left(\frac{\partial \alpha}{\partial r} \right)^2 \right] \left(\frac{\partial \beta}{\partial r} \right)^2 \right) \Bigg\} \quad \text{(A.1.12)}$$

$$\frac{\delta E_{nuc,s}^{Fay}}{\delta \beta} = - \frac{4}{3} \varepsilon_F^0 \hat{n}_{sat} a_\beta^s r_0^2 g_\beta \Bigg\{$$

$$\nabla^2 \beta - g_\beta c_\beta^s \sigma_\beta^s \alpha^{\sigma_\beta^s - 1} \left(\frac{\partial \alpha}{\partial r} \frac{\partial \beta}{\partial r} \right) - 2 g_\beta d_\beta^s r_0^2 \left[\left(\frac{\partial^2 \alpha}{\partial r^2} \frac{\partial \alpha}{\partial r} \right) \frac{\partial \beta}{\partial r} \right] \Bigg\} \quad \text{(A.1.13)}$$

These formulas were derived supposing spherical symmetry, so that the final expression gets significantly simpler. More details on the derivation can be found in below in Section A.3.

As for the Coulomb mean field, since the exchange part of $\mathcal{E}_{Coul,ex}^{Fay}$ depends on α ($\delta E_{Coul} / \delta \alpha \neq 0$), there will be a contribution of the Coulomb exchange potential to the neutron mean field as well, which mimics a beyond mean field effect

$$\begin{aligned} V_{Coul,p}^{ex} &= \frac{\delta E_{Coul}}{\delta n_p} = \left(\frac{3}{\pi} \right)^{\frac{1}{3}} e^2 n_p^{\frac{1}{3}} \left(h_C \alpha^{\sigma_\alpha^C} - 1 + \frac{3}{4} \frac{n_p}{2 \hat{n}_{sat}} h_C \sigma_\alpha^C \alpha^{\sigma_\alpha^C - 1} \right) \\ V_{Coul,n}^{ex} &= \frac{\delta E_{Coul}}{\delta n_n} = \left(\frac{3}{\pi} \right)^{\frac{1}{3}} e^2 \frac{3}{4} \frac{n_p^{\frac{4}{3}}}{2 \hat{n}_{sat}} h_C \sigma_\alpha^C \alpha^{\sigma_\alpha^C - 1} \end{aligned} \quad \text{(A.1.14)}$$

while the direct part is identical to the first term of Eq. (1.47). Finally, since the spin-orbit contribution is formally the same as Skyrme's, except for the $\boldsymbol{J}^2$ terms, the mean field potential is the same as well.

A.2 Fayans nuclear equation of state

Similarly to the Skyrme case (1.61), to write the Fayans nEOS one should retain just the volume part of $\mathcal{E}_{nuc}^{Fay}$ of Eq. (A.1.2) (with $\alpha = n/n_{sat}$ and $\beta = n/n_{sat} \delta$

$$\begin{aligned} e^{Fay}(n, \delta) = &\frac{3}{5} \frac{\hbar^2}{2m} \left(\frac{3\pi^2}{2} \right)^{2/3} n_B^{2/3} F_{5/3}(\delta) \\ &+ \frac{2}{3} \varepsilon_F^0 \hat{n}_{sat} \left[a_\alpha^v f_\alpha \left(\frac{n_B}{n_{sat}} \right) \left(\frac{n_B}{n_{sat}} \right)^2 + a_\beta^v f_\beta \left(\frac{n_B}{n_{sat}} \right) \left(\frac{\delta \cdot n_B}{n_{sat}} \right)^2 \right] \end{aligned} \quad \text{(A.2.1)}$$

where the function $F_m(\delta)$ is defined as $F_m(\delta) = [(1 + \delta)^m + (1 - \delta)^m]/2$.

A.3 Fayans computation details

In deriving the Fayans mean field expressions, it is useful to write the derivatives of the functions f Eq. (A.1.4) and g Eq. (A.1.5) as

$$\begin{aligned}
\frac{\partial f}{\partial \alpha} &= -\frac{\sigma\alpha^{\sigma-1}}{1+c\alpha^{\sigma}}(b+cf(\alpha)) = -\frac{\sigma\alpha^{\sigma-1}}{(1+c\alpha^{\sigma})^2}(b+c); \quad \frac{\partial f}{\partial(\boldsymbol{\nabla}\alpha)} = 0 \\
\frac{\partial g}{\partial \alpha} &= -c\sigma\alpha^{\sigma-1}g(\alpha,\boldsymbol{\nabla}\alpha)^2; \quad \frac{\partial g}{\partial(\boldsymbol{\nabla}\alpha)} = -2dr_0^2 g(\alpha,\boldsymbol{\nabla}\alpha)^2\boldsymbol{\nabla}\alpha
\end{aligned} \tag{A.3.1}$$

where, for readability, we omitted all the different subscripts.

One must pay attention to the terms containing $\boldsymbol{\nabla}\alpha$. For example, following the rule for the functional derivative Eq. (A.4.2), one encounters the following expression computing the surface term of the mean field potential Eq. (A.1.10)

$$\left.\frac{\delta E^s}{\delta\alpha}\right|_{a^s_\beta=0} = \frac{2}{3}\varepsilon_F^0 \hat{n}_{sat} a^s_\alpha r_0^2 \left\{(\boldsymbol{\nabla}\alpha)^2\frac{\partial g}{\partial\alpha} - 2\nabla\cdot\left(g_\alpha\boldsymbol{\nabla}\alpha - d^s_\alpha r_0^2(\boldsymbol{\nabla}\alpha)^2 g_\alpha^2\boldsymbol{\nabla}\alpha\right)\right\} \tag{A.3.2}$$

where we set to zero the parameter a^s_β to improve the readability. Now, following the product rule for divergences $\nabla\cdot(f(x)\mathbf{v}(x)) = f(x)\nabla\cdot\mathbf{v}(x) + \boldsymbol{\nabla}f(x)\cdot\mathbf{v}(x)$, one comes across terms of the form

$$\boldsymbol{\nabla}\left[(\boldsymbol{\nabla}\alpha)^2\right] = 2\boldsymbol{\nabla}\left[\boldsymbol{\nabla}\alpha\right]\boldsymbol{\nabla}\alpha = 2\mathcal{H}(\alpha)\boldsymbol{\nabla}\alpha \tag{A.3.3}$$

where $\mathcal{H}(\alpha)$ is the Hessian matrix of α. Explicitly, it reads

$$\nabla_j\left[(\nabla\alpha)^2\right] = 2\sum_i\left(\partial_j\partial_i\alpha\right)\left(\partial_i\alpha\right), \tag{A.3.4}$$

Since we are working in spherical symmetry, Eq. (A.3.3) gets significantly simplified

$$\frac{\partial}{\partial r}\left[\left(\frac{\partial\alpha}{\partial r}\right)^2\right] = 2\frac{\partial^2\alpha}{\partial r^2}\frac{\partial\alpha}{\partial r}. \tag{A.3.5}$$

The fact that expressions like Eq. (A.3.4) appear in the potential means that terms like Eq. (A.4.3) will appear in the residual interaction of the RPA equations, Eq. (1.30).

A.4 Functional derivative

Given a functional $H[\rho]$ of the form

$$H[\rho] = \int h(\mathbf{r};\rho,\boldsymbol{\nabla}\rho,\boldsymbol{\nabla}\boldsymbol{\nabla}\rho,\dots)d^3\boldsymbol{r} \tag{A.4.1}$$

the functional derivative with respect to the function $\rho(\boldsymbol{r})$ reads

$$\frac{\delta H}{\delta\rho} = \frac{\partial h}{\partial\rho} - \boldsymbol{\nabla}\cdot\left(\frac{\partial h}{\partial(\nabla\rho)}\right) + \boldsymbol{\nabla}\boldsymbol{\nabla}:\left(\frac{\partial h}{\partial(\boldsymbol{\nabla}\boldsymbol{\nabla}\rho)}\right) + \dots \tag{A.4.2}$$

where the last term is a compact notation for the Frobenius inner product

$$\boldsymbol{\nabla}\boldsymbol{\nabla}:\left(\frac{\partial h}{\partial(\boldsymbol{\nabla}\boldsymbol{\nabla}\rho)}\right) = \sum_{i,j}\partial_i\partial_j\left(\frac{\partial h}{\partial(\partial_i\partial_j\rho)}\right) \tag{A.4.3}$$

Appendix B

Skyrme NMP

Below, we write explicitly the Eq.s (1.60) for the Skyrme EDF. For the X^k_{sat}:

$$
\begin{aligned}
E_{sat} &= \frac{3}{10}\frac{\hbar^2}{m}\left(\frac{3\pi^2}{2}\right)^{2/3} n_{sat}^{2/3} + \frac{3}{8}t_0 n_{sat} + \frac{3}{80}\Theta_s\left(\frac{3\pi^2}{2}\right)^{2/3} n_{sat}^{5/3} \\
&+ \frac{1}{16}t_3 n_{sat}^{\sigma+1} \\
n_{sat} &= \frac{\hbar^2}{5m}\left(\frac{3\pi^2}{2}\right)^{2/3} n_{sat}^{2/3} + \frac{3}{8}t_0 n_{sat} + \frac{3}{80}\Theta_s\left(\frac{3\pi^2}{2}\right)^{2/3} n_{sat}^{5/3} \\
&+ \frac{1}{16}(\sigma+1)t_3 n_{sat}^{\sigma+1} \\
K_{sat} &= -\frac{3}{5}\frac{\hbar^2}{m}\left(\frac{3\pi^2}{2}\right)^{2/3} n_{sat}^{2/3} + \frac{3}{8}\Theta_s\left(\frac{3\pi^2}{2}\right)^{2/3} n_{sat}^{5/3} \\
&+ \frac{9}{16}t_3\sigma(\sigma+1) n_{sat}^{\sigma+1} \\
Q_{sat} &= \frac{12}{5}\frac{\hbar^2}{m}\left(\frac{3\pi^2}{2}\right)^{2/3} n_{sat}^{2/3} - \frac{3}{8}\Theta_s\left(\frac{3\pi^2}{2}\right)^{2/3} n_{sat}^{5/3} \\
&+ \frac{27}{16}(\sigma-1)\sigma(\sigma+1) n_{sat}^{\sigma+1} t_3 \\
Z_{sat} &= -\frac{84}{5}\frac{\hbar^2}{m}\left(\frac{3\pi^2}{2}\right)^{2/3} n_{sat}^{2/3} + \frac{3}{2}\Theta_s\left(\frac{3\pi^2}{2}\right)^{2/3} n_{sat}^{5/3} \\
&+ \frac{81}{16}(\sigma-2)(\sigma-1)\sigma(\sigma+1) n_{sat}^{\sigma+1} t_3
\end{aligned}
\tag{B.0.1}
$$

where $\Theta_s = 3t_1 + t_2(5 + 4x_2)$. The second condition defines $L_{sat} = 0$, and is solved numerically to find n_{sat}.

For the X^k_{sym}:

$$\begin{aligned}
E_{sym} =&\frac{\hbar^2}{6m}\left(\frac{3\pi^2}{2}\right)^{2/3} n_{sat}^{2/3} - \frac{t_0}{8}\left(2x_0+1\right) n_{sat} - \frac{1}{48}t_3\left(2x_3+1\right) n_{sat}^{\sigma+1} \\
&+ \frac{1}{24}\left(\frac{3\pi^2}{2}\right)^{2/3}\Theta_{sym} n_{sat}^{5/3} \\
L_{sym} =&\frac{\hbar^2}{3m}\left(\frac{3\pi^2}{2}\right)^{2/3} n_{sat}^{2/3} - \frac{3t_0}{8}\left(2x_0+1\right) n_{sat} - \frac{1}{16}t_3\left(2x_3+1\right)\left(\sigma+1\right) n_{sat}^{\sigma+1} \\
&+ \frac{5}{24}\left(\frac{3\pi^2}{2}\right)^{2/3}\Theta_{sym} n_{sat}^{5/3} \\
K_{sym} =&-\frac{\hbar^2}{3m}\left(\frac{3\pi^2}{2}\right)^{2/3} n_{sat}^{2/3} - \frac{3}{16}t_3\left(2x_3+1\right)\left(\sigma+1\right)\sigma n_{sat}^{\sigma+1} \\
&+ \frac{5}{12}\left(\frac{3\pi^2}{2}\right)^{2/3}\Theta_{sym} n_{sat}^{5/3} \\
\\
Q_{sym} =&\frac{4\hbar^2}{3m}\left(\frac{3\pi^2}{2}\right)^{2/3} n_{sat}^{2/3} - \frac{9}{16}t_3\left(2x_3+1\right)\left(\sigma+1\right)\sigma\left(\sigma-1\right) n_{sat}^{\sigma+1} \\
&- \frac{5}{12}\left(\frac{3\pi^2}{2}\right)^{2/3}\Theta_{sym} n_{sat}^{5/3} \\
Z_{sym} =&\frac{28\hbar^2}{3m}\left(\frac{3\pi^2}{2}\right)^{2/3} n_{sat}^{2/3} - \frac{27}{16}t_3\left(2x_3+1\right)\left(\sigma+1\right)\sigma\left(\sigma-1\right)(\sigma-2) n_{sat}^{\sigma+1} \\
&+ \frac{5}{3}\left(\frac{3\pi^2}{2}\right)^{2/3}\Theta_{sym} n_{sat}^{5/3}
\end{aligned} \tag{B.0.2}$$

where $\Theta_{sym} = t2(4+5x_2) - 3t_1x_1$.

Appendix C

Validation

The following Tables report the discrepancy percentages, i.e., the percentage of time the emulator guess was more distant than the inference error from the `hfbcs-qrpa` result, of all the observables for the various inferences we analysed within the text. The emulator always meets the validation criterion, which, we remind the reader, is guessing the code value within the inference errors (see Table 4.5) at least 90 times out of 100.

Table C.1: Emulator performance ("*B.E.* R_{ch}" inference).

Ground-state properties		
	$B.E.$	R_{ch}
^{208}Pb	0 %	0 %
^{48}Ca	0 %	0 %
^{40}Ca	0 %	0 %
^{56}Ni	0 %	-
^{68}Ni	0 %	-
^{100}Sn	0 %	-
^{132}Sn	0 %	0 %
^{90}Zr	0 %	0 %

Table C.2: Emulator performance ("+ΔE_{SO}" inference).

Ground-state properties			
	$B.E.$	R_{ch}	ΔE_{SO}
^{208}Pb	0 %	0 %	0 %
^{48}Ca	0 %	0 %	0 %
^{40}Ca	0 %	0 %	-
^{56}Ni	0 %	-	-
^{68}Ni	0 %	-	-
^{100}Sn	0 %	-	-
^{132}Sn	0 %	0 %	-
^{90}Zr	0 %	0 %	-

Table C.3: Emulator performance ("+α_D" inference).

Ground-state properties			
	$B.E.$	R_{ch}	ΔE_{SO}
^{208}Pb	0 %	0 %	0 %
^{48}Ca	0 %	0 %	0 %
^{40}Ca	0 %	0 %	-
^{56}Ni	0 %	-	-
^{68}Ni	0 %	-	-
^{100}Sn	0 %	-	-
^{132}Sn	0 %	0 %	-
^{90}Zr	0 %	0 %	-

Isovector properties			
	α_D	$m(1)$	A_{PV}
^{208}Pb	0 %	X	X
^{48}Ca	0 %	-	X

Table C.4: Emulator performance ("+GR" inference.)

Ground-state properties			
	$B.E.$	R_{ch}	ΔE_{SO}
^{208}Pb	0 %	0 %	0 %
^{48}Ca	0 %	0 %	0 %
^{40}Ca	0 %	0 %	-
^{56}Ni	0 %	-	-
^{68}Ni	0 %	-	-
^{100}Sn	0 %	-	-
^{132}Sn	0 %	0 %	-
^{90}Zr	0 %	0 %	-

Isoscalar resonances		
	$E^{\text{IS}}_{\text{GMR}}$	$E^{\text{IS}}_{\text{GQR}}$
^{208}Pb	0 %	4.8 %
^{90}Zr	0 %	-

Isovector properties			
	α_D	$m(1)$	A_{PV}
^{208}Pb	0 %	0 %	X
^{48}Ca	0 %	-	X

Table C.5: Emulator performance ("+A_{PV} (^{208}Pb only)" inference).

Ground-state properties			
	$B.E.$	R_{ch}	ΔE_{SO}
^{208}Pb	0 %	0 %	0 %
^{48}Ca	0 %	0 %	0 %
^{40}Ca	0 %	0 %	-
^{56}Ni	0 %	-	-
^{68}Ni	0 %	-	-
^{100}Sn	0 %	-	-
^{132}Sn	0 %	0 %	-
^{90}Zr	0 %	0 %	-

Isoscalar resonances		
	$E^{\text{IS}}_{\text{GMR}}$	$E^{\text{IS}}_{\text{GQR}}$
^{208}Pb	0 %	0.4 %
^{90}Zr	0 %	-

Isovector properties			
	α_D	$m(1)$	A_{PV}
^{208}Pb	0 %	0 %	0 %
^{48}Ca	0 %	-	X

Table C.6: Emulator performance ("+A_{PV} (^{48}Ca only)" inference).

Ground-state properties			
	$B.E.$	R_{ch}	ΔE_{SO}
^{208}Pb	0 %	0 %	0 %
^{48}Ca	0 %	0 %	0 %
^{40}Ca	0 %	0 %	-
^{56}Ni	0 %	-	-
^{68}Ni	0 %	-	-
^{100}Sn	0 %	-	-
^{132}Sn	0 %	0 %	-
^{90}Zr	0 %	0 %	-

Isoscalar resonances		
	$E^{\text{IS}}_{\text{GMR}}$	$E^{\text{IS}}_{\text{GQR}}$
^{208}Pb	0 %	0.8 %
^{90}Zr	0 %	-

Isovector properties			
	α_D	$m(1)$	A_{PV}
^{208}Pb	0 %	0 %	X
^{48}Ca	0 %	-	0 %

Table C.7: Emulator performance ("+A_{PV}(^{208}Pb and ^{48}Ca)" inference).

Ground-state properties			
	$B.E.$	R_{ch}	ΔE_{SO}
^{208}Pb	0 %	0 %	0 %
^{48}Ca	0 %	0 %	0 %
^{40}Ca	0 %	0 %	-
^{56}Ni	0 %	-	-
^{68}Ni	0 %	-	-
^{100}Sn	0 %	-	-
^{132}Sn	0 %	0 %	-
^{90}Zr	0 %	0 %	-

Isoscalar resonances		
	$E^{\text{IS}}_{\text{GMR}}$	$E^{\text{IS}}_{\text{GQR}}$
^{208}Pb	0 %	1.0 %
^{90}Zr	0 %	-

Isovector properties			
	α_D	$m(1)$	A_{PV}
^{208}Pb	0 %	0 %	0 %
^{48}Ca	0 %	-	0 %

Table C.8: Emulator performance ("With OS' in Fig. 4.9).

Ground-state properties			
	$B.E.$	R_{ch}	ΔE_{SO}
^{208}Pb	2 %	2 %	2 %
^{48}Ca	2 %	2 %	2 %
^{68}Ni	2 %	-	-
^{132}Sn	2 %	2 %	-
^{90}Zr	2 %	2 %	-

New Data from open shell nuclei			
	$B.E.$	R_{ch}	Δ_n
^{50}Ca	2 %	2 %	-
^{46}Ca	2 %	-	-
^{44}Ca	2 %	-	-
^{42}Ca	2 %	-	-
^{120}Sn	3 %	2 %	5 %
^{112}Sn	2 %	-	-
^{124}Sn	2 %	-	-

Table C.9: Emulator performance ("With OS New E^{IS}_{GMR} in Fig. 4.11").

Ground-state properties			
	$B.E.$	R_{ch}	ΔE_{SO}
^{208}Pb	2 %	2 %	2 %
^{48}Ca	2 %	2 %	2 %
^{68}Ni	2 %	-	-
^{132}Sn	2 %	2 %	-
^{90}Zr	2 %	2 %	-

Isoscalar resonances		
	E^{IS}_{GMR}	E^{IS}_{GQR}
^{208}Pb	2 %	5.7 %
^{90}Zr	2 %	-

Isovector properties			
	α_D	$m(1)$	A_{PV}
^{208}Pb	2 %	2 %	2 %
^{48}Ca	2 %	-	2 %

New Data from open shell nuclei			
	$B.E.$	R_{ch}	Δ_n
^{50}Ca	2 %	2 %	-
^{46}Ca	2 %	-	-
^{44}Ca	2 %	-	-
^{42}Ca	2 %	-	-
^{120}Sn	2 %	2 %	2 %
^{112}Sn	2 %	-	-
^{124}Sn	2 %	-	-

Table C.10: Emulator performance ("With OS New E^{IS}_{GMR} New A_{PV}" in Fig. 4.11).

Ground-state properties			
	$B.E.$	R_{ch}	ΔE_{SO}
^{208}Pb	2 %	2 %	2 %
^{48}Ca	2 %	2 %	2 %
^{68}Ni	2 %	-	-
^{132}Sn	2 %	2 %	-
^{90}Zr	2 %	2 %	-

Isoscalar resonances		
	E^{IS}_{GMR}	E^{IS}_{GQR}
^{208}Pb	2 %	4.9 %
^{90}Zr	2 %	-

Isovector properties			
	α_D	$m(1)$	A_{PV}
^{208}Pb	3 %	2 %	2 %
^{48}Ca	2 %	-	2 %

New Data from open shell nuclei			
	$B.E.$	R_{ch}	Δ_n
^{50}Ca	2 %	2 %	-
^{46}Ca	2 %	-	-
^{44}Ca	2 %	-	-
^{42}Ca	2 %	-	-
^{120}Sn	2 %	2 %	3 %
^{112}Sn	2 %	-	-
^{124}Sn	2 %	-	-

Table C.11: Emulator performance ("With OS New E^{IS}_{GMR} New ^{48}CaA_{PV}" in Fig. 4.11).

Ground-state properties			
	$B.E.$	R_{ch}	ΔE_{SO}
^{208}Pb	1 %	1 %	1 %
^{48}Ca	1 %	1 %	1 %
^{68}Ni	1 %	-	-
^{132}Sn	1 %	1 %	-
^{90}Zr	1 %	1 %	-

Isoscalar resonances		
	E^{IS}_{GMR}	E^{IS}_{GQR}
^{208}Pb	1 %	6.3 %
^{90}Zr	1 %	-

Isovector properties			
	α_D	$m(1)$	A_{PV}
^{208}Pb	1 %	1 %	X
^{48}Ca	1 %	-	1 %

New Data from open shell nuclei			
	$B.E.$	R_{ch}	Δ_n
^{50}Ca	1 %	1 %	-
^{46}Ca	1 %	-	-
^{44}Ca	1 %	-	-
^{42}Ca	1 %	-	-
^{120}Sn	1 %	1 %	1 %
^{112}Sn	1 %	-	-
^{124}Sn	1 %	-	-

Appendix D

Neutron Stars Details

We summarize in this brief appendix all the details regarding our computation of NS EOS.

D.1 Sampled Skyrme

We present in Table D.1 the parameters of the two sampled Skyrme SkmSmpl1 and SkmSmpl2 used throughout the text.

D.2 Equation of stat interpolation details

In this section we will give the mathematical details of the EoS interpolation.

D.2.1 Bernstein polynomial

A Bernstein polynomial of third-order can be written as

$$B_3(x) = \sum_{i=0}^{i=3} a_i \frac{(x-n_1)^i (n_2-x)^{(3-i)}}{(n_2-n_1)^3} \tag{D.2.1}$$

In our scheme, n_1 is the last baryon density where the crust computation did not fail, and n_2 the estimated n_{cc}. The following choice of the coefficients a_i ensures the continuity of

Table D.1: Skyrme parameters of the two sampled Skyrme SkmSmpl1 and SkmSmpl2 used throughout the text.

		SkmSmpl1	SkmSmpl2
t_0	[MeV fm^3]	-1992.157	-1983.031
t_1	[MeV fm^5]	440.755	334.366
t_2	[MeV fm^5]	96.649	-124.556
t_3	[MeV fm$^{3+3\alpha}$]	11910.389	13066.227
x_0	[-]	0.439	0.385
x_1	[-]	-0.708	0.197
x_2	[-]	-2.999	0.334
x_3	[-]	0.616	0.315
σ	[-]	0.256	0.276
W_0	[MeV fm^5]	144.399	116.148

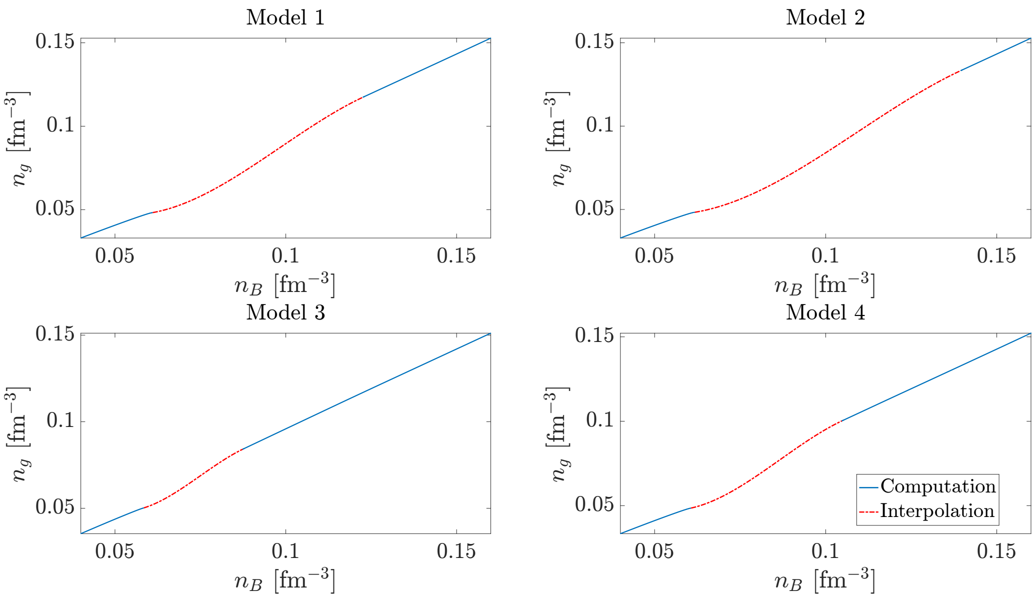

Figure D.1: In red, the interpolation of the free neutrons density.

energy density and pressure

$$\begin{aligned} a_0 &= \mathcal{E}(n_1) \\ a_1 &= 3\mathcal{E}(n_1) + (n_2 - n_1)\mathcal{E}'(n_1) \\ a_2 &= 3\mathcal{E}(n_2) - (n_2 - n_1)\mathcal{E}'(n_2) \\ a_3 &= 3\mathcal{E}(n_2) \end{aligned} \tag{D.2.2}$$

where $\mathcal{E}'$ is the derivative of the energy density, which can be easily derived from the pressure P

$$\mathcal{E}'(n_B) = \frac{(P + \mathcal{E})|_{n_B}}{n_B} \tag{D.2.3}$$

Furthermore, to ensure that the interpolation makes sense, the energy density and its derivative must satisfy the following relations:

$$\mathcal{E}(n_1) < \mathcal{E}(n_2) \tag{D.2.4}$$

and

$$\mathcal{E}'(n_1) < \frac{\mathcal{E}(n_2) - \mathcal{E}(n_1)}{n_2 - n_1} < \mathcal{E}'(n_2) \tag{D.2.5}$$

The latter ensures that the energy density remains convex, i.e., no pressure drop in the interpolation region.

Once the energy density is interpolated, we can access the pressure

$$P(n_B) = \mathcal{E}'(n_B)n_B - \mathcal{E}(n_B) \tag{D.2.6}$$

D.2.2 Proton fraction interpolation

The proton fraction is interpolated linearly between the last computed density in the inner-crust n_1 until the estimated crust-core transition density $n_2 = n_{cc}$

$$y_p(n_B) = \frac{y_p(n_1)(n_2 - n_B) + y_p(n_2)(n_B - n_1)}{n_2 - n_1} \tag{D.2.7}$$

D.2.3 Free neutrons density interpolation

The free neutron density n_g is computed by interpolation with a polynomial of third order. We used the values corresponding to the last five computed points in the inner crust, and the first five of the core. Figure D.1 shows an example of such a fit for four randomly selected models.

Bibliography

[1] D. Vautherin and D. M. Brink, Phys. Rev. C **5**, 626–647 (1972).

[2] G. Colò, Advances in Physics: X **5**, 1740061 (2020).

[3] G. Colò, "Nuclear density functional theory (dft)", in *Handbook of nuclear physics*, edited by I. Tanihata, H. Toki, and T. Kajino (Springer Nature Singapore, Singapore, 2020), pp. 1–30.

[4] P. Hohenberg and W. Kohn, Phys. Rev. **136**, 864–871 (1964).

[5] R. G. Parr and R. G. P. W. Yang, *Density-functional theory of atoms and molecules* (Oxford university press, 1989).

[6] M. Levy, Phys. Rev. A **26**, 1200–1208 (1982).

[7] E. H. Lieb, International Journal of Quantum Chemistry **24**, 243–277 (1983).

[8] J. Dechargé and D. Gogny, Phys. Rev. C **21**, 1568–1593 (1980).

[9] J. D. Walecka, Annals of Physics **83**, 491–529 (1974).

[10] S. A. Fayans, ZhETF Pisma Redaktsiiu **68**, 161 (1998).

[11] D. M. Brink and R. A. Broglia, *Nuclear superfluidity: pairing in finite systems*, Cambridge Monographs on Particle Physics, Nuclear Physics and Cosmology (Cambridge University Press, 2005).

[12] X. Roca-Maza and N. Paar, Progress in Particle and Nuclear Physics **101**, 96–176 (2018).

[13] U. Garg and G. Colò, Progress in Particle and Nuclear Physics **101**, 55–95 (2018).

[14] S. L. Shapiro and S. A. Teukolsky, *Black holes, white dwarfs and neutron stars: the physics of compact objects* (John Wiley & Sons, 2024).

[15] P. Haensel, A. Y. Potekhin, and D. G. Yakovlev, *Neutron stars 1: equation of state and structure*, Vol. 326 (Springer, New York, USA, 2007).

[16] J. Antoniadis, P. C. C. Freire, N. Wex, T. M. Tauris, R. S. Lynch, M. H. van Kerkwijk, M. Kramer, C. Bassa, V. S. Dhillon, T. Driebe, J. W. T. Hessels, V. M. Kaspi, V. I. Kondratiev, N. Langer, T. R. Marsh, M. A. McLaughlin, T. T. Pennucci, S. M. Ransom, I. H. Stairs, J. van Leeuwen, J. P. W. Verbiest, and D. G. Whelan, Science **340**, 448 (2013).

[17]T. E. Riley, A. L. Watts, S. Bogdanov, P. S. Ray, R. M. Ludlam, S. Guillot, Z. Arzoumanian, C. L. Baker, A. V. Bilous, D. Chakrabarty, K. C. Gendreau, A. K. Harding, W. C. G. Ho, J. M. Lattimer, S. M. Morsink, and T. E. Strohmayer, The Astrophysical Journal Letters **887**, L21, L21 (2019).

[18]M. C. Miller, F. K. Lamb, A. J. Dittmann, S. Bogdanov, Z. Arzoumanian, K. C. Gendreau, S. Guillot, A. K. Harding, W. C. G. Ho, J. M. Lattimer, R. M. Ludlam, S. Mahmoodifar, S. M. Morsink, P. S. Ray, T. E. Strohmayer, K. S. Wood, T. Enoto, R. Foster, T. Okajima, G. Prigozhin, and Y. Soong, The Astrophysical Journal Letters **887**, L24, L24 (2019).

[19]B. P. e. a. Abbott (LIGO Scientific Collaboration and Virgo Collaboration), Phys. Rev. Lett. **119**, 161101 (2017).

[20]B. P. Abbott, others (LIGO Scientific Collaboration, and V. Collaboration), Physical Review X **9**, 011001, 011001 (2019).

[21]H. Dinh Thi, C. Mondal, and F. Gulminelli, Universe **7** (2021).

[22]C. Y. Tsang, M. B. Tsang, W. G. Lynch, R. Kumar, and C. J. Horowitz, Nature Astronomy **8**, 328–336 (2024).

[23]B. K. Pradhan, D. Pathak, and D. Chatterjee, Astrophysical Journal **956**, 38, 38 (2023).

[24]P. Char, C. Mondal, F. Gulminelli, and M. Oertel, Phys. Rev. D **108**, 103045 (2023).

[25]T. Malik, H. Pais, and C. Providência, Astron. Astrophys. **689**, A242 (2024).

[26]G. Montefusco, M. Antonelli, and F. Gulminelli, Astronomy and Astrophysical **694**, A150, A150 (2025).

[27]D. J. C. Mackay, *Information Theory, Inference and Learning Algorithms* (Cambridge University press, 2003).

[28]A. Gelman, J. Carlin, H. Stern, D. Dunson, A. Vehtari, and D. Rubin, *Bayesian data analysis, third edition*, Chapman & Hall/CRC Texts in Statistical Science (Taylor & Francis, 2013).

[29]C. E. Rasmussen and C. K. I. Williams, *Gaussian Processes for Machine Learning* (MIT Press, 2006).

[30]K. P. Murphy, *Machine learning: a probabilistic perspective* (The MIT Press, 2012).

[31]T. Skyrme, Nuclear Physics **9**, 615–634 (1958).

[32]W. J. Huang, M. Wang, F. G. Kondev, G. Audi, and S. Naimi, Chinese Physics C **45**, 030002, 030002 (2021).

[33]I. Angeli and K. P. Marinova, At. Data and Nucl. Data Tab. **99**, 69–95 (2013).

[34]M. Zalewski, J. Dobaczewski, W. Satuła, and T. R. Werner, **77**, 024316, 024316 (2008).

[35]A. Tamii et al., Phys. Rev. Lett. **107**, 062502 (2011).

[36]J. Birkhan et al., Phys. Rev. Lett. **118**, 252501 (2017).

[37]D. Patel, U. Garg, M. Fujiwara, T. Adachi, H. Akimune, G. P. A. Berg, M. N. Harakeh, M. Itoh, C. Iwamoto, A. Long, J. T. Matta, T. Murakami, A. Okamoto, K. Sault, R. Talwar, M. Uchida, and M. Yosoi, Physics Letters B **726**, 178–181 (2013).

[38]D. Adhikari, H. Albataineh, D. Androic, K. A. Aniol, D. S. Armstrong, T. Averett, C. Ayerbe Gayoso, S. K. Barcus, V. Bellini, R. S. Beminiwattha, J. F. Benesch, H. Bhatt, D. Bhatta Pathak, D. Bhetuwal, B. Blaikie, J. Boyd, Q. Campagna, A. Camsonne, G. D. Cates, Y. Chen, C. Clarke, J. C. Cornejo, S. Covrig Dusa, M. M. Dalton, P. Datta, A. Deshpande, D. Dutta, C. Feldman, E. Fuchey, C. Gal, D. Gaskell, T. Gautam, M. Gericke, C. Ghosh, I. Halilovic, J.-O. Hansen, O. Hassan, F. Hauenstein, W. Henry, C. J. Horowitz, C. Jantzi, S. Jian, S. Johnston, D. C. Jones, S. Kakkar, S. Katugampola, C. Keppel, P. M. King, D. E. King, K. S. Kumar, T. Kutz, N. Lashley-Colthirst, G. Leverick, H. Liu, N. Liyanage, J. Mammei, R. Mammei, M. McCaughan, D. McNulty, D. Meekins, C. Metts, R. Michaels, M. Mihovilovic, M. M. Mondal, J. Napolitano, A. Narayan, D. Nikolaev, V. Owen, C. Palatchi, J. Pan, B. Pandey, S. Park, K. D. Paschke, M. Petrusky, M. L. Pitt, S. Premathilake, B. Quinn, R. Radloff, S. Rahman, M. N. H. Rashad, A. Rathnayake, B. T. Reed, P. E. Reimer, R. Richards, S. Riordan, Y. R. Roblin, S. Seeds, A. Shahinyan, P. Souder, M. Thiel, Y. Tian, G. M. Urciuoli, E. W. Wertz, B. Wojtsekhowski, B. Yale, T. Ye, A. Yoon, W. Xiong, A. Zec, W. Zhang, J. Zhang, and X. Zheng (CREX Collaboration), Phys. Rev. Lett. **129**, 042501 (2022).

[39]D. Adhikari, H. Albataineh, D. Androic, K. Aniol, D. S. Armstrong, T. Averett, C. Ayerbe Gayoso, S. Barcus, V. Bellini, R. S. Beminiwattha, J. F. Benesch, H. Bhatt, D. Bhatta Pathak, D. Bhetuwal, B. Blaikie, Q. Campagna, A. Camsonne, G. D. Cates, Y. Chen, C. Clarke, J. C. Cornejo, S. Covrig Dusa, P. Datta, A. Deshpande, D. Dutta, C. Feldman, E. Fuchey, C. Gal, D. Gaskell, T. Gautam, M. Gericke, C. Ghosh, I. Halilovic, J.-O. Hansen, F. Hauenstein, W. Henry, C. J. Horowitz, C. Jantzi, S. Jian, S. Johnston, D. C. Jones, B. Karki, S. Katugampola, C. Keppel, P. M. King, D. E. King, M. Knauss, K. S. Kumar, T. Kutz, N. Lashley-Colthirst, G. Leverick, H. Liu, N. Liyange, S. Malace, R. Mammei, J. Mammei, M. McCaughan, D. McNulty, D. Meekins, C. Metts, R. Michaels, M. M. Mondal, J. Napolitano, A. Narayan, D. Nikolaev, M. N. H. Rashad, V. Owen, C. Palatchi, J. Pan, B. Pandey, S. Park, K. D. Paschke, M. Petrusky, M. L. Pitt, S. Premathilake, A. J. R. Puckett, B. Quinn, R. Radloff, S. Rahman, A. Rathnayake, B. T. Reed, P. E. Reimer, R. Richards, S. Riordan, Y. Roblin, S. Seeds, A. Shahinyan, P. Souder, L. Tang, M. Thiel, Y. Tian, G. M. Urciuoli, E. W. Wertz, B. Wojtsekhowski, B. Yale, T. Ye, A. Yoon, A. Zec, W. Zhang, J. Zhang, and X. Zheng (PREX Collaboration), Phys. Rev. Lett. **126**, 172502 (2021).

[40]F. J. Fattoyev, J. Piekarewicz, and C. J. Horowitz, Phys. Rev. Lett. **120**, 172702 (2018).

[41]B. T. Reed, F. J. Fattoyev, C. J. Horowitz, and J. Piekarewicz, Phys. Rev. Lett. **126**, 172503 (2021).

[42]J. Margueron, R. Hoffmann Casali, and F. Gulminelli, Phys. Rev. C **97**, 025805 (2018).

[43]J. Margueron, R. Hoffmann Casali, and F. Gulminelli, Phys. Rev. C **97**, 025806 (2018).

[44]R. M. Dreizler and E. K. U. Gross, *Density functional theory*, en, 1st ed. (Springer, Berlin, Germany, Apr. 1996).

[45]W. Kohn and L. J. Sham, Phys. Rev. **140**, A1133–A1138 (1965).

[46]R. O. Jones, Rev. Mod. Phys. **87**, 897–923 (2015).

[47]M. Valiev and G. W. Fernando, arXiv e-prints, cond-mat/9702247, cond–mat/9702247 (1997).

[48]W. Kohn, Rev. Mod. Phys. **71**, 1253–1266 (1999).

[49]T. Helgaker and A. M. Teale, arXiv e-prints, arXiv:2204.12216, arXiv:2204.12216 (2022).

[50]J. Engel, Phys. Rev. C **75**, 014306 (2007).

[51]N. Barnea, Phys. Rev. C **76**, 067302 (2007).

[52]J. Messud, M. Bender, and E. Suraud, Phys. Rev. C **80**, 054314 (2009).

[53]A. Bohr and B. R. Mottelson, *Nuclear structure* (World Scientific Publishing Company, 1998).

[54]P. Ring, P. Schuck, and M. R. Strayer, Physics Today **36**, 70 (1983).

[55]C. A. Bertulani, *Nuclear physics in a nutshell* (Princeton University Press, 2007).

[56]G. Colò, European Physical Journal Plus **133**, 553, 553 (2018).

[57]T. Nakatsukasa, K. Matsuyanagi, M. Matsuo, and K. Yabana, Rev. Mod. Phys. **88**, 045004 (2016).

[58]D. Davesne, J. Navarro, J. Meyer, K. Bennaceur, and A. Pastore, Phys. Rev. C **97**, 044304 (2018).

[59]J. Dobaczewski and J. Dudek, Phys. Rev. C **52**, 1827–1839 (1995).

[60]F. Raimondi, B. G. Carlsson, and J. Dobaczewski, Phys. Rev. C **83**, 054311 (2011).

[61]P. Becker, D. Davesne, J. Meyer, A. Pastore, and J. Navarro, Journal of Physics G: Nuclear and Particle Physics **42**, 034001 (2015).

[62]D. Davesne, J. Navarro, P. Becker, R. Jodon, J. Meyer, and A. Pastore, Phys. Rev. C **91**, 064303 (2015).

[63]Y. Engel, D. Brink, K. Goeke, S. Krieger, and D. Vautherin, Nuclear Physics A **249**, 215–238 (1975).

[64]J. Dobaczewski and J. Dudek, Acta Phys. Polon. B **27**, edited by J. Skalski and Z. Sujkowski, 45–58 (1996).

[65]P.-G. Reinhard and H. Flocard, Nuc. Phys. A **584**, 467–488 (1995).

[66]P. Ring, Progress in Particle and Nuclear Physics **37**, 193–263 (1996).

[67]M. Dutra, O. Louren ço, S. S. Avancini, B. V. Carlson, A. Delfino, D. P. Menezes, C. Providência, S. Typel, and J. R. Stone, Phys. Rev. C **90**, 055203 (2014).

[68]T. Nik ši ć, D. Vretenar, and P. Ring, Phys. Rev. C **78**, 034318 (2008).

[69]P. Möller, W. D. Myers, H. Sagawa, and S. Yoshida, Phys. Rev. Lett. **108**, 052501 (2012).

[70]P. Möller, A. Sierk, T. Ichikawa, and H. Sagawa, Atomic Data and Nuclear Data Tables **109-110**, 1–204 (2016).

[71]S. Goriely, N. Chamel, and J. M. Pearson, Phys. Rev. C **88**, 024308 (2013).

[72]M. Wang, W. J. Huang, F. G. Kondev, G. Audi, and S. Naimi, Chinese Physics C **45**, 030003, 030003 (2021).

[73]E. Chabanat, P. Bonche, P. Haensel, J. Meyer, and R. Schaeffer, Nuc. Phys. A **627**, 710–746 (1997).

[74]M. Kortelainen, T. Lesinski, J. Moré, W. Nazarewicz, J. Sarich, N. Schunck, M. V. Stoitsov, and S. Wild, Phys. Rev. C **82**, 024313 (2010).

[75]P. Bortignon, A. Bracco, and R. Broglia, *Giant resonances: nuclear structure at finite temperature* (Harwood Academic Publishers, June 2019).

[76]A. Bracco, E. Lanza, and A. Tamii, Progress in Particle and Nuclear Physics **106**, 360–433 (2019).

[77]G. Co', Universe **9** (2023).

[78]E. Lipparini and S. Stringari, Physics Reports **175**, 103–261 (1989).

[79]S. Goriely, S. Péru, G. Colò, X. Roca-Maza, I. Gheorghe, D. Filipescu, and H. Utsunomiya, **102**, 064309, 064309 (2020).

[80]D. Patel, "A study of the isoscalar giant monopole resonance", PhD thesis (University of Notre Dame, 2014).

[81]J. Wambach, Reports on Progress in Physics **51**, 989 (1988).

[82]C. Yannouleas, Phys. Rev. C **35**, 1159–1161 (1987).

[83]S. Shen, G. Colò, and X. Roca-Maza, Phys. Rev. C **101**, 044316 (2020).

[84]Z. Z. Li, Y. F. Niu, and G. Colò, Phys. Rev. Lett. **131**, 082501 (2023).

[85]E. Litvinova, Phys. Rev. C **107**, L041302 (2023).

[86]E. Chabanat, P. Bonche, P. Haensel, J. Meyer, and R. Schaeffer, Nuclear Physics A **635**, 231–256 (1998).

[87]J. Bartel, P. Quentin, M. Brack, C. Guet, and H.-B. Håkansson, Nuclear Physics A **386**, 79–100 (1982).

[88]M. Beiner, H. Flocard, N. Van Giai, and P. Quentin, Nuclear Physics A **238**, 29–69 (1975).

[89]N. Chamel, S. Goriely, and J. M. Pearson, Phys. Rev. C **80**, 065804 (2009).

[90]G. Bertsch and H. Esbensen, Annals of Physics **209**, 327–363 (1991).

[91]M. Baldo, *Nuclear methods and the nuclear equation of state* (WORLD SCIENTIFIC, 1999).

[92]M. Oertel, M. Hempel, T. Klähn, and S. Typel, Reviews of Modern Physics **89**, 015007, 015007 (2017).

[93]J. M. Lattimer, Annual Review of Nuclear and Particle Science **62**, 485–515 (2012).

[94]H. De Vries, C. De Jager, and C. De Vries, Atomic Data and Nuclear Data Tables **36**, 495–536 (1987).

[95]X. Roca-Maza, M. Centelles, X. Viñas, and M. Warda, Phys. Rev. Lett. **106**, 252501 (2011).

[96]J. P. Blaizot, Phys. Rep. **64**, 171 (1980).

[97]X. Roca-Maza, M. Brenna, G. Colò, M. Centelles, X. Viñas, B. K. Agrawal, N. Paar, D. Vretenar, and J. Piekarewicz, Phys. Rev. C **88**, 024316 (2013).

[98]X. Roca-Maza, X. Viñas, M. Centelles, B. K. Agrawal, G. Colò, N. Paar, J. Piekarewicz, and D. Vretenar, Phys. Rev. C **92**, 064304 (2015).

[99]W. Busza, K. Rajagopal, and W. van der Schee, Annual Review of Nuclear and Particle Science **68**, 339–376 (2018).

[100]A. Sorensen, K. Agarwal, K. W. Brown, Z. Chajecki, P. Danielewicz, C. Drischler, S. Gandolfi, J. W. Holt, M. Kaminski, C.-M. Ko, R. Kumar, B.-A. Li, W. G. Lynch, A. B. McIntosh, W. G. Newton, S. Pratt, O. Savchuk, M. Stefaniak, I. Tews, M. B. Tsang, R. Vogt, H. Wolter, H. Zbroszczyk, N. Abbasi, J. Aichelin, A. Andronic, S. A. Bass, F. Becattini, D. Blaschke, M. Bleicher, C. Blume, E. Bratkovskaya, B. A. Brown, D. A. Brown, A. Camaiani, G. Casini, K. Chatziioannou, A. Chbihi, M. Colonna, M. D. Cozma, V. Dexheimer, X. Dong, T. Dore, L. Du, J. A. Dueñas, H. Elfner, W. Florkowski, Y. Fujimoto, R. J. Furnstahl, A. Gade, T. Galatyuk, C. Gale, F. Geurts, F. Gramegna, S. Grozdanov, K. Hagel, S. P. Harris, W. Haxton, U. Heinz, M. P. Heller, O. Hen, H. Hergert, N. Herrmann, H. Z. Huang, X.-G. Huang, N. Ikeno, G. Inghirami, J. Jankowski, J. Jia, J. C. Jiménez, J. Kapusta, B. Kardan, I. Karpenko, D. Keane, D. Kharzeev, A. Kugler, A. Le Fèvre, D. Lee, H. Liu, M. A. Lisa, W. J. Llope, I. Lombardo, M. Lorenz, T. Marchi, L. McLerran, U. Mosel, A. Motornenko, B. Müller, P. Napolitani, J. B. Natowitz, W. Nazarewicz, J. Noronha, J. Noronha-Hostler, G. Odyniec, P. Papakonstantinou, Z. Paulínyová, J. Piekarewicz, R. D. Pisarski, C. Plumberg, M. Prakash, J. Randrup, C. Ratti, P. Rau, S. Reddy, H.-R. Schmidt, P. Russotto, R. Ryblewski, A. Schäfer, B. Schenke, S. Sen, P. Senger, R. Seto, C. Shen, B. Sherrill, M. Singh, V. Skokov, M. Spaliński, J. Steinheimer, M. Stephanov, J. Stroth, C. Sturm, K.-J. Sun, A. Tang, G. Torrieri, W. Trautmann, G. Verde, V. Vovchenko, R. Wada, F. Wang, G. Wang, K. Werner, N. Xu, Z. Xu, H.-U. Yee, S. Yennello, and Y. Yin, Progress in Particle and Nuclear Physics **134**, 104080 (2024).

[101]J. Xu and P. Papakonstantinou, **105**, 044305, 044305 (2022).

[102]H. Gil, Y. Oh, C. H. Hyun, and P. Papakonstantinou, New Physics: Sae Mulli **67**, 456–461 (2017).

[103]H. Gil, P. Papakonstantinou, C. H. Hyun, T. .-.-S. Park, and Y. Oh, Acta Physica Polonica B **48**, 305 (2017).

[104]P. Papakonstantinou, T.-S. Park, Y. Lim, and C. H. Hyun, **97**, 014312, 014312 (2018).

[105]J. M. Lattimer and M. Prakash, Science **304**, 536–542 (2004).

[106]G. Baym, H. A. Bethe, and C. J. Pethick, **175**, 225–271 (1971).

[107]H. Heiselberg and V. Pandharipande, Annual Review of Nuclear and Particle Science **50**, 481–524 (2000).

[108]G. Burgio, H.-J. Schulze, I. Vidaña, and J.-B. Wei, Progress in Particle and Nuclear Physics **120**, 103879 (2021).

[109]A. Bauswein, A. Nikolaidis, G. Lioutas, H. Kochankovski, P. Char, C. Mondal, M. Oertel, L. Tolos, N. Chamel, and S. Goriely, *Stellar properties indicating the presence of hyperons in neutron stars*, 2025.

[110]J. M. Lattimer, Annual Review of Nuclear and Particle Science **71**, 433–464 (2021).

[111]D. G. Yakovlev, P. Haensel, G. Baym, and C. J. Pethick, Phys. Usp. **56**, 289–295 (2013).

[112]W. Baade and F. Zwicky, Phys. Rev. **46**, 76–77 (1934).

[113]W. Baade and F. Zwicky, Phys. Rev. **45**, 138 (1934).

[114]S. Woosley and T. Janka, Nature Physics **1**, 147–154 (2005).

[115]H.-T. Janka, K. Langanke, A. Marek, G. Martínez-Pinedo, and B. Müller, Physics Reports **442**, The Hans Bethe Centennial Volume 1906-2006, 38–74 (2007).

[116]A. Burrows and D. Vartanyan, Nature **589**, 29–39 (2021).

[117]L. Boccioli and L. Roberti, Universe **10** (2024).

[118]G. Gamow, Phys. Rev. **53**, 595–604 (1938).

[119]M. Wiescher, C. A. Bertulani, C. R. Brune, R. J. deBoer, A. Diaz-Torres, L. R. Gasques, K. Langanke, P. Navrátil, W. Nazarewicz, J. Okołowicz, D. R. Phillips, M. Płoszajczak, S. Quaglioni, and A. Tumino, Rev. Mod. Phys. **97**, 025003 (2025).

[120]S. Chandrasekhar, **74**, 81 (1931).

[121]M. V. Beznogov, D. Page, and E. Ramirez-Ruiz, The Astrophysical Journal **888**, 97 (2020).

[122]M. V. Beznogov, J. Novak, D. Page, and A. R. Raduta, The Astrophysical Journal **942**, 72 (2023).

[123]C. J. Pethick and D. G. Ravenhall, Annual Review of Nuclear and Particle Science **45**, 429–484 (1995).

[124]R. N. Manchester, Journal of Astrophysics and Astronomy **38**, 42 (2017).

[125]A. P. Igoshev, S. B. Popov, and R. Hollerbach, *Evolution of neutron star magnetic fields*, 2021.

[126]A. Hewish, S. J. Bell, J. D. H. Pilkington, P. F. Scott, and R. A. Collins, Nature **217**, 709–713 (1968).

[127]Fuentes, J. R., Espinoza, C. M., Reisenegger, A., Shaw, B., Stappers, B. W., and Lyne, A. G., AA **608**, A131 (2017).

[128]M. Antonelli, A. Montoli, and P. M. Pizzochero, "Insights into the physics of neutron star interiors from pulsar glitches", in *Astrophysics in the xxi century with compact stars* (World Scientific, 2022) Chap. Chapter 7, pp. 219–281.

[129]D. Viganò, N. Rea, J. A. Pons, R. Perna, D. N. Aguilera, and J. A. Miralles, Monthly Notices of the Royal Astronomical Society **434**, 123–141 (2013).

[130]A. Y. Potekhin, Physics-Uspekhi **57**, 735 (2014).

[131]G. Baym, C. Pethick, and P. Sutherland, **170**, 299 (1971).

[132]N. Chamel and P. Haensel, Living Reviews in Relativity **11**, 10 (2008).

[133]J. M. Pearson, S. Goriely, and N. Chamel, **83**, 065810, 065810 (2011).

[134]Fantina, A. F., De Ridder, S., Chamel, N., and Gulminelli, F., AA **633**, A149 (2020).

[135]A. Gezerlis, C. J. Pethick, and A. Schwenk, arXiv e-prints, arXiv:1406.6109, arXiv:1406.6109 (2014).

[136]B. Haskell and A. Sedrakian, "Superfluidity and superconductivity in neutron stars", in *The physics and astrophysics of neutron stars*, edited by L. Rezzolla, P. Pizzochero, D. I. Jones, N. Rea, and I. Vidaña (Springer International Publishing, Cham, 2018), pp. 401–454.

[137]D. G. Ravenhall, C. J. Pethick, and J. R. Wilson, **50**, 2066–2069 (1983).

[138]G. Baym, T. Hatsuda, T. Kojo, P. D. Powell, Y. Song, and T. Takatsuka, Reports on Progress in Physics **81**, 056902, 056902 (2018).

[139]A. Sedrakian, J.-J. Li, and F. Weber, "Hyperonization in Compact Stars", in *Astrophysics in the xxi century with compact stars. edited by c.a.z. vasconcellos. eisbn 978-981-12-2094-4. singapore: world scientific*, edited by C. A. Z. Vasconcellos (2022), pp. 153–199.

[140]R. C. Tolman, Phys. Rev. **55**, 364–373 (1939).

[141]J. R. Oppenheimer and G. M. Volkoff, Phys. Rev. **55**, 374–381 (1939).

[142]K. C. Gendreau, Z. Arzoumanian, and T. Okajima, in Space telescopes and instrumentation 2012: ultraviolet to gamma ray, Vol. 8443, edited by T. Takahashi, S. S. Murray, and J.-W. A. den Herder (International Society for Optics and Photonics, 2012), p. 844313.

[143]K. C. Gendreau, Z. Arzoumanian, P. W. Adkins, C. L. Albert, J. F. Anders, A. T. Aylward, C. L. Baker, E. R. Balsamo, W. A. Bamford, S. S. Benegalrao, D. L. Berry, S. Bhalwani, J. K. Black, C. Blaurock, G. M. Bronke, G. L. Brown, J. G. Budinoff, J. D. Cantwell, T. Cazeau, P. T. Chen, T. G. Clement, A. T. Colangelo, J. S. Coleman, J. D. Coopersmith, W. E. Dehaven, J. P. Doty, M. D. Egan, T. Enoto, T. W. Fan, D. M. Ferro, R. Foster, N. M. Galassi, L. D. Gallo, C. M. Green, D. Grosh, K. Q. Ha, M. A. Hasouneh, K. B. Heefner, P. Hestnes, L. J. Hoge, T. M. Jacobs, J. L. Jørgensen, M. A. Kaiser, J. W. Kellogg, S. J. Kenyon, R. G. Koenecke, R. P. Kozon, B. LaMarr, M. D. Lambertson, A. M. Larson, S. Lentine, J. H. Lewis, M. G. Lilly, K. A. Liu, A. Malonis, S. S. Manthripragada, C. B. Markwardt, B. D. Matonak, I. E. Mcginnis, R. L. Miller, A. L. Mitchell, J. W. Mitchell, J. S. Mohammed, C. A. Monroe, K. M. Montt de Garcia, P. D. Mulé, L. T. Nagao, S. N. Ngo, E. D. Norris, D. A. Norwood, J. Novotka, T. Okajima, L. G. Olsen, C. O. Onyeachu, H. Y. Orosco, J. R. Peterson, K. N. Pevear, K. K. Pham, S. E. Pollard, J. S. Pope, D. F. Powers, C. E. Powers, S. R. Price, G. Y. Prigozhin, J. B. Ramirez, W. J. Reid, R. A. Remillard, E. M. Rogstad, G. P. Rosecrans, J. N. Rowe, J. A. Sager, C. A. Sanders, B. Savadkin, M. R. Saylor, A. F. Schaeffer, N. S. Schweiss, S. R. Semper, P. J. Serlemitsos, L. V. Shackelford, Y. Soong, J. Struebel, M. L. Vezie, J. S. Villasenor, L. B. Winternitz, G. I. Wofford, M. R. Wright, M. Y. Yang, and W. H. Yu, in Space telescopes and instrumentation 2016: ultraviolet to gamma ray, Vol. 9905, edited by J.-W. A. den Herder, T. Takahashi, and M. Bautz, Society of Photo-Optical Instrumentation Engineers (SPIE) Conference Series (July 2016), 99051H.

[144]E. Fonseca, H. T. Cromartie, T. T. Pennucci, P. S. Ray, A. Y. Kirichenko, S. M. Ransom, P. B. Demorest, I. H. Stairs, Z. Arzoumanian, L. Guillemot, A. Parthasarathy, M. Kerr, I. Cognard, P. T. Baker, H. Blumer, P. R. Brook, M. DeCesar, T. Dolch, F. A. Dong, E. C. Ferrara, W. Fiore, N. Garver-Daniels, D. C. Good, R. Jennings, M. L. Jones, V. M. Kaspi, M. T. Lam, D. R. Lorimer, J. Luo, A. McEwen, J. W. McKee, M. A. McLaughlin, N. McMann, B. W. Meyers, A. Naidu, C. Ng, D. J. Nice, N. Pol, H. A. Radovan, B. Shapiro-Albert, C. M. Tan, S. P. Tendulkar, J. K. Swiggum, H. M. Wahl, and W. W. Zhu, Tha Astrophysical Journal Letters **915**, L12, L12 (2021).

[145]G. F. Burgio and I. Vidaña, Universe **6** (2020).

[146]J. B. Hartle, The Astrophysical Journal **150**, 1005 (1967).

[147]A. Montoli, “Constraints on neutron star structure from pulsar glitches”, PhD thesis (Universitá degli studi di Milano, 2020).

[148]B. Link, R. I. Epstein, and J. M. Lattimer, Phys. Rev. Lett. **83**, 3362–3365 (1999).

[149]A. Montoli, M. Antonelli, B. Haskell, and P. Pizzochero, Universe **7** (2021).

[150]D. Page and S. Reddy, Phys. Rev. Lett. **111**, 241102, 241102 (2013).

[151]É. É. Flanagan and T. Hinderer, **77**, 021502, 021502 (2008).

[152]I. I. Shapiro, Physical Review Letters **13**, 789–791 (1964).

[153]R. A. Hulse and J. H. Taylor, **195**, L51–L53 (1975).

[154] P. B. Demorest, T. Pennucci, S. M. Ransom, M. S. E. Roberts, and J. W. T. Hessels, Nature Astronomy **467**, 1081–1083 (2010).

[155] I. Vidaña, The European Physical Journal Plus **133**, 445 (2018).

[156] R. W. Romani, D. Kandel, A. V. Filippenko, T. G. Brink, and W. Zheng, Tha Astrophysical Journal Letters **934**, L17, L17 (2022).

[157] M. C. Miller, F. K. Lamb, A. J. Dittmann, S. Bogdanov, Z. Arzoumanian, K. C. Gendreau, S. Guillot, W. C. G. Ho, J. M. Lattimer, M. Loewenstein, S. M. Morsink, P. S. Ray, M. T. Wolff, C. L. Baker, T. Cazeau, S. Manthripragada, C. B. Markwardt, T. Okajima, S. Pollard, I. Cognard, H. T. Cromartie, E. Fonseca, L. Guillemot, M. Kerr, A. Parthasarathy, T. T. Pennucci, S. Ransom, and I. Stairs, The Astrophysical Journal Letters **918**, L28, L28 (2021).

[158] D. Choudhury, T. Salmi, S. Vinciguerra, T. E. Riley, Y. Kini, A. L. Watts, B. Dorsman, S. Bogdanov, S. Guillot, P. S. Ray, D. J. Reardon, R. A. Remillard, A. V. Bilous, D. Huppenkothen, J. M. Lattimer, N. Rutherford, Z. Arzoumanian, K. C. Gendreau, S. M. Morsink, and W. C. G. Ho, The Astrophysical Journal Letters **971**, L20, L20 (2024).

[159] L. Mauviard, S. Guillot, T. Salmi, D. Choudhury, B. Dorsman, D. González-Caniulef, M. Hoogkamer, D. Huppenkothen, C. Kazantsev, Y. Kini, J.-F. Olive, P. Stammler, A. L. Watts, M. Mendes, N. Rutherford, A. Schwenk, I. Svensson, S. Bogdanov, M. Kerr, P. S. Ray, L. Guillemot, I. Cognard, and G. Theureau, arXiv e-prints, arXiv:2506.14883, arXiv:2506.14883 (2025).

[160] T. E. Riley, A. L. Watts, P. S. Ray, S. Bogdanov, S. Guillot, S. M. Morsink, A. V. Bilous, Z. Arzoumanian, D. Choudhury, J. S. Deneva, K. C. Gendreau, A. K. Harding, W. C. G. Ho, J. M. Lattimer, M. Loewenstein, R. M. Ludlam, C. B. Markwardt, T. Okajima, C. Prescod-Weinstein, R. A. Remillard, M. T. Wolff, E. Fonseca, H. T. Cromartie, M. Kerr, T. T. Pennucci, A. Parthasarathy, S. Ransom, I. Stairs, L. Guillemot, and I. Cognard, The Astrophysical Journal Letters **918**, L27, L27 (2021).

[161] T. Hinderer, B. D. Lackey, R. N. Lang, and J. S. Read, Phys. Rev. D **81**, 123016 (2010).

[162] L. Blanchet, Living Reviews in Relativity **17**, 2, 2 (2014).

[163] K. Chatziioannou, General Relativity and Gravitation **52**, 109, 109 (2020).

[164] B. P. Abbott, others (LIGO Scientific Collaboration, and V. Collaboration), Phys. Rev. Lett. **121**, 161101, 161101 (2018).

[165] M. Onsi, A. K. Dutta, H. Chatri, S. Goriely, N. Chamel, and J. M. Pearson, **77**, 065805, 065805 (2008).

[166] J. Negele and D. Vautherin, Nuclear Physics A **207**, 298–320 (1973).

[167] F. Douchin and P. Haensel, **380**, 151–167 (2001).

[168] J. M. Pearson, N. Chamel, A. Y. Potekhin, A. F. Fantina, C. Ducoin, A. K. Dutta, and S. Goriely, **481**, 2994–3026 (2018).

[169] M. Fortin, C. Providência, A. R. Raduta, F. Gulminelli, J. L. Zdunik, P. Haensel, and M. Bejger, Phys. Rev. C **94**, 035804 (2016).

[170] J. M. Pearson, N. Chamel, S. Goriely, and C. Ducoin, Phys. Rev. C **85**, 065803 (2012).

[171] G. Grams, N. N. Shchechilin, T. Diverrès, A. F. Fantina, N. Chamel, and F. Gulminelli, Universe **11** (2025).

[172] T. Carreau, F. Gulminelli, N. Chamel, A. F. Fantina, and J. M. Pearson, Astronomy and Astrophysics **635**, A84, A84 (2020).

[173] W. G. Newton, M. Gearheart, and B.-A. Li, The Astrophysical Journal Supplement Series **204**, 9 (2012).

[174] T. Carreau, "Modeling the (proto)neutron star crust: toward a controlled estimation of uncertainties", PhD thesis (University of Normandie-Caen, 2020).

[175] U. J. Furtado and F. Gulminelli, Journal of Physics G: Nuclear and Particle Physics **48**, 015102 (2020).

[176] H. D. Thi, "A unified state equation for neutron stars and core-collapse supernovae", PhD thesis (University of Normandie-Caen, 2023).

[177] T. Carreau, F. Gulminelli, and J. Margueron, The European Physical Journal A **55**, 188 (2019).

[178] J. M. Pearson, N. Chamel, and A. Y. Potekhin, Phys. Rev. C **101**, 015802 (2020).

[179] F. Grill, J. Margueron, and N. Sandulescu, Phys. Rev. C **84**, 065801 (2011).

[180] A. Pastore, S. Baroni, and C. Losa, Phys. Rev. C **84**, 065807 (2011).

[181] M. Shelley and A. Pastore, Universe **6** (2020).

[182] Y. Lim and J. W. Holt, European Physical Journal A **55**, 209, 209 (2019).

[183] W. G. Newton, R. Preston, L. Balliet, and M. Ross, Physics Letters B **834**, 137481, 137481 (2022).

[184] F. Grill, H. Pais, C. Providência, I. Vidaña, and S. S. Avancini, Phys. Rev. C **90**, 045803 (2014).

[185] M. Brack, C. Guet, and H. .-.-B. Håkansson, Phys. Rep. **123**, 275–364 (1985).

[186] M. Pi, X. Vinas, M. Barranco, A. Polls, and A. Perez-Canyellas, Astronomy and Astrophysics supplement series **64**, 439–451 (1986).

[187] M. Onsi, H. Przysiezniak, and J. M. Pearson, Phys. Rev. C **55**, 3139–3148 (1997).

[188] P. Papakonstantinou, J. Margueron, F. Gulminelli, and A. R. Raduta, Phys. Rev. C **88**, 045805 (2013).

[189] F. Aymard, F. Gulminelli, and J. Margueron, Phys. Rev. C **89**, 065807 (2014).

[190] C. Ducoin, J. Margueron, C. Providência, and I. Vidaña, Phys. Rev. C **83**, 045810 (2011).

[191] C. Ducoin, P. Chomaz, and F. Gulminelli, Nuclear Physics A **789**, 403–425 (2007).

[192] C. Ducoin, "Rôle de l'isospin dans la transition de phase liquide-gaz de la matière nucléaire", Theses (Université de Caen, Oct. 2006).

[193] C. Ducoin, P. Chomaz, and F. Gulminelli, Nuclear Physics A **789**, 403–425 (2007).

[194] N. Martin and M. Urban, Phys. Rev. C **92**, 015803 (2015).

[195] J. M. Pearson, N. Chamel, and A. Y. Potekhin, Phys. Rev. C **101**, 015802, 015802 (2020).

[196] H. Dinh Thi, T. Carreau, A. F. Fantina, and F. Gulminelli, Astronomy and Astrophysics **654**, A114, A114 (2021).

[197] L. Scurto, H. Pais, and F. Gulminelli, Phys. Rev. D **109**, 103015 (2024).

[198] C. Huang, G. Raaijmakers, A. L. Watts, L. Tolos, and C. Providência, Monthly Notices of the Royal Astronomical Society **529**, 4650–4665 (2024).

[199]J. S. Read, B. D. Lackey, B. J. Owen, and J. L. Friedman, Phys. Rev. D **79**, 124032 (2009).

[200]D. Mroczek, M. Coleman Miller, J. Noronha-Hostler, and N. Yunes, Journal of Physics: Conference Series **2536**, 012006 (2023).

[201]W. Long, J. Meng, N. V. Giai, and S.-G. Zhou, Phys. Rev. C **69**, 034319 (2004).

[202]W. K. Hastings, Biometrika **57**, 97–109 (1970).

[203]"Model and D. A. Initiative", https://madai.phy.duke.edu/index-2.html.

[204]P. Klausner, G. Colò, X. Roca-Maza, and E. Vigezzi, Phys. Rev. C **111**, 014311 (2025).

[205]N. Schunck, ed., *Energy density functional methods for atomic nuclei*, 2053-2563 (IOP Publishing, 2019).

[206]M. Kortelainen, J. McDonnell, W. Nazarewicz, E. Olsen, P.-G. Reinhard, J. Sarich, N. Schunck, S. M. Wild, D. Davesne, J. Erler, and A. Pastore, Phys. Rev. C **89**, 054314 (2014).

[207]P. Becker, D. Davesne, J. Meyer, J. Navarro, and A. Pastore, Phys. Rev. C **96**, 044330 (2017).

[208]J. Erler, N. Birge, M. Kortelainen, W. Nazarewicz, E. Olsen, A. M. Perhac, and M. Stoitsov, Nature **486**, 509–512 (2012).

[209]P.-G. Reinhard, X. Roca-Maza, and W. Nazarewicz, Phys. Rev. Lett. **127**, 232501 (2021).

[210]R. Essick, I. Tews, P. Landry, and A. Schwenk, Phys. Rev. Lett. **127**, 192701 (2021).

[211]P.-G. Reinhard, X. Roca-Maza, and W. Nazarewicz, Phys. Rev. Lett. **129**, 232501 (2022).

[212]E. Yüksel and N. Paar, Phys. Lett. B **836**, 137622 (2023).

[213]L. Neufcourt, Y. Cao, S. A. Giuliani, W. Nazarewicz, E. Olsen, and O. B. Tarasov, Phys. Rev. C **101**, 044307 (2020).

[214]R. Navarro Pérez and N. Schunck, Phys. Lett. B **833**, 137336 (2022).

[215]Bayesian Methods in Nuclear Physics Workshop at INT (Seattle) https://archive.int.washington.edu/ 2a/.

[216]J. Stone and P.-G. Reinhard, Prog. in Part. and Nucl. Phys. **58**, 587–657 (2007).

[217]L.-W. Chen, B.-J. Cai, C. M. Ko, B.-A. Li, C. Shen, and J. Xu, Phys. Rev. C **80**, 014322 (2009).

[218]L.-W. Chen, C. M. Ko, B.-A. Li, and J. Xu, **82**, 024321, 024321 (2010).

[219]B. Sun, S. Bhattiprolu, and J. M. Lattimer, **109**, 055801, 055801 (2024).

[220]Y. K. Gupta, U. Garg, K. B. Howard, J. T. Matta, M. Şenyiğit, M. Itoh, S. Ando, T. Aoki, A. Uchiyama, S. Adachi, M. Fujiwara, C. Iwamoto, A. Tamii, H. Akimune, C. Kadono, Y. Matsuda, T. Nakahara, T. Furuno, T. Kawabata, M. Tsumura, M. N. Harakeh, and N. Kalantar-Nayestanaki, Phys. Lett. B **760**, 482–485 (2016).

[221]D. H. Youngblood, Y. .-.-W. Lui, H. L. Clark, B. John, Y. Tokimoto, and X. Chen, **69**, 034315, 034315 (2004).

[222]G. Colò and X. Roca-Maza, *User guide for the hfbcs-qrpa(v1) code*, 2021.

[223]G. Colò, L. Cao, N. Van Giai, and L. Capelli, Computer Physics Communications **184**, 142–161 (2013).

[224]F. Salvat, A. Jablonski, and C. J. Powell, Computer Physics Communications **165**, 157–190 (2005).

[225]M. D. McKay, R. J. Beckman, and W. J. Conover, Technometrics **21**, 239–245 (1979).

[226]P. S. Koliogiannis, E. Yuksel, T. Ghosh, and N. Paar, arXiv e-prints, arXiv:2503.17143, arXiv:2503.17143 (2025).

[227]G. Colò, N. Van Giai, J. Meyer, K. Bennaceur, and P. Bonche, Phys. Rev. C **70**, 024307 (2004).

[228]J. M. Lattimer and Y. Lim, ApJ **771**, 51 (2013).

[229]M. Kortelainen, T. Lesinski, J. Moré, W. Nazarewicz, J. Sarich, N. Schunck, M. V. Stoitsov, and S. Wild, **82**, 024313, 024313 (2010).

[230]S. Shlomo, V. M. Kolomietz, and G. Colò, Eur. Phys. Jou. A **30**, 23–30 (2006).

[231]E. Khan, J. Margueron, and I. Vidaña, **109**, 092501, 092501 (2012).

[232]X. Roca-Maza, M. Brenna, B. K. Agrawal, P. F. Bortignon, G. Colò, L.-G. Cao, N. Paar, and D. Vretenar, Phys. Rev. C **87**, 034301 (2013).

[233]E. Yüksel, T. Marketin, and N. Paar, **99**, 034318, 034318 (2019).

[234]Z. Zhang and L.-W. Chen, **108**, 024317, 024317 (2023).

[235]J. Xu, J. Zhou, Z. Zhang, W.-J. Xie, and B.-A. Li, Phys. Lett. B **810**, 135820, 135820 (2020).

[236]J. Xu, Chinese Physics Letters **38**, 042101, 042101 (2021).

[237]J. Xu, Z. Zhang, and B.-A. Li, **104**, 054324, 054324 (2021).

[238]Z. Zhang and L.-W. Chen, Phys. Rev. C **94**, 064326 (2016).

[239]R. Furnstahl, Nuclear Physics A **706**, 85–110 (2002).

[240]D. M. Rossi, P. Adrich, F. Aksouh, H. Alvarez-Pol, T. Aumann, J. Benlliure, M. Böhmer, K. Boretzky, E. Casarejos, M. Chartier, A. Chatillon, D. Cortina-Gil, U. Datta Pramanik, H. Emling, O. Ershova, B. Fernandez-Dominguez, H. Geissel, M. Gorska, M. Heil, H. T. Johansson, A. Junghans, A. Kelic-Heil, O. Kiselev, A. Klimkiewicz, J. V. Kratz, R. Krücken, N. Kurz, M. Labiche, T. Le Bleis, R. Lemmon, Y. A. Litvinov, K. Mahata, P. Maierbeck, A. Movsesyan, T. Nilsson, C. Nociforo, R. Palit, S. Paschalis, R. Plag, R. Reifarth, D. Savran, H. Scheit, H. Simon, K. Sümmerer, A. Wagner, W. Walu ś, H. Weick, and M. Winkler, Phys. Rev. Lett. **111**, 242503 (2013).

[241]S. Huth, C. Wellenhofer, and A. Schwenk, Physical Review C **103**, 025803, 025803 (2021).

[242]J. Piekarewicz, B. K. Agrawal, G. Colò, W. Nazarewicz, N. Paar, P.-G. Reinhard, X. Roca-Maza, and D. Vretenar, Phys. Rev. C **85**, 041302 (2012).

[243]W. Satuła and R. Wyss, Physics Letters B **393**, 1–6 (1997).

[244]W. Satuła, D. Dean, J. Gary, S. Mizutori, and W. Nazarewicz, Physics Letters B **407**, 103–109 (1997).

[245]W. Satuła and R. Wyss, Nuclear Physics A **676**, 120–142 (2000).

[246]W. Satuła, J. Dobaczewski, and W. Nazarewicz, Phys. Rev. Lett. **81**, 3599–3602 (1998).

[247]Y. K. Gupta, K. B. Howard, U. Garg, J. T. Matta, M. Şenyi ğit, M. Itoh, S. Ando, T. Aoki, A. Uchiyama, S. Adachi, M. Fujiwara, C. Iwamoto, A. Tamii, H. Akimune, C. Kadono, Y. Matsuda, T. Nakahara, T. Furuno, T. Kawabata, M. Tsumura, M. N. Harakeh, and N. Kalantar-Nayestanaki, Phys. Rev. C **97**, 064323 (2018).

[248]X. Roca-Maza and D. H. Jakubassa-Amundsen, Phys. Rev. Lett. **134**, 192501 (2025).

[249]W. G. Newton and G. Crocombe, Phys. Rev. C **103**, 064323 (2021).

[250]J. Xu, W.-J. Xie, and B.-A. Li, Phys. Rev. C **102**, 044316 (2020).

[251]J. M. Lattimer, Particles **6**, 30–56 (2023).

[252]S. Terashima, H. Sakaguchi, H. Takeda, T. Ishikawa, M. Itoh, T. Kawabata, T. Murakami, M. Uchida, Y. Yasuda, M. Yosoi, J. Zenihiro, H. P. Yoshida, T. Noro, T. Ishida, S. Asaji, and T. Yonemura, Phys. Rev. C **77**, 024317 (2008).

[253]A. Krasznahorkay, M. Fujiwara, P. van Aarle, H. Akimune, I. Daito, H. Fujimura, Y. Fujita, M. N. Harakeh, T. Inomata, J. Jänecke, S. Nakayama, A. Tamii, M. Tanaka, H. Toyokawa, W. Uijen, and M. Yosoi, Phys. Rev. Lett. **82**, 3216–3219 (1999).

[254]A. Trzci ńska, J. Jastrz bski, P. Lubi ński, F. J. Hartmann, R. Schmidt, T. von Egidy, and B. Kłos, Phys. Rev. Lett. **87**, 082501 (2001).

[255]P. Klausner, M. Antonelli, and F. Gulminelli, *Neutron star crust informed by nuclear structure data*, 2025.

[256]M. Antonelli, A. Montoli, and P. Pizzochero, "Insights into the physics of neutron star interiors from pulsar glitches", in (World Scientific, 2022), pp. 219–281.

[257]A. Pastore, M. Shelley, S. Baroni, and C. A. Diget, Journal of Physics G: Nuclear and Particle Physics **44**, 094003 (2017).

[258]CompOSE Core Team, S. Typel, M. Oertel, T. Klähn, D. Chatterjee, V. Dexheimer, C. Ishizuka, M. Mancini, J. Novak, H. Pais, C. Providência, A. R. Raduta, M. Servillat, and L. Tolos, European Physical Journal A **58**, 221, 221 (2022).

[259]M. Warda, X. Viñas, X. Roca-Maza, and M. Centelles, Phys. Rev. C **81**, 054309 (2010).

[260]X. Viñas, C. Gonzalez-Boquera, B. K. Sharma, and M. Centelles, Acta Phys. Pol. B Proc. Suppl. **10**, 259 (2017).

[261]F. Douchin and P. Haensel, Astron. Astrophys. **380**, 151–167 (2001).

[262]N. N. Shchechilin, N. Chamel, J. M. Pearson, A. I. Chugunov, and A. Y. Potekhin, Phys. Rev. C **109**, 055802 (2024).

[263]N. Shchechilin, *Private communication*, 2025.

[264]D. G. Ravenhall, C. J. Pethick, and J. M. Lattimer, Nuc. Phys. A **407**, 571–591 (1983).

[265]J. M. Lattimer and D. F. Swesty, Nuc. Phys. A **535**, 331–376 (1991).

[266]S. Antić, D. Chatterjee, T. Carreau, and F. Gulminelli, Journal of Physics G Nuclear Physics **46**, 065109 (2019).

[267]L. E. Balliet, W. G. Newton, S. Cantu, and S. Budimir, The Astrophysical Journal **918**, 79 (2021).

[268]G. Grams, J. Margueron, R. Somasundaram, and S. Reddy, Few-Body Systems **62**, 116, 116 (2021).

[269]A. Y. Potekhin, A. F. Fantina, N. Chamel, J. M. Pearson, and S. Goriely, Astronomy and Astrophysics **560**, A48, A48 (2013).

[270]B. Link, R. I. Epstein, and J. M. Lattimer, Phys. Rev. Lett. **83**, 3362–3365 (1999).

[271]N. Andersson, K. Glampedakis, W. C. G. Ho, and C. M. Espinoza, Phys. Rev. Lett. **109**, 241103 (2012).

[272]N. Chamel, Phys. Rev. C **85**, 035801 (2012).

[273]N. Chamel, Journal of Astrophysics and Astronomy **38**, 43, 43 (2017).

[274]L. Gavassino, M. Antonelli, and B. Haskell, Universe **7**, 28, 28 (2021).

[275]J. A. Sauls, N. Chamel, and M. A. Alpar, arXiv e-prints, arXiv:2001.09959, arXiv:2001.09959 (2020).

[276]Y. Minami and G. Watanabe, Phys. Rev. Res. **4**, 033141 (2022).

[277]K. Sekizawa, S. Kobayashi, and M. Matsuo, Phys. Rev. C **105**, 045807, 045807 (2022).

[278]N. Chamel, Phys. Rev. C **111**, 045803 (2025).

[279]G. Almirante and M. Urban, arXiv e-prints, arXiv:2503.21635, arXiv:2503.21635 (2025).

[280]N. Martin and M. Urban, Phys. Rev. C **94**, 065801 (2016).

[281]T. Delsate, N. Chamel, N. Gürlebeck, A. F. Fantina, J. M. Pearson, and C. Ducoin, Phys. Rev. D **94**, 023008, 023008 (2016).

[282]B. T. Reed, F. J. Fattoyev, C. J. Horowitz, and J. Piekarewicz, Phys. Rev. C **109**, 035803 (2024).

[283]E. Giliberti, G. Cambiotti, M. Antonelli, and P. M. Pizzochero, Monthly Notices of the Royal Astronomical Society **491**, 1064–1078 (2020).

[284]O. Komoltsev and A. Kurkela, Phys. Rev. Lett. **128**, 202701 (2022).

[285]O. Komoltsev, R. Somasundaram, T. Gorda, A. Kurkela, J. Margueron, and I. Tews, Phys. Rev. D **109**, 094030 (2024).

[286]Schlimme, Sören, Aulenbacher, Kurt, Baunack, Sebastian, Berger, Niklaus, Denig, Achim, Doria, Luca, Khoukaz, Alfons, Maas, Frank, Merkel, Harald, Sfienti, Concettina, and Thiel, Michaela, EPJ Web Conf. **303**, 06002 (2024).

[287]B.-A. Li, B.-J. Cai, W.-J. Xie, and N.-B. Zhang, Universe **7** (2021).

[288]A. Abac, R. Abramo, S. Albanesi, A. Albertini, A. Agapito, M. Agathos, C. Albertus, N. Andersson, T. Andrade, I. Andreoni, F. Angeloni, M. Antonelli, J. Antoniadis, F. Antonini, M. A. Sedda, M. C. Artale, S. Ascenzi, P. Auclair, M. Bachetti, C. Badger, B. Banerjee, D. Barba-Gonzalez, D. Barta, N. Bartolo, A. Bauswein, A. Begnoni, F. Beirnaert, M. Bejger, E. Belgacem, N. Bellomo, L. Bernard, M. G. Bernardini, S. Bernuzzi, C. P. L. Berry, E. Berti, G. Bertone, D. Bettoni, M. Bezares, S. Bhagwat, S. Bisero, M. A. Bizouard, J. J. Blanco-Pillado, S. Blasi, A. Bonino, A. Borghese, S. Borhanian, E. Bortolas, M. T. Botticella, M. Branchesi, M. Breschi, R. Brito, E. Brocato, F. S. Broekgaarden, T. Bulik, A. Buonanno, F. Burgio, A. Burrows, G. Calcagni, S. Canevarolo, E. Cappellaro, G. Capurri, C. Carbone, R. Casadio, R. Cayuso, P. Cerda-Duran, P. Char, S. Chaty, T. Chiarusi, M. Chruslinska, F. Cireddu, P. Cole, A. Colombo, M. Colpi, G. Compere, C. Contaldi, M. Corman, F. Crescimbeni, S. Cristallo, E. Cuoco, G. Cusin, T. D. Canton, G. Dalya, P. D'Avanzo, N. Davari, V. D. Luca, V. D. Renzis, M. D. Valle, W. D. Pozzo, F. D. Santi, A. L. D. Santis, T. Dietrich, E. Dimastrogiovanni, G. Domenech, D. Doneva, M. Drago, U. Dupletsa, H. Duval, I. Dvorkin, N. Elias-Rosa, S. Fairhurst, A. F. Fantina, M. Fasiello, M. Fays, R. Fender, T. Fischer, F. Foucart, T. Fragos, S. Foffa, G. Franciolini, J. Fumagalli, J. Gair, R. Gamba, J. Garcia-Bellido, C. Garcia-Quiros, L. A. Gergely, G. Ghirlanda, A. Ghosh, B. Giacomazzo, F. Gittins, I. F. Giudice, B. Goncharov, A. Gonzalez, S. Goriely, L. Graziani, G. Greco, L. Gualtieri, G. M. Guidi, I. Gupta, M. Haney, M. Hannam, J. Harms, A. Harutyunyan, B. Haskell, A. Haungs, N. Hazra, G. Hemming, I. S. Heng, T. Hinderer, A. van der Horst, Q. Hu, S. Husa, F. Iacovelli, G. Illuminati, G. Inguglia, D. I. Villalba, J. Janquart, K. Janssens,

A. C. Jenkins, I. Jones, B. Kacskovics, R. S. Klessen, K. Kokkotas, H.-J. Kuan, S. Kumar, S. Kuroyanagi, D. Laghi, A. Lamberts, G. Lambiase, F. Larrouturou, P. Leaci, M. Lenzi, A. Levan, T. G. F. Li, Y. Li, D. Liang, M. Limongi, B. Liu, F. J. Llanes-Estrada, E. Loffredo, O. Long, E. Lope-Oter, G. Lukes-Gerakopoulos, E. Maggio, M. Maggiore, M. Mancarella, M. Mapelli, P. Marchant, A. Margiotta, A. Mariotti, A. Marriott-Best, S. Marsat, G. Martinez-Pinedo, A. Maselli, S. Mastrogiovanni, I. Matos, A. Melandri, R. F. P. Mendes, J. M. S. de Souza, G. Mentasti, M. Mezcua, P. Mosta, C. Mondal, M. Moresco, T. Mukherjee, N. Muttoni, A. Nagar, H. Narola, L. Nava, P. N. Moreno, G. Nelemans, A. B. Nielsen, S. Nissanke, M. Obergaulinger, M. Oertel, G. Oganesyan, F. Onori, C. Pacilio, G. Pagliaroli, C. Palomba, P. T. H. Pang, P. Pani, L. Papalini, B. Patricelli, A. Patruno, A. Pedrotti, A. Perego, M. A. Perez-Garcia, C. Perigois, G. Perna, C. Peroux, J. Perret, D. Perrodin, A. Pesci, H. P. Pfeiffer, O. J. Piccinni, M. Pieroni, S. Piranomonte, L. Pompili, E. K. Porter, R. A. Porto, A. Pound, J. Powell, M. Puech, G. Pratten, A. Puecher, O. Pujolas, M. Quartin, A. R. Raduta, A. Ramos-Buades, A. Rase, M. Razzano, N. Rea, T. Regimbau, A. Renzini, P. Rettegno, A. Ricciardone, A. Riotto, A. Romero-Rodriguez, S. Ronchini, D. Rosinska, A. Rossi, S. Roy, D. Rubiera-Garcia, J. Rubio, P. Ruiz-Lapuente, V. Sagun, M. Sakellariadou, O. S. Salafia, A. Samajdar, N. Sanchis-Gual, A. Sanna, F. Santoliquido, B. Sathyaprakash, P. Schmidt, S. Schmidt, F. R. N. Schneider, R. Schneider, A. Sedrakian, G. Servant, A. Sevrin, L. Shao, H. O. Silva, P. Simakachorn, S. Smartt, T. P. Sotiriou, M. Spera, A. Stamerra, D. A. Steer, J. Steinhoff, N. Stergioulas, R. Sturani, D. Suarez, J. Suresh, S. Swain, M. Tagliazucchi, N. Tamanini, G. Tasinato, T. M. Tauris, J. Tissino, G. M. Tomaselli, S. Toonen, A. Torres-Forne, C. Turski, C. Ugolini, E. C. Vagenas, L. V. Dall'Armi, E. Valenti, R. Valiante, C. V. D. Broeck, M. van de Meent, L. A. C. van Son, M. Vanvlasselaer, M. Vaglio, V. Varma, J. Veitch, V. Vaskonen, S. D. Vergani, M. Wils, H. Witek, I. C. F. Wong, S. Yazadjiev, G. Yim, F. Acernese, H. Ahn, A. Allocca, A. Amato, M. Andres-Carcasona, G. Avallone, M. Bachlechner, P. Baer, S. Bagnasco, G. Balbi, F. Barone, E. Benedetti, C. Benning, S. Bini, J. L. B. Salcedo, V. Bozza, M. Bruno, T. Butz, M. Califano, E. Calloni, G. Carapella, A. Cardini, S. C. Subrahmanya, F. Chiadini, A. Chiummo, S. Cianetti, G. Ciani, E. Coccia, A. Contu, R. Cornelissen, A. Cozzumbo, L. Croney, M. Crosta, R. D'Agostino, S. Danilishin, S. D'Antonio, J. D. Bolle, J. Degallaix, M. D. Laurentis, R. della Monica, F. D. Marco, I. de Martino, R. D. Rosa, R. D. Salvo, R. D. Simone, C. Detavernier, G. Diaferia, M. D. Cesare, L. D. Fiore, M. D. Giovanni, S. D. Pace, J. Docherty, D. D'Urso, O. E. Mecherfi, L. Errico, F. Fabrizi, V. Fafone, V. Fanti, R. Fittipaldi, V. Fiumara, A. Freise, S. Funk, M. Gaedtke, F. Garufi, O. Gerberding, E. Giangrandi, C. Giunchi, V. Graham, M. Granata, V. Granata, A. Green, K. Haughian, L. Heisenberg, M. Hennig, S. Hild, V. L. Hoang, N. Holland, G. Iannone, K.-S. Isleif, R. Joppe, C.-H. Kim, C. Kim, K. Kim, E. Korb, M. Korobko, L. Kranzhoff, T. Kuhlbusch, G. Lacaille, A. Lartaux-Vollard, L. Lavezzi, P. Laycock, S. Lee, S. Lee, S. Lee, G. Losurdo, L. Lucchesi, H. Luck, A. Macquet, E. Majorana, V. Mangano, F. Martelli, I. Martin, M. Martinez, A. Masoni, L. Massaro, D. Melini, A. Mercurio, L. Mereni, A. L. Miller, L. Mirasola, A. Mitchell, I. Molinari, M. Montani, C. Mow-Lowry, R. Murgia, P. G. Murray, G. Muscas, L. Naticchioni, A. Nela, M. Nery, T. Niggemann, N. Nippe, J. Novak, A. Numic, M. Olivieri, M. Orsini, J. G. Park, D. Pascucci, A. Perreca, F. Piergiovanni, V. Pierro, L. Pinard, I. Pinto, M. Punturo, P. Puppo, F. Quochi, R. O. Rading, P. Rapagnani, M. Ricci, D. Rodrigues, R. Romano, D. Rozza, P. Saffarieh, F. Santucci, S. Schramm, B. Schwab, V. Sequino, L. S. Neto, L. Silenzi, A. M. Sintes, C. F. Sopuerta, A. Spencer, A. Stahl, J. Steinlechner, S. Steinlechner, R. Szabo, T. Thummler, E. Tofani, S. Torniamenti, R. Travaglini, L. Trozzo, M. P. Vaccaro, M. Valentini, P. Van, J. van Dongen, J. van Heijningen,

Z. van Ranst, M. Vardaro, P. Verdier, D. Vernieri, N. Wagner, J. Woehler, J. Wolf, G. Zavattini, A. Zink, and A. Zmija, *The science of the einstein telescope*, 2025.

[289] D. Reitze, R. X. Adhikari, S. Ballmer, B. Barish, L. Barsotti, G. Billingsley, D. A. Brown, Y. Chen, D. Coyne, R. Eisenstein, M. Evans, P. Fritschel, E. D. Hall, A. Lazzarini, G. Lovelace, J. Read, B. S. Sathyaprakash, D. Shoemaker, J. Smith, C. Torrie, S. Vitale, R. Weiss, C. Wipf, and M. Zucker, *Cosmic explorer: the u.s. contribution to gravitational-wave astronomy beyond ligo*, 2019.

[290] P. S. Ray, P. W. A. Roming, A. Argan, Z. Arzoumanian, D. R. Ballantyne, S. Bogdanov, V. Bonvicini, T. J. Brandt, M. Bursa, E. M. Cackett, D. Chakrabarty, M. Christophersen, K. M. Coderre, G. D. Geronimo, E. D. Monte, A. DeRosa, H. R. Dietz, Y. Evangelista, M. Feroci, J. J. Ford, C. Froning, C. L. Fryer, K. C. Gendreau, A. Goldstein, A. H. Gonzalez, D. Hartmann, M. Hernanz, A. Hutcheson, J. in ‘t Zand, P. Jenke, J. Kennea, N. M. Lloyd-Ronning, T. J. Maccarone, D. Maes, C. B. Markwardt, M. Michalska, T. Okajima, A. Patruno, S. C. Persyn, M. L. Phillips, C. Prescod-Weinstein, J. A. Redfern, R. A. Remillard, A. Santangelo, C. L. Schwendeman, C. Sleator, J. Steiner, T. E. Strohmayer, J. Svoboda, C. Tenzer, S. P. Thompson, R. W. Warwick, A. L. Watts, C. A. Wilson-Hodge, X. Wu, E. A. Wulf, and G. Zampa, *Strobe-x mission overview*, 2024.

[291] S.-N. Zhang, A. Santangelo, Y. Xu, H. Feng, F. Lu, Y. Chen, M. Ge, K. Nandra, X. Wu, M. Feroci, M. Hernanz, C. Liu, H. He, Y. Wang, W. Jiang, W. Cui, Y. Yang, J. Wang, W. Li, X. Liu, B. Meng, X. Wen, A. Zhang, J. Ma, M. Li, G. Li, L. Qi, J. Sun, T. Luo, H. Liu, X. Liu, F. Zhang, L. Luo, Y. Zhu, Z. Zhao, L. Sun, X. Yang, Q. Wu, J. Jiang, H. Shi, J. Liu, Y. Xu, S. Yang, L. Zhang, D. Han, N. Gao, J. Huo, Z. Zhang, H. Wang, X. Zhao, W. Cui, J. Wang, S. Wang, Z. Li, Z. Bao, Y. Liu, K. Wang, N. Wang, B. Wang, L. Wang, D. Wang, F. Ding, L. Sheng, P. Qiang, Y. Yan, Y. Liu, Z. Wu, Y. Liu, H. Chen, Y. Zhang, H. Liu, A. Altmann, T. Bechteler, V. Burwitz, C. Fiorini, P. Friedrich, N. Meidinger, R. Strecker, L. Baldini, R. Bellazzini, R. Bonino, A. Frassà, L. Latronico, S. Maldera, A. Manfreda, M. Minuti, M. Pesce-Rollins, C. Sgrò, S. Tugliani, G. Pareschi, S. Basso, G. Sironi, D. Spiga, G. Tagliaferri, A. Tykhonov, S. Paltani, E. Bozzo, C. Tenzer, J. Bayer, Y. Tuo, H. Liu, Y. Zhang, Z. Cai, H. Liu, W. Chen, C. Wang, T. He, Y. Chen, C. Qiu, Y. Zhang, J. Feng, X. Zhu, H. Zhou, S. Zheng, L. Song, H. Shi, J. Wang, S. Jia, Z. Jiang, X. Li, H. Zhao, J. Guan, J. Zhang, C. Li, Y. Huang, J. Liao, Y. You, H. Zhang, W. Wang, S. Wang, G. Ou, H. Hu, J. Shi, T. Cui, X. Jiang, Y. Cheng, H. Li, Y. Xu, S. Zane, C. Bambi, Q. Bu, S. Dall’Osso, A. D. Rosa, L. Gou, S. Guillot, L. Ji, A. Li, J. Mao, A. Patruno, G. Stratta, R. Taverna, S. Tsygankov, P. Uttley, A. L. Watts, X. Wu, R. Xu, S. Yi, G. Zhang, L. Zhang, W. Zhao, and P. Zhou, *The enhanced x-ray timing and polarimetry mission – extp for launch in 2030*, 2025.

[292] A. Bauswein, N.-U. F. Bastian, D. B. Blaschke, K. Chatziioannou, J. A. Clark, T. Fischer, and M. Oertel, Phys. Rev. Lett. **122**, 061102 (2019).

[293] A. Sharma, N. Schunck, and K. Wendt, Phys. Rev. Res. **7**, 023179 (2025).

[294] A. C. Semposki, C. Drischler, R. J. Furnstahl, J. A. Melendez, and D. R. Phillips, Phys. Rev. C **111**, 035804 (2025).

[295] W. Lynch and M. Tsang, Physics Letters B **830**, 137098 (2022).

[296] C. Ciampi, S. Mallik, F. Gulminelli, D. Gruyer, J. Frankland, N. Le Neindre, R. Bougault, A. Chbihi, L. Baldesi, S. Barlini, B. Borderie, A. Camaiani, G. Casini, I. Dekhissi, J. Dueñas, Q. Fable, F. Gramegna, M. Henri, B. Hong, S. Kim, A. Kordyasz, T. Kozik, I. Lombardo, O. Lopez, T. Marchi, S. Nam, J. Park, M. Pârlog, G. Pasquali,

S. Piantelli, G. Poggi, S. Valdré, G. Verde, and E. Vient, Physics Letters B **868**, 139815 (2025).

[297]H. Wolter, M. Colonna, D. Cozma, P. Danielewicz, C. M. Ko, R. Kumar, A. Ono, M. B. Tsang, J. Xu, Y.-X. Zhang, E. Bratkovskaya, Z.-Q. Feng, T. Gaitanos, A. Le Fèvre, N. Ikeno, Y. Kim, S. Mallik, P. Napolitani, D. Oliinychenko, T. Ogawa, M. Papa, J. Su, R. Wang, Y.-J. Wang, J. Weil, F.-S. Zhang, G.-Q. Zhang, Z. Zhang, J. Aichelin, W. Cassing, L.-W. Chen, H.-G. Cheng, H. Elfner, K. Gallmeister, C. Hartnack, S. Hashimoto, S. Jeon, K. Kim, M. Kim, B.-A. Li, C.-H. Lee, Q.-F. Li, Z.-X. Li, U. Mosel, Y. Nara, K. Niita, A. Ohnishi, T. Sato, T. Song, A. Sorensen, N. Wang, and W.-J. Xie, Progress in Particle and Nuclear Physics **125**, 103962 (2022).

[298]P.-G. Reinhard and W. Nazarewicz, Phys. Rev. C **95**, 064328 (2017).

[299]P.-G. Reinhard, J. O'Neal, S. M. Wild, and W. Nazarewicz, Journal of Physics G: Nuclear and Particle Physics **51**, 105101 (2024).

[300]X. Roca-Maza, Private communication, Mar. 20, 2023.

[301]A. Bulgac and V. R. Shaginyan, Nuclear Physics A **601**, 103–116 (1996).

Riassunto in Italiano

Nuclear Theory

I sistemi nucleari sono caratterizzati da una duplice difficoltà: da un lato, l'interazione tra nucleoni non è nota in modo esatto; dall'altro, i nuclei sono sistemi a molti corpi: anche conoscendo l'Hamiltoniana esatta, la risoluzione del problema resterebbe di difficoltà estrema. Per questo motivo, in fisica nucleare si sono sviluppate strategie approssimate, che spaziano dai metodi a campo medio, formulati nel quadro delle *Energy Density Functionals* (EDF), fino a tecniche *ab-initio* fondate su interazioni nucleone-nucleone realistiche.

Gli EDF, nati dalla teoria del funzionale di densità, (*Density Functional Theory*, DFT), nata in ambito elettronico ma oggi applicata con successo anche ai sistemi nucle, sono una delle strategie che hanno riscosso più successo negli anni. Il teorema di Hohenberg-Kohn stabilisce che la densità di particella singola $n(\mathbf{r})$ determina univocamente tutte le proprietà del sistema nello stato fondamentale. L'energia totale può essere espressa come funzionale della densità:

$$E[n] = F[n] + \int v_e(\mathbf{r}) n(\mathbf{r})\, d^3r,$$

dove $F[n]$ è un funzionale universale che comprende i contributi cinetici, diretti (Hartree) e di correlazione-scambio, e v_e è il campo esterno cui è sottopost il sistema. Il teorema garantisce che la densità che minimizza $E[n]$ rappresenta lo stato fondamentale del sistema. Tuttavia, poiché la forma esatta di $F[n]$ è ignota, la DFT si fonda su approssimazioni di natura fenomenologica. Dalla minimizzazione di $E[n]$, supponendo orbitali di particella singola, si trovano le equazioni di Kohn-Sham, formalmente simili a quelle di Schrödinger.

L'approccio di riferimento per i sistemi nucleari è l'approssimazione di *Hartree-Fock* (HF), che assume uno stato fondamentale espresso come determinante di Slater Φ di funzioni d'onda a singola particella. L'energia del sistema è data da

$$E_{HF} = \langle \Phi | T + V | \Phi \rangle,$$

dove T rappresenta l'energia cinetica e V l'interazione effettiva tra i nucleoni. La variazione di questa energia rispetto alle funzioni d'onda produce le equazioni di campo medio, analoghe alle equazioni di Kohn-Sham. La teoria di Hartree-Fock può essere riscritta nella più ampia, e in principio esatta, DFT.

L'introduzione di interazioni efficaci dipendenti dalla densità ha rappresentato un progresso fondamentale. Tali interazioni, come quella di Skyrme, permettono di riprodurre accuratamente le energie di legame e il comportamento di saturazione della materia nucleare. La forza di Skyrme, a raggio nullo, semplifica notevolmente i calcoli ed è uno degli EDF più utilizzati. In alternativa, la forza di Gogny introduce termini a raggio finito ma conserva una struttura dipendente dalla densità analoga a Skyrme. Questi modelli, pur fenomenologici, hanno mostrato un grande successo nel descrivere proprietà nucleari statiche e dinamiche. Tuttavia, la precisione sperimentale di molte osservabili sperimentali, come le energie di legame o i raggi di carica dei nuclei, è ancora oggi fuori dalla portata degli EDF.

La teoria è valida anche per descrivere eccitazioni collettive attraverso la *Random Phase Approximation* (RPA), ottenuta come limite lineare della teoria dipendente dal tempo (TDDFT) o dal formalismo particella-buco. La RPA considera le eccitazioni collettive dei nuclei, le cosiddette *risonanze giganti*, come combinazioni lineari di configurazioni particella-buco. Le risonanze giganti comprendono oscillazioni di diversa natura: isoscalari, dove protoni e neutroni oscillano in fase, e isovettoriali, dove oscillano fuori fase. Esse sono classificate per momento angolare L e spin S (monopolo, dipolo, quadrupolo, ecc.). In RPA, si possono ricavare le energie d'eccitazione di tali risonanze con un ragionevole accordo con le osservazioni sperimentali. Tuttavia, le larghezze non vengono riprodotte in modo adeguato. Metodi più sofisticati, come la seconda RPA o il *particle-vibration coupling*, migliorano notevolmente tale descrizione.

Il formalismo degli EDF è utile per descrivere anche la così detta materia nucleare. La materia nucleare è un sistema infinito e uniforme composto da neutroni e protoni a temperatura zero, che interagiscono esclusivamente tramite la forza nucleare. Sebbene rappresenti un'idealizzazione, la materia nucleare descrive bene l'interno dei nuclei, dove la densità è quasi costante e dominano le interazioni forti, e l'interno delle stelle di neutroni, caratterizzato da densità superiori a quella nucleare. I nuclei forniscono informazioni sulla materia simmetrica o quasi simmetrica, mentre le stelle di neutroni permettono di sondare materia altamente asimmetrica.

Di particolare interesse è l'equazione di stato nucleare (nEOS), cioè l'energia per particella e ub funzione della densità barionica totale $n_B = n_n + n_p$ e dell'asimmetria d'isospin $\delta = (n_n - n_p)/n_B$. Così $e(n_B, 0)$ rappresenta la materia simmetrica, mentre $e(n_B, 1)$ la materia pura di neutroni. Si può sviluppare $e(n_B, \delta)$ rispetto a δ:

$$e(n_B, \delta) \approx e(n_B, 0) + S(n_B)\delta^2 + o(\delta^4),$$

trattenendo solo i termini pari per via della simmetria di isospin. $S(n_B)$ definisce l'energia di simmetria, che rappresenta l'energia necessaria per trasformare tutti i protoni in neutroni.

La forza nucleare è caratterizzata dal fenomeno della saturazione: gli esperimenti di scattering d'elettroni mostrano che la densità interna dei nuclei è pressoché costante e pari a circa 0.16 fm^{-3}, indipendentemente dalla specie nucleare, il che implica una pressione nulla nel bulk nucleare. Dato che nell'interno dei nuclei la materia è pressoché simmetrica, questo implica che $e(n_B, 0)$ ha un minimo a circa 0.16 fm^{-3}. Questa densità viene definita n_{sat}, densità di saturazione nucleare. Di particolare interesse sono le derivate rispetto alla densità di $e(n_B, 0)$ e di $S(n_B)$

$$e(n_B, 0) = \sum_{k=0}^{4} \frac{1}{k!} \left(\frac{n_B - n_{\mathrm{sat}}}{3n_{\mathrm{sat}}} \right)^k X_{sat}^k + o(n_B - n_{\mathrm{sat}})^5,$$

$$S(n_B) = \sum_{k=0}^{4} \frac{1}{k!} \left(\frac{n_B - n_{\mathrm{sat}}}{3n_{\mathrm{sat}}} \right)^k X_{sym}^k + o(n_B - n_{\mathrm{sat}})^5,$$

dove i coefficienti

$$X_{sat}^k = (3n_{sat})^k \frac{\partial^k e(n_B, 0)}{\partial n_B^k}\bigg|_{n_B = n_{sat}}$$

$$X_{sym}^k = (3n_{sat})^k \frac{\partial^k S(n_B)}{\partial n_B^k}\bigg|_{n_B = n_{sat}}$$

sono detti parametri della materia nucleare (NMP). Gli NMP associati alla parte simmetrica includono: $E_{sat} = X_{sat}^0$, energia per particella a saturazione; $L_{sat} = X_{sat}^1 = 0$, condizione che definisce n_{sat}; $K_{sat} = X_{sat}^2$, incomprimibilità della materia nucleare. I parametri di ordine più alto (Q_{sat}, Z_{sat}) sono difficili da determinare poiché nuclei e osservabili note sondano solo densità attorno a n_{sat}.

In modo analogo, i parametri della simmetria comprendono: $E_{sym} = X_{sym}^0$, energia di simmetria a saturazione; $L_{sym} = X_{sym}^1$, che è connesso alla pressione della materia di neutroni a n_{sat}; $K_{sym} = X_{sym}^2$, la cui determinazione è complessa per via della correlazione con L_{sym}. Anche per Q_{sym} e Z_{sym} le conoscenze sono scarse.

Gli esperimenti nucleari e le osservazioni astrofisiche contribuiscono a determinare gli NMP. Le misure di raggi nucleari mostrano che le densità interne sono costanti e pari a n_{sat}, mentre le energie di legame indicano che $e(n_{sat}, 0) \approx -16$ MeV, valore associato al termine di volume del modello a goccia liquida. Le misure della pelle neutronica (*neutron skin*) dei nuclei ricchi di neutroni, ottenute tramite la differenza di sezione d'urto di scattering elastico di elettroni con elicità positiva e negativa (*parity-violating asymmetry*), permettono di stimare la pressione della materia neutronica e forniscono vincoli su L_{sym}. Altre informazioni provengono dalle risonanze giganti: le isoscalari sono sensibili alle proprietà di compressibilità (e quindi a K_{sat}), mentre le isovettoriali, come la polarizzabilità dipolare, sono collegate all'energia di simmetria e al suo andamento con la densità.

Le stelle di neutroni esplorano regioni di densità molto superiori a quelle nucleari, rendendole laboratori ideali per investigare il comportamento della materia neutronica densa. Le loro proprietà macroscopiche — masse, raggi, deformabilità tidale — dipendono direttamente dall'equazione di stato, e quindi dagli NMP.

Per ricavare l'nEOS da una EDF, è sufficiente mantenere i termini che sopravvivono nella materia uniforme, eliminando contributi di gradiente e spin-orbita.

Neutron stars

Le stelle di neutroni sono ciò che rimane del collasso gravitazionale di stelle massicce che segue l'esuarimento del combustibile nucleare. A seguito dell'esplosione di supernova, il nucleo della stella originale si contrae fino a raggiungere densità comparabili o superiori a quella di saturazione n_{sat}. In queste condizioni, protoni ed elettroni si combinano tramite cattura elettronica dando origine a un fluido denso di neutroni degeneri, da cui deriva il nome di stella di neutroni.

L'equilibrio idrostatico di tali oggetti è descritto dalle equazioni di Tolman-Oppenheimer-Volkoff (TOV), che rappresentano la generalizzazione relativistica delle classiche equazioni di equilibrio idrostatico. La soluzione di tali equazioni richiede la conoscenza dell'equazione di stato (*equation of state*, EOS) della materia stellare, che esprima la dipendenza della pressione P dalla densità n_B, e costituisce pertanto il principale legame tra la microfisica nucleare e le osservazioni astrofisiche.

La struttura di una stella di neutroni può essere idealmente suddivisa in diverse regioni concentriche, ognuna caratterizzata da una composizione e da un comportamento fisico differente. Lo strato più esterno, detto crosta esterna, è costituito da nuclei pesanti immersi in un gas di elettroni degeneri. Progredendo verso l'interno, la pressione crescente induce la cattura di elettroni sui protoni, dando origine a nuclei sempre più ricchi di neutroni. Quando la densità supera il cosiddetto *neutron drip point* ($\sim 10^{-4}\,\mathrm{fm}^{-3}$), i neutroni iniziano a fuoriuscire dai nuclei e formano un fluido libero che coesiste con il reticolo cristallino di nuclei, segnando il passaggio alla crosta interna. Tale regione, che si estende fino a densità prossime a $0.08\,\mathrm{fm}^{-3} \sim n_{sat}/2$, è di particolare interesse, poiché i neutroni liberi formano un superfluido macroscopico, che ha effetti su alcuni fenomeni che caratterizzano le stelle di neutroni, come i glitch. Negli stati più profondi della crosta interna si specula che appaiano nuclei con configurazioni esotiche, le cosiddette *pasta phases*, determinate dal bilanciamento tra forze nucleari e coulombiane.

Oltre la crosta interna vi è il cuore (*core*) della stella, dove neutroni e protoni formano un fluido omogeneo e fortemente interagente, con elettroni e muoni a garantire la neutralità elettrica. In questa regione, la composizione chimica della stella è determinata dal $\beta-$equilibrio beta e dalla condizione di neutralità elettrica: le reazioni $n \leftrightarrow p+e^-+\bar{\nu}_e$ stabiliscono il rapporto tra neutroni e protoni, mentre l'aggiunta dei muoni avviene quando il potenziale chimico degli elettroni supera la massa del muone. Il comportamento della materia nucleare in tali condizioni è regolato dalla EOS, che si ricava a partire dalla nEOS. Differenti EOS possono variare in termini di rigidità, cioè di risposta della pressione all'aumento di densità: EOS più rigide producono stelle di neutroni con massa massima più elevata e raggio maggiore, mentre EOS più morbide portano a configurazioni più compatte.

Risolvendo le equazioni TOV per diverse condizioni iniziali, si ottiene una relazione tra la massa e il raggio di una stella di neutroni. La relazione massa-raggio rappresenta uno dei principali strumenti osservativi per testare i modelli microscopici della materia densa, dato che l'unica incognita nelle TOV è l'EOS, che rappresenta la nostra ipotesi sul comportamento della materia all'interno delle stelle. Osservazioni di pulsar binarie hanno permesso di determinare con grande precisione masse di circa due masse solari, come nel caso delle sorgenti PSR J0348+0432 e PSR J0740+6620. Al contrario, la misura dei raggi è più complessa e soggetta a incertezze sistematiche, ma le osservazioni di raggi X mediante la missione NICER riescono a misurare massa e raggio di una singola stella, quindi determinando un'area nel piano massa-raggio dove la relazione imposta dalle TOV deve passare.

Un'altra importante osservabile astrofisica che dipende unicamente dalla EOS è la così detta deformabilità tidale. Un sistema binario di stelle di neutroni emette costantemente onde gravitazionali. Nel tempo la distanza tra le due stelle diminuisce, e si deformano progressivamente a causa del campo gravitazionale della compagna. In prossimità del collasso (*binary neutron star merger*, BNM), le onde gravitazionali sono particolarmente distorte dalla deformazione, e, rilevandole, possiamo misurare la deformabilità tidale (evento classificato come GW170817).

Come anticipato, L'EOS si calcola, nelle diverse regioni della stella, a partire dalla nEOS. Nella crosta interna, bisogna tenere conto della presenza del reticolo: spesso si divide in celle usando l'approssimazione di Wiegner–Seitz, accoppiata con tecniche Hartree–Fock–Bogoliubov o Extended Thomas–Fermi per trovarne la composizione ideale. Nel cuore della stella, si minimizza l'energia del gas di protoni, neutroni, elettroni e muoni con il vincolo del $\beta-$equilibrio e della neutralità elettrica. L'EOS quindi rappresenta il collegamento fondamentale tra la microfisica delle interazioni nucleari e la macrofisica delle osservazioni astrofisiche. Se una EOS predice proprietà della stella non compatibili con le osservazioni astrofisiche, allora va scartata.

Tra le possibili scelte per la descrizione della materia nucleare a densità superiori della saturazione, il meta-model (MM) è sicuramente una delle strade che offre più flessibilità.

Fu ideato per imitare il comportamento delle nEOS tipo Skyrme a densità sotto saturazione, ma per essere più libero nel comportamento sopra. I suoi paramentri sono i NMP definiti nel primo capitolo. Le nostre analisi sulle stelle di neutroni saranno eseguite con questo strumento matematico.

Bayesian inference with Skyrme EDF

Vogliamo quindi, per prima cosa, studiare le proprietà della materia nucleare attraverso gli esperimenti sui nuclei. Mostreremo i risultati di un'analisi dei parametri del funzionale di Skyrme, con l'obiettivo di ottenere una stima quantitativa delle incertezze teoriche e la capacità di riprodurre contemporaneamente una serie di osservabili di diverso tipo (*ground state*, eccitazioni collettive). Attraverso l'inferenza Bayesiana, potremo ricostruire la distribuzione di probabilità dei parametri di un modello, invece di stime dei loro miglior valori. Questo permette di valurarne meglio l'errore e di studiarne le potenzialità predittive.

Abbiamo eseguito due inferenze: una utilizzando solo dati da nuclei doppiamente magici e una includendo anche nuclei open-shell. La differenza risiede unicamente nella scelta delle osservabili; per il resto, il setup è identico. Abbiamo espresso gli usuali parametri $t_0, x_0, \ldots$ di Skyrme in funzione di cinque NMP (n_{sat}, E_{sat}, K_{sat}, E_{sym} e L_{sym}, le masse efficaci isoscalare m_0^*/m e isovettoriale m_1^*/m, due parametri di superficie G_0 e G_1 e il parametro di spin orbita W_0. Poiché dall'esperienza passata conosciamo, a grandi linee, gli intervalli entro cui questi parametri si trovano, abbiamo assunto un prior uniforme.

Per le osservabili, abbiamo selezionato proprietà dello stato fondamentale e proprietà di eccitazioni collettive. Per il *ground state*, abbiamo l'energie di legame $B.E.$, raggi di carica R_{ch} e splitting spin-orbita ΔE_{SO}, assegnandovi come errore la tipica precisione con cui EDF riescono a riprodurre queste osservabili (2 MeV per $B.E.$, 0.05 fm per R_{ch} e 0.5 MeV per ΔE_{SO}). Per le risonanze isoscalari e isovettori abbiamo scelto le energie giganti delle risonanze giganti isoscalari di monopolo (ISGMR) e quadrupolo (ISGQR) E^{IS}_{GMR}, E^{IS}_{GQR}, con errori di 0.5 MeV, e la *energy weighted sum rule* EWSR $m(1)$ della risonanza gigante di dipolo isovettoriale (IVGDR), la polarizzabilità α_D e la *parity-violating asymmetry* A_{PV}. Per queste ultime tre abbiamo usato errori sperimentali.

Utilizziamo il codice `hfbcs-qrpa` per calcolare tutte le osservabili a partire da un set di parametri, usando tecniche Hartree–Fock per le proprietà di *ground state* e RPA per quelle eccitate; fa eccezione A_{PV}, per cui utilizziamo il codice ELSEPA.

L'inferenza Bayesiana, per campionare la posterior, ha bisogno di calcolare per diversi milioni di set di parametri il valore di ciascuna osservabile. È un metodo quindi applicabile solo se i nostri metodi numerici hanno un tempo d'esecuzione istantaneo. Al contrario, i conti RPA richiedono diversi minuti. Per ovviare a questo problema, impieghiamo un emulatore, il software MADAI, che si basa sui processi Gaussiani. Questo software, imparando da una griglia di risultati rappresentativi dei codici `hfbcs-qrpa` e ELSEPA, è in grado di emulare tutti i risultati dei nostri codici in un tempo trascurabile. Poiché il risultato dell'inferenza è legato alla capacità dell'emulatore di riprodurre correttamente i codici originali, ne valutiamo la *performance* in ciò che chiamiamo validazione. Preso un campione di parametri di test, la validazione confronta i valori emulati con i risultati del codice originale; un emulatore è accettabile se almeno il 90% dei punti rientra nell'intervallo di errore. Tutte le inferenze hanno superato questa verifica.

Nella prima inferenza consideriamo osservabili dei nuclei doppiamente magici, aggiungendole progressivamente per valutare l'impatto sul posterior: prima le energie di legami e i raggi di carica, poi gli splitting spin-orbita, poi le polarizzabilità, quindi le energie

Table D.2: Medie μ e deviazioni standard σ delle distribuzioni posteriori marginalizzate per tutte le inferenze. Le loro unità sono: fm^{-3} per n_{sat}; MeV per E_{sat}, K_{sat}, E_{sym} e L_{sym}; MeV·fm^5 per G_0, G_1 e W_0. Le masse efficaci isoscalare e isovettoriale $m^*_{0,1}/m$ sono numeri.

		Solo nuclei Doppiamente magici	Nuovi dati + open-shell	Nuovi dati + open-shell (no ^{208}Pb A_{PV})
n_{sat}	μ	0.161	0.160	0.160
	σ	0.004	0.003	0.003
E_{sat}	μ	-15.94	-16.08	-16.05
	σ	0.10	0.09	0.09
K_{sat}	μ	219	238	236
	σ	10	10	10
E_{sym}	μ	29.4	32.3	30.5
	σ	1.6	2.0	2.0
L_{sym}	μ	16.1	39.8	24.9
	σ	14.7	16.6	16.7
G_0	μ	125	133	129
	σ	10	12	11
G_1	μ	9	8	2
	σ	36	44	44
W_0	μ	129	134	132
	σ	15	17	17
m^*_0/m	μ	0.91	0.89	0.91
	σ	0.08	0.08	0.08
m^*_1/m	μ	0.71	0.71	0.71
	σ	0.02	0.02	0.02
v_0	μ	–	222	223
	σ	–	28	27

d'eccitazione delle risonanze giganti e la EWSR, e infine le due A_{PV}. Masse e raggi vincolano rispettivamente E_{sat}, W_0 e n_{sat}; gli spin-orbit splitting riducono leggermente la media e la larghezza di W_0 e favoriscono m^*_0 nella parte alta dell'intervallo. K_{sat} e le masse efficaci sono poco vincolate fino all'inclusione delle risonanze, che determinano K_{sat}, m^*_0/m e m^*_1/m tramite l'EWSR IVGDR. La polarizzabilità α_D restringe significativamente E_{sym} e L_{sym}, inizialmente poco vincolati, ma legati da una correlazione positiva. L'inclusione dei A_{PV} di ^{48}Ca e ^{208}Pb genera qualche leggera modifica, nelle distribuzioni di E_{sym} e L_{sym}, ma non si sposta drasticamente dai valori determinati con la polarizzabilità. Le distribuzioni marginali dei parametri confrontate con Skyrme pubblicati mostrano E_{sat} e n_{sat} compatibili, K_{sat} leggermente più basso, masse efficaci, G_0, G_1, W_0 in linea. Invece, troviamo valori di E_{sym} e L_{sym} più bassi di quanto trovato nel passato. I risultati dell'ultima inferenza sono riassunti nella prima colonna della Tabella D.2.

Il motivo è il seguente: le energie di legame, impongono vincoli severi sulla correlazione tra E_{sym} e L_{sym}. Le polarizzabilità α_D di ^{208}Pb e ^{48}Ca mostrano una dipendenza molto ripida da L_{sym}. Le asimmetrie A_{PV}, invece, dipendono da L_{sym} in modo più dolce. Questo meccanismo spinge la soluzione verso valori relativamente bassi di E_{sym} e L_{sym}, in particolare per $E_{sym} \in (28, 30)$ MeV, dove la likelihood presenta un massimo netto. Di conseguenza, la richiesta simultanea di riprodurre $B.E.$ e α_D entro le incertezze sperimentali conduce a posteriori concentrati verso valori relativamente bassi dei parametri isovettori, spiegando la differenza rispetto ad altri studi che attribuiscono pesi minori alle energie di legame.

Per mitigare possibili *bias* dovuti all'uso esclusivo di nuclei doppiamente magici, particolarmente complessi per gli EDF da descrivere, abbiamo esteso il set di osservabili includendo nuclei open-shell, rimuovendo quelli simmetrici. Il nuovo insieme comprende energie di legame di isotopi di Ca, Sn e Pb, il raggio di carica di ^{50}Ca e il gap di pairing neutronico Δ_n di ^{120}Sn. L'inclusione di nuclei aperti richiede l'aggiunta del termine di pairing volumetrico con forza v_0, trattata come nuovo parametro con prior uniforme $v_0 \in (150, 350)$ MeV fm^3.

Abbiamo aggiornato inoltre il valore sperimentale di due osservabili rilevanti: (i) l'energia del risonanza monopolare isoscalare di ^{90}Zr, ora misurata a $E^{IS}_{GMR} = 18.7$ MeV, che spinge K_{sat} verso valori maggiori e quindi n_{sat} verso valori leggermente minori; (ii) le A_{PV}, che richiedono una correzione QED. La correzione riduce il valore sperimentale efficace, spingendo L_{sym} verso valori più alti in virtù della correlazione inversa tra A_{PV} e L_{sym}.

Le distribuzioni posteriori risultanti mostrano che n_{sat} ed E_{sat} subiscono variazioni moderate dovute principalmente al nuovo valore del monopolo isoscalare, mentre E_{sym} e L_{sym} aumentano rispetto al caso senza open-shell: E_{sym} tende a valori intorno a 30–32 MeV, e L_{sym} si sposta verso 25–40 MeV a seconda dell'inclusione o meno della A_{PV} di ^{208}Pb. Gli altri parametri (come G_0, G_1, W_0 e le masse efficaci) rimangono sostanzialmente stabili. Nonostante la maggiore libertà introdotta, il vincolo delle polarizzabilità continua a favorire valori relativamente bassi di L_{sym}. I risulati delle inferenze con o senza ^{208}Pb A_{PV} sono nelle ultime due colonne della Tabella D.2.

La qualità della riproduzione delle osservabili rimane paragonabile a quella ottenuta senza i nuclei open-shell. L'uso del nuovo E^{IS}_{GMR} peggiora la riproduzione del monopolo di ^{208}Pb, mentre sorgono dubbi sull'utilità di inserire ^{208}Pb A_{PV} in queste analisi, dato che ha un effetto notevole sui risultati, senza però che il modello sia in grado di riprodurlo.

Bayesian Inference on Nuetron star properties

Utilizziamo ora la distribuzione posterior dei funzionali Skyrme appena ricavata come prior in una nuova inferenza Bayesiana, dove le osservabili ora provengono da osservazioni astrofisiche.

L'inferenza bayesiana valuta quali EOS soddisfano vincoli astrofisici, tra cui massa massima di una stella di neutroni, deformabilità tidale da GW170817 e misure massa-raggio da NICER, oltre a osservabili della crosta come il momento d'inerzia, rilevante per i glitch dei pulsar.

L'EOS nella crosta è calcolata tramite l'approssimazione ETF, parametrizzando i profili di densità con funzioni tipo Woods-Saxon. Introduciamo ulteriori approssimazioni per ridurre il costo computazionale, che riducono il numero di parametri variazionali da 8 a 5. L'algoritmo incontra purtroppo instabilità numeriche prima della transizione crosta-cuore. Per tale ragione, estrapoliamo linearmente la densità a cui avviene questa transizione come la densità in cui la fase inomogenea diventa meno conveniente, dal punto di vista energetico, di quella omogenea. Abbiamo testato questo metodo sulla nota interazione SLy4, e abbiamo trovato risultati assai simili a quelli pubblicati in letteratura. Lo confronteremo, a livello statistico, con metodi alternativi per trovare il punto di transizione: la crosta calcolata con il compressible liquid drop model (CLDM) o con l'instabilità spinodale dinamica.

Per descrivere la materia omogenea nel cuore della stella, invece di usare direttamente la nEOS derivata da Skyrme, ne utilizziamo l'equivalente MM. La mappa da Skyrme a

MM è pensata in modo tale che, a densità sotto saturazione, dove le informazioni degli esperimenti nucleari sono più rilevanti, il MM si comporti come Skyrme; a densità sopra saturazione, dove non abbiamo molte informazioni, il comportamento del MM potrà essere radicalmente diverso da quello di Skyrme.

La likelihood totale combina informazioni da: massima massa di PSR J0740+6620, deformabilità tidale GW170817, misure massa-raggio NICER, e coerenza con le bande χ-EFT per la materia neutronica. Per la stima del posteriori si estraggono 10^5 campioni dal prior nucleare, per ciascuno si calcola la EOS $\beta-$equilibrata e si scartano i modelli instabili (pressione che diminuisce con la densità) o acausali (velocità del suono superiore a quella della luce). La distribuzione di quelli rimanenti, pesata con la likelihood, è il posterior.

Guardiamo ora i risultati. Le distribuzioni dei parametri isoscalari sono simili tra prior e posteriori, tranne Q_{sat} che viene spostato verso valori positivi dalle osservazioni astrofisiche, indicando che il settore isoscalare è già ben vincolato dai dati di fisica nucleare, eccetto ad alte densità, dove la necessità di sostenere stelle di neutroni molto massicce comporta un indurimento dell'EOS. I parametri isovettori sono influenzati principalmente dai vincoli teorici di tipo chiral, con un incremento dei valori medi di E_{sym} e L_{sym}, mentre i vincoli astrofisici apportano modifiche marginali. I parametri di superficie e le masse efficaci risultano ben determinati dai dati di struttura nucleare e non sono significativamente modificati dai vincoli aggiuntivi.

I corner plot evidenziano le correlazioni tra i parametri, confermando che l'informazione astrofisica non altera le correlazioni imposte dai dati nucleari. L'energia per particella della materia di neutroni puri (PNM) calcolata con Skyrme mostra una buona compatibilità con le predizioni chiral, con la posterior fortemente coincidente con la banda prevista dalle simulazioni ab-initio.

Per quanto riguarda il punto di transizione crosta-core (*crust-core*, CC), il posterior bayesiano indica valori di densità n_{cc} e pressione P_{cc} coerenti tra le stime ETF e CLDM, mentre la stima basata sull'instabilità spinodale dinamica tende a sottostimare sia il valore medio sia la dispersione, fornendo quindi un limite inferiore. La composizione della crosta, calcolata tramite metodo variazionale ETF, mostra un aumento del numero di nucleoni del cluster e della densità del gas di neutroni verso il nucleo, mentre il numero di protoni Z diminuisce, rispecchiando l'arricchimento in neutroni.

Passando a proprietà globali della stella, il raggio della crosta R_c e il momento d'inerzia I_c sono strettamente correlati alle proprietà della transizione crosta-nucleo e mostrano buone convergenze tra ETF e CLDM, mentre lo spinodal fornisce valori inferiori.

L'attività dei glitch, come osservata nel pulsar Vela, può essere spiegata con il momento d'inerzia della crosta se si assume un ipotetico scenario di entrainment minimo, in cui solo i neutroni legati al cluster contribuiscono al momento d'inerzia superfluido, compatibile con le osservazioni a meno che la massa di Vela superi $2M_\odot$. In caso di forte entrainment, la spiegazione crostale dei glitch sarebbe possibile solo per masse stellari molto basse ($M \lesssim 1.1M_\odot$).

L'EOS della stella e la densità di energia mostrano una debole dipendenza dall'interazione nucleare fino a circa $4n_{sat}$. La pressione risultante è in accordo con le limitazioni derivanti dalle osservazioni GW170817, ma con distribuzioni più strette, evidenziando l'apporto informativo della fisica nucleare. L'EOS è morbida vicino a saturazione e si irrigidisce rapidamente per raggiungere la massa massima osservata di 2 $M_\odot$. La velocità del suono mostra un aumento rapido tra $1-2n_{sat}$, corrispondente all'indurimento dell'EOS. L'energia di simmetria è ben determinata fino a saturazione e più dispersa ad alte densità, riflettendo la libertà dei parametri di ordine superiore.

Infine, la relazione massa-raggio mostra buone corrispondenze con i dati NICER e con risultati precedenti, con distribuzioni più strette e raggi leggermente più piccoli per stelle di massa inferiore a $1.5M_{\odot}$, effetto diretto della morbidezza dell'energia di simmetria predetta dai dati di struttura nucleare.

Conclusions

In questa tesi abbiamo studiato le proprietà dell'equazione di stato nucleare attraverso un approccio bayesiano in due fasi: la prima basata su dati sperimentali nucleari, la seconda utilizzando i risultati della prima per analizzare osservazioni di stelle di neutroni. Abbiamo impiegato il tradizionale Skyrme EDF all'interno di un *framework* bayesiano, considerando proprietà allo stato fondamentale (energie di legame, raggi di carica, splitting spin-orbita) e stati eccitati (risonanze giganti isoscalari e isovettori), inclusi l'asimmetria che viola la parità A_{PV} e la polarizzabilità dipolare α_D per ^{48}Ca e ^{208}Pb. Queste osservabili sono rilevanti per la materia asimmetrica e lo studio delle NS, anche se nessun modello riproduce simultaneamente ^{208}Pb A_{PV} e gli altri osservabili al livello 1σ, evidenziando la tensione PREX–CREX.

A causa dell'elevato costo computazionale dei calcoli, abbiamo utilizzato emulatori basati su processi gaussiani tramite il pacchetto MADAI. Le prime inferenze hanno riguardato nuclei doppiamente magici, aggiungendo progressivamente vincoli per comprenderne l'influenza. I posterior multidimensionali dei parametri Skyrme, espressi in termini di parametri della materia nucleare e parametri di superficie e spin-orbita dell'EDF, risultano in accordo con la letteratura precedente, tranne per L_{sym} e, in misura minore, E_{sym}, che risultano più bassi ($L_{sym} = 16.1 \pm 14.7$ MeV, $E_{sym} = 29.4 \pm 1.6$ MeV). Questi valori bassi derivano dalla necessità di riprodurre contemporaneamente energie di legame e polarizzabilità dipolare, mentre ^{208}Pb A_{PV} richiederebbe L_{sym} più alto, accentuando la tensione.

Affinando il *dataset*, includendo nuclei open-shell e rimuovendo quelli $N = Z$, i posteriori di E_{sym} e L_{sym} aumentano ($E_{sym} = 32.3 \pm 2.0$ MeV, $L_{sym} = 39.8 \pm 16.6$ MeV), mentre escludendo ^{208}Pb A_{PV} si ottengono valori più moderati ($E_{sym} = 30.5 \pm 2.0$ MeV, $L_{sym} = 24.9 \pm 16.6$ MeV). I risultati restano compatibili con la maggior parte degli osservabili, pur permanendo la tensione PREX–CREX, che richiede nuovi esperimenti come MREX.

La seconda parte della tesi ha utilizzato i posteriori nucleari come prior per un'analisi bayesiana dell'EOS delle NS, combinando vincoli da massa massima osservata, deformabilità tidale di GW170817, misure simultanee massa-raggio da NICER e calcoli ab initio della materia neutronica a bassa densità. L'approccio integrato consente di considerare correttamente le correlazioni nucleari e migliora la stima della transizione crosta-nucleo. Troviamo un EOS più morbido attorno alla saturazione, con concavità in $n_{sat} \lesssim n_B \lesssim 2n_{sat}$, riflettendo l'energia di simmetria morbida derivata dai dati nucleari. I vincoli astrofisici influenzano significativamente E_{sym} e L_{sym}, spostandone le distribuzioni verso circa 30 MeV e scartando valori negativi di L_{sym} incompatibili con χEFT.

Questo lavoro fornisce una base per studi futuri, inclusi EDF più flessibili (ad esempio Fayans, Gogny, RMF o KIDS) per ridurre le incertezze legate al modello e tecniche bayesiane avanzate come il model mixing per ottenere distribuzioni di parametri della materia nucleare più indipendenti dal modello utilizzato. È inoltre importante identificare il set minimo di osservabili nucleari necessari per vincolare la materia nucleare e migliorare la modellizzazione della crosta con metodi più raffinati come ETF o HFB combinati con emulatori. Nuovi posteriori nucleari basati su EDF differenti potrebbero avere un impatto significativo nello studio dell'EOS delle NS, in particolare per i parametri di ordine superiore e le densità estreme.

Résumé en Français

Malheureusement, ma connaissance du français n'est pas suffisamment approfondie pour me permettre de rédiger un résumé détaillé de ma thèse. Pour cette raison, j'ai traduit, avec l'aide de l'intelligence artificielle, le résumé italien en français.

Nuclear Theory

Les systèmes nucléaires sont caractérisés par une double difficulté : d'une part, l'interaction entre nucléons n'est pas connue de manière exacte ; d'autre part, les noyaux sont des systèmes à plusieurs corps : même en connaissant l'Hamiltonien exact, la résolution du problème resterait extrêmement complexe. Pour cette raison, la physique nucléaire a développé des stratégies approximatives allant des méthodes de champ moyen, formulées dans le cadre des *Energy Density Functionals* (EDF), jusqu'aux techniques *ab-initio* fondées sur des interactions nucléon-nucléon réalistes.

Les EDF, issus de la théorie du fonctionnel de densité (*Density Functional Theory*, DFT), initialement développée dans le domaine électronique mais aujourd'hui appliquée avec succès aux systèmes nucléaires, constituent l'une des stratégies qui ont obtenu le plus grand succès au fil des années. Le théorème de Hohenberg-Kohn établit que la densité à une particule $n(\mathbf{r})$ détermine de manière univoque toutes les propriétés du système dans son état fondamental. L'énergie totale peut être exprimée comme un fonctionnel de la densité :

$$E[n] = F[n] + \int v_e(\mathbf{r})n(\mathbf{r})\, d^3r,$$

où $F[n]$ est un fonctionnel universel comprenant les contributions cinétiques, directes (Hartree) et d'échange-corrélation, et où v_e est le champ externe auquel est soumis le système. Le théorème garantit que la densité minimisant $E[n]$ représente l'état fondamental du système. Cependant, comme la forme exacte de $F[n]$ est inconnue, la DFT repose sur des approximations phénoménologiques. La minimisation de $E[n]$, en supposant des orbitales à une particule, conduit aux équations de Kohn-Sham, formellement similaires à celles de Schrödinger.

L'approche de référence pour les systèmes nucléaires est l'approximation de *Hartree-Fock* (HF), qui suppose un état fondamental exprimé comme un déterminant de Slater Φ de fonctions d'onde à particule unique. L'énergie du système est donnée par :

$$E_{HF} = \langle \Phi | T + V | \Phi \rangle,$$

où T représente l'énergie cinétique et V l'interaction effective entre nucléons. La variation de cette énergie par rapport aux fonctions d'onde produit les équations de champ moyen, analogues aux équations de Kohn-Sham. La théorie Hartree-Fock peut être réécrite dans le cadre, plus général et en principe exact, de la DFT.

L'introduction d'interactions effectives dépendantes de la densité a représenté un progrès fondamental. De telles interactions, comme celle de Skyrme, permettent de reproduire précisément les énergies de liaison et le comportement de saturation de la matière nucléaire. La force de Skyrme, à portée nulle, simplifie considérablement les calculs et est l'une des EDF les plus utilisées. Alternativement, la force de Gogny introduit des termes à portée finie mais conserve une structure dépendante de la densité similaire à Skyrme. Ces modèles, bien que phénoménologiques, ont montré un grand succès dans la description des propriétés nucléaires statiques et dynamiques. Cependant, la précision expérimentale de nombreuses observables, comme les énergies de liaison ou les rayons de charge, dépasse encore aujourd'hui les capacités des EDF.

La théorie est également valable pour décrire les excitations collectives via la *Random Phase Approximation* (RPA), obtenue comme limite linéaire de la théorie dépendante du temps (TDDFT) ou du formalisme particule-trou. La RPA considère les excitations collectives des noyaux, les *résonances géantes*, comme des combinaisons linéaires de configurations particule-trou. Les résonances géantes comprennent des oscillations de natures différentes : isoscalaires, où protons et neutrons oscillent en phase, et isovectorielles, où ils oscillent en opposition de phase. Elles sont classées selon le moment angulaire L et le spin S (monopole, dipôle, quadrupole, etc.). En RPA, on peut obtenir les énergies d'excitation de ces résonances en accord raisonnable avec les observations expérimentales. Cependant, les largeurs ne sont pas correctement reproduites. Des méthodes plus sophistiquées, comme la seconde RPA ou le *particle-vibration coupling*, améliorent significativement cette description.

Le formalisme EDF est également utile pour décrire la matière nucléaire. La matière nucléaire est un système infini et uniforme de protons et neutrons à température nulle, interagissant uniquement par la force nucléaire. Bien qu'il s'agisse d'une idéalisation, elle décrit correctement l'intérieur des noyaux, où la densité est presque constante et les interactions nucléaires dominent, ainsi que l'intérieur des étoiles à neutrons, caractérisé par des densités supérieures à la densité de saturation. Les noyaux renseignent sur la matière symétrique ou presque symétrique, tandis que les étoiles à neutrons permettent d'étudier la matière fortement asymétrique.

Un aspect d'intérêt particulier est l'équation d'état nucléaire (nEOS), c'est-à-dire l'énergie par particule e en fonction de la densité baryonique totale $n_B = n_n + n_p$ et de l'asymétrie d'isospin $\delta = (n_n - n_p)/n_B$. Ainsi, $e(n_B, 0)$ représente la matière symétrique, et $e(n_B, 1)$ la matière pure de neutrons. On peut développer $e(n_B, \delta)$ par rapport à δ :

$$e(n_B, \delta) \approx e(n_B, 0) + S(n_B)\delta^2 + o(\delta^4),$$

où seuls les termes pairs sont conservés en raison de la symétrie d'isospin. $S(n_B)$ définit l'énergie de symétrie, représentant l'énergie nécessaire pour transformer tous les protons en neutrons.

La force nucléaire est caractérisée par le phénomène de saturation : les expériences de diffusion d'électrons montrent que la densité interne des noyaux est approximativement constante et vaut environ 0.16 fm^{-3}, indépendamment du noyau, ce qui implique une pression nulle dans le bulk nucléaire. Comme la matière au cœur des noyaux est presque symétrique, cela implique que $e(n_B, 0)$ atteint un minimum autour de 0.16 fm^{-3}, définissant ainsi n_{sat}, la densité de saturation nucléaire. Les dérivées de $e(n_B, 0)$ et $S(n_B)$

par rapport à la densité définissent les paramètres de la matière nucléaire (NMP) :

$$e(n_B, 0) = \sum_{k=0}^{4} \frac{1}{k!} \left(\frac{n_B - n_{\rm sat}}{3n_{\rm sat}} \right)^k X^k_{sat} + o(n_B - n_{\rm sat})^5,$$

$$S(n_B) = \sum_{k=0}^{4} \frac{1}{k!} \left(\frac{n_B - n_{\rm sat}}{3n_{\rm sat}} \right)^k X^k_{sym} + o(n_B - n_{\rm sat})^5,$$

avec

$$X^k_{sat} = (3n_{sat})^k \frac{\partial^k e(n_B, 0)}{\partial n_B^k}\bigg|_{n_B = n_{sat}}$$

$$X^k_{sym} = (3n_{sat})^k \frac{\partial^k S(n_B)}{\partial n_B^k}\bigg|_{n_B = n_{sat}}$$

Les NMP isoscalaires incluent : $E_{sat} = X^0_{sat}$, énergie par particule à saturation ; $L_{sat} = X^1_{sat} = 0$ (définition de n_{sat}) ; $K_{sat} = X^2_{sat}$, l'incompressibilité. Les paramètres d'ordre plus élevé (Q_{sat}, Z_{sat}) sont difficiles à déterminer, car les noyaux sondent uniquement les densités proches de n_{sat}.

De même, les paramètres de symétrie sont : $E_{sym} = X^0_{sym}$; $L_{sym} = X^1_{sym}$, relié à la pression de la matière neutronique à n_{sat} ; $K_{sym} = X^2_{sym}$, difficile à déterminer en raison de sa corrélation avec L_{sym}.

Les expériences nucléaires et les observations astrophysiques aident à contraindre les NMP. Les rayons nucléaires montrent que les densités internes sont constantes et valent n_{sat}, tandis que les énergies de liaison montrent que $e(n_{sat}, 0) \approx -16$ MeV. Les mesures de la *neutron skin* via la diffusion d'électrons polarisés donnent des informations sur L_{sym}. Les résonances géantes isoscalaires renseignent sur K_{sat}, tandis que les isovectorielles (polarizabilité dipolaire) sont liées à l'énergie de symétrie.

Les étoiles à neutrons explorent des densités bien supérieures à n_{sat}, ce qui en fait des laboratoires uniques. Leurs propriétés — masse, rayon, déformabilité tidale — dépendent directement de l'EOS, et donc des NMP.

Pour obtenir la nEOS à partir d'un EDF, il suffit de conserver les termes qui subsistent dans la matière uniforme, en éliminant les gradients et l'interaction spin-orbite.

Neutron stars

Les étoiles à neutrons sont ce qui reste de l'effondrement gravitationnel d'étoiles massives après l'épuisement du combustible nucléaire. À la suite de l'explosion de supernova, le cœur de l'étoile originale se contracte jusqu'à atteindre des densités comparables ou supérieures à la densité de saturation n_{sat}. Dans ces conditions, les protons et les électrons se combinent par capture électronique, donnant naissance à un fluide dense de neutrons dégénérés, d'où le nom d'étoile à neutrons.

L'équilibre hydrostatique de tels objets est décrit par les équations de Tolman Oppenheimer Volkoff (TOV), qui représentent la généralisation relativiste des équations classiques d'équilibre hydrostatique. La solution de ces équations nécessite la connaissance de l'équation d'état (*equation of state*, EOS) de la matière stellaire, laquelle exprime la dépendance de la pression P par rapport à la densité baryonique n_B, constituant ainsi le principal lien entre la microphysique nucléaire et les observations astrophysiques.

La structure d'une étoile à neutrons peut être idéalement divisée en différentes régions concentriques, chacune caractérisée par une composition et un comportement physique spécifiques. La couche la plus externe, appelée croûte externe, est constituée de noyaux lourds plongés dans un gaz d'électrons dégénérés. En progressant vers l'intérieur, la pression croissante induit la capture d'électrons par les protons, produisant des noyaux de plus en plus riches en neutrons. Lorsque la densité dépasse le *neutron drip point* ($\sim 10^{-4}\,\mathrm{fm}^{-3}$), les neutrons commencent à s'échapper des noyaux et forment un fluide libre coexistant avec le réseau cristallin de noyaux, marquant le passage à la croûte interne. Cette région, qui s'étend jusqu'à des densités proches de $0.08\,\mathrm{fm}^{-3} \sim n_{sat}/2$, présente un intérêt particulier, car les neutrons libres y forment un superfluide macroscopique, influençant certains phénomènes caractéristiques des étoiles à neutrons, tels que les *glitches*. Dans les couches les plus profondes de la croûte interne, il est supposé que des noyaux adoptent des configurations exotiques appelées *pasta phases*, résultant de l'équilibre entre les forces nucléaires et coulombiennes.

Au-delà de la croûte interne se trouve le cœur (*core*) de l'étoile, où les neutrons et les protons forment un fluide homogène fortement interagissant, avec des électrons et des muons assurant la neutralité électrique. Dans cette région, la composition chimique est déterminée par l'équilibre β et par la condition de neutralité électrique : les réactions $n \leftrightarrow p + e^- + \bar{\nu}_e$ fixent le rapport entre neutrons et protons, tandis que l'apparition des muons se produit lorsque le potentiel chimique des électrons dépasse la masse du muon. Le comportement de la matière nucléaire dans de telles conditions est régi par l'EOS, elle-même dérivée de la nEOS. Différentes EOS peuvent varier en termes de rigidité, c'est-à-dire en fonction de la réponse de la pression à l'augmentation de densité : des EOS plus rigides produisent des étoiles à neutrons avec une masse maximale plus élevée et un rayon plus grand, tandis que des EOS plus molles conduisent à des configurations plus compactes.

En résolvant les équations TOV pour différentes conditions initiales, on obtient une relation entre la masse et le rayon d'une étoile à neutrons. La relation masse-rayon représente l'un des principaux outils observationnels pour tester les modèles microscopiques de la matière dense, puisque l'unique inconnue dans les équations TOV est l'EOS, qui représente notre hypothèse concernant le comportement de la matière à l'intérieur des étoiles. Les observations de pulsars binaires ont permis de déterminer avec grande précision des masses proches de deux masses solaires, comme pour les sources PSR J0348+0432 et PSR J0740+6620. En revanche, la mesure des rayons est plus complexe et sujette à d'importantes incertitudes systématiques, mais les observations en rayons X de la mission NICER permettent de mesurer simultanément masse et rayon d'une seule étoile, déterminant ainsi une région dans le plan masse-rayon que la courbe imposée par les TOV doit traverser.

Une autre observable astrophysique importante dépendant uniquement de l'EOS est la déformabilité tidale. Un système binaire d'étoiles à neutrons émet continuellement des ondes gravitationnelles. Avec le temps, la distance entre les deux étoiles diminue, et elles se déforment progressivement sous l'effet du champ gravitationnel de la compagne. À l'approche de la coalescence (*binary neutron star merger*, BNM), les ondes gravitationnelles sont fortement modifiées par cette déformation et, en les détectant, on peut mesurer la déformabilité tidale (comme lors de l'événement GW170817).

Comme mentionné précédemment, l'EOS se calcule, dans les différentes régions de l'étoile, à partir de la nEOS. Dans la croûte interne, il faut tenir compte de la présence du réseau cristallin : on divise souvent l'espace en cellules selon l'approximation de Wigner–Seitz, couplée à des techniques Hartree–Fock–Bogoliubov ou Extended Thomas Fermi pour en déterminer la composition idéale. Dans le cœur de l'étoile, on minimise l'énergie du gaz de protons, neutrons, électrons et muons, sous les contraintes d'équilibre β et de neutralité électrique. L'EOS représente donc le lien fondamental entre la microphysique des interactions nucléaires et la macrophysique des observations astrophysiques. Si une EOS prédit des propriétés stellaires incompatibles avec les observations, elle doit être rejetée.

Parmi les différentes approches possibles pour décrire la matière nucléaire à des densités supérieures à la saturation, le méta-modèle (MM) est certainement l'une des plus flexibles. Il a été conçu pour imiter le comportement des nEOS de type Skyrme en dessous de la saturation, tout en laissant une plus grande liberté au-dessus. Ses paramètres sont les NMP définis dans le premier chapitre. Nos analyses sur les étoiles à neutrons seront effectuées à l'aide de cet outil mathématique.

Bayesian inference with Skyrme EDF

Nous voulons donc, dans un premier temps, étudier les propriétés de la matière nucléaire à travers les expériences sur les noyaux. Nous présenterons les résultats d'une analyse des paramètres du fonctionnel de Skyrme, avec pour objectif d'obtenir une estimation quantitative des incertitudes théoriques et la capacité de reproduire simultanément une série d'observables de nature différente (*ground state*, excitations collectives). Grâce à l'inférence bayésienne, nous pouvons reconstruire la distribution de probabilité des paramètres d'un modèle, au lieu d'estimations ponctuelles de leurs meilleures valeurs. Cela permet d'évaluer plus précisément leurs incertitudes et d'étudier leur pouvoir prédictif.

Nous avons effectué deux inférences : l'une utilisant uniquement des noyaux doublement magiques, l'autre incluant également des noyaux open-shell. La différence réside uniquement dans le choix des observables ; pour le reste, le *setup* est identique. Nous avons exprimé les paramètres usuels $t_0, x_0, \ldots$ de Skyrme en fonction de cinq NMP (n_{sat}, E_{sat}, K_{sat}, E_{sym} et L_{sym}), des masses effectives isoscalaires m_0^*/m et isovectrices m_1^*/m, de deux paramètres de surface G_0 et G_1, ainsi que du paramètre de spin-orbite W_0. Comme l'expérience passée nous donne une idée des intervalles dans lesquels ces paramètres sont susceptibles de se trouver, nous avons supposé un *prior* uniforme.

Pour les observables, nous avons sélectionné des propriétés de l'état fondamental et des propriétés d'excitations collectives. Pour le *ground state*, nous utilisons les énergies de liaison $B.E.$, les rayons de charge R_{ch} et les splittings spin-orbite ΔE_{SO}, en leur assignant comme incertitude la précision typique avec laquelle les EDF parviennent à reproduire ces observables (2 MeV pour $B.E.$, 0.05 fm pour R_{ch} et 0.5 MeV pour ΔE_{SO}). Pour les résonances isocalaires et isovectrices, nous avons choisi les énergies des résonances géantes isoscalaires de monopole (ISGMR) et de quadrupole (ISGQR) E_{GMR}^{IS}, E_{GQR}^{IS}, avec des incertitudes de 0.5 MeV, ainsi que la *energy weighted sum rule* EWSR $m(1)$ de la résonance géante de dipole isovectrice (IVGDR), la polarisabilité α_D et l'asymétrie à parité violée A_{PV}. Pour ces trois dernières, nous avons utilisé les incertitudes expérimentales.

Nous utilisons le code `hfbcs-qrpa` pour calculer toutes les observables à partir d'un ensemble de paramètres, en employant les techniques Hartree–Fock pour les propriétés du *ground state* et la RPA pour les états excités ; seule exception : A_{PV}, pour laquelle nous utilisons le code ELSEPA.

L'inférence bayésienne, pour échantillonner la *posterior*, nécessite de calculer, pour plusieurs millions d'ensembles de paramètres, la valeur de chaque observable. C'est une méthode applicable uniquement si nos méthodes numériques ont un temps d'exécution quasi instantané. Au contraire, les calculs RPA nécessitent plusieurs minutes. Pour contourner ce problème, nous employons un émulateur, le logiciel MADAI, basé sur les processus gaussiens. Ce logiciel, apprenant à partir d'une grille de résultats représentatifs des codes `hfbcs-qrpa` et ELSEPA, est capable d'émuler tous leurs résultats en un temps négligeable. Comme le résultat de l'inférence dépend de la capacité de l'émulateur à reproduire correctement les codes originaux, nous évaluons sa *performance* dans ce que nous appelons la validation. À partir d'un échantillon de paramètres de test, la validation compare les valeurs émulées aux résultats du code original ; un émulateur est jugé acceptable si au moins 90% des points tombent dans l'intervalle d'erreur. Toutes les inférences ont satisfait ce critère.

Dans la première inférence, nous considérons les observables des noyaux doublement magiques, en les ajoutant progressivement pour évaluer leur impact sur la *posterior* : d'abord les énergies de liaison et les rayons de charge, puis les splittings spin-orbite, puis les polarisabilités, ensuite les énergies d'excitation des résonances géantes et l'EWSR, et enfin les deux A_{PV}. Les masses et rayons contraignent respectivement E_{sat}, W_0 et n_{sat} ; les splittings spin-orbite réduisent légèrement la moyenne et la largeur de W_0 et favorisent des valeurs de m_0^* dans la partie haute de l'intervalle. K_{sat} et les masses effectives sont peu contraints jusqu'à l'inclusion des résonances, qui déterminent K_{sat}, m_0^*/m et m_1^*/m via l'EWSR IVGDR. La polarisabilité α_D resserre significativement E_{sym} et L_{sym}, initialement peu contraints mais reliés par une corrélation positive. L'inclusion des A_{PV} de ^{48}Ca et ^{208}Pb apporte quelques modifications légères dans les distributions de E_{sym} et L_{sym}, mais ne modifie pas drastiquement les valeurs déterminées par les polarisabilités. Les distributions marginales des paramètres comparées avec les Skyrme publiées montrent E_{sat} et n_{sat} compatibles, K_{sat} légèrement plus bas, masses effectives, G_0, G_1, et W_0 cohérents. En revanche, nous trouvons des valeurs de E_{sym} et L_{sym} plus basses que dans des études antérieures. Les résultats de la dernière inférence sont résumés dans la première colonne du tableau D.3.

La raison est la suivante : les énergies de liaison imposent des contraintes sévères sur la corrélation entre E_{sym} et L_{sym}. Les polarisabilités α_D de ^{208}Pb et ^{48}Ca présentent une dépendance très raide à L_{sym}. Les asymétries A_{PV}, en revanche, dépendent de manière plus douce de L_{sym}. Ce mécanisme pousse la solution vers des valeurs relativement basses de E_{sym} et L_{sym}, en particulier pour $E_{sym} \in (28, 30)$ MeV, où la *likelihood* présente un maximum net. Par conséquent, la demande simultanée de reproduire $B.E.$ et α_D dans les incertitudes expérimentales conduit à des *posteriors* concentrées vers des valeurs relativement basses des paramètres isovecteurs, expliquant la différence par rapport à d'autres études attribuant un poids moindre aux énergies de liaison.

Pour atténuer les possibles *bias* dus à l'usage exclusif de noyaux doublement magiques, particulièrement difficiles à décrire pour les EDF, nous avons étendu l'ensemble des observables aux noyaux open-shell, retirant les noyaux symétriques. Le nouvel ensemble comprend les énergies de liaison des isotopes de Ca, Sn et Pb, le rayon de charge de ^{50}Ca, et le gap de *pairing* neutronique Δ_n de ^{120}Sn. L'inclusion des noyaux ouverts requiert l'ajout du terme de *pairing* volumique de force v_0, traité comme un nouveau paramètre avec un *prior* uniforme $v_0 \in (150, 350)$ MeV fm^3.

Nous avons également mis à jour la valeur expérimentale de deux observables importantes : (i) l'énergie de la résonance monopolaire isoscalaires de ^{90}Zr, désormais mesurée à $E_{GMR}^{IS} = 18.7$ MeV, ce qui pousse K_{sat} vers des valeurs plus élevées et donc n_{sat} vers des valeurs légèrement plus basses ; (ii) les A_{PV}, qui nécessitent une correction QED. Cette correction réduit la valeur expérimentale effective, poussant L_{sym} vers des valeurs plus élevées en raison de la corrélation inverse entre A_{PV} et L_{sym}.

Les distributions *postérieures* résultantes montrent que n_{sat} et E_{sat} subissent des variations modérées dues principalement à la nouvelle valeur du monopole isoscalaires, tandis que E_{sym} et L_{sym} augmentent par rapport au cas sans open-shell : E_{sym} tend vers des valeurs autour de 30–32 MeV, et L_{sym} se déplace vers 25–40 MeV selon l'inclusion ou non de la A_{PV} de ^{208}Pb. Les autres paramètres (tels que G_0, G_1, W_0, et les masses effectives) restent globalement stables. Malgré la plus grande liberté introduite, la contrainte des

Table D.3: Moyennes μ et écarts types σ des distributions postérieures marginalisées pour toutes les inférences. Leurs unités sont : fm^{-3} pour n_{sat} ; MeV pour E_{sat}, K_{sat}, E_{sym} et L_{sym} ; MeV·fm^5 pour G_0, G_1 et W_0. Les masses effectives isoscalaire et isovectorielle $m^*_{0,1}/m$ sont des nombres.

		Seulement noyaux Doublement magiques	Nouvelles données + open-shell	Nouvelles données + open-shell (sans ^{208}Pb A_{PV})
n_{sat}	μ	0.161	0.160	0.160
	σ	0.004	0.003	0.003
E_{sat}	μ	−15.94	−16.08	−16.05
	σ	0.10	0.09	0.09
K_{sat}	μ	219	238	236
	σ	10	10	10
E_{sym}	μ	29.4	32.3	30.5
	σ	1.6	2.0	2.0
L_{sym}	μ	16.1	39.8	24.9
	σ	14.7	16.6	16.7
G_0	μ	125	133	129
	σ	10	12	11
G_1	μ	9	8	2
	σ	36	44	44
W_0	μ	129	134	132
	σ	15	17	17
m^*_0/m	μ	0.91	0.89	0.91
	σ	0.08	0.08	0.08
m^*_1/m	μ	0.71	0.71	0.71
	σ	0.02	0.02	0.02
v_0	μ	−	222	223
	σ	−	28	27

polarisabilités continue de favoriser des valeurs relativement basses de L_{sym}. Les résultats des inférences avec ou sans la A_{PV} de ^{208}Pb se trouvent dans les deux dernières colonnes du tableau D.3.

La qualité de la reproduction des observables demeure comparable à celle obtenue sans les noyaux open-shell. L'usage du nouveau E^{IS}_{GMR} dégrade la reproduction du monopole de ^{208}Pb, tandis que surgissent des doutes sur l'utilité d'inclure la A_{PV} de ^{208}Pb dans ces analyses, puisqu'elle a un effet notable sur les résultats sans que le modèle soit capable de la reproduire.

Bayesian Inference on Nuetron star properties

Nous utilisons maintenant la distribution *posterior* des fonctionnels de Skyrme précédemment obtenue comme *prior* dans une nouvelle inférence bayésienne, dans laquelle les observables proviennent cette fois d'observations astrophysiques.

L'inférence bayésienne évalue quelles EOS satisfont les contraintes astrophysiques, parmi lesquelles la masse maximale d'une étoile à neutrons, la déformabilité tidale de GW170817, les mesures masse–rayon de NICER, ainsi que des observables de la croûte comme le moment d'inertie, pertinent pour les *glitches* des pulsars.

L'EOS dans la croûte est calculée via l'approximation ETF, en paramétrisant les profils de densité par des fonctions de type Woods–Saxon. Nous introduisons des approximations supplémentaires pour réduire le coût computationnel, ce qui ramène le nombre de paramètres variationnels de 8 à 5. Malheureusement, l'algorithme rencontre des instabilités numériques avant la transition croûte–cœur. Pour cette raison, nous extrapolons linéairement la densité à laquelle a lieu cette transition comme la densité pour laquelle la phase inhomogène devient moins favorable énergétiquement que la phase homogène. Nous avons testé cette méthode sur l'interaction bien connue SLy4 et obtenu des résultats très proches de ceux publiés dans la littérature. Nous la comparerons, au niveau statistique, à des méthodes alternatives pour déterminer le point de transition : la croûte calculée avec le *compressible liquid drop model* (CLDM) ou avec l'instabilité spinodale dynamique.

Pour décrire la matière homogène dans le cœur de l'étoile, au lieu d'utiliser directement la nEOS issue de Skyrme, nous employons son équivalent MM. La correspondance Skyrme MM est conçue de telle sorte qu'à densité sous-saturation, où les informations provenant des expériences nucléaires sont les plus pertinentes, le MM se comporte comme Skyrme ; à densité supra-saturation, où les contraintes sont faibles, le comportement du MM peut diverger radicalement de celui de Skyrme.

La *likelihood* totale combine les informations de : la masse maximale de PSR J0740+6620, la déformabilité tidale de GW170817, les mesures masse–rayon de NICER, et la cohérence avec les bandes de χEFT pour la matière neutronique. Pour estimer la *posterior*, nous extrayons 10^5 échantillons du *prior* nucléaire ; pour chacun, nous calculons l'EOS en β-équilibre et éliminons les modèles instables (pression décroissante avec la densité) ou acausaux (vitesse du son supérieure à celle de la lumière). La distribution des modèles restants, pondérée par la *likelihood*, constitue la *posterior*.

Examinons maintenant les résultats. Les distributions des paramètres isoscalaires sont similaires entre *prior* et *posterior*, à l'exception de Q_{sat}, qui est déplacé vers des valeurs positives par les observations astrophysiques, indiquant que le secteur isoscalaires est déjà bien contraint par les données de physique nucléaire, sauf à hautes densités, où la nécessité de soutenir des étoiles à neutrons très massives requiert un durcissement de l'EOS. Les paramètres isovecteurs sont principalement influencés par les contraintes théoriques chirales, avec une augmentation des valeurs moyennes de E_{sym} et L_{sym}, tandis que les contraintes astrophysiques apportent des modifications marginales. Les paramètres de surface et les masses effectives sont bien déterminés par les données de structure nucléaire et ne sont pas significativement modifiés par les contraintes supplémentaires.

Les *corner plots* mettent en évidence les corrélations entre les paramètres, confirmant que l'information astrophysique n'altère pas les corrélations imposées par les données nucléaires. L'énergie par particule de la matière de neutrons pure (PNM) calculée avec Skyrme montre une bonne compatibilité avec les prédictions chirales, la *posterior* coïncidant fortement avec la bande prédite par les calculs *ab initio*.

Concernant le point de transition croûte–cœur (*crust–core*, CC), le *posterior* bayésien indique des valeurs de densité n_{cc} et de pression P_{cc} cohérentes entre les estimations ETF et CLDM, tandis que l'estimation fondée sur l'instabilité spinodale dynamique tend à sous-estimer à la fois la valeur moyenne et la dispersion, fournissant ainsi une limite inférieure. La composition de la croûte, calculée via la méthode variationnelle ETF, montre une augmentation du nombre de nucléons du cluster et de la densité du gaz de neutrons vers le cœur, tandis que le nombre de protons Z décroît, reflétant l'enrichissement en neutrons.

En ce qui concerne les propriétés globales de l'étoile, le rayon de la croûte R_c et le moment d'inertie I_c sont fortement corrélés aux propriétés de la transition croûte–cœur et montrent une bonne convergence entre ETF et CLDM, tandis que l'approche spinodale fournit des valeurs inférieures.

L'activité des *glitches*, telle qu'observée dans le pulsar Vela, peut être expliquée par le moment d'inertie de la croûte si l'on adopte un scénario d'*entrainment* minimal, dans lequel seuls les neutrons liés au cluster contribuent au moment d'inertie superfluide, compatible avec les observations sauf si la masse de Vela dépasse $2M_\odot$. En cas de fort *entrainment*, l'explication croûtale des *glitches* ne serait possible que pour des masses stellaires très faibles ($M \lesssim 1.1M_\odot$).

L'EOS de l'étoile et la densité d'énergie montrent une faible dépendance à l'interaction nucléaire jusqu'à environ $4n_{sat}$. La pression résultante est en accord avec les contraintes déduites des observations GW170817, mais avec des distributions plus étroites, mettant en évidence l'apport informatif de la physique nucléaire. L'EOS est souple près de la saturation et se rigidifie rapidement pour permettre d'atteindre la masse maximale observée de $2M_\odot$. La vitesse du son augmente rapidement entre 1 et $2n_{sat}$, correspondant au durcissement de l'EOS. L'énergie de symétrie est bien déterminée jusqu'à la saturation et plus dispersée à hautes densités, reflétant la liberté des paramètres d'ordre supérieur.

Enfin, la relation masse–rayon montre de bonnes correspondances avec les données NICER et avec les résultats antérieurs, avec des distributions plus étroites et des rayons légèrement plus petits pour les étoiles de masse inférieure à $1.5M_\odot$, conséquence directe de la souplesse de l'énergie de symétrie déduite des données de structure nucléaire.

Conclusions

In cette thèse, nous avons étudié les propriétés de l'équation d'état nucléaire au moyen d'une approche bayésienne en deux étapes : la première basée sur des données expérimentales nucléaires, la seconde utilisant les résultats de la première pour analyser des observations d'étoiles à neutrons. Nous avons employé le traditionnel EDF de Skyrme dans un *framework* bayésien, en considérant les propriétés de l'état fondamental (énergies de liaison, rayons de charge, splitting spin-orbite) ainsi que les états excités (résonances géantes isoscalaires et isovectrices), y compris l'asymétrie violant la parité A_{PV} et la polarisabilité dipolaire α_D pour ^{48}Ca et ^{208}Pb. Ces observables sont pertinentes pour la matière asymétrique et pour l'étude des NS, bien qu'aucun modèle ne reproduise simultanément ^{208}Pb A_{PV} et les autres observables au niveau 1σ, révélant la tension PREX–CREX.

En raison du coût computationnel élevé des calculs, nous avons utilisé des emulateurs basés sur des processus gaussiens via le paquet MADAI. Les premières inférences ont porté sur des noyaux doublement magiques, en ajoutant progressivement des contraintes afin d'en comprendre l'influence. Les posteriors multidimensionnels des paramètres de Skyrme, exprimés en termes de paramètres de la matière nucléaire, ainsi que de paramètres de surface et de spin-orbite de l'EDF, sont cohérents avec la littérature antérieure, à l'exception de L_{sym} et, dans une moindre mesure, de E_{sym}, qui résultent plus faibles ($L_{sym} = 16.1 \pm 14.7$ MeV, $E_{sym} = 29.4 \pm 1.6$ MeV). Ces valeurs basses proviennent de la nécessité de reproduire simultanément les énergies de liaison et la polarisabilité dipolaire, alors que ^{208}Pb A_{PV} exigerait un L_{sym} plus élevé, accentuant la tension.

En affinant le *dataset*, en incluant des noyaux open-shell et en retirant ceux avec $N = Z$, les posteriors de E_{sym} et L_{sym} augmentent ($E_{sym} = 32.3 \pm 2.0$ MeV, $L_{sym} = 39.8 \pm 16.6$ MeV), tandis qu'en excluant ^{208}Pb A_{PV}, on obtient des valeurs plus modérées ($E_{sym} = 30.5 \pm 2.0$ MeV, $L_{sym} = 24.9 \pm 16.6$ MeV). Les résultats restent compatibles avec la majorité des observables, bien que la tension PREX–CREX persiste, nécessitant de nouvelles expériences telles que MREX.

La seconde partie de la thèse a utilisé les posteriors nucléaires comme prior pour une analyse bayésienne de l'EOS des NS, combinant des contraintes provenant de la masse maximale observée, de la déformabilité tidale de GW170817, des mesures simultanées masse–rayon de NICER et des calculs *ab initio* de la matière neutronique à basse densité. L'approche intégrée permet de prendre correctement en compte les corrélations nucléaires et améliore l'estimation de la transition croûte–noyau. Nous trouvons une EOS plus molle autour de la saturation, avec une concavité dans $n_{sat} \lesssim n_B \lesssim 2n_{sat}$, reflétant l'énergie de symétrie molle issue des données nucléaires. Les contraintes astrophysiques influencent significativement E_{sym} et L_{sym}, déplaçant leurs distributions autour de 30 MeV et excluant les valeurs négatives de L_{sym} incompatibles avec χEFT.

Ce travail fournit une base pour des études futures, incluant des EDF plus flexibles (par exemple Fayans, Gogny, RMF ou KIDS) afin de réduire les incertitudes liées au modèle, ainsi que des techniques bayésiennes avancées comme le *model mixing* pour obtenir des distributions de paramètres de la matière nucléaire plus indépendantes du modèle utilisé. Il est également important d'identifier l'ensemble minimal d'observables nucléaires nécessaires pour contraindre la matière nucléaire et d'améliorer la modélisation de la croûte avec des méthodes plus raffinées comme ETF ou HFB combinées à des emulateurs. De nouveaux posteriors nucléaires basés sur des EDF différents pourraient avoir un impact significatif sur l'étude de l'EOS des NS, en particulier pour les paramètres d'ordre supérieur et les densités extrêmes.

Publication List

- **P. Klausner et al.**, Microscopic calculation of the pinning energy of a vortex in the inner crust of a neutron star - doi.org/10.1103/PhysRevC.108.035808
- **P. Klausner et al.**, Impact of ground-state properties and collective excitations on the Skyrme ansatz: A Bayesian study - doi.org/10.1103/PhysRevC.111.014311
- **P. Klausner et al.**, Neutron Star crust informed by nuclear structure data - arXiv:2505.16929 (*submitted to PRC, under peer-review*)
- **P. Klausner et al.**, Bayesian inferences of Skyrme Energy Density Functionals - *EPJ Web Conf., accepted, in publication*

Acknowledgements

I have always believed that one of the most interesting parts of a thesis is the acknowledgements. They allow you to peek into the life of the otherwise mysterious student who wrote the manuscript. Who was that person? What did they love to do? Who were the people who supported them during the challenging journey of the PhD? During these three years, whenever I happened to read a thesis, I always made sure to look at the acknowledgements, trying to know a little better the person whose hard work I was studying and trying to understand. Now it is my turn, and I hope that this short page will be interesting for future readers stumbling across my thesis.

First, I would like to thank Professor Niels Paar, Dr. Esra Yüksel, Dr. Wouter Ryssens, and Dr. Anthea Fantina for kindly accepting to be jury members and for coming to Milano for the defence. I would also like to thank Professor William Newton and Dr. Esra Yüksel (a second time) for carefully reading the first draft of this manuscript and for the useful comments and insightful observations that improved the final version.

I am deeply grateful to my supervisors, Gianluca and Francesca. Your guidance has been essential for the completion of this work, and I will cherish it forever. In this regard, I wish to express my profound gratitude to Xavi as well, who was my supervisor during the first year of the thesis and introduced me to the world of scientific research. I also want to show my appreciation to Enrico for his guidance and for the constant interest he showed in my work.

Besides the excellent mentors I had, I was also extremely lucky with the colleagues I found, both in Milano and in Caen. A heartfelt appreciation goes to the whole Milano nuclear group. Giovanna, Simone, Agnese, Silvia, Franco, Oliver, and my fellow PhD students: Francesco, my first office mate, Marta, Imane (okay, you were a postdoc in Milano, but we are past the formality part now :)), Stefano, Fabio, Davide, Massi, and Giacomo. Every day in my very cold/very hot office was lighter and easier thanks to you. I also wish to thank Rossella, Matilde, and Davide, who are not part of the nuclear group, but with whom I shared a very... scary part of my PhD journey.

When I moved to Caen, I was a bit disoriented. I had never left Milano and my safe space before, and I was a bit scared; as it turned out, already after the first week, those fears were groundless. Thanks to the incredible people I found there, the year I spent in Normandy felt like a month. First, the PhD students of LPC: Guille, Raissa, Audrey, Alex, Ivan, Aurelien, Louis, Victor, Adarsh, Francesco... you guys were great. Then all the other people I met in the lab or through the lab: Phil, Giulia, Chantal, Chiara, Laura, and Caterina. Curiously, all of you (yes, you too, Phil!) are Italian. I'm told we tend to cluster together when we are abroad.

In the memories of my French adventure, a special place is occupied by my three office mates: Andrej, Kaciel, and Romain. I cannot even begin to express my gratitude to you three. We were indeed the best office, with the best door too! Finally, I want to end my *remerciements français* with my Italian family: Sara and the other three penguins, Marco, Bianca, and Luigi. I am so, so happy to have met you, and I will always cherish the incredible memories we forged together.

The people I am grateful to are not limited to the academic world. First, my friends from the Canottieri, with whom I shared many outdoor adventures: Annalaura, Borella, Camilla, Colombo, Maneo... well, for you I have said enough. You know where to look. Then Marcello, probably one of the best rowers I had the honour to row with and with whom I always love to talk about everything. And finally Cristiano, my fellow runner and "gymbro", thank you for running with me and listening to me vent about work and life. Well, for the first ten minutes of each run. You are too fast.

I also want to thank my university friends, Bea and Dave, with whom I hope one day I will play diendi again, Camilla, with whom I hope to defeat another deadly virus, and Stefano and Noemi; and my lifelong friends Leo, Giovanni, Mattia, Sara, Chiara, Martina, and Calca. We've known each other for more or less fifteen years; let's hope we will still spend time together for at least the next fifteen.

A special thanks goes to my family: Flavia with the immaculate Cooper, la Zia Genni, lo Zio Ippo, Maddalena, my dearest cousin Alice, to whom I will always be grateful for introducing me to physics, and my mother, the strongest woman I know, always able to weather the most ferocious storms.

And, finally, thank you, Marina. Where would I be without you?